Metasurface Polarimetry: Fabrication and Characterization of In-line Stokes Polarimeters Based on Polarization Sensitive Nanoantenna Arrays

Michael Juhl

Faculty of Physical Sciences
University of Iceland
2018

Metasurface Polarimetry: Fabrication and Characterization of In-line Stokes Polarimeters Based on Polarization Sensitive Nanoantenna Arrays

Michael Juhl

Dissertation submitted in partial fulfillment of a
Philosophiae Doctor degree in Physics

Advisor
Kristján Leósson

PhD Committee
Kristján Leósson
Hafliði P. Gíslason
J. P. Balthasar Müller

Opponents
N. Asger Mortensen
Slawomir M. Koziel

Faculty of Physical Sciences
School of Engineering and Natural Sciences
University of Iceland
Reykjavik, October 2018

Metasurface Polarimetry: Fabrication and Characterization of In-line Stokes Polarimeters Based on Polarization Sensitive Nanoantenna Arrays

Dissertation submitted in partial fulfillment of a *Philosophiae Doctor* degree in Physics

Faculty of Physical Sciences
School of Engineering and Natural Sciences
University of Iceland
Dunhagi 5
107, Reykjavik
Iceland

Telephone: +354 525-4000

Bibliographic information:
Michael Juhl, 2018, *Metasurface Polarimetry: Fabrication and Characterization of In-line Stokes Polarimeters Based on Polarization Sensitive Nanoantenna Arrays*, PhD dissertation, Faculty of Physical Sciences, University of Iceland, 173 pp.

ISBN 978-9935-9320-7-5

Printing: Háskólaprent
Reykjavik, Iceland, October 2018

Abstract

The polarization of electromagnetic waves (the direction of transversal vibration of its electric field vector) provides essential information about the emitting sources and scattering objects. Its measurement, i.e., optical polarimetry, has a history of more than 200 years and has found various applications in virtually every branch of science and technology.

Fabrication of optical metasurfaces that allow the manipulation of electromagnetic waves with sub-wavelength scale structures has become possible thanks to the rapid development of nanotechnology in the last 50 years. Metasurfaces have the potential of simplifying and miniaturizing existing optical components, including polarimeters.

This thesis explores the details of a promising metasurface design for the polarimetric measurement of light. This in-line (signal-saving) metasurface polarimeter is based on subwavelength-spaced phased arrays of gold nanorod antennas that provide an intensity modulation of scattered light depending on the polarization of the incident light to measure the full Stokes vector. An analytical model of the radiation pattern of the metasurface is presented and compared with numerical simulations. Polarimeters operating at telecom wavelengths have been fabricated in compact fiber-coupled packages, comprising an ultra-thin metasurface aligned to four or six photodetectors and characterized with high sampling rates. Non-terminating measurements of the polarization state of light by sampling only a small part of the total light intensity have been performed in in-plane and out-of-plane configurations. The error of the polarimeter has been analyzed and analytical and numerical models for the systematic error are presented.

The capacity of the miniatuarization of the metasurface polarimeter has been demonstrated by transferring the metasurface to the facet of a single-mode near-infrared optical fiber. To realize such a fiber-based metasurface polarimeter, a novel template stripping transfer lithography method has been developed. The gold nanopattern is stripped from a silicon wafer and transferred to the fiber facet by means of a UV-curable hybrid polymer. In-line polarimetric measurement has been demonstrated by measuring the intensity of four out-of-plane scattering orders while coupling the non-scattered light back into an optical fiber.

Útdráttur

Skautunarástand rafsegulbylgju veitir upplýsingar um uppsprettu hennar og eðliseiginleika þeirra hluta sem rafsegulbylgjan hefur víxlverkað við. Rafsegulbylgjur á ákveðnu tíðnibili köllum við ljós. Mælingar á skautunarástandi ljóss eiga sér yfir 200 ára sögu og hafa þær haft veruleg áhrif á flestum sviðum vísinda og tækni. Hin hraða þróun sem átt hefur sér stað á sviði nanótækni á síðustu árum hefur gert okkur kleift að móta yfirborð sem hafa áhrif á rafsegulbylgjur allt niður á sýnilega bylgjulengdasviðið og nýta til þess mynstur þar sem minnstu einingar eru minni en ein bylgjulengd. Slík yfirborð geta m.a. nýst til að einfalda og smækka íhluti sem notaðir eru í ljóstækni í dag, svo sem linsur og hvers kyns ljóssíur en einnig ljósskautunarmæla.

Í þessari ritgerð er rannsökuð hönnun yfirborðs til greiningar á skautunarástandi rafsegulbylgju fyrir nær-innrauðar bylgjulengdir. Yfirborðið er samsett úr fylki örloftneta úr gulli sem hvert um sig er um fjórðungur úr bylgjulengd að stærð. Saman dreifa loftnetin litlum hluta ljóssins sem lendir á yfirborðinu í ákveðnar stefnur, eftir því hvert upprunalegt skautunarástand ljóssins er. Með því að mæla ljósdreifinguna má fá mælingu á Stokes-vigur ljósbylgjunnar sem lýsir skautunarástandi hennar fyllilega.

Skautunarmælar ætlaðir sérstaklega fyrir þær bylgjulengdir ljóss sem nýttar eru í ljósleiðarasamskiptatækni voru hannaðir og smíðaðir með það fyrir augum að tengja þá beint við hefðbundna ljósleiðara. Skautunarmælarnir samanstanda af örþunnu yfirborði með fylki loftneta og fjórum eða sex ljósnemum sem geta mælt skautunarástandið á hárri mælitíðni, án verulegrar truflunar á upprunalega merkinu. Fræðilegt líkan af útgeislun yfirborðsins var smíðað og niðurstöður þess voru bornar saman við tölvuhermanir. Bornir voru saman skautunarmælar sem nýta ólíkar dreifingarstefnur ljóssins, bæði með reikningum og tilraunum. Mælinákvæmnin í skautunargreiningunni var metin og fræðileg líkön þróuð til að lýsa kerfisbundnum mæliskekkjum. Sýnt var fram á möguleika á smækkun ljósskautunargreinisins með því að flytja mynstur loftneta yfir á endaflöt ljósleiðara. Þróuð var sérstök aðferð til mynsturyfirfærslu af kísilskífum yfir á ljósleiðara með hjálp sérstakra lífrænna/ólífrænna blendingsfjölliða. Sýnt var fram á að þannig megi framkvæma skautunarmælingar beint á ljósleiðaranum sjálfum án þess að fórna mælinákvæmni og á sama tíma kúpla stærstum hluta ljósmerkisins aftur inn í annan ljósleiðara.

Table of Contents

List of Figures

List of Tables

List of Original Papers

[84] Michael Juhl, Carlos Mendoza, J. P. Balthasar Mueller, Federico Capasso, and Kristjan Leosson, "Performance characteristics of 4-port in-plane and out-of-plane in-line metasurface polarimeters," *Optics Express*, vol. 25, no. 23, pp. 28697-28709, 2017.

[106] Einar B. Magnusson, J. P. Balthasar Mueller, Michael Juhl, Carlos Mendoza, and Kristjan Leosson, "Neural Polarimeter and Wavemeter," *ACS Photonics*, vol. 5, no. 7, pp. 2682–2687, 2018.

[10] Noah Rubin, Aun Zaidi, Michael Juhl, Ruoping Li, J. P. Balthasar Mueller, Robert Devlin, Kristjan Leosson, and Federico Capasso, "Parallel polarization state generation and measurement with a single metasurface," *Optics Express*, vol. 26, pp. 21455-21478, 2018.

[108] Michael Juhl, J. P. Balthasar Mueller, and Kristjan Leosson. "Metasurface polarimeter on optical fiber facet by nano-transfer to UV-curable hybrid polymer," Submitted for publication, 2018.

Conference papers:

[105] Michael Juhl, Carlos Mendoza, J. P. Balthasar Mueller, Federico Capasso, and Kristjan Leosson, "Packaged inline metasurface polarimeters with in-plane and out-of-plane detection," in *The European Conference on Lasers and Electro-Optics*, Optical Society of America, 2017.

[107] Michael Juhl, Carlos Mendoza, J. P. Balthasar Mueller, Federico Capasso, and Kristján Leósson, "Self-aligned nano-transfer of metasurface polarimeter to an optical fiber tip using uv-curable hybrid polymer", In *Conference on Lasers and Electro-Optics*, page SF1J.8. Optical Society of America, 2018.

Acknowledgments

I am very grateful to Kristján Leossón for giving me the opportunity to study and construct metasurface polarimeters; a very interesting project spanning the fields of optics, nanotechology, and polarimetry. Thank you for the giving me the freedom to work independently and for all your help, advice, input, and for taking the time to revise my drafts thoroughly.

I would also like to thank J. P. Balthasar Müller for helping me getting started with the project, for inviting me to Harvard School of Engineering and Science (SEAS) and showing generous hospitality.

The contributions to the project by Carlos Mendoza and Einar Bui Magnusson are greatly appreciated. Carlos has designed and built the electronic circuit for data collection and programmed the microcontroller and Einar made the code for automatic measurement.

I want to thank Federico Capasso for giving me the opportunity to visit his group at Harvard SEAS, and Noah Rubin for inviting me to help with the characterization of his polarization grating metasurface polarimeter. It was a pleasure working together with Noah and Rouping Li. I learned a lot working with them, not only about science and computer programming, but also about their scientific methods.

I would also like to thank Unnar B. Arnalds, who has been very kind to help me with the equipment in the cleanroom at the University of Iceland, Birgir Jóhannesson, Jón Matthíasson from Nýsköpunarmiðstöð, and Kesara M. Jónsson from University of Iceland for help with electronic microscopes, Snorri Þ. Ingvarsson for loan of optical equipment, and all the people at Nýsköpunarmiðstöð and VRIII who helped during this project.

Special thanks goes to Nýsköpunarmiðstöð and the University of Iceland, who constructed the organizational frame for this PhD project.

I thank the Icelandic research fund for providing the financial means to the project and I thank AFOSR for covering travel expenses and acquisition of optical equipment.

Chapter 1

Introduction

In December of 1959, Richard Feynman gave a talk called "There's Plenty of Room at the Bottom" at an annual meeting of the American Physical Society at Caltech [1]. In this famous speech he laid the foundation for the fields of micro and nanotechnology by predicting the miniturization of computers, individual manipulation of atoms and micromachines. He even envisioned the face/object recognition that has now become reality through neural network algorithms in the field of computer vision. While addressing the subject of nanoscale electronic circuits, he anticipated the research on nanoantennas by posing the question: "Is it possible, for example, to emit light from a whole set of antennas, like we emit radio waves from an organized set of antennas to beam the radio programs to Europe?" Since then the development in semiconductor electronics has been a driving force in nanotechnology, enabling large-scale production of nano-scale structures. Technologies like electron-beam lithography, deep UV lithography and nano-imprint lithography have given scientists the ability to create sub-wavelength structures for operating in the visible and infrared frequency regimes of the electromagnetic spectrum [2, 3]. The field of metamaterials where the manipulation of electromagnetic waves with sub-wavelength structures in the microwave regime had already been studied, now found new opportunities in a large range of applications [4]. Since 3D materials are still relative difficult to fabricate, attention has gathered around 2D metamaterials, the so-called *metasurfaces*. Metasurfaces get the full benefit of recent technological advances by employing semiconductor processing technologies to create optical nano-structures on surfaces of materials. The field of metasurfaces is promising as it allows traditional bulk optics to be replaced with "flat optics," in addition to providing new functions that cannot easily be realized using conventional optics [5–7]. Furthermore, metasurfaces can be configured to operate in wavelength ranges where conventional optical elements are expensive or unavailable,

such as in the mid-infrared range. In the present project, engineered metasurfaces are applied to construct a *Stokes polarimeter*, to perform measurements of the full polarization state of light.

It has been speculated that the manipulation of the polarization properties of light using birefringent materials (a material with two modes of propagation with different refractive indices) has occured as early as the viking age, where the viking sailors might have used Iceland spar (or calcite, see Fig. 1.1) for navigational purposes [8]. However,

Figure 1.1. Photo of a calcite crystal, demonstrating double refraction.

it was not until the late 17th century that Rasmus Bartholin discovered the phenomenon of double refraction in Iceland spar [9]; a discovery that inspired C. Huygens to make a wave theory of light and much later, T. Young, A. Fresnel, and finally J. C. Maxwell to theorize the transverse nature of electromagnetic waves. The invention of polariod film in the 1920's presented a low-cost/high-volume alternative to calcite-based polarizers like Nicol prisms or Glan-Thompson prisms. However, for high precision polarization analysis, Glan-Thompson prisms are still one of the best choices because of their high extinction ratio [10].

For hundreds of years, most optical elements like lenses and polarizers have been fabricated using carefully polished pieces of glass or crystals and assembled in optical systems such as cameras, microscopes and polarimeters. Metasurfaces, on the other hand, represent an opportunity to reduce the cost, size, and complexity, not only of polarimeters [10–12], but also of a large range of existing devices such as flat lenses [13–15] and spectrometers [16].

The history of polarimetry dates back to 1815 when J. B. Biot demonstrated optical rotation in an organic material [17, 18]. A polarimeter design that is able to measure the complete polarization of light, i.e. the full information about the polarization, was invented in 1851 by G. G. Stokes [19]. It consists of a rotatable quarter-wave plate followed by a linear polarizer; both elements made of crystals. Despite of the size and cost of the crystals and the use of moving elements that affect the speed and accuracy of the system, this type of polarimeter is still produced and dominates in some applications. Several other methods have been demonstrated including fiber based polarimeters [20], liquid-crystal-based polarimeters [21], and polarimeters based on photoelastic modulators [22]. Different metasurface polarimeter designs can now be added to this list [23–25].

The aim of the project on which this thesis is based is to gain a thorough understanding of the scattering properties of polarization-sorting metallic metasurfaces and generate device designs for full Stokes vector characterization of incident light in an in-line geometry. Furthermore, the goal is to construct and test prototype polarimeter devices mainly for fiber-based applications.

1.1 Organization of this thesis

The outline of this thesis is as follows. In Chapter 2, the mathematical formalism and methodologies necessary for the following chapters are provided, including Jones and Stokes description of polarization, mathematical background for Stokes polarimetry, calibration procedure, and error propagation formulas. Chapter 3 contains an introduction to metasurfaces and an analysis of the nanoantenna-based polarization selective metasurface, including the presentation of an analytical model of the radiation pattern and numerical simulations. Chapter 4 describes the study of a parallel in-line metasurface polarimeter, fabricated both in compact fiber-coupled packages and directly on the facet of single-mode fibers, and measured in in-plane and out-of-plane configurations. The conclusions of the presented work are provided in Chapter 5. The appendix presents additional information.

Chapter 2

Introduction to polarimetry

Light is electromagnetic waves and represents a part of the electromagnetic spectrum (infrared, visible, ultraviolet). Electromagnetic waves consist of oscillating electrical and magnetic fields, characterized by their amplitude (related to its intensity or brightness), wavelength, velocity, coherence, and polarization. Measuring these characteristics is of interest in physics and applications ranging from lighting to heat dissipation, optical communication, laser cutting and surgery, optical material characterization and countless other examples. Much attention has been directed towards measurement of intensity and wavelength, but other properties of light are also very useful, especially the polarimetric information, which is crucial in a large number of applications. In materials characterization the measurement of polarization is used, e.g., to determine film thickness and refractive index [26]; in telecommunication it is used to monitor effects such as polarization-mode dispersion, polarization-dependent loss, and polarization dependent properties of optical devices [27]; in remote sensing the polarization information allows to distinguish between surfaces of different structures, remove clutter and image through dust and clouds [28]; in chemistry and biotechnology, polarization is used to measure the concentration and/or purity of optically active substances (such as sugars and antibiotics) using angle of rotation or evanescent chiral sensing [29], or to detect cancer or glaucoma in the human eye [30, 31]. Because of the geometric nature of polarization, however, it is not straightforward to measure. Advancing the field of polarimetry could therefore not only strengthen the known applications but also create new and exciting applications for the use of polarimetric information.

2.1 Polarization

Polarization is a property of light that describes the geometrical orientation of its electric field oscillation. If the wave is coherent, the direction of the field will follow a linear, circular or elliptical path in the plane perpendicular to the propagation direction of the light. In the language of quantum mechanics, polarization is associated with the spin angular momentum of light. A single photon can take a spin angular momentum of $\pm\hbar$ corresponding to left/right circular polarization. All linear and elliptical polarizations are obtained by superposition of these two states. However, the polarization of light can be fully described classically from Maxwell's equations.

$$\nabla \times \mathbf{E}(\mathbf{r},t) = -\mu_\circ \frac{\partial}{\partial t}\mathbf{H}(\mathbf{r},t) - \mu_\circ \frac{\partial}{\partial t}\mathbf{M}(\mathbf{r},t) \tag{2.1}$$

$$\nabla \times \mathbf{H}(\mathbf{r},t) = \varepsilon_\circ \frac{\partial}{\partial t}\mathbf{E}(\mathbf{r},t) + \frac{\partial}{\partial t}\mathbf{P}(\mathbf{r},t) \tag{2.2}$$

$$\nabla \cdot \varepsilon_o \mathbf{E}(\mathbf{r},t) = -\nabla \cdot \mathbf{P}(\mathbf{r},t) \tag{2.3}$$

$$\nabla \cdot \mathbf{H}(\mathbf{r},t) = -\nabla \cdot \mathbf{M}(\mathbf{r},t) \tag{2.4}$$

The field terms **E** and **H** are the two complementary components of the electromagnetic wave and the polarization density **P** and magnetization density **M** are means to describe the interaction of the electromagnetic field with matter. In a vacuum, the vectors **P** and **M** are zero and in that case the Helmholtz equation or the eletromagnetic wave equation can be derived from Maxwell's equations as

$$\nabla^2 \mathbf{E} = -\mu_o \varepsilon_o \frac{\partial^2}{\partial t^2}\mathbf{E} \tag{2.5}$$

A monochromatic solution to Eq. (2.5) is

$$\mathbf{E}(\mathbf{r},t) = \mathbf{E}_o e^{i(\omega t - \mathbf{k}\cdot\mathbf{r})} \tag{2.6}$$

Substituting this solution back in Gauss's law (Eq. (2.3)) it can be seen that the direction of the electric field vector is perpendicular to the propagation direction of the wave ($\mathbf{k}\cdot\ \mathbf{E} = 0$). Therefore, if the light is propagating in the z-direction, the electric field vector can be presented as

$$\mathbf{E}(z,t) = \begin{pmatrix} E_x e^{j\delta_x} \\ E_y e^{j\delta_y} \end{pmatrix} e^{i(\omega t - kz)} = E_x \cos(\omega t - kz)\hat{\mathbf{x}} + E_y \cos(\omega t - kz + \delta)\hat{\mathbf{y}} \tag{2.7}$$

δ is the relative phase shift. The column vector describing the amplitude of the field is called the Jones polarization vector. From Eq. (2.7) it is seen that the polarization can

be described as the superposition of two orthognal linear polarizations with amplitudes E_x and E_y and a relative phase shift $\delta = \delta_y - \delta_x$ between the x and y component. The Jones vector in normalized form is written as

$$\mathbf{E} = E_0 \begin{pmatrix} \cos(\psi) \\ \sin(\psi) e^{i\delta} \end{pmatrix} \tag{2.8}$$

where $E_0 = \sqrt{E_x^2 + E_y^2}$ and $\psi = \arctan(E_y/E_x)$. The revolution of the electric field of Eq. (2.7) describes the polarization ellipse that becomes a circle if the x and y amplitudes are equal, $E_x = E_y$ (equivalent to $\psi = \pi/4$) and the phase shift is $\delta = \pm\pi/2$, or collapses to a line if the relative phase difference is zero, see Fig. 2.1).

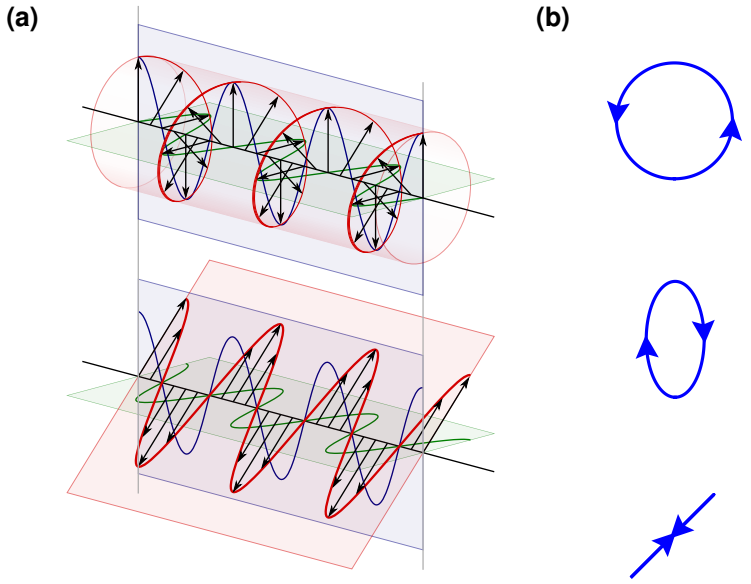

Figure 2.1. (a) Illustration of how all polarizations can be expressed as a superposition of two orthogonal linear polazations (green and blue lines). In the top image there is a $\pi/2$ phase shift resulting in circular polarization. In the bottom image there is no phase shift between the blue and green curve and the result is 45° linear polarization (from Wikimedia Commons). (b) Illustrations of different polariation as revolution of the field electric field in 2D. From top to bottom: left-hand circular polarization, right-hand elliptical polarization, 45° linear polarization.

The Jones description of polarization specifies the polarization directly from the electric field and it keeps track of the overall phase. However, the Jones vector only

describes a fully polarized wave. In order to define partially polarized light or unpolarized light a workaround like the coherency matrix is needed [32]. Furthermore, the Jones vector can't be measured directly, since the common phase information is lost in an intensity measurement. The Stokes vector provides an alternative description of polarization that includes both full and partial polarizations and can be measured directly. The Stokes vector is a 4-by-1 vector that is related to intensity measurements with an inherent averaging in time, and it is defined from the principal polarizations as [26, 32, 33]

$$\mathbf{S} = \begin{pmatrix} S_0 \\ S_1 \\ S_2 \\ S_3 \end{pmatrix} = \begin{pmatrix} I \\ pIs_1 \\ pIs_2 \\ pIs_3 \end{pmatrix} = \begin{pmatrix} \langle I_x \rangle + \langle I_y \rangle \\ \langle I_x \rangle - \langle I_y \rangle \\ \langle I_{45} \rangle - \langle I_{135} \rangle \\ \langle I_{RCP} \rangle - \langle I_{LCP} \rangle \end{pmatrix} \tag{2.9}$$

where S_0-S_3 are called the Stokes parameters, I is the intensity of the light beam, p is the degree of polarization (DOP), $s = (s_1, s_2, s_3)$ is the normalized state of polarization, and ps is the state of polarization (SOP). $I_x, I_y, I_{45}, I_{135}$ are intensities measured after a polarizer with the indicated polarizations and I_{RCP}, I_{LCP} are intensities measured after a polarizer and a quarter wave-plate with the ordinary axis rotated $\pm 45°$ from the transmission axis of the polarizer. In terms of Stokes parameters, the degree of polarization of a light beam is defined as

$$p = \frac{\sqrt{S_1^2 + S_2^2 + S_3^2}}{S_0} \tag{2.10}$$

where $p = 0$ corresponds to unpolarized light and $p = 1$ corresponds to fully polarized light. Since p is a value between 0 and 1, Eq. (2.10) can be written as an inequality.

$$S_0 \leq \sqrt{S_1^2 + S_2^2 + S_3^2} \tag{2.11}$$

The normalized SOP is related to the Jones vector by

$$s = \begin{pmatrix} s_1 \\ s_2 \\ s_3 \end{pmatrix} = \begin{pmatrix} \cos(2\psi) \\ \sin(2\psi)\cos(\delta) \\ \sin(2\psi)\sin(\delta) \end{pmatrix} \tag{2.12}$$

The polarization state is thus fully described by the three last elements in the Stokes vector. However, the intensity parameter (S_0) is necessary in order to distinguish between a change in intensity or DOP for a given measurement. The consequence of the averaging Stokes approach to describing polarization is that it is easily measured,

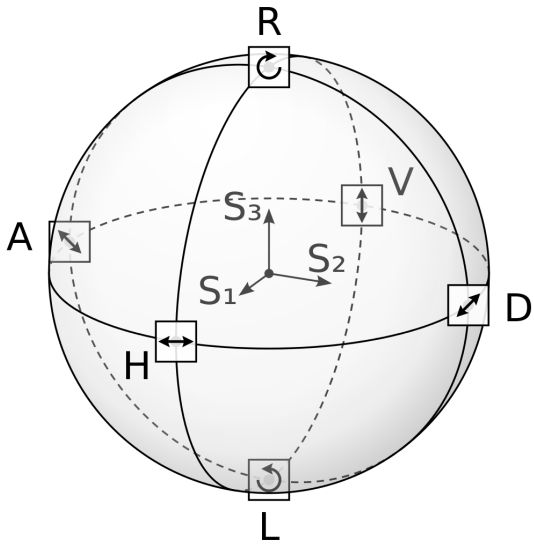

Figure 2.2. Illustration of the Poincaré sphere which is a geometric representation of all possible polarization states. The positions of the principal polarization states are shown (from Wikimedia Commons).

it contains information about partial polarization, while information about absolute phase is lost. The normalized SOP, s can be geometrically represented as a point on the surface of a unit sphere named the Poincaré sphere, see Fig. 2.2. All linear polarizations are represented as points on the equator, circular polarizations are at the poles and elliptical polarization constitute the rest of the points on the Poincaré sphere. Note that orthogonal polarizations are not perpendicular on the Poincaré sphere. Instead they are antinodal and separated by 180°. The graphical representation of a full Stokes vector would be a four-dimensional cone [34]. Inspired by the Poincaré sphere the polarization is sometimes expressed in spherical coordinates with the azimuth angle

$$\vartheta = \tfrac{1}{2}\arctan\left(\frac{S_2}{S_1}\right) \tag{2.13}$$

and the ellipticity

$$\varepsilon = \tfrac{1}{2}\arctan\left(\frac{S_3}{\sqrt{S_1^2+S_2^2}}\right) \tag{2.14}$$

From Eq. (2.10) the degree of polarization is a scalar value between 0 and 1. A monochromatic wave is fully polarized ($p = 1$) when all polarizations in a light beam oscillate coherently. The light from a laser is, for example, fully polarized. Partially

polarized light can be created from a laser beam if it is combined with an orthogonally polarized copy of itself delayed by more than the coherence time [10]. Sunlight is depolarized ($p = 0$), since it is completely incoherent, i.e. it has an uncorrelated phase across a band of wavelengths. For depolarized light, a polarizer rotated to any angle will always transmit half the incident intensity when averaged over time. The wave from an incoherent light source, like sunlight, can be polarized by placing a polarizer in the light path. Combining polarized incoherent light of orthogonal polarizations will result in depolarized light, whereas the combined polarized light of orthogonal polarizations from two monchromatic coherent light sources, like lasers, will result in a DOP of one, as long as the polarization is measured over a time scale much shorter than the coherence time of the lasers. This shows that the concepts of partially polarized light and depolarized light should be taken with care, because it is a result of an averaging which can be spectral, spatial or temporal, and therefore depends on the specific setup used for a particular experiment.

The change of a Stokes vector S as a result of its linear interaction with a transmitting, reflecting or scattering optical element or object like, e.g., a polarizer or a waveplate is represented by the matrix transformation [33]

$$\mathbf{S}' = \mathbf{MS} \tag{2.15}$$

with $\mathbf{M}$ being the so-called Mueller matrix, a 4×4 real-valued matrix. The Mueller matrix contains all the polarizing, retarding, depolarizating and absorbing properties of the optical element.

2.2 Stokes polarimetry

Due to the 4-dimensional nature of the Stokes vector, a complete Stokes polarimeter must perform at least four different intensity measurements. To carry out these measurements, the same amount of *polarization analyzers* are required. A polarization analyzer is an optical element whose intensity transmission is proportional to the content of a certain polarization state in the incoming electromagnetic wave [33]. Assuming linearity

the output intensities are related to the Stokes vector by an *analyzer matrix* **A**

$$\mathbf{I} = \mathbf{AS} = \begin{pmatrix} \mathbf{a}_1 \\ \mathbf{a}_2 \\ \vdots \\ \mathbf{a}_n \end{pmatrix} \mathbf{S} \tag{2.16}$$

where n is the number of measurements and the analyzer matrix consists of rows of four-element vectors, $\mathbf{a_1} - \mathbf{a_n}$, called *analyzer vectors*. The analyzer vectors contain the polarization that the polarization analyzer selects for, i.e. the polarization with maximum intensity, measured after the analyzer. **I** is an n-by-1-dimensional vector containing the intensity measurements. The analyzer matrix can be determined through knowledge of the physics of the given analyzer, but in most cases it is found through an experimental procedure. Different calibration methods have been presented in literature [35–38], some of which are specific to a particular setup. Here, a general calibration method is used where no knowledge about the analyzers and no special order of input polarizations is required. All that is needed for the calibration is a number of known polarizations and the corresponding intensity measurements. Once the full analyzer matrix is determined through a calibration procedure, the Stokes vector can be calculated simply by inverting the analyzer matrix

$$\mathbf{S} = \mathbf{A}^{-1}\mathbf{I} \tag{2.17}$$

Equation (2.17) requires that **A** is a 4-by-4 matrix. If the number of measurements is larger than 4, the inverted analyzer matrix can be obtained by taking the pseudo-inverse

$$\mathbf{S} = (\mathbf{A}^T\mathbf{A})^{-1}\mathbf{A}^T\mathbf{I} \tag{2.18}$$

where the pseudo-inverse provides a solution that minimizes the mean-square error. However, if the general calibration method is used, the error is minimized by omitting the inversion of the analyzer matrix [38]

$$\mathbf{S} = \mathbf{DI} \tag{2.19}$$

D can now be calculated from any set of known input polarization ($\boldsymbol{\mathcal{S}}$) and intensity measurement ($\boldsymbol{\mathcal{I}}$) by taking the pseudo-inverse of the intensities

$$\mathbf{D} = \boldsymbol{\mathcal{S}}(\boldsymbol{\mathcal{I}}^T\boldsymbol{\mathcal{I}})^{-1}\boldsymbol{\mathcal{I}}^T \tag{2.20}$$

where $\boldsymbol{\mathcal{S}}$ and $\boldsymbol{\mathcal{I}}$ are $4 \times$ n matrices, with n being the number measurements used for the calibration. The choice of analyzer vector should be such that the linear transformation

through **D** should have the lowest possible sensitivity to pertubations in input intensity and calibration. This is determined by the *condition number*.

$$\kappa(\mathbf{A}) = ||\mathbf{A}^{-1}|| \cdot ||\mathbf{A}|| \tag{2.21}$$

The lower the condition number the less sensitive Eq. (2.19) is to pertubations. It can be shown that in case of a complete Stokes polarimeter (all four Stokes parameters are measured) the minimum condition number for **D** (and **A**) is $\sqrt{3}$ [34]. The minimum condition number is obtained when the analyzer vectors span the largest possible volume on the Poincaré sphere [35, 39]. In case of 4 polarization analyzers the analyzer vectors would therefore span a regular tetrahedron in SOP space.

From Eqs. (2.19) and (2.20) it is seen that measurements of intensities, reference polarization measurements, and pseudoinversion contributes to the uncertainty in the determination of the Stokes vector. The uncertainties on polarization measurements are calculated from the general error propagation formula [40]

$$cov(S_i^{in}, S_j^{in}) = \sum_{kl} D_{ik} D_{jl} cov(I_k^{out}, I_l^{out}) + \sum_{\alpha\beta} I_\alpha^{out} I_\beta^{out} cov(D_{i\alpha}, D_{j\beta}) \tag{2.22}$$

S_i^{in} is the ith parameter in the Stokes vector of the incoming light. **D** is still the inverse analyzer matrix (or transformation matrix) and $\mathbf{I}^{out}$ is measured intensity. The first contribution takes into account uncertainty in the intensity measurements of the scattered light. The second contribution takes into account the uncertainty in the knowledge about the analyzer matrix. The covariance matrix of $\mathbf{I}^{out}$ is restricted to be diagonal and therefore equal to the variances of the intensities ($cov(I_k^{out}, I_l^{out}) = \sigma(\mathbf{I}^{out})_k^2 \delta_{kl}$), since it is assumed, for simplicity, that elements of the intensity vector are statistically independent. The analyzer matrix is calculated as $\mathbf{D} = \boldsymbol{\mathcal{S}}\boldsymbol{\mathcal{I}}^T(\boldsymbol{\mathcal{I}}\boldsymbol{\mathcal{I}}^T)^{-1} = \boldsymbol{\mathcal{S}}\boldsymbol{\mathcal{I}}^+$, where $\boldsymbol{\mathcal{S}}$ is a number of known Stokes vectors and $\boldsymbol{\mathcal{I}}^+$ is the pseudoinverse of the corresponding intensity measurements [38]. Using the general error propagation formula, the covariance matrix of the matrix elements of the inverse analyzer matrix is given by

$$cov(D_{\alpha\beta}, D_{ab}) = \sum_{kl} \mathcal{S}_{ak} \mathcal{S}_{\alpha l} cov(\mathcal{I}_{k\beta}^+, \mathcal{I}_{lb}^+) + \sum_{mn} \mathcal{I}_{m\beta}^+ \mathcal{I}_{nb}^+ cov(\mathcal{S}_{am}, \mathcal{S}_{\alpha n}) \tag{2.23}$$

where the first term takes into account the uncertainty associated with inverting the matrix and measuring the intensities and the second term takes into account the uncertainty of measuring the Stokes vectors. Since the intensity matrix $\boldsymbol{\mathcal{I}}$ is not square, the covariance of $\boldsymbol{\mathcal{I}}^+$ becomes

$$\begin{aligned} cov(\mathcal{I}_{\alpha\beta}^+, \mathcal{I}_{ab}^+) = &\sum_{ij} \sigma(\boldsymbol{\mathcal{I}})_{ij}^2 \times [B_{\beta i}^{-1} \delta_{\alpha j} - B_{\beta i}^{-1} \sum_n \mathcal{I}_{\alpha n}^+ \mathcal{I}_{nj} - \mathcal{I}_{\alpha i}^+ \mathcal{I}_{j\beta}^+] \\ &\times [B_{bi}^{-1} \delta_{aj} - B_{bi}^{-1} \sum_m \mathcal{I}_{am}^+ \mathcal{I}_{mj} - \mathcal{I}_{ai}^+ \mathcal{I}_{jb}^+] \end{aligned} \tag{2.24}$$

where $\sigma(\boldsymbol{\mathcal{I}})^2_{ij}$ is the variance of the measured intensities, $\mathbf{B} = \boldsymbol{\mathcal{I}}\boldsymbol{\mathcal{I}}^T$ and δ is the Kronecker delta. To obtain a realistic value of the covariance matrix for reference polarization measurements, an error propagation analysis similar to the one shown here would have to be performed. Such an analysis requires details about the reference polarimeter that are unavailable, such as its intensity measurements and knowledge of its calibration procedure. Therefore, the covariance matrix for reference polarization measurements can be approximated simply with the variance of a number of polarization measurements ($cov(\mathcal{S}_{am}, \mathcal{S}_{\alpha n}) \approx \sigma(\boldsymbol{\mathcal{S}})^2_{am}$). This means that the covariance will be underestimated and the second term in Eq. (2.23) will typically be negligible.

As stated in the beginning of the section, the practical challenge of constructing a Stokes polarimeter is that a number of intensity measurements (a minimum of 4) must be performed, with the same number of polarization analyzers. This can be realized in different ways. One of the most common methods is the time-sequential approach, where measurements are separated over time, generally employing a single photodetector. Such polarization analysis can be carried out using mechanically rotating [41, 42] or oscillating waveplates [21], or through photoelastic modulators [22]. Products based on all three different approaches are commercially available. All suffer from an inherently limited sampling rate since the measurement is spread out over time.

Another method is division-of-amplitude polarimetry, where the beam is split up and measured simultaneously using several detectors, e.g. by employing a sequence of beamsplitters and waveplates [35, 43]. Signal saving polarimeter designs using the division-of-amplitude method can be realized by employing polarization state analyzers that use only a small fraction of the incident light intensity to measure its polarization [44]. A modern-day example of this configuration is the in-line fiber polarimeter, where two (or more) polarization-dependent tilted fiber Bragg gratings, separated by the fiber-based equivalent of a quarter-wave plate, split off a small proportion of the transmitted optical power to four photodetectors [20]. Some of the measurement sensitivity and accuracy is sacrificed by only measuring a fraction of the signal intensity. The division-of-amplitude method offers a higher sampling rate than the time-sequential method, at the expense of using a larger number of optical elements separated in space.

A third method is division-of-wavefront polarimetry [12, 23, 45]. The polarimeter analyzes simultaneously different parts of a wavefront with separate polarization elements, operating side-by-side. The method is suitable for imaging polarimeters. A reduction in resolution of the detector by the number of different elements and the spatial displacement of information within the polarization element pattern are disadvantages.

An overview of different polarimeter configurations is given by Tyo, et al. [46]

Chapter 3

Properties of the metasurface

3.1 Metasurfaces, general background

The electromagnetic theory of metasurfaces can be dated back to 1902, when Wood reported his notable anomaly [47, 48] and Levi-Civita gave the boundary relations for a metallic sheet with vanishing thickness [49]. However, it was not until the start of this millenium that a widespread interest in metasurfaces was sparked with demonstration of some unusual properties, like simulateneous negative or zero permeability and permittivity [50, 51]. Ten years later, negative refraction at a metasurface was further theorized and demonstrated at optical frequencies by the Capasso group at Harvard [52, 53] causing the field to grow rapidly.

Metasurfaces are one-dimensional thin films with properties not occurring in natural materials or two-dimensional optical nano-structures that enable the tailoring of the amplitude, phase or polarization of light using dense arrays of sub-wavelength scale optical antennas [5, 54–56], see illustrations in Fig. 3.1. The metal and/or dielectric nano-structures resonantly couple to the electric or magnetic or both components of the incident electromagnetic fields, exhibiting novel effective electric and/or magnetic responses. In addition to displaying interesting optical phenomena, such as negative refraction and near-zero permittivity or permeability [50, 51, 57, 58], metasurfaces also provide a promising platform for simplifying and miniaturizing existing optical components [5, 59–61]. The very short optical thickness in the direction of wave propagation can suppress undesirable optical losses by using appropriately chosen materials and metasurface structures, while still suplying a sufficiently strong interaction with the incident field to obtain useful functionalities.

The first demonstrated optical metasurfaces were all made of noble metal nanostruc-

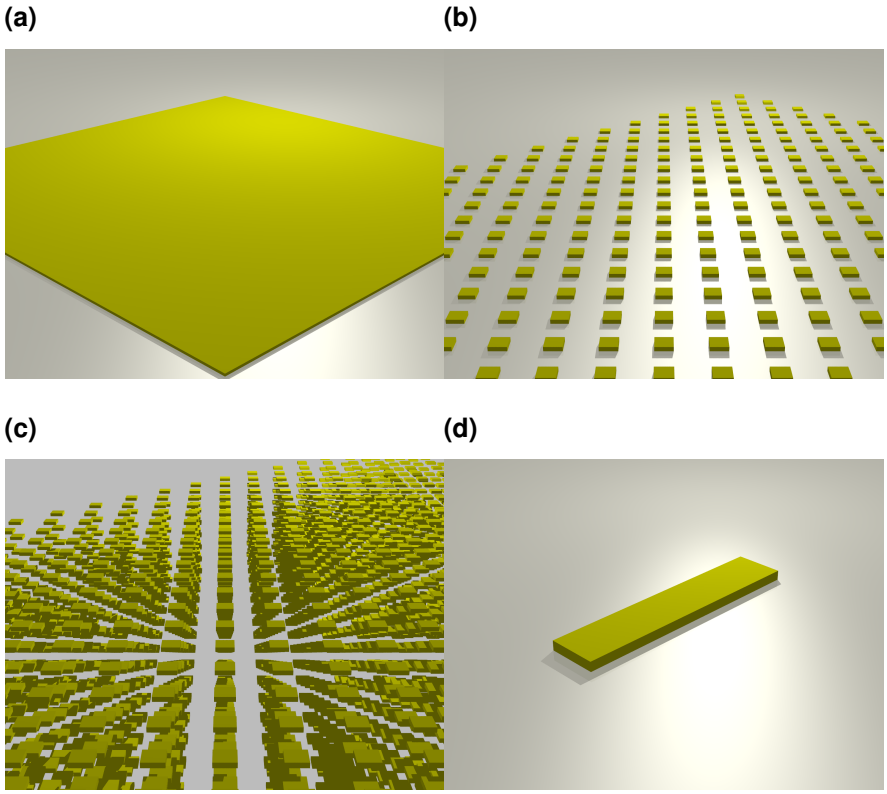

Figure 3.1. (a) Illustration of a thin-film (one-dimensional) metasurface. (b) Illustration of a metasurface as the two-dimensional counterpart of the three-dimensional metamaterial, which is illustrated in (c). (d) The nanorod is one example of the countless of different shapes used as elements in a metasurface.

tures utilizing their strong plasmonic resonant properties. Using a library of V-shaped antennas, gradient metasurfaces were fabricated that could introduce a phase shift covering the range of 0 to 2π [52, 53]. Since every point on a wavefront is a source of secondary wavelets as stated in the Huygens-Fresnel principle [62], the metasurface makes it possible to create arbitrary wavefronts to obtain e.g. negative refraction or holograms. With gap-plasmon metasurfaces the effeciency of plasmonic metasurfaces was increased significantly [63, 64]. However, plasmonic metasurfaces are typically operated only in reflective mode due to the high losses in the metal. Therefore, dielectric metasurfaces were introduced to obtain high transmission effeciency, which is important in applications like optical lenses that typically operate in transmission mode [65–67]. Huygens metasurfaces control the electric and magnetic polarizability to impedance-match the metasurface with the surrounding media, thereby boosting the transmission efficiency [68, 69].

Gradient metasurfaces obtain the phase shift that allows the manipulation of a wavefront at the metasurface either by employing the concept of resonant response [70], or by using geometrically-induced phase shifts [71]. The former method can be realized, for example, with a library of cylindrical nanopillars that feature a size-dependent phase delay [72]. The latter method is based on varying antenna geometry; using the Pancharatnam–Berry-phase, also known as geometric phase, to achieve full control of the phase of circularly polarized incident light [73]. This can be accomplished, e.g., by adjusting the orientation angle of nanorods or ellipses [60, 71].

Other types of metasurfaces include hyperbolic metasurfaces that appear metallic in one direction and dielectric in the other direction [6, 74], and thin-film metasurfaces made of ultrathin, highly absorbing materials that selectively absorb various frequency ranges of the incident light [75].

Active metasurfaces is an area of research that has received much attention lately. Dynamic control over the optical properties of the metasurface can be achieved by changing the shape of the resonators or the distance between them [76–79].

Metasurfaces have been applied to demonstrate many different optical phenoma and useful devices, including polarization manipulation [10, 53, 80, 81], polarization detection [82–84], flat lenses [85, 86], meta-holograms [87, 88], optical vortex generation [89, 90], color filters [91], absorbers and antireflection coatings [92–94], etc. The rapid development that the field of metasurface research has experienced is driven not only by scientific interest, but also by industrial interest, since applications such as mobile phones and augmented reality displays could benefit from flat optics. There are,

however, still issues with transmission effeciency, broadband operation, and tunability that must be improved before a large scale commercial breakthrough of metasurfaces will come about.

The main fabrication techniques for optical metasurfaces are direct-write lithography and pattern-transfer lithography. The most common direct-write method is photolithography, which is widely used in the semiconductor industry [95]. It is, needless to say, the most promising technology for optical metasurfaces because of high yield, large area, and large volume mass production. Thanks to huge investments in development of deep-UV technologies, photolithography has reached the resolution needed for optical metasurfaces [96, 97]. However, for research purposes, high throughput is not necessary. Therefore, another way of achieving high resolution and more versatile equipment is requested. Particle-beam lithography suits very well for these needs [3]. Electron-beam lithography and focused-ion-beam milling are two well established particle beam methods, where the electron-beam method is the dominant approach, since focused-ion-beam milling tends to produce rough, defect-ridden structures [74]. Probe scanning lithography is an alternative direct-write method that employs the technique of atomic force microscopy, but is not widely used because of its poor aspect ratio. The electron-beam lithography method is used in this work because of its high resolution, good pattern quality, and versatility. However, even though particle beam methods are cheaper than deep-UV lithography, the cost of these systems are still relatively high. Therefore, pattern transfer methods like self-assembly lithography exists as alternatives to direct-write lithograhy. In self-assembly lithography a monolayer of colloidal nanospheres are formed and transferred to a substrate, which can be used as a mask for deposition or as a hard mask for etching [98]. Self-assembled lithography is a simple and cheap method that can be applied to large-scale substrates, but uniformity is a challenge and it is limited to simple periodic patterns. Nano-imprint lithography on the other hand is not limited in regards of pattern design and it offers high resolution, but it still has the advantages of large area fabrication and low cost [99]. Nano-imprint lithography uses mechanical deformation to replicate nanostructures. A master mold is pressed against a polymer-coated substrate. When the mold is detached, the polymer preserves its form and the negative of the mold's structure is transferred. The disadvantage of the nano-imprint method is the fabrication of the mold that requires another high resolution method like electron-beam lithography. Nano-imprint lithography is therefore a very promising low-cost alternative to photolithography, but is not as versatile as particle-beam lithography. There exist alternatives to direct-write

lithography and pattern-transfer lithography. One of the most interesting alternatives is two-photon polymerization lithography, where ultrashort laser pulses causes molecules to polymerize once they are excited to a higher energy state by absorbing two photons [100]. The technique has gained attention because of its flexibility in geometry and scalable resolution. It might be a future solution to the problems of low quality that 3D metamaterials are facing.

3.2 Polarization sensitive metasurfaces based on nanoantenna arrays

The metasurface described in this section consists of columns of metallic nanorods acting as phased optical antenna arrays. The antenna response is enhanced by tuning the geometry to match the localized surface plasmon resonance of the antenna. Surface plasmons are electron oscillations that can occur at metal-dielectric interfaces [101]. These electromagnetic surface waves arise via the coupling of electromagnetic fields to oscillations of the conductor's electron plasma. Localized surface plasmons are non-propagating electromagnetic excitations in small metallic particles. Due to the small size, such particles support resonance modes that can be excited by direct light illumination, similar to resonant radiowave antennas. These nano-particles are therefore often refered to as optical antennas.

In 2013 J. Lin, J. P. B. Mueller et al. presented a so-called fishbone pattern of narrow apertures in a gold film [102]. A schematic of the pattern is shown in Fig. 3.2a. The physics of the fishbone pattern will be explained in this chapter. The metasurface allowed for polarization sensitive directional coupling of surface plasmon polaritons (SPP) based on the circular polarization state of incident light. The surface plasmon coupling was measured using near-field scanning optical microscopy. In a later article by Mueller et al., the fishbone patterned metasurface containing gold nano-antennas on a gold film, was used for coupling to long-range SPP waveguides [103]. This allowed for intensity measurements and calculation of analyzer vectors. This work paved the way to realizing a full Stokes polarimeter. In 2016, Mueller et al. presented the concept of a metasurface-based in-line polarimeter for near-infrared wavelengths [11]. Using a laboratory setup, it was demonstrated that all four polarization state analyzers of a parallel polarimeter that measured the full state-of-polarization could be combined in a single-layered array of sub-wavelength nanoantennas, complementable with the

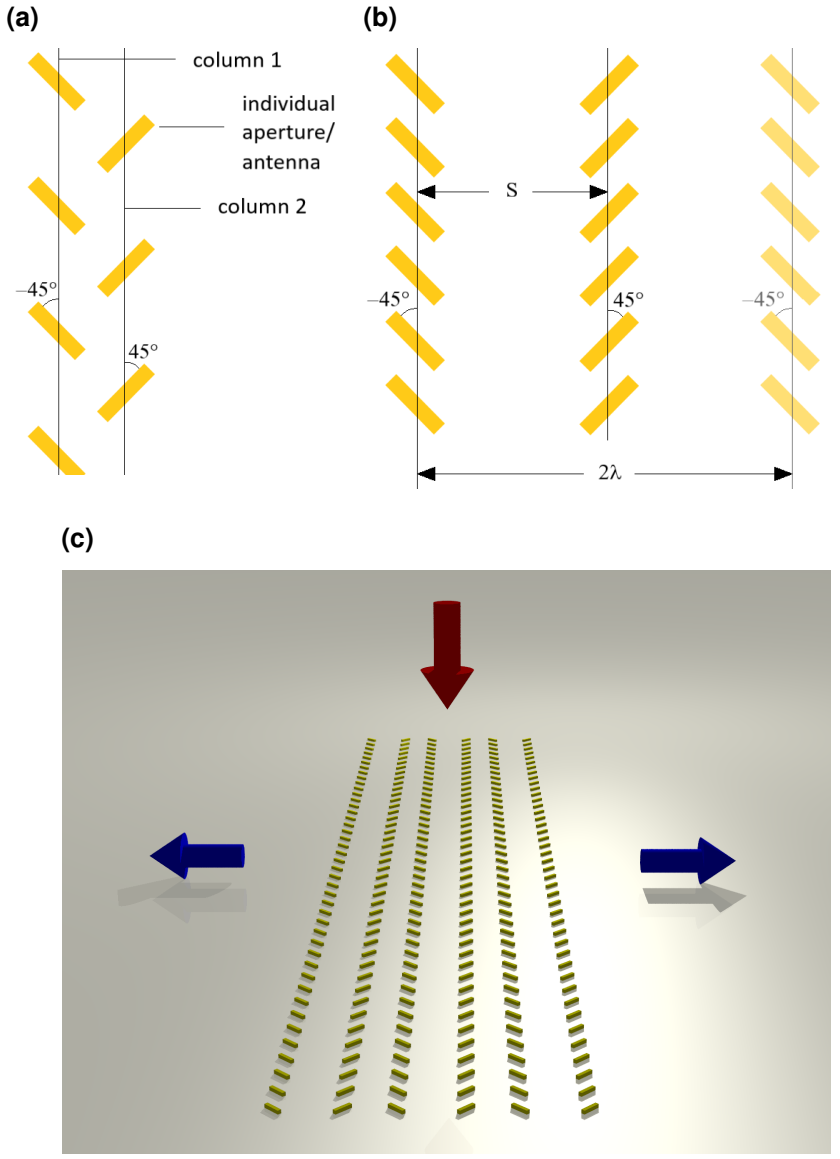

Figure 3.2. (a) Schematic of the fishbone pattern used for directional coupling of surface plasmon polaritons [102]. It consists of two columns of apertures in a gold film (or gold antennas). All antennas in each column are rotated $\pm 45°$ from the column axis. The distance (S) between columns is approximately a quarter of a SPP wavelength to allow for directional coupling of circularly polarized light. The columns are offset with half the row distance to minimize nearfield coupling. (b) Schematic of the pattern used in a metasurface polarimeter [11]. The distance between columns, (S), is 9/8 of a wavelength and the distance between column-pairs in the metasurface is two wavelengths (2λ). (c) Schematic of a 3-column-pair metasurface showing the direction of the incoming light (red arrow) and directions of SPPs/scattered light (blue arrows).

apertures of the original pattern through Babinet's principle [104], see schematic of pattern in Fig. 3.2b. The ultra-compact design of the metasurface polarimeter, combined with its non-destructive, polarization-preserving features, allows for applications such as feedback-driven polarization generation and large-scale online polarization monitoring in optical communication. In addition to the ultra-compact design that allows for planar integration, the benefits of the metasurface polarimeter include a detection-limited response time, simple and versatile design that can be tailored for operation across a wide range of wavelengths simply by changing the dimensions of the metasurface structure, increased robustness and reduced costs due to the replacement of movable parts and optical components like waveplates with structures produced by conventional lithographic process technology. In 2017, an analytical model for the radiation pattern of the metasurface was presented as part of the present project and in-plane and out-of-plane polarimeters were fabricated based on a new design, where individual photodetectors are placed directly in the path of the scattered light beams [84, 105]. The absence of optical elements between the metasurface and detectors makes packaging easier and allows for integrating the photodetector and metasurface on the same chip. Furthermore, artificial neural networks were used to take advantage of the inhererent wavelength sensitivity of the metasurface to improve calibration of the polarimeter, removing its wavelength dependence in the operating range, and extending its functionality to work as a wavemeter [106]. Subsequently, a further step in the miniaturization of the polarimeter was taken by demonstrating a fiber-based metasurface polarimeter, where a new nano-transfer method using template stripping was employed to transfer a 4-output metasurface to the facet of a single-mode fiber [107, 108]. Inspired by the original article from 2013 [102], the fishbone design has found new applications in other research groups such as plasmonic focusing and plasmonic vortex compounds carrying arbitrary orbital momentum [109, 110].

3.2.1 Simulations of individual nanoantennas

Finite-difference time-domain (FDTD) simulations of the optical response of individual gold nanorods, using the Lumerical solver FDTD Solutions (see Appendix A1), are shown in Fig. 3.3. Figure 3.3a shows the scattering cross section, absorption cross section, and extinction cross section of a 225 nm $\times$ 50 nm $\times$ 20 nm gold nanorod embedded in a dielectric with n = 1.535, illuminated with a plane wave that is linearly polarized along the long axis of the rod. The plot shows a resonance peak quite close to the

design wavelength of the polarimeter (1550 nm). The scattered power is normalized to the source intensity obtaining the scattering cross section. Alternatively, the scattered power could be normalized to the source power to obtain a normalized power between 0 and 1. The problem with this approach is that the gold particle bends the power flow (the pointing vector deviates from being perpendicular to the injection plane) causing the power to flow into the monitor from the sides, i.e. the light that interacts with the particle has a larger cross section than the particle. The source power only accounts for the power from the primary injection plane, i.e. the power that flows in from the sides of the monitor is not accounted for. This can lead to non-intuitive results where the normalized power is larger than one (indicating that the scattered power is larger than the injected power). The scattering cross section is therefore larger than the geometrical cross section indicating that gold is an excellent scattering object. As seen in Fig. 3.3a, the absorption of the gold nanorod is roughly of the same magnitude as the scattering.

When electromagnetic radiation is normally incident on a metallic nanorod, the rod can be modelled as a thin optical dipole antenna emitting radiation, as long as the incident wavelength is within resonance and the incoming light contains a component of polarization along the long axis of the rod. Figure 3.3b is a plot of the scattering cross section where the polarization of the incident light is perpendicular to the nanorod. The curve is decreasing to the fourth power of the wavelength around the design wavelength, since the size of the short axis is within the range of Rayleigh scattering (less than 10 % of the wavelength) [111]. Therefore, much less light is scattered for the perpendicular polarization

$$\gamma_{1550nm} = \frac{\sigma_{max,90}}{\sigma_{max,0}} = 1700 \tag{3.1}$$

and the nanorod can be reasonably approximated as a thin dipole. Figure 3.3c-d are plots of the simulated scattering cross section for varying lengths and widths of the nanorod. They show how the nanoantenna response can be modified by adjusting the relative sizes of the antenna. For varying lengths in particularly, the power and wavelength shift is linear around 1550 nm to a good approximation.

3.2.2 Analytical model and simulations of radiation pattern

A graphical representation of the overall metasurface design is seen in Fig. 3.4a. The far-field radiation pattern of a plasmonic nanoantenna with length less than a wavelength

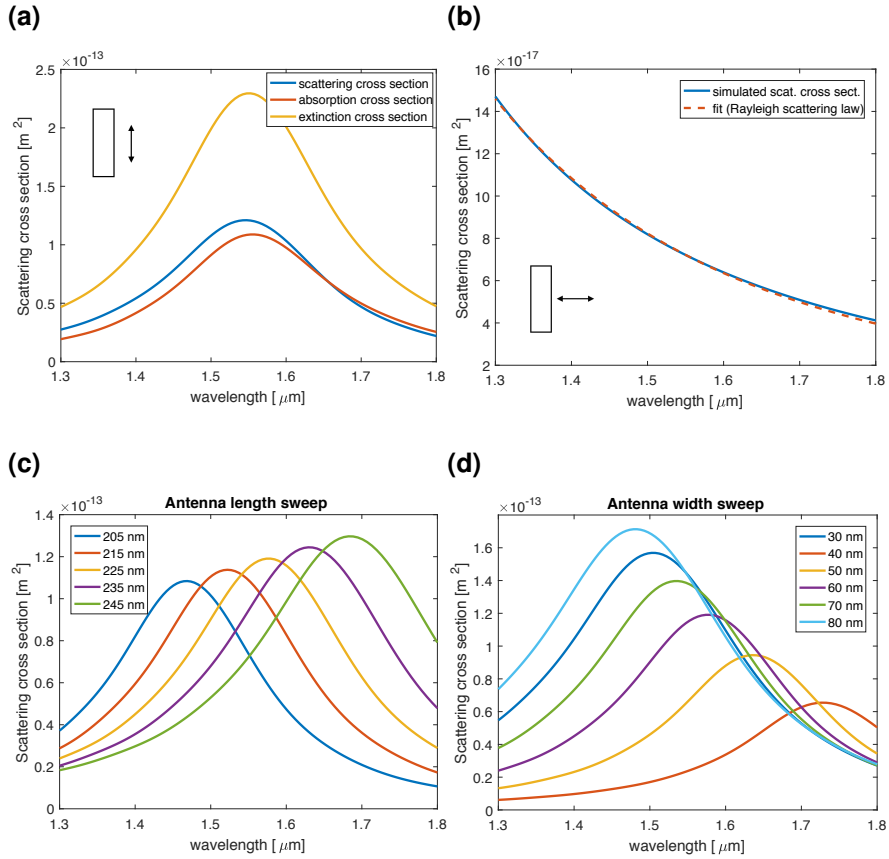

Figure 3.3. (a) FDTD-simulated scattering cross section versus wavelength of a single gold nanorod (225 nm × 50 nm× 20 nm) embedded in a dielectric with n = 1.535, plotted together with the absorption cross section and extinction cross section. The incident wave is polarized parallel to the long axis of the antenna (illustrated schematically in the upper left corner). (b) When the incident wave is polarized perpendicular to the long axis of the antenna (illustrated schematically in the lower left corner) the scattering cross section versus wavelength of the nanorod is four orders of magnitude smaller and can be fitted to the Rayleigh scattering law ($\sigma_s \propto \lambda^{-4}$). (c) Scattering cross section vs wavelength for varying lengths of the nanorod with incident polarization parallel to the long axis of the nanorod. The width is 50 nm and the height is 20 nm. (d) Scattering cross section vs wavelength for varying widths of the nanorod with incident polarization parallel to the long axis of the nanorod. The length is 225 nm and the height is 20 nm.

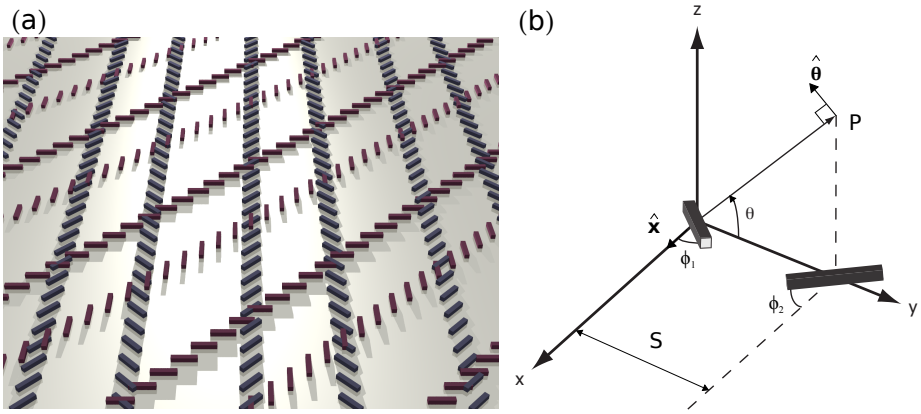

Figure 3.4. (a) Graphical representation of the metasurface design. The metasurface consists of columns of sub-wavelength spaced nano-antennas. The antennas in each column are rotated 90° relative to the antennas in the neighboring column. The distance between every second column is twice the design wavelength within the dielectric matrix, 2λ, and the distance between the two arrays in a column-pair is $\lambda(1+1/8)$. The red antenna columns are arranged in a pattern identical to the blue columns except from an overall 45° rotation relative to the blue antenna columns. The height of the antennas are 2 times larger than their designed proportions for visual purposes. (b) Geometry of a phased array with two elements with individual orientation (ϕ_1 and ϕ_2) in the xy-plane. The point of observation (P) is established by the angle θ. One antenna (n = 1) is placed at (0, 0, 0) and the other antenna (n = 2) is positioned at (0, S, 0). The direction of the unit vectors $\hat{\mathbf{x}}$ and $\hat{\boldsymbol{\theta}}$ in Equation 3.6 is shown in the figure. Incident light is propagating parallel to the z-axis.

can be modelled reasonably well as a short dipole [112]. The electric field of a short dipole antenna in the far-field is given by [113, 114]

$$\mathbf{E} = i\eta kl\frac{e^{-ikr}}{4\pi r}\mathbf{F}(\theta,\phi)I \tag{3.2}$$

where $k = 2\pi/\lambda$ is the angular wavenumber, l is the length of the antenna, the characteristic impedance is a function of the permittivity and permeability $\eta = \sqrt{\mu/\varepsilon}$, r is the distance depending on the observation point and θ, ϕ are the corresponding angles. I is the excitation current. The angular-dependent vector $\mathbf{F}(\theta,\phi)$ gives the directional characteristics of the antenna. If the antenna is parallel to the z-axis, the angular-dependent vector becomes $cos(\theta)\hat{\boldsymbol{\theta}}$ [113]. The total electric field of an N element antenna array along the y-axis (see Fig. 3.4b) is the sum of the electric fields of the individual antennas, with positions r_n. In the far-field $1/r_n$ is approximated with $1/r$ and $exp(-ikr_n)$ with $exp(-ik(r - y_n cos(\theta)))$, where y_n is position of the antennas on the y-axis. The electric field of multiple antennas, therefore, becomes

$$\mathbf{E} = i\eta kl\frac{e^{-ikr}}{4\pi r}\sum_{n=1}^{N}\mathbf{F_n}(\theta,\phi)e^{iky_n cos(\theta)}I_n = i\eta kl\frac{e^{-ikr}}{4\pi r}\mathbf{AF} \tag{3.3}$$

where **AF** is the so-called array factor that determines the radiation pattern. If identical antennas are placed in an infinite subwavelength-spaced 1-dimensional array, the azimuthal radiation pattern is invariant along the array. Two parallel columns individually oriented ±45° with respect to the orientation of the columns of each array in a fishbone pattern will scatter most efficiently two orthogonal linear polarization components of an incident electromagnetic field [102]. Therefore, the antenna columns will emit an interference pattern similar to the radiation pattern of a phased array with two elements. The interference pattern depends on the polarization of the incoming wave, the orientation of the columns, and the distance between the two columns. The distance between the two columns can be tuned to fit the phase difference between the two orthogonal components of a preferred incoming polarization to obtain a maximum of scattered field intensity in the directions of interest for that particular (generally elliptical) polarization state. Defining the vector $\Phi_n = \mathbf{F_n}(\theta,\phi)e^{iky_n cos(\theta)}$, the array factor of a two-pair column is given by [11, 114]

$$\mathbf{AF} = \Phi_1 I_1 + \Phi_2 I_2 \tag{3.4}$$

where

$$I_n = cos(\phi_n + pi/4)cos(\psi) + sin(\phi_n + pi/4)sin(\psi)e^{i\delta}$$

are the excitation currents for each antenna and

$$\Phi_n = \left[cos(\phi_n)\hat{\mathbf{x}} - sin(\phi_n)sin(\theta)\hat{\boldsymbol{\theta}}\right]e^{i(n-1)kScos(\theta)}$$

describes the radiation as a function of the position and spatial orientation of the n^{th} dipole for n = 1, 2. ψ and δ describe the polarization of the incoming light using the Jones vector model of polarization in complex number representation. ψ is related to the amplitudes $\psi = \arctan(E_y/E_x)$ and δ is the relative phase difference between the x and y components of the field. The position of the first dipole (n = 1) is in (0, 0, 0). S is the distance between columns and the azimuthal angle θ is the angle in the yz-plane between y-axis in the sample plane and the axis from the origin to the point of measurement P. The x-axis is parallel to the column axes and ϕ_n is the rotation of the n^{th} dipole away from the x axis in the xy-plane normal to the incident light. $\hat{\mathbf{x}}$ is a unit vector parallel to the x-axis, and $\hat{\boldsymbol{\theta}}$ is a unit vector in the angular tangential direction associated to the rotation of θ.

The polarization-selective nanoantenna-array metasurface design scatters two orthogonal linear components of the incoming lights polarization state ($|\phi_2 - \phi_1| = 90°$) and optimizes the coupling effeciency ($\phi_n = \pm 45°$) [102]. With these restrictions the excitation currents are reduced to

$$I_1 = cos(\psi), I_2 = sin(\psi)e^{i\delta} \tag{3.5}$$

and the arrray factor (equation 3.4) becomes

$$\begin{aligned} \mathbf{AF} = &\left[cos(\phi_1)\hat{\mathbf{x}} - sin(\phi_1)sin(\theta)\hat{\boldsymbol{\theta}}\right] cos(\psi) \; + \\ &\left[cos(\phi_2)\hat{\mathbf{x}} - sin(\phi_2)sin(\theta)\hat{\boldsymbol{\theta}}\right] sin(\psi)e^{i(\delta + kScos(\theta))} \end{aligned} \tag{3.6}$$

A sketch of the geometry of an individually rotated two-element array is shown in Fig. 3.4b and radiation patterns for 4 different input polarizations are shown in Fig. 3.5, with two antennas embeded in a dielectric with $n = 1.535$ at 1550 nm. $S = \lambda(1 + 1/8)$ and $\phi_n = \pm 45°$, where λ is the metasurface design wavelength $\lambda = \lambda_0/n \approx 1000$ nm, when designed for an incident wavelength (in vacuum) of $\lambda_0 = 1550$ nm and a dielectric matrix with refractive index $n = 1.535$.

The inter-antenna distance of structures modelled in Fig. 3.5, $S = \lambda(1 + 1/8)$, is designed to maximize the array factor, Eq. (3.6), at $\theta = 0°$ and $\theta = 180°$ (in-plane output) for elliptically polarized light with $\psi = \pi/4$ and $\delta = \pm\pi/4$ (elliptically polarized light midway between circular polarization and vertically oriented linear polarization, [102]). It is seen that the analytical model fits very well to a FDTD simulation of two gold antennas with dimensions of 250 nm×50 nm×20 nm. Correcting the analytical model for mutual coupling and parasitic antennas (see Eq. (3.1)) improves the fit even further.

$$\mathbf{AF} = \sum_{n=1}^{2} \left(\mathbf{F_n}(\theta,\phi)D_nI_n - Z\mathbf{F_n^{mut}}(\theta,\phi)D_nI_n^{mut} + C\mathbf{F_n^{mut}}(\theta,\phi)D_nI_n\right) \tag{3.7}$$

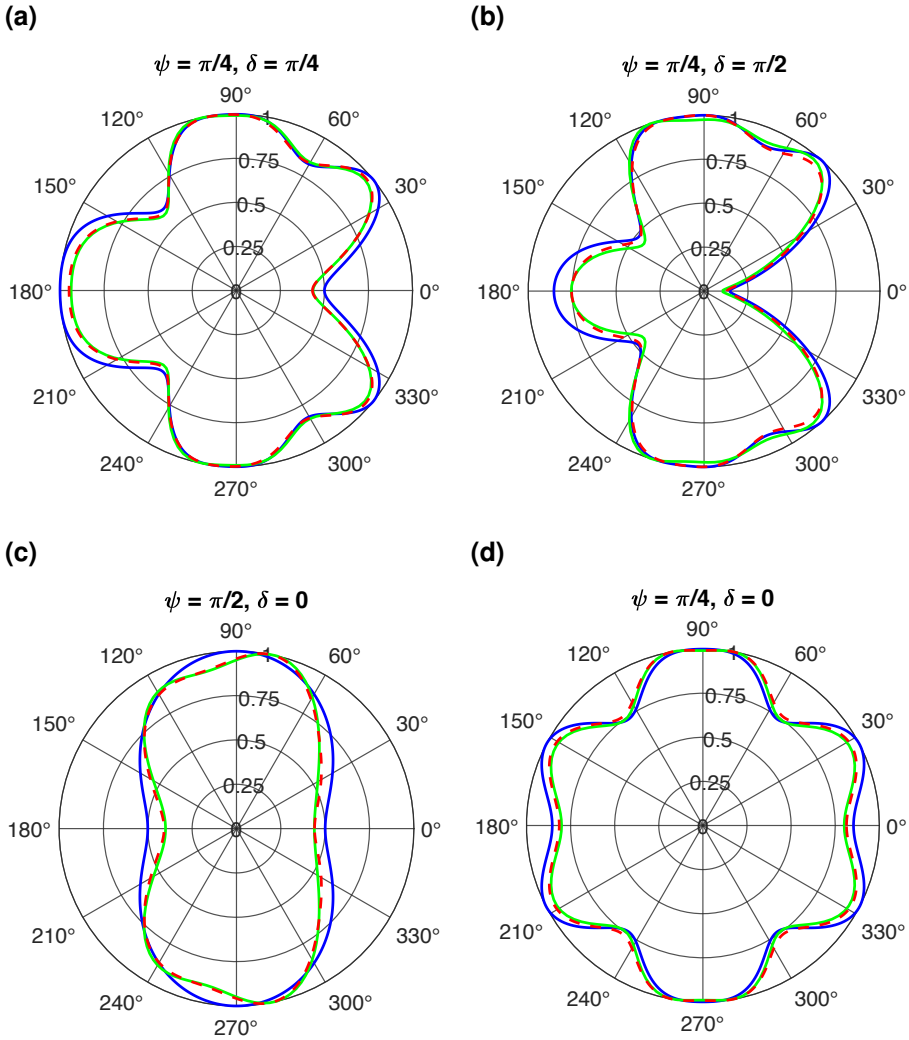

Figure 3.5. Radiation patterns of two nanoantennas oriented perpendicularly to each other (±45°) for different polarizations of the incoming light. The blue line is $|\mathbf{AF}|^2$ vs θ in the yz-plane (see Fig. 3.4b) normalized to unity using the analytical model Eq. (3.6), the red dashed line corrects the analytical model for mutual coupling and parasitic antennas and the green line is $|E|^2$ vs θ normalized to unity using a finite-difference time-domain (FDTD) simulation. (a) is elliptically polarized light with $(\psi, \delta) = (\pi/4, \pi/4)$, (b) is circularly polarized light, (c) is linearly polarized light at 45°, and (d) is vertically polarized light.

The second term in the summation is correcting the analytical model (the first term in the summation) for mutual coupling. The third term corrects for parasitic antennas. $I_1^{mut} = I_2$, $I_2^{mut} = I_1$, and the same rule applies for $\mathbf{F_n^{mut}}(\theta,\phi)$. Z, the mutual impedance [113], is a complex number, whereas C is a real constant. $D_n = e^{iky_n cos(\theta)}$. The fit of elliptical and circular polarizations (Figs. 3.5a and 3.5b) is improved by subtracting an empirical correction to the summation in Eq. 3.7, $Z_e\mathbf{F_n}(\theta,\phi)D_nI_n^{mut}$. The radiation pattern is left/right asymmetric for all elliptical and circular polarizations, as a result of the difference in phase between the two linear orthogonal components of the incoming light's polarization state. The asymmetry observed in Fig. 3.5c shows the effect of the mutual coupling and that the dipole approximation is not perfect, i.e. the non-zero scattered field from the antenna, which is oriented perpendicular to the polarization of the incident light, causes a disturbance in farfield radiation pattern compared to the analytically calculated pattern that assumes a perfect dipole.

The polarization for which the measured power of a given scattered field output channel (proportional to $|\mathbf{AF}|^2$) is maximal corresponds to the analyzer vector. At $\theta = 0°$ or $\theta = 180°$ the second term in Φ_n vanishes and a signal contrast of 100 % on each detector is possible. In the case where θ is 60° or 120°, Φ_1 and Φ_2 in Eq. (3.6) will no longer be equal and a theoretical polarization-dependent contrast of only 25 % of the overall signal is possible. Light scattered into the in-plane orders contains only a field component in the x-direction. This is illustrated with a FDTD simulation in Fig. 3.6a showing a plot of the electric field from one antenna column, where it is seen that E_y and E_z die out in the farfield (in accordance with the results in [11] using a dipole approximation). In out-of-plane orders on the other hand, as a result of the perpendicularly oriented antennas, scattered light contains both x and θ-components that cancels out the polarization-dependent intensity variation because the polarization dependent interference of the two components is completely opposite (maximum intensities occur at orthogonal incoming polarizations for the two scattered polarization components). Figure 3.6b is an FDTD simulation of the scattered electric field from one column in the direction parallel to the incoming beam. It shows that light is scattered into two orthogonal polarizations with a relative phase shift of 180°. Since there is no phase shift for the orthogonal antenna (Fig. 3.6c) the interference between the two antenna-columns of the two orthogonal polarizations in the metasurface is changed causing the cancelling out of the signal. In the cases plotted in Fig. 3.6b and c when θ is 90°, the amplitudes of the E_y field and the E_x field are equal which leads to a signal contrast in this order of 0 %, which means that the intensity of the light scattered in this direction is completely

independent of the polarization of the incoming light.

Instead of explaining the signal contrast from Eq. (3.6), the same conclusion can be obtained from a pure geometrical point of view. We know that the scattered field from a short dipole in the farfield is perpendicular to the direction of propagation and perpendicular to the azimuthal direction (which means that there is only a vector component in the polar direction). Therefore, the scattered fields from the two dipoles are parallel for in-plane orders and signal contrast is 100 % because the complete field of each dipole is allowed to intefere. However, as θ is increased, the direction of the electric fields is splitting and an increasing fraction of the field is mutually perpendicular, until the direction of the scattered fields of the two dipoles are completely perpendicular at $\theta = 90°$. Since orthogonally-polarized waves can not interfere, there will be no variation of the scattered field intensity with incoming polarization and the signal contrast vanishes.

Repeating the column-pairs in an array of $2N+1$ elements with a period of $d = 2\lambda$ will form a meta-grating that covers a larger area and results in a highly directional intensity distribution. To account for the repeated column-pairs the array factor is multiplied with [11]

$$G_N = \sum_{n=-N}^{N} e^{inkdcos(\theta)} \tag{3.8}$$

In our case, the interesting angles for measurement are the first and second orders of the grating, corresponding to azimuthal angles θ in the yz-plane (see Fig. 3.4) of 0°, 180° and 60°, 120°, as illustrated in Fig. 3.7. Figure 3.7a is a plot that shows FDTD simulations, plotted at different wavelengths, of a full metasurface containing five column-pairs and the same distance S and antenna dimensions as in Fig. 3.5. Equation 3.8 is plotted in Fig. 3.7b at different wavelengths and shows the effect of the meta-grating alone. The plot illustrates that the meta-grating is responsible for a difference in sensitivity to wavelength fluctuations between the in-plane and the out-of-plane design.

The four analyzer vectors in the analyzer matrix are defined in a manner analogous to Stokes vectors and they form a basis for the SOP space. If detectors for intensity measurements are placed in the xy-plane at the four angles of the two grating orders mentioned above the basis will be incomplete and, theoretically, it will not be possible to measure the full SOP. The position of all analyzer vectors will remain in the S1-S3 plane and there will be no vector component in the S2 direction. This is illustrated in Fig. 3.8a with $S = \lambda(1+1/8)$. Furthermore, a complete polarimeter that measures the intensity and SOP as well as the DOP needs to have analyzer vectors that span a

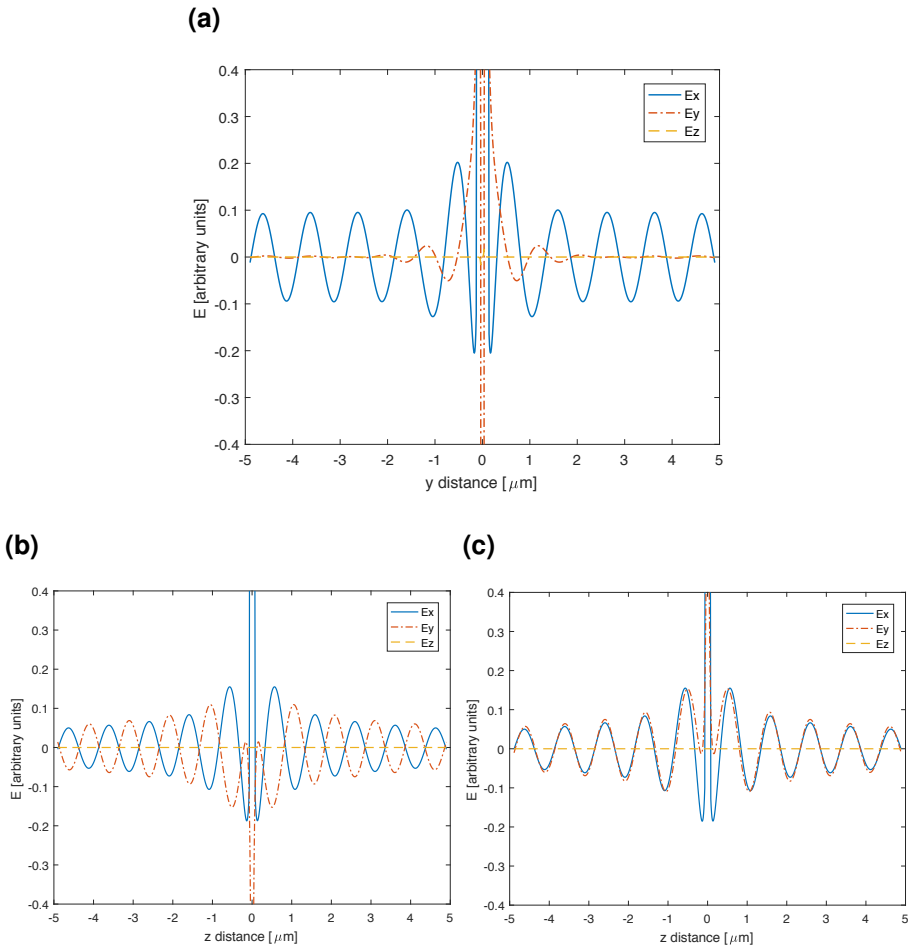

Figure 3.6. FDTD simulations of electric field versus distance for one column of antennas. The incoming light is vertically polarized (along the x-axis). (a) The electric field scattered in the direction of the y-axis (in the plane of the sample). The antennas are rotated -45° from the x-axis. (b) The electric field scattered in the direction of the z-axis (the direction of the incoming light) for antennas rotated -45° from the x-axis. (c) The electric field scattered in the direction of the z-axis (the direction of the incoming light) for antennas rotated 45° from the x-axis.

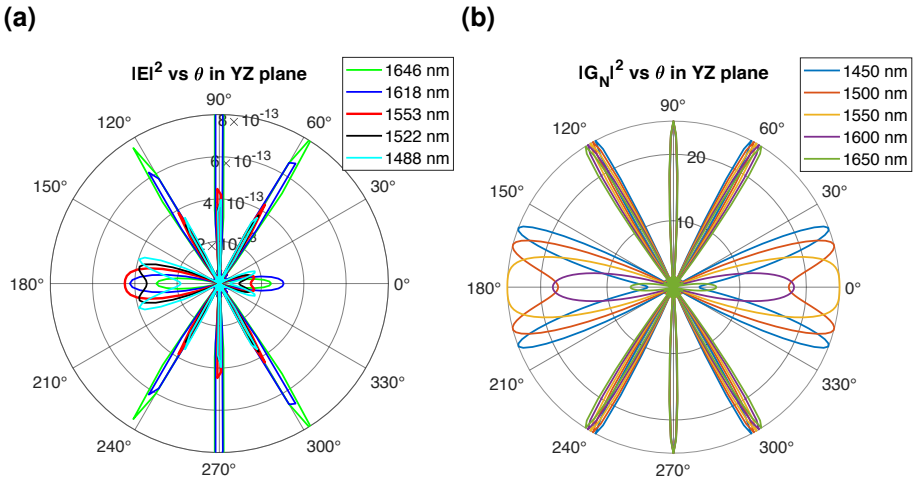

Figure 3.7. (a) Wavelength dependence of the FDTD simulated radiation pattern, $|E|^2$ versus θ in the yz-plane, of a metasurface consisting of five column-pairs of ±45°-oriented antennas. Incoming light is elliptically polarized with $(\psi, \delta) = (\pi/4, \pi/4)$. (b) Diffraction pattern of a meta-grating with $N = 2$ and $d = 2\lambda$ using Eq. (3.8), $|G_N|^2$ versus θ in the yz-plane, plotted versus different wavelengths. Equation (3.8) isolates the meta-grating's contribution to the array factor.

volume in SOP space [11]. All possible polarizations described by the Stokes vector are contained within a four-dimensional cone (see equation 2.11). In each of the 3-dimensional "planes" along the S_0 axis of the cone is a Poincaré sphere with maximum at S_0 and minimum at zero (when $p = 0$). If the analyzer vectors only span a plane, it will not be possible to distinguish between polarizations on the two spheres with same radius but different p and S_0 parameter (these geometrical considerations might be easier in a three-dimensional case (a 3D cone) where only linear polarizations are taken into account).

Both of these problems are solved by superimposing another column-pair grating at a 45° angle relative to the first. A distance of $S = \lambda(1 + 1/4)$ and an out-of-plane measurement of the first column-pair grating would theoretically result in an analyzer vector with two elliptically polarized states, $(\psi, \delta) = (\pi/4, \pm 3\pi/4)$. Measuring the second column-pair at 0° and 60° would produce an analyzer vector with a circularly polarized state $(\psi, \delta) = (\pi/4, \pi/2)$, and another with an elliptically polarized state $(\psi, \delta) = (\pi/4, -3\pi/4)$, see Fig. 3.8b.

A different way to allow the full SOP measurement that does not require superimposing a rotated column-pair grating would be to break the symmetry. This can be done either by introducing a third column or by changing the orientation of the antennas in one of the columns so that they are no longer orthogonal to the orientation of the antennas in the other column. Figure 3.9 shows a schematic of antennas oriented $\phi_1 = 0$ and $\phi_2 = \pi/4$ and a plot of the corresponding analyzer vector positions if $S = 1.2\lambda$. The same result can be obtained by adding a third antenna to the symmetric design at the same position as the antenna with $n = 1$, but rotated 90° with respect to the first antenna ($\phi_3 = \pi/4$). The disadvantages of this method are that the coupling efficiencies are not equal, the metasurface is more sensitive to mutual coupling at certain polarizations (Fig. 3.9c) and that the analyzer vectors still do not theoretically form the basis for a complete polarimeter, since they do not span a volume on the Poincaré sphere. Out-of-plane and in-plane measurements, however, come with different traits, so in the following we will, for simplicity, focus only on purely in-plane or out-of-plane designs.

3.2.3 Properties of the metasurface as polarimeter

The in-plane metasurface polarimeter is designed with two 45° superimposed column-pair gratings and distances of $S = \lambda(1 + 1/8)$ to obtain (ideally) the best basis for a four-output polarimeter with the constraint that the analyzer vectors consists of two

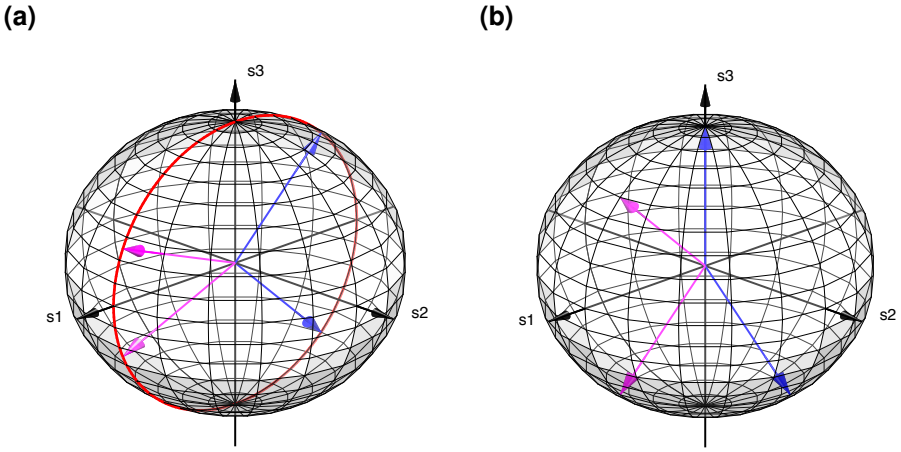

Figure 3.8. (a) The analyzer vectors of a polarimeter with one metasurface measured on both in-plane and out-of-plane orders will all be positioned at points on the red circle regardless of the distance S. The magenta arrows (out-of-plane orders) and blue arrows (in-plane orders) illustrates an example where $S = \lambda(1+1/8)$. (b) The four analyzer vectors of a complete Stokes polarimeter, consisting of two superimposed metasurfaces, depicted on the Poincaré sphere. It is seen that the four polarizations span a volume in SOP space and it is therefore possible to distinguish between the intensity and the DOP.

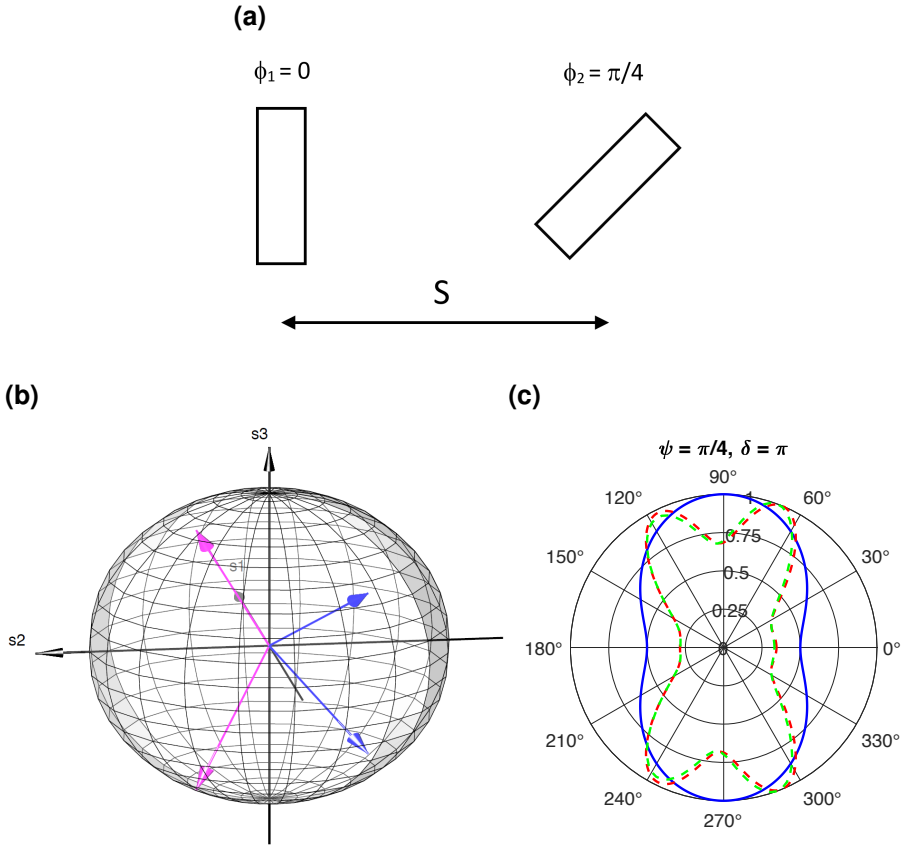

Figure 3.9. (a) A schematic of an example of non-orthogonal antenna orientations. (b) The analyzer vectors of a metasurface where the individual antenna-orientation in one column is parallel to the column-orientation and 45° with respect to the column-orientation in the other column. When $\phi_1 = 0$ and $\phi_2 = \pi/4$ and $S = 1.2\lambda$, the azimuthal difference between the two analyzer vector pairs are 90°. (c) Normalized radiation patterns of two columns for horizontally polarized incoming light and $\phi_1 = 0$ and $\phi_2 = \pi/4$ and $S = \lambda(1 + 1/8)$, using the analytical model (blue line), the analytical model corrected for mutual coupling (red dashed line), and finite-difference time-domain simulations (green dashed line). It is seen that the metasurface is very sensitive to mutual coupling when the polarization of the incoming light is orthogonal to the orientation of one of the antennas (to compare this with the fishbone design, see Fig. 3.5c).

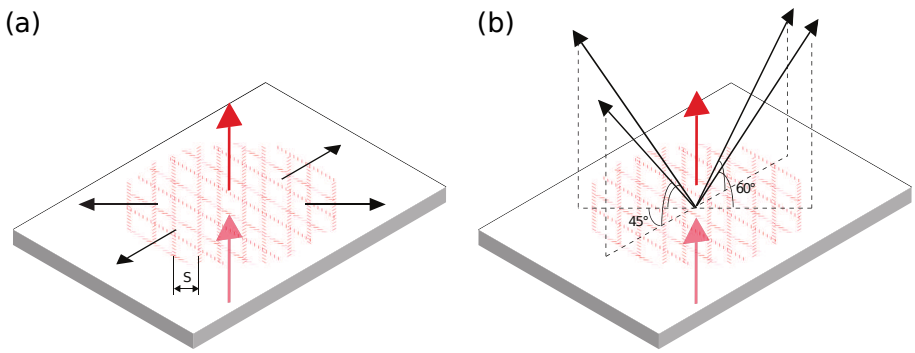

Figure 3.10. Schematics of a metasurface polarimeter showing the geometry of the antenna structure placed onto a transparent substrate. The red arrows illustrate the incident light beam and the light transmitted through the sample. (a) The black arrows represent the directions of scattered light, propagating in the plane of the sample surface. (b) The black arrows indicate the angles that can be used for out-of-plane measurements. The scattered field intensity is measured behind the sample (seen from the perspective of the light source).

pairs of vectors mirrored about the equator of the Poincaré sphere [35]. Figure 3.10 shows schematics of a full metasurface, with two superimposed columns-pair gratings, each grating consisting of 5 column-pairs. The arrows illustrate the direction of the incoming light and direction of the scattered light of interest for in-plane and out-of-plane measurements. Theoretically, the analyzer vectors of these two designs do not span a volume in SOP space, but deviations of the analyzer vectors caused by antenna interactions, geometric imperfections, internal reflections and/or wavelength dependence are nevertheless large enough that changes in DOP and intensity can be distinguished. Because of the symmetry of the phased array (which leads to the constraint that the analyzer vector pairs have the same polarization but with different helicity) the four analyzer vectors can not form a regular tetrahedron in the Poincaré sphere and the optimum condition number (Eq. (2.21)) can not be obtained. Increasing the number of polarization analyzers to six, by superimposing a third metasurface the optimum basis can be achieved and a condition number of $\sqrt{3}$ is theoretically feasible [115]. With six polarization measurements the polarimeter is overdetermined and the error is further improved simply by the increase in statistical data. Furthermore, it was shown that a larger number of outputs can be used to train a neural network model to improve the performance of the polarimeter and extend its functionality to act as a wavemeter [106]. In the case of the 6-output polarimeter, the optimum positions of the analyzer vectors are obtained by rotating the three metasurfaces 60° relative to each other and by setting

the column-pair distance to $S = \lambda(1 + 1/4)$ for out-of-plane orders and $S = \lambda(1 + 1/8)$ for in-plane orders. Illustrations of the metasurface for the 4-output design and the 6-output design are shown in Fig. 3.11, together with the predicted analyzer vector positions on the Poincaré sphere.

The in-plane design is well suited for coupling the scattered radiation directly to planar waveguides and could therefore be advantageous in an on-chip polarimeter array design. Also, as disscussed earlier (Eq. (3.6) and Fig. 3.6) the signal contrast is better for this configuration. Furthermore, the maximum power to the detector at the designed wavelength (Fig. 3.7a) is larger, presupposing that all the power in the in-plane lobe is acquired by the detector. The out-of-plane design shows a less pronounced wavelength dependence, which is mainly an effect of the meta-grating as seen in Fig. 3.7b. Furthermore, there are no rescattering or absorption losses from neighboring antennas in the out-of-plane design, since the scattered field does not propagate along the plane of the metasurface. Such losses were found to be significant in the in-plane case (Chapter 4). There is therefore no limit to the overall size of the metasurface in the out-of-plane configuration, making alignment with the incoming light beam a simpler task.

The FDTD simulations presented in figures 3.5 and 3.7a are based on antennas embedded in a dielectric, without interfaces with other materials. The purpose of the dielectric layer is to create a waveguide for the scattered light in the in-plane orders to improve their directionality. Simulations of the electric field show that embedding the antennas is not only advantagous for the in-plane orders, it is absolutely necessary. When there is an interface between two materials of different refractive index, the intensity of the light scattered in-plane drops substantially (see Fig. 3.12). In actual experiments, surface roughness at the interface will quench the signal completely. Simulations of a 4 µm thick cladding layer are displayed in Fig. 3.13. The simulations show that the waveguide squeezes the in-plane field together to a more directional lobe. The reflections from the interfaces makes the radiation pattern more complicated and causes lower symmetry. Furthermore, the reflections also seem to affect the intensity distribution between orders and thereby the position of the analyzer vectors.

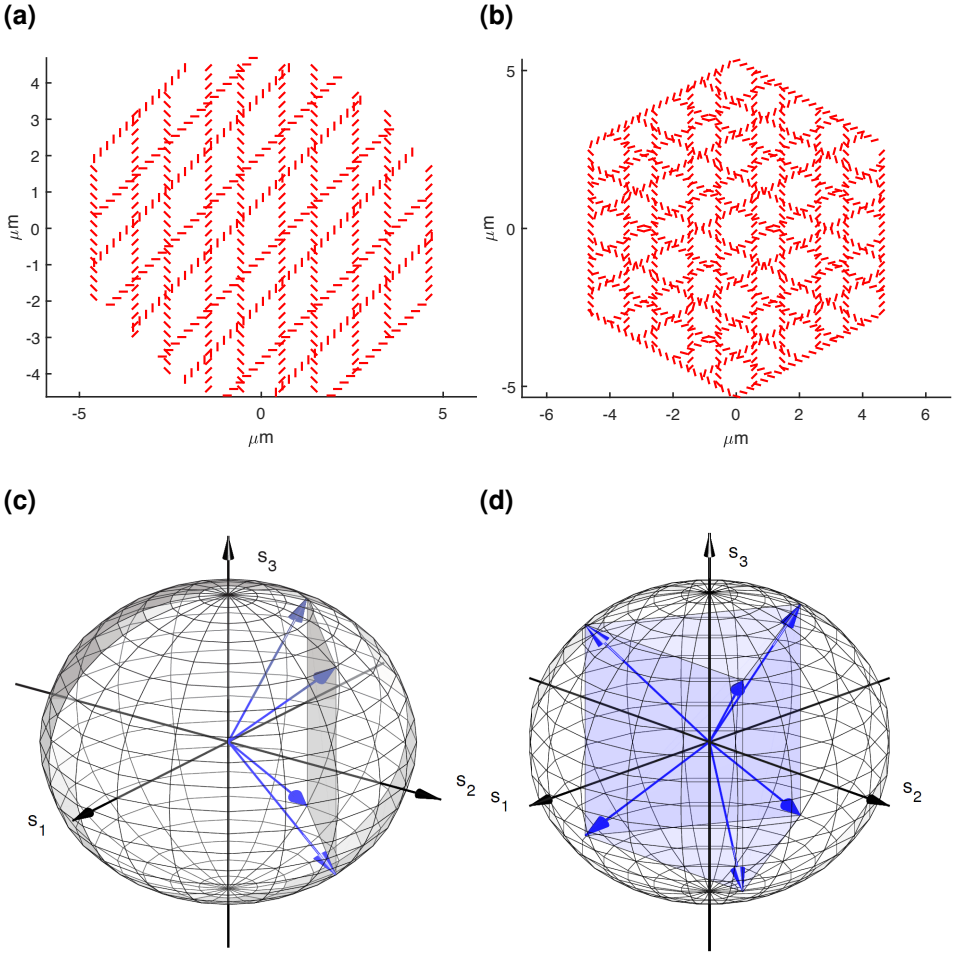

Figure 3.11. The two images in the top row are illustrations of metasurfaces designed for in-plane configuration ($S = \lambda(1 + 1/8)$) with (a) 4-output design (2 superimposed metasurfaces rotated 45° with respect to each other) and (b) 6-output design (3 superimposed metasurfaces rotated 60° (or 120°) with respect to each other). The two images in the bottom row are Poincaré spheres showing the analyzer vector positions of (c) the 4-output device and (d) the 6-output device

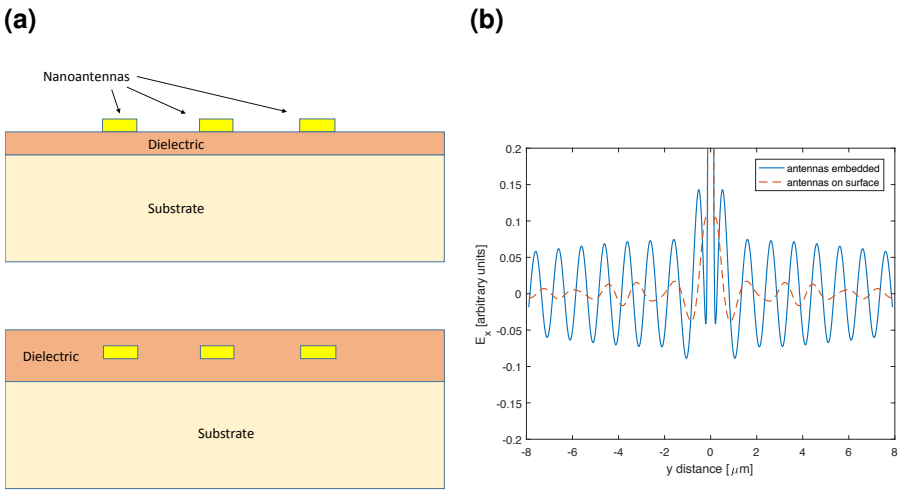

Figure 3.12. (a) Schematics of antennas placed on the surface of a dielectric layer (upper image) and antennas embedded in a dielectric layer (lower image). (b) FDTD simulations of electric field (E_x), scattered in-plane, from one column of nanoantennas, showing the improvement of embedding the metasurface in a dielectric layer.

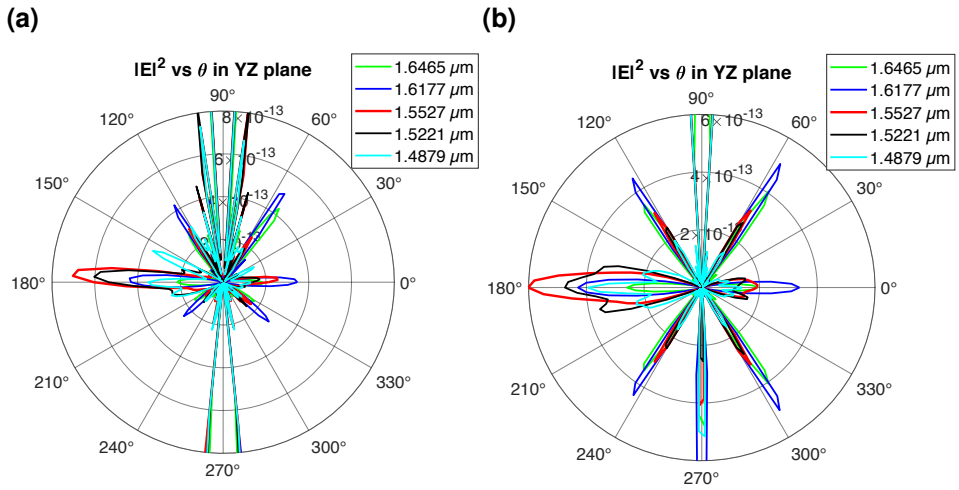

Figure 3.13. (a) Radiation pattern simulation of a five column-pair metasurface embedded in a dielectric cladding layer with n = 1.535 waveguide surrounded by SiO_2 (n = 1.44) and air. (b) The metasurface is embedded in dielctric and surrounded by SiO_2 on both sides

Chapter 4

Experimental realization of metasurface polarimeters

4.1 Fabrication of wafer-based metasurface polarimeters

The arrays of nanoantennas forming the metasurface were fabricated on fused silica substrates with a thickness of 1 mm. The substrates were diced into sizes of 20 mm$\times$ 20 mm. The metasurface was embedded within a 25 – 30 µm layer of benzocyclobutene (BCB) polymer. A first layer of BCB was deposited prior to the nanopatterning. To assure good adhesion between the glass substrate and BCB, the sample was wiped with cloth soaked in soap, rinsed in organic solvents (acetone and isopropyl alcohol (IPA) followed by deionized water rinse), and placed in an O_2/Ar plasma for 1 min using a plasma asher. Cyclotene 3022-57 (DOW® Chemical), commonly referred to as BCB, was spun onto the substrates for 30 s at 1000 rpm and softbaked in an oven for 40 min at 210 °C. The metasurface structures were patterned using electron-beam lithography (20kV EHT voltage and 850 pC/cm line dose) on polymethyl methacrylate (PMMA 950 2 % from MicroChem) spun onto the BCB layer at 2000 rpm for 30 s. Aluminium (20 – 30 nm) was deposited on top of the PMMA to avoid charging effects during electron-beam writing. After e-beam writing the aluminium was removed in a dilute NaOH solution (maD331 photoresist developer from MicroResist Technology) for 50 – 60 s, and the e-beam resist was subsequently developed for 50 s in MIBK(methyl isobutyl ketone):IPA 1:3. Cr/Au (1.5/20 nm) was deposited using electron-beam evaporation followed by liftoff in acetone. Then the second BCB layer was spin-coated and hard baked at 250 °C

for 60 min. Finally the sample was diced into a size and shape suitable for optical measurements. The nanolithography process is illustrated in Fig. 4.1.

The resulting nanorods had a thickness of 20 – 25 nm (confirmed with measurements in an atomic force microscope), width of approximately 50 nm and a length of around 250 nm (approximately 1/4 of a wavelength in the dielectric). The full metasurface covers an area of 100 µm × 100 µm. Scanning electron micrograph (SEM) images of the four and six output metasurfaces are shown in Fig. 4.2.

In the case of in-plane detection, the substrate was diced such that the substrate edges were perpendicular to the propagation directions of the scattered light. The substrates were fitted and glued (with epoxy) into a 3D-printed holder that aligned the sample with four or six individual TO-canned PIN photodiodes. The 3D-printed holders were made in two different designs to allow measurement in the in-plane as well as the out-of-plane configuration. One half of a fiber mating sleeve was glued onto the holder to allow coupling of light into the polarimeter with a standard fiber connector, as shown in Fig. 4.3. More detailed drawings of the 3D-printed holder can be found in the appendix, Fig. A4.1. The ceramic ferrule of the fiber connector is brought in contact with the metasurface. Since the mode size is around 10 – 10.5 µm, approximately five column-pairs of antennas are overlapping with the incident light beam, which amounts to only a small fraction of the total number of antennas in the patterned structure. It is therefore relatively simple to assure that the light beam is aligned with the metasurface before fixing the sample to the holder.

4.2 Experiments on wafer-based metasurface polarimeters

4.2.1 Optical setup

A schematic of the experimental setup is seen in Fig. 4.4. 1510 – 1610 nm light from a tunable laser was coupled into a deterministic polarization controller (DPC) and directed to the metasurface. The optical fiber between the DPC and the sample inevitably changes the polarization of the light. Therefore, the polarization of the light transmitted through the sample was additionally measured using a commercial free-space rotating-wave-plate polarimeter (POL). A manual polarization controller was used to ensure that the

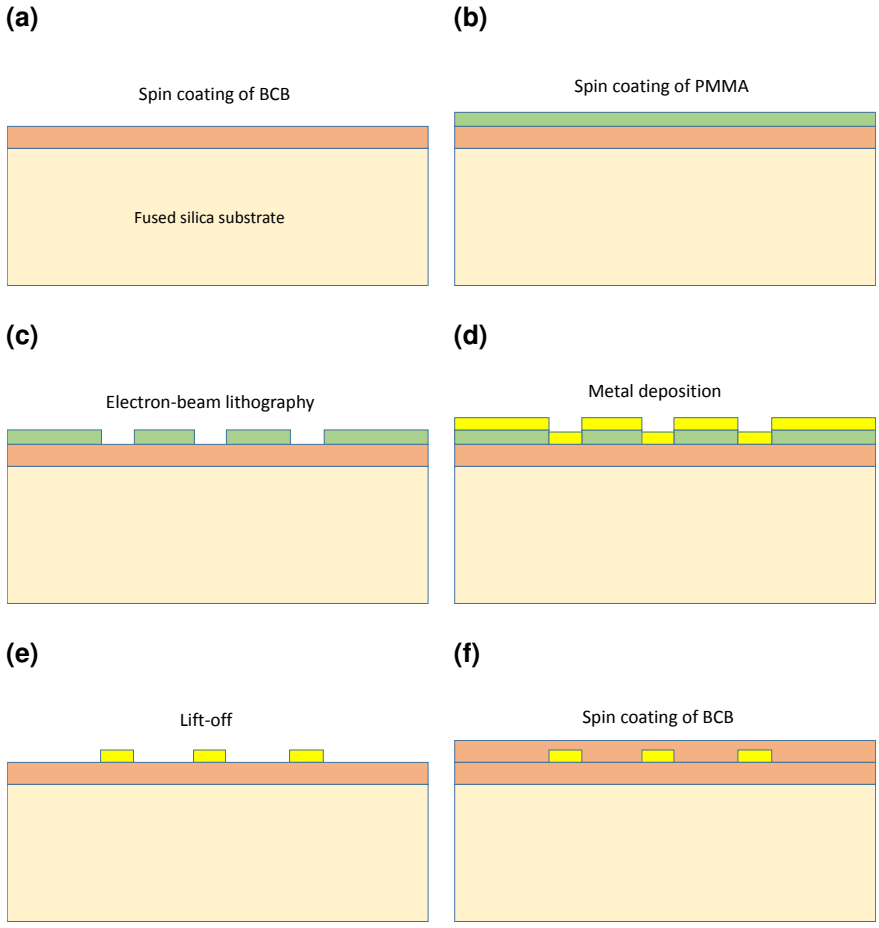

Figure 4.1. Schematics of the metasurface fabrication process. (a) BCB spin-on and softbake. (b) PMMA spin-on and bake. (c) e-beam writing and development. (d) Cr/Au evaporation (e) Lift-off process (f) BCB spin-on and hardbake.

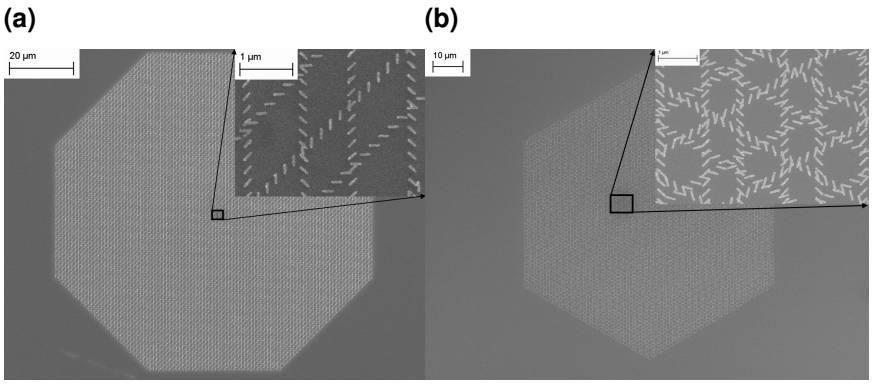

Figure 4.2. Scanning electron micrograph images of the fabricated metasurfaces showing the total metasurface structure. Inset: zoom-in of the metasurfaces displaying the individual antennas of the array. (a) Four output design with two superimposed metasurfaces (b) Six output design with three superimposed metasurfaces.

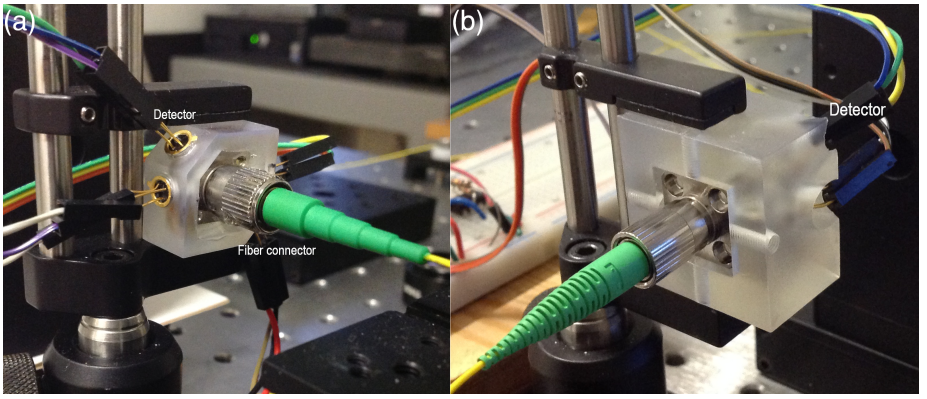

Figure 4.3. Photographs of the 4-output in-plane metasurface polarimeter (a) and the 4-output out-of-plane polarimeter (b). The incident light enters each device through the optical fiber which is placed in contact with the sample perpendicular to the metasurface. The transmitted light exits through a hole in the back of the 3D holder. Four TO-canned photodiodes are glued into each holder.

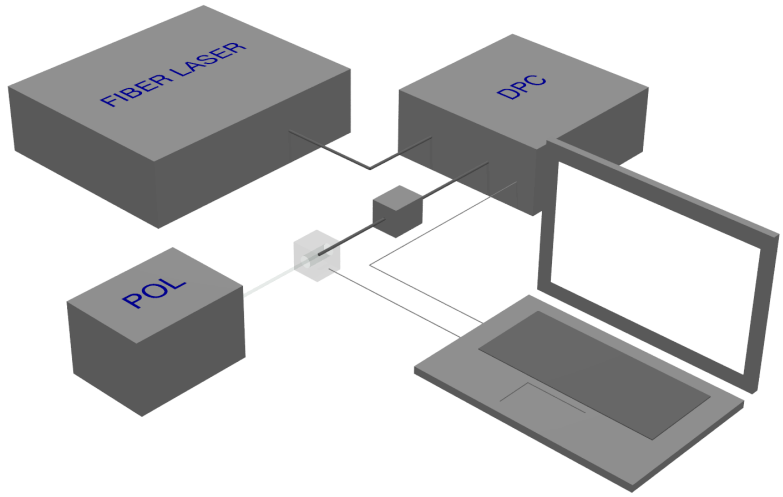

Figure 4.4. An illustration of the experimental setup. Light from a tunable fiber laser is coupled through a standard single-mode fiber to a deterministic polarization controller (DPC). The DPC and the metasurface polarimeter (light grey box) are connected with a second optical fiber. A 3-paddle polarization controller (the dark grey box) on the second optical fiber corrects for polarization changes caused by the fiber. A commercial freespace polarimeter (POL) is placed behind the sample. Four or six photodiodes are fitted onto the sample holder and the measured signal is picked up by a microcontroller.

DPC and the rotating-waveplate polarimeter registered the same polarization state. The output signals from the four detectors on the metasurface polarimeter were fed through an amplification circuit and measured in photoconductive mode. A microcontroller collected a 300-sample set from the four photo-detectors at a rate of 1 kHz. This sampling rate is limited only by the electronics. Approximately 25 % of the input power is lost in the metasurface at 1550 nm due to absorption and scattering. Approximately 0.4 % of the total incoming power is scattered to each photodetector. The setup can be operated in a semiautomatic mode, where the DPC is used for reference polarization, or in an automatic mode where the POL is used for reference. In the semiautomatic mode the user must assure that the DPC and the microcontroller are aligned in time. In automatic mode, the DPC and POL are triggered from the computer. Futhermore, the power and wavelength of the fiber laser can be controlled automatically. The power on the metasurface is calibrated manually with a large-area photodetector when using the automated setup, since only a fraction of the light impinges on the free-space polarimeter.

4.3 Performance of wafer-based metasurface polarimeters

A number of polarization measurements were performed on 4 and 6-output in-plane and out-of-plane devices using the calibration procedure presented in chapter 2 [38] and the results were compared to the polarization state measured by the DPC or the POL. Each metasurface polarimeter was tested at several wavelengths within the telecommunication C-band (1530 – 1565 nm). One set of measurements performed at a wavelength of 1550 nm is shown in Fig. 4.5 using a 6-output polarimeter measured in-plane. The uncertainty of the measurements, shown with red errorbars, are calculated using Eq. (2.22). The uncertainty is a sum of the contributions from noise in the intensity measurements and from error propagation through the calibration process, of which the former contribution is dominant. Errorbars on the reference polarizations are not shown on the plot, since they are too small to be seen. As discussed in section 2.2, the standard deviation of a number of measurements overestimates the precision of the reference polarimeter. The root-mean-square error (RMSE) between polarization states measured by the metasurface polarimeter and reference polarization states at 1550 nm with 3mW

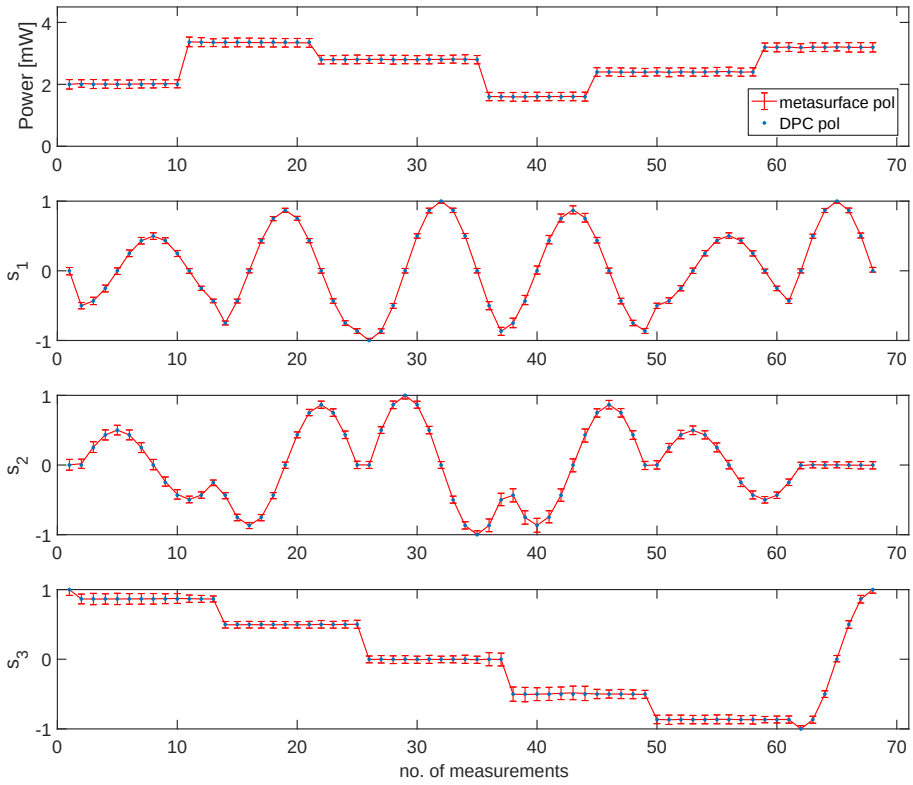

Figure 4.5. Polarization measurements at a wavelength of 1550 nm using a 6-output device with an in-plane design. Each subplot contains one element of the Stokes vector. The first subplot is the power of the incident light, which is proportional to S_0. The next three subplots are the parameters characterizing the state of polarization (SOP), $s_1 - s_3$. The red line with errorbars are the polarization measurements of the metasurface polarimeter, the blue dots are the reference polarizations set by the deterministic polarization controller (DPC).

incident laser power is

$$RMSE = \sqrt{\frac{\sum_{t=1}^{T}(\Delta s_{1,t})^2 + (\Delta s_{2,t})^2 + (\Delta s_{3,t})^2}{3T}} = 0.0012 \tag{4.1}$$

As seen in Fig. 4.5, the accuracy is good whereas the polarimetric sensitivity is relatively

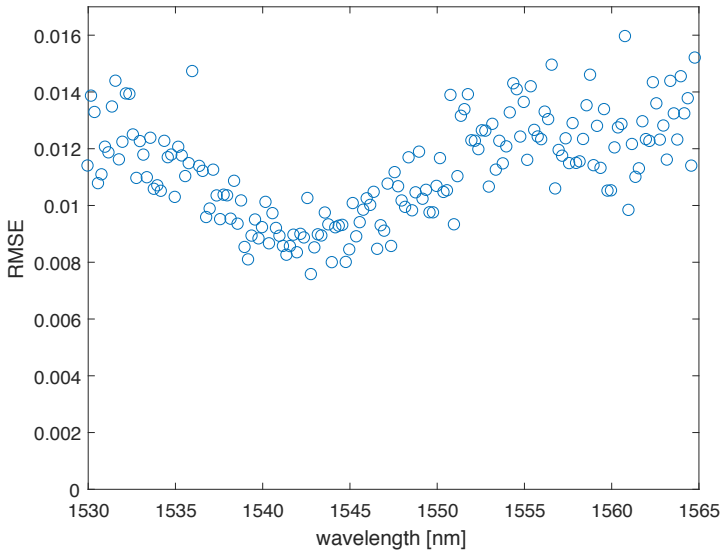

Figure 4.6. Root-mean-square error (RMSE) on all SOP parameters at wavelengths between 1530 nm and 1565 nm. The laser power is varied between 1-3 mW

low. This is of course partly a result of the signal-saving design. However, it is expected that electronic noise, especially amplifier noise and electromagnetic interference (EMI), can be significantly reduced by optimizing the electronic circuit.

Figure 4.6 shows the RMSE for a 6-output polarimeter measured in the out-of-plane design at wavelengths between 1530 nm and 1565 nm with the automated setup. A metasurface design with antenna column spacing of $\lambda(1+1/8)$ was used. The device calibration was repeated for each wavelength, since the polarimeter response is inherently wavelength-dependent, as shown in Fig. 3.7. The same metasurface polarimeter design can therefore be applied across a wide range of wavelengths as long as the spectral information of the incident light source is known *a priori*. The plot shows that the variation in RMSE is low over the measured wavelength range. Other measurements show that this is true even within a larger wavelength range of 1510 – 1610 nm [84]. The error increases on each side of the design-wavelength, which

is 1550 nm. This is expected, since the scattered light intensity decreases away from resonance (see Fig. 3.3a). The minimum is approximately 7 nm lower than the design wavelength, corresponding to a 0.5 % shift from the intended response. The reason for this deviation could be that the resonance wavelength of the antennas are slightly blueshifted from the intended value. This is supported by the fact that the combined mean power on the detectors has a maximum around 1540 nm. Another source of deviation in the RMSE is wavelength dependency of the position of the analyzer vectors. This wavelength dependency is surprisingly strong. The analyzer vectors for wavelengths between 1530 nm and 1565 nm are shown in Fig. 4.7, using the same data as in Fig. 4.6. 2D plots are shown in appendix A5. As documented in Fig. 4.8, the error is considerable even when the polarimeter is measured at a wavelength only a few tens of a nanometer away from the calibration wavelength and increases about tenfold only one nanometer away from the calibration wavelength. In order to assure accurate results it is therefore necessary to make a very fine calibration library and the input wavelength must be known very precisely. However, what seems to be an obstacle to a practical device can be turned into a benefit by adding an extra layer of software. By using deep neural networks trained on calibration data, it was found that the metasurface polarimeter can accurately measure polarization over a wide wavelength range without a-priori knowledge of input wavelength, and the functionality of the polarimeter can simultaneously be enhanced to measure the input wavelength as well [106].

4.3.1 Error and polarization response

From Eq. (2.19) it is seen that, assuming linearity, the polarimeter error is generally affected by two factors. First, $\mathbf{D}$ deviates due to, for example, errors in reference polarization measurement, fiber position changes, and matrix inversion in the calibration calculation. Secondly, the intensity measurement is subject to errors, e.g. detector noise, nonlinarity of detector response, and source power fluctuations. To minimize the error, the transformation should be well conditioned, i.e. the condition number $\kappa(\mathbf{A})$ defined in Eq. (2.21), should be as low as possible. As mentioned in section 2.2, the minimum condition number corresponds to the analyzer vectors spanning the largest possible volume in the Poincaré sphere. Therfore, we need to control the polarization selected by the polarization analyzers of the metasurface polarimeter. This polarization is set by the design parameters of the metasurface, the distance, S, between antenna columns (see Eq. (3.6)) and the orientation of the columns in the plane of the

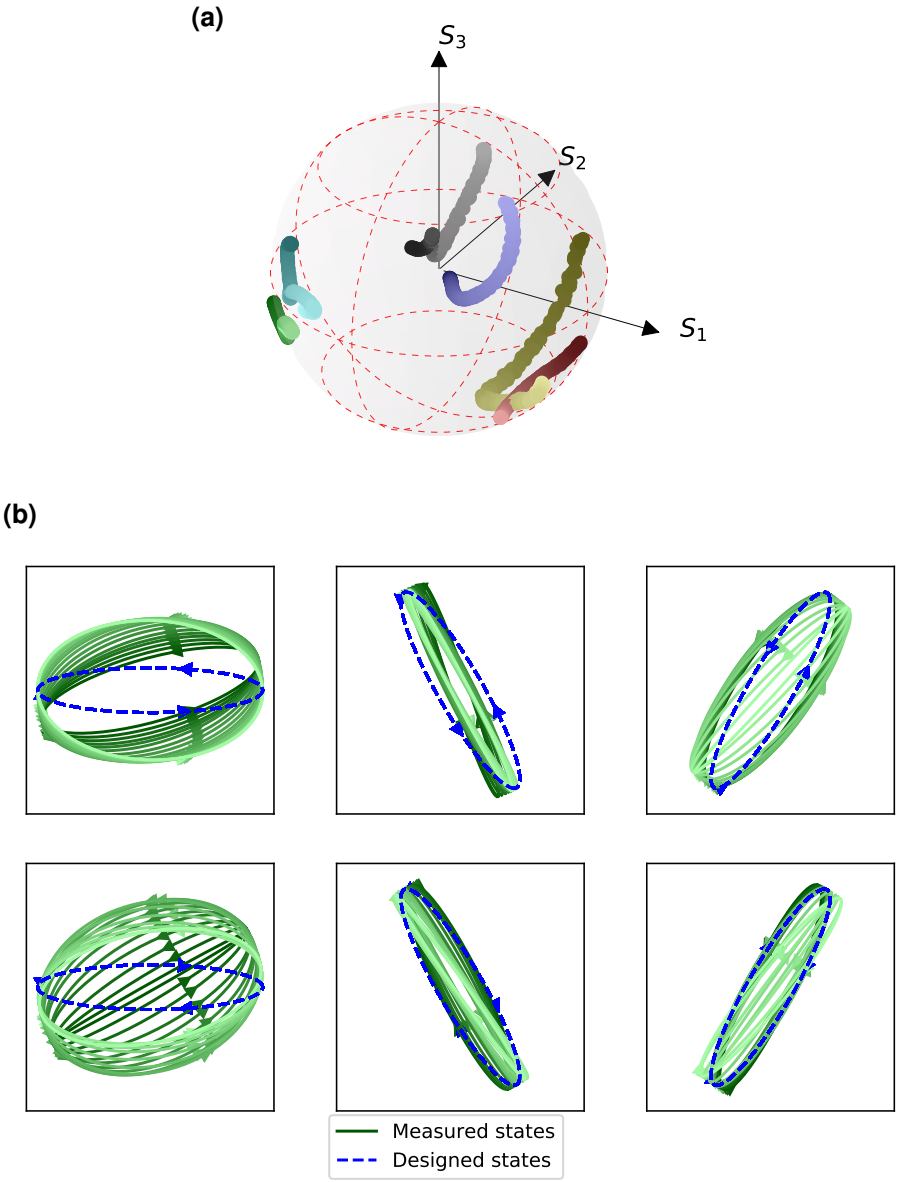

Figure 4.7. Analyzer vector wavelength dependence of a 6-output metasurface polarimeter measured in out-of-plane configuration from 1530 nm – 1565 nm in steps of 0.2 nm. In (a) the analyzer vectors are depicted as colored circles on a Poincaré sphere as normalized state of polarization parameters. The dark-colored circles are analyzer vector positions at short wavelengths and the light-colored circles show the positions at long wavelengths. In (b) the analyzer vector positions are shown as polarization ellipses (see Fig. 2.1b). Dark green ellipses corresponds to short wavelengths and light green ellipses to long wavelengths. Only every 10th measurement is shown (equal integer wavelengths). The dashed blue polarization ellipses are the designed analyzer vector positions.

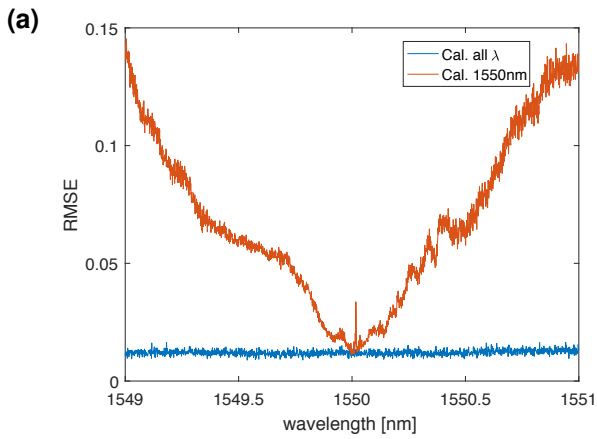

Figure 4.8. (a) Root-mean-square error between metasurface polarimeter measurements and reference measurements using a 6-output device in out-of-plane configuration measured in automatic mode. The polarization measurements are repeated for different wavelengths. The data shown with a blue line is obtained when the polarimeter is calibrated for each wavelength. The data shown with the red line is obtained when the polarimeter is calibrated only at 1550 nm. (b) Polarization measurements with a 4-output metasurface polarimeter in out-of-plane configuration (blue circles) and DPC reference polarizations (red circles) at 1550 nm (upper left), 1550.1 nm (lower left), 1550.2 nm (upper right), 1550.3 nm (lower right); all using the 1550 nm calibration

sample (see Fig. 3.10). There are, however, several sources of error in the polarization response of the polarimeter such as internal reflections, wavelength dependence, antenna interactions, geometric deviations, deviations in the angle of the incoming light, and rescattering. Experiments show that such deviations are surprisingly large. The analyzer vector positions of two 4-output metasurfaces are shown in Fig. 4.9, illustrating the magnitude of the divergence. Deviations in the polarization response have been reported

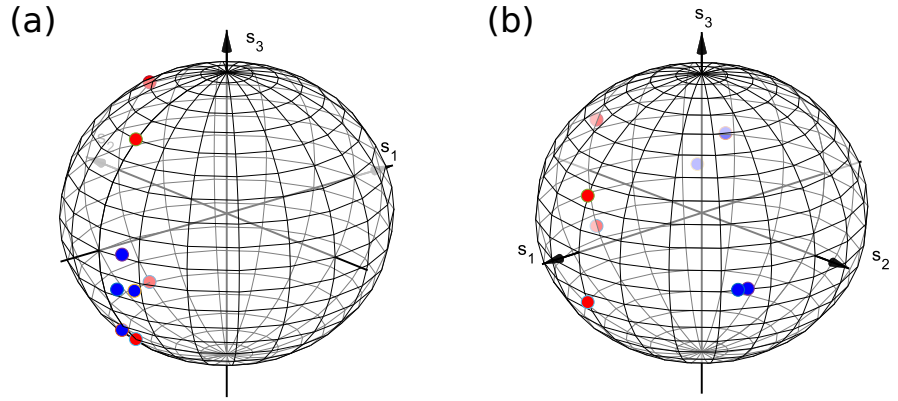

Figure 4.9. Analyzer vector position on the Poincaré sphere for a device with (a) in-plane design and (b) out-of-plane design. The analyzer vectors are normalized to unit length. Red dots are the theoretically predicted positions. Blue dots are the measured positions.

earlier for a single (2-output) fishbone metasurface, but not of the same magnitude [103]. Figure 4.10 shows the analyzer vectors of two metasurfaces measured in-plane and fabricated as described earlier in this chapter, but with a metasurface design that only has two in-plane outputs, i.e. the superimposed metasurface with columns rotated 45° has been omitted. It is seen that even though there is still some deviation from the design polarization, it is much less than the divergence seen in Fig. 4.9a. This suggests that antenna interactions due to the superimposing of two metasurfaces are non-negligible. Assuming no near-field interaction, the only scattering order that should be affected by a superimposed metasurface are the ones parallel to the incident light beam. Figure 4.11 shows FDTD simulations of a 5-column-pair, 9-row metasurface. It is seen that the meta-grating is affected when there is a superimposed metasurface, since several new 'noisy' orders appear. Furthermore, more power is coupled into the meta-grating scattering orders and the polarization response is affected. A number of FDTD simulations have been performed with different polarizations, sampling the entire Poincaré to get a more quantitative idea of the change of the analyzer vectors.

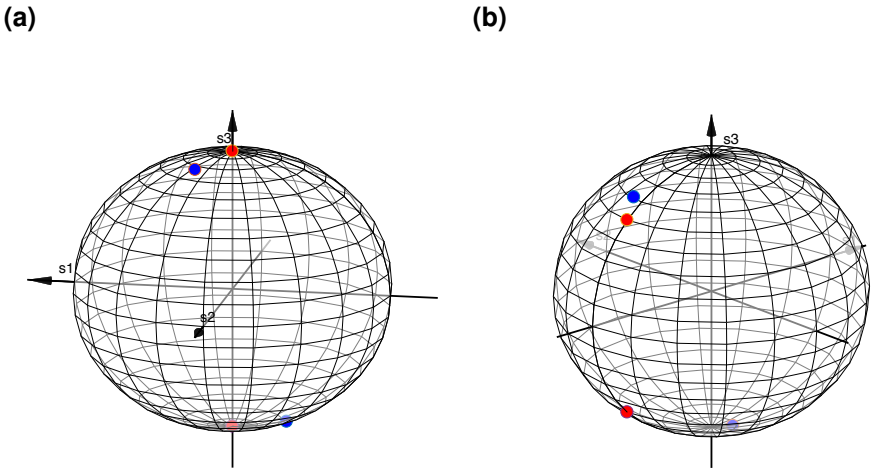

Figure 4.10. Analyzer vector position on the Poincaré sphere for devices measured in-plane and designed for (a) circular polarized light and (b) elliptical polarized light. Red dots are the theoretically predicted positions. Blue dots are the measured positions.

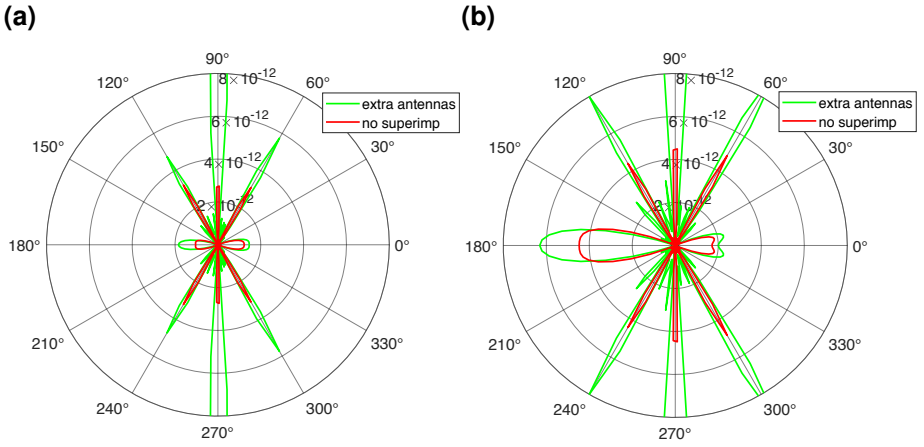

Figure 4.11. Radiation patterns of the scattered field in the yz plane from FDTD simulations of 5 column-pair, 9 row metasurface with (green curve) and without (red curve) a superimposed metasurface. (a) Elliptically polarized incoming light $(\psi,\delta) = (\pi/4,\pi/4)$ (b) 45° linearly polarized incident light $(\psi,\delta) = (\pi/2,0)$

The simulations are performed on a rectangular area containing a 5-column-pair, 9-row metasurface and repeated with a superimposed metasurface, with columns rotated 45° with respect to the first metasurface. The superimposed antenna arrays are cropped to fit with the rectangular area of the first metasurface. The simulated number of antennas is not as large as experimentally realized. However, the simulation area is limited by the memory of the simulation computer (64 GB). Results show that the polarization response is changed ca. $2\Delta\varepsilon = 10°$ on the Poincaré sphere upon the introduction of the superimposed metasurface. The simulation model is limited by the relative short column length (9 antennas). Furthermore, it does not take into account the changes in polarization response that arise from, e.g., reflections and proximity effects at overlapping antennas during e-beam writing. However, the simulation shows a clear effect on the polarization response from superimposing a 45° rotated metasurface.

Further experiments have been performed to investigate the influence that the superimposed metasurface has on the polarization response. Two additional 4-output polarimeters were fabricated, where the two metasurfaces were separated by a BCB spacer with thickness of 2 µm, instead of superimposing them in the same layer. This means that the polarimeters consist of two stacked metasurfaces; each metasurface supplying the polarimeter with two polarization analyzers. The polarimeters were measured in in-plane and out-of-plane configurations. The magnitude of the scattered power to the detectors was more than doubled compared to the single-layered metasurface polarimeters indicating that superimposing metasurfaces indeed affect the meta-grating scattering orders. The analyzer vectors of in-plane measurements are shown in Fig. 4.12 and out-of-plane measurements in Fig. 4.13. Each figure shows two devices measured twice at different light source positions on the sample. To allow for the repositioning of the incoming light, the samples were measured in a slightly different setup. Instead of using a fiber connector and half of a mating sleeve, the light beam was directed to the metasurface from a bare fiber (only cladding and core) with a cleaved fiber facet. The fiber was placed on an xyz stage for alignment to the metasurface. Figure 4.12 shows that there is no immediate improvement in the control of the in-plane measured analyzer vector positions by vertically separating the superimposed metasurfaces. The polarization response is completely arbitrary. There seems to be no relation between samples as well as between measurements on the same sample at different positions. This result suggests that rescattering from neighboring antennas (when passing them on the way to the detectors), and especially antennas from the superimposed metasurface where half of the antennas are parallel to the field, is the limiting factor when it comes

to controlling the position of the in-plane analyzer vectors. This theory is supported by the fact that the signal to the detectors is completely quenched, when the metasurface is embedded in a 4 µm waveguide, instead of the 25 µm waveguide used in all wafer-based polarimeters presented in this work. When the waveguide is thinner the scattered field is larger at the position of the neighboring antennas and the entire field is scattered out of plane before exiting the metasurface (remember that the incident beam only covers a circular area with a diameter of ca. 10 µm, whereas the entire metasurface area is a hexagon/octogon within a writefield of 100 µm × 100 µm). The experiments therefore show that interaction with neighboring antennas are larger than basic intuition suggests.

Out-of-plane measurements on the same two devices are presented in Fig. 4.13. The analyzer vector positions are much closer to the polarizations the metasurface is designed for. The deviations from predicted polarizations are still clearly observed, but comparable to the deviations observed with 2-output metasurfaces. These measurements therefore strongly indicate that part of the deviations in Fig. 4.9b are caused by antenna interactions with the superimposed metasurface. The analyzer vectors are almost completely unaffected by fiber position change. This supports the theory that rescattering has an extensive influence on the in-plane analyzer vectors. An exception is the analyzer vectors of one of the metasurfaces of sample A (Fig. 4.13a and Fig. 4.13b). The lift-off process for this metasurface only partially succeeded resulting in delamination of many antennas. This increase in geometric deviations naturally affects the polarization response as a function of fiber position.

Geometrical variation of individual antennas is another source of error in the polarization response. FDTD simulations of 5 column-pairs and 9 rows of antennas are performed with antennas varying from the designed dimensions ([220–270 nm] × [40–60 nm] × [16–30 nm]), which is a considerably larger variation than observed experimentally. The in-plane analyzer vector positions are found by sampling the polarization over the Poincaré sphere. The simulations show a clear shift of the polarization response of $\Delta\vartheta = 16°$ and $\Delta\varepsilon = 6°$. The shift in polarization response depends on row distance (nearfield coupling) and the spatial distribution of the size variations. FDTD simulations of 5 column-pairs and 5 rows of antennas with double row spacing ($\lambda/2$) and a different spatial distribution of the size variations result in a change in polarization response of less than 3° (the resolution on azimuth and ellipticity). FDTD simulations of 5 column-pairs and 9 rows of antennas (and a row distance of $\lambda/4$) are performed with a smaller antenna variation ([230–260 nm] × [45–55 nm] × [18–24 nm]) resulting in a change in polarization response of $\Delta\vartheta = 10°$. A way to experimentally investigate the sensitivity

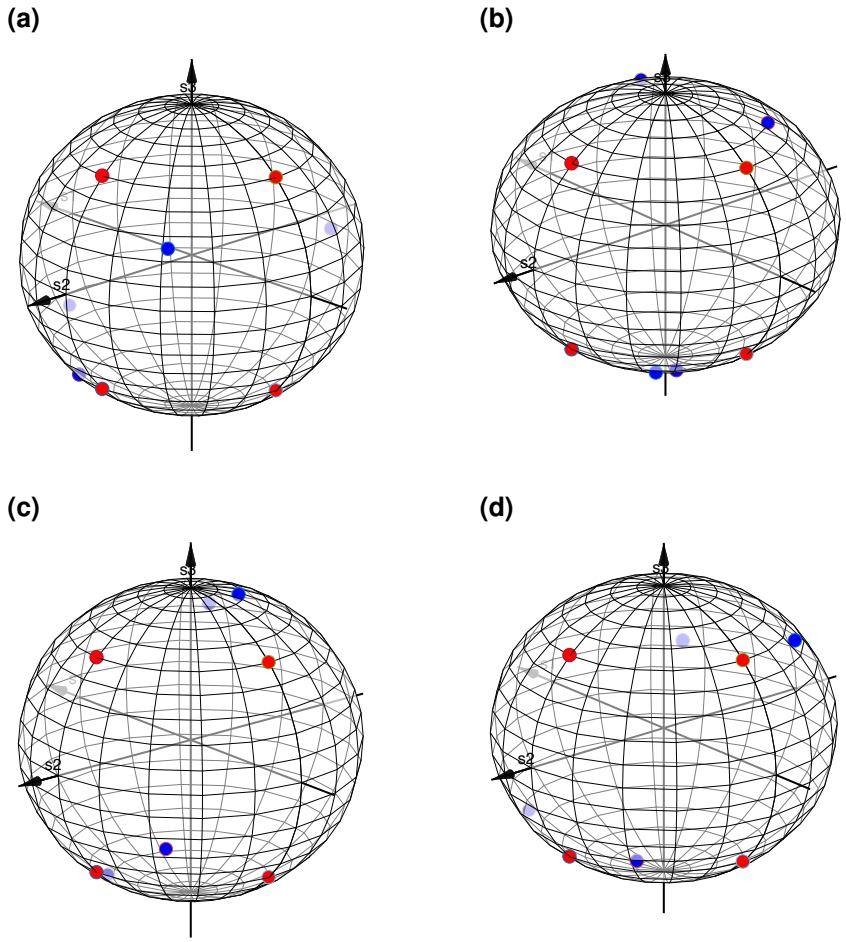

Figure 4.12. Experimentally measured position of analyzer vectors for 4-output polarimeter measured in-plane. The two superimposed metasurfaces, each delivering 2 outputs are spatially split with a distance of approximately 2 µm. (a) Sample A, fiber position one. (b) Sample A, fiber position two (c) Sample B, fiber position one (d) Sample B, fiber position two.

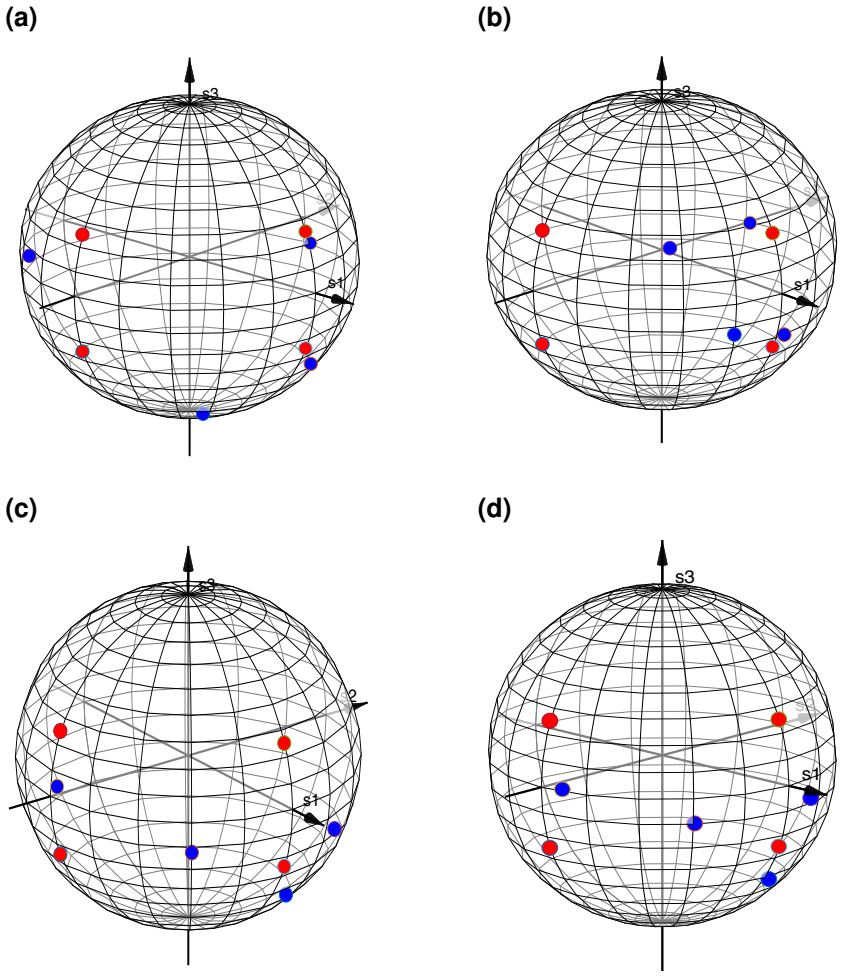

Figure 4.13. Experimentally measured position of analyzer vectors for 4-output polarimeter measured out-of-plane (a) Sample A, fiber position one. (b) Sample A, fiber position two (c) Sample B, fiber position one (d) Sample B, fiber position two.

of polarization response to geometrical variation is to fabricate a metasurface polarimeter with varying antenna sizes. Another experiment could be to illuminate a larger area of antennas by terminating the fiber with a collimator to statistically smoothen out the effect of geometrical variation of antennas. This experiment, however, requires a larger metasurface than the $100\,\mu m \times 100\,\mu m$, which is the largest possible writefield available for this project. The experiments are recommended for future work, also because the latter provides a good experimental setup for measuring the error caused by angular deviations of the incident light.

4.3.2 Systematic error

In the previous sections the uncertainty of metasurface polarimeter measurements was calculated from the formulas derived in chapter 2 (equations 2.22 – 2.24), that show how the error in $\mathbf{D}$ and $\mathbf{I}$ propagates to the final Stokes vector $\mathbf{S}$. Furthermore, the polarization response of the metasurface was discussed because the determined Stokes vector is most immune to error when the condition number (Eq. (2.21)) is at its minimum, i.e. when the analyzer vectors span the largest possible volume on the Poincaré sphere. In this section, the focus is solely on systematic errors, thereby excluding random errors, which for the metasurface polarimeter is equivalent to detector/amplifier noise (although it can be argued that detector noise can be interpreted as a systematic error in case of a short acquisition time). The polarimeter is subject to a number of systematic errors such as deviation in wavelength, angle of incidence, fiber position, reference polarizations, source power fluctuation, nonlinearity, and temperature-dependent effects. These errors occur because the polarization measurement is indirect, i.e. it is assumed that the measurement is performed under the same conditions as the calibration. However, as a result of the systematic errors the *perceived* inversed analyzer matrix, $\mathbf{D}_p$, used to calculate the *percieved* Stokes vector, $\mathbf{S}_p$, will differ from the *actual* inversed analyzer matrix, $\mathbf{D}_a$, measured during calibration. Using Eqs. (2.19) and (2.16) the perceived Stokes vector can be expressed as [34, 116]

$$\mathbf{S}_p = \mathbf{D}_p\mathbf{I} = \mathbf{D}_p\mathbf{A}_a\mathbf{S}_a = \mathbf{Q}\mathbf{S}_a \tag{4.2}$$

where the distortion matrix, $\mathbf{Q} = \mathbf{D}_p\mathbf{A}_a$, maps the actual Stokes vector to the perceived Stokes vector. The mapping is illustrated schematically in Fig. 4.14. The model for the error caused by miscalibration permit a simulation of the error for a known calibration error. It can be used to analyze the distribution of error over the parameter space of all

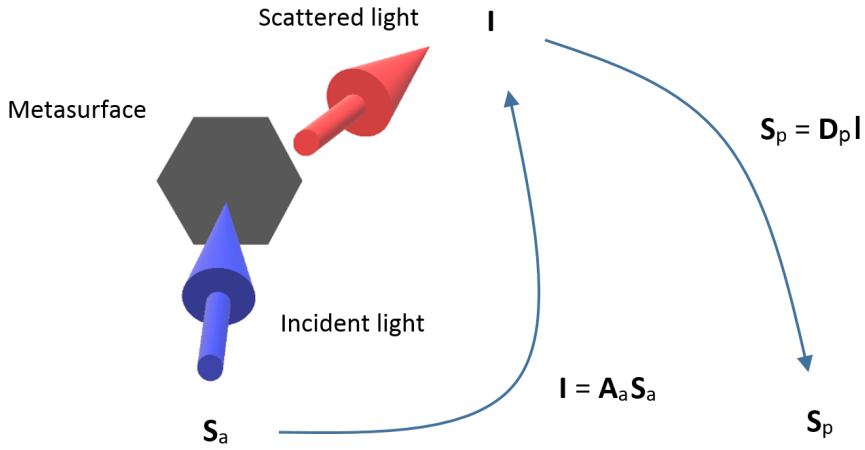

Figure 4.14. Illustration of linear transformation with systematic errors. The incident light is characterized by an actual polarization $\mathbf{S}_a$, which is related to the measured intensities of the scattered light by $\mathbf{I} = \mathbf{A}_a\mathbf{S}_a$. However, if the measurement is performed under different circumstances than the calibration, the inversed analyzer matrix is wrong and we arrive at a different Stokes vector, $\mathbf{S}_p$.

polarizations and to find the value of a given physical parameter that causes error (e.g. angle or wavelength) that corresponds to the maximum tolerated error. Figures 4.15 and 4.16 shows the error simulation using the analyzer matrices from the data shown in Fig. 4.8b, where the wavelength is varied between 1550 nm and 1550.3 nm in steps of 0.1 nm. The incoming polarizations are parameterized using a spiral sampling to achieve an even distribution of polarizations on the Poincaré sphere [117]

$$\mathbf{S}_a = (1 \;\; cos(k) \;\; sin(k) \;\; x)^T \tag{4.3}$$

where $x \in [-1,1]$ and $k \in [0,2\pi]$. A total of 800 points and 30 revolutions on the Poincaré sphere were used. The actual analyzer matrix is obtained by calibrating at each wavelength (1550.1 nm, 1550.2 nm, and 1550.3 nm). The analyzer matrix found by calibration of the 1550 nm data is selected as the perceived analyzer matrix. Figure 4.15 shows the error of all three wavelength shifts on 2D plots; each containing the error on the four Stokes parameters. Figure 4.16 shows the error of the measurement with a 0.3 nm wavelength shift (Fig. 4.15c) on a Poincaré sphere, where the absolute error is illustrated as a color change on the spiral locus of the input polarizations ($\mathbf{S}_a$). The wavelength discrepancies of 0.1 – 0.3 nm are selected for illustration purposes only, as a

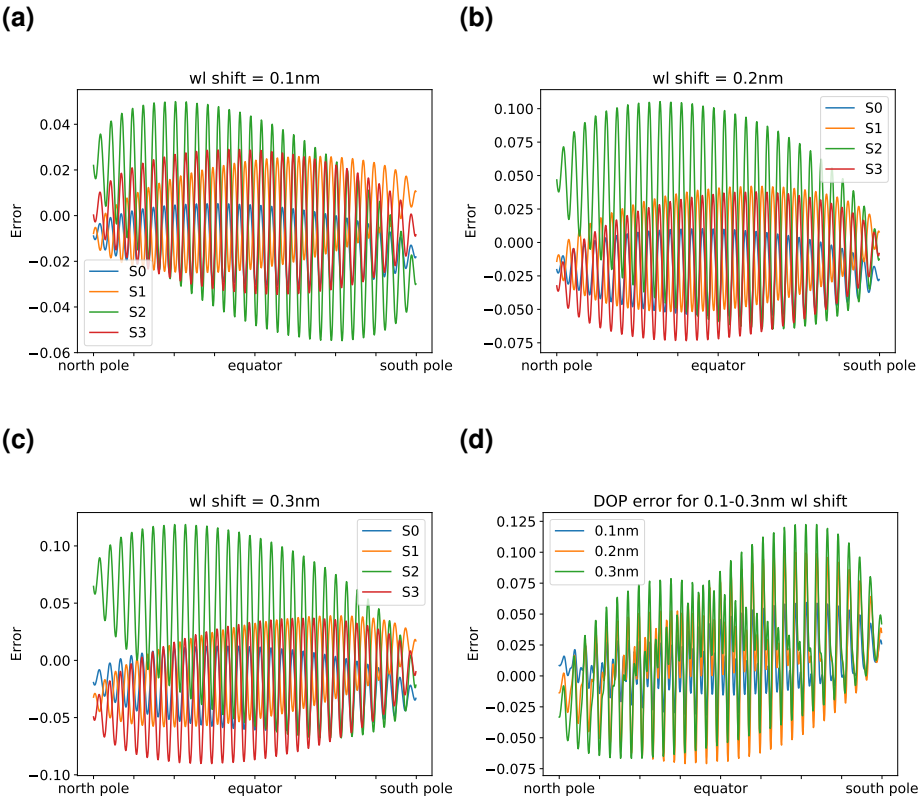

Figure 4.15. Simulation of the systematic error for each sampling point along a spiral locus around the Poincaré sphere for a wavelength shift from a 1550 nm incoming narrow linewidth light source of (a) 0.1 nm, (b) 0.2 nm, and (c) 0.3 nm. The error on the degree of polarization (DOP) is shown in (d) for all three wavelength shifts.

case where the wavelength shift is small, but the error considerable.

Because of the unevenly distributed error over the Poincaré sphere it would be useful to analytically predict the polarization of maximum error from the analyzer matrices alone. This is possible using the method of Lagrange multipliers [118]. The Lagrangian method is employed for optimization problems that are subject to constraints. With a constraint that we have fully polarized light and intensity normalized to unity the

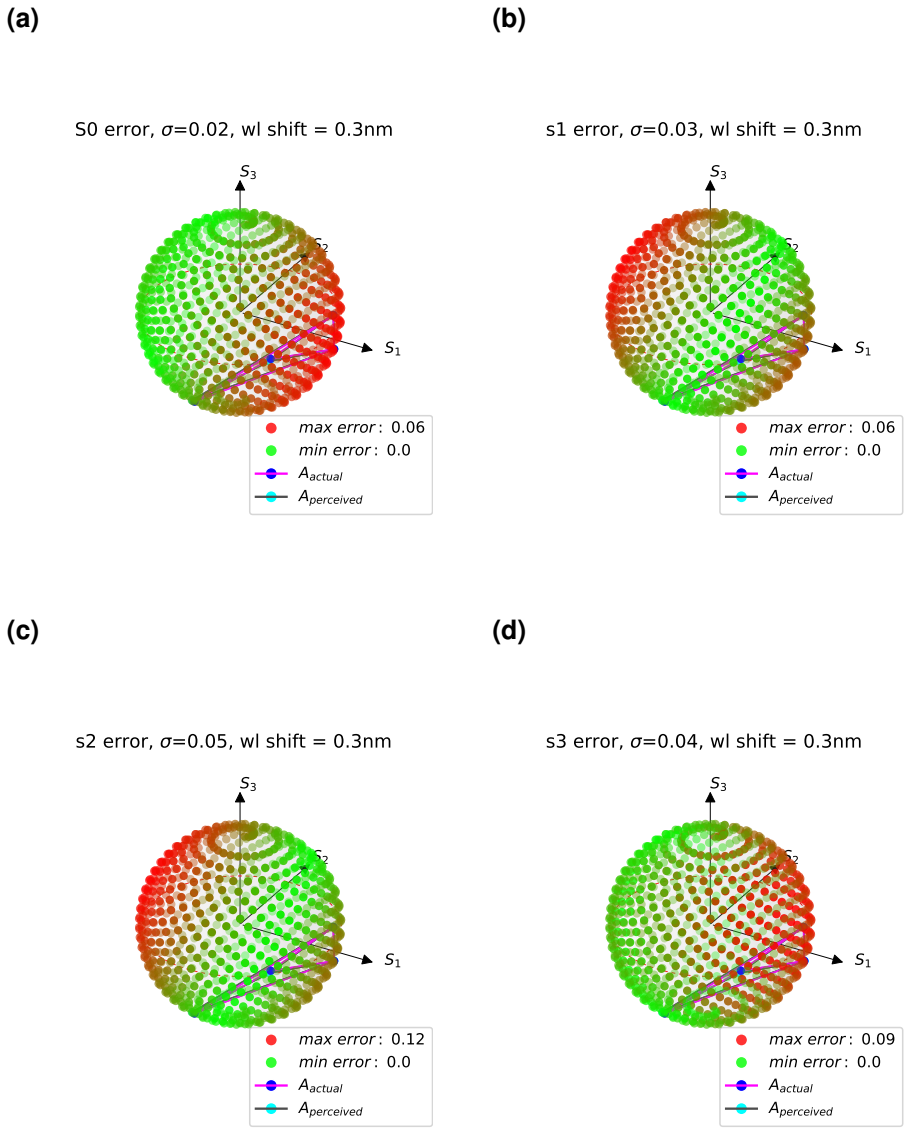

Figure 4.16. Simulation of the systematic error at a wavelength shift of 0.3 nm shown on the Poincaré sphere as a color change. The connected points illustrate the positions of the percieved analyzer vectors (cyan dots, black lines) and the actual analyzer vectors (blue dots, magenta lines).

functions for the error on the Stokes parameters are

$$\begin{aligned}
\varepsilon_{S_0}(S_1,S_2,S_3) &= 1-(Q_{11}+S_1Q_{12}+S_2Q_{13}+S_3Q_{14})\\
\varepsilon_{S_1}(S_1,S_2,S_3) &= S_1-(Q_{21}+S_1Q_{22}+S_2Q_{23}+S_3Q_{24})\\
\varepsilon_{S_2}(S_1,S_2,S_3) &= S_2-(Q_{31}+S_1Q_{32}+S_2Q_{33}+S_3Q_{34})\\
\varepsilon_{S_3}(S_1,S_2,S_3) &= S_3-(Q_{41}+S_1Q_{42}+S_2Q_{43}+S_3Q_{44})
\end{aligned} \tag{4.4}$$

and the condition is written as

$$c(S_1,S_2,S_3) = S_1^2+S_2^2+S_3^2 = 1 \tag{4.5}$$

To find the maxima of a function using the Lagrangian method we need to find all stationary points of the *Lagrange function* and establish which of the stationary points are the global maximum of the function. Introducing the Lagrange Multiplier (λ), the Langrange function is given by

$$\varepsilon_{S_x}(S_1,S_2,S_3)-\lambda c(S_1,S_2,S_3) \tag{4.6}$$

and the stationary points are the points where the partial derivatives of the Langrange function are zero. In the case of the error on S_1, we obtain

$$\begin{aligned}
1-Q_{11} = 2\lambda S_1 &\Leftrightarrow S_1 = \frac{1-Q_{11}}{2\lambda}\\
-Q_{12} = 2\lambda S_2 &\Leftrightarrow S_2 = \frac{-Q_{12}}{2\lambda}\\
-Q_{13} = 2\lambda S_3 &\Leftrightarrow S_3 = \frac{-Q_{13}}{2\lambda}
\end{aligned} \tag{4.7}$$

This leaves us with 4 equations (Eqs. (4.5) and (4.7)) and 4 unknown variables. Therefore, λ is

$$\lambda = \pm\frac{\sqrt{(1-Q_{22})^2+Q_{23}^2+Q_{24}^2}}{2} \tag{4.8}$$

which can be inserted in Eq. (4.7) to reveal the values of S_1-S_3. To establish the global maximum the two candidates are fed into the error function. In a more general case the constraint is relaxed to allow for partial polarized light and the condition becomes an inequality (all points inside the Poincaré sphere)

$$S_1^2+S_2^2+S_3^2 \leq 1 \tag{4.9}$$

This problem can be solved using the Karush-Kuhn-Tucker (KKT) conditions, which are similar to Lagrange optimization. The KKT method, however, contains two extra

conditions: λ must be zero or positive and either the condition or the Lagrange multiplier must be zero, $\lambda(c(S_1,S_2,S_3)-1)=0$. Table 4.1 shows the maxima found numerically and analytically, when polarization is measured at a wavelength of 1550.3 nm and expected to be 1550 nm (Fig. 4.16).

4.3.3 6-output vs 4-output error

As explained in chapter 3, the position of the analyzer vectors on the Poincaré sphere is not optimal for the 4-output polarimeter. However, fiber-coupled metasurface polarimeters with 6 outputs were also fabricated using the metasurface design illustrated in Fig. 3.11b. Devices with 3 superimposed metasurfaces has been made as well as 3-layer devices where the metasurfaces are separated by two 2 µm thick layers of BCB. Photographs of packaged devices are shown in Fig. 4.17. Adding two extra outputs

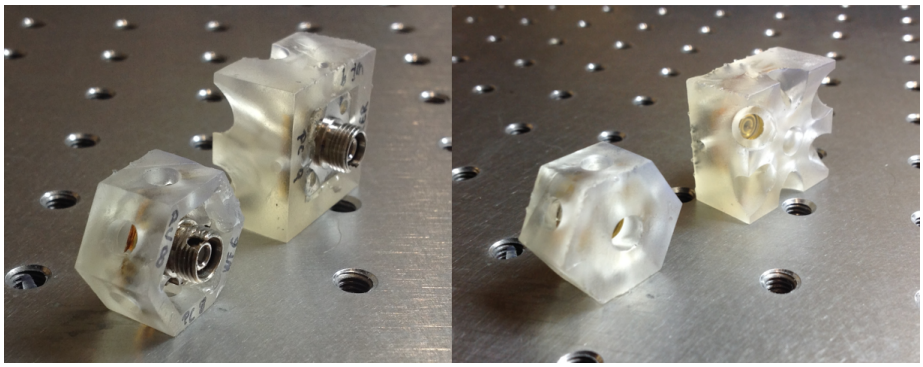

Figure 4.17. Photographs of front and back side of two packaged 6-output in-plane and out-of-plane polarimeters.

will naturally cause a statistical improvement of the error [119]. There will also be an additional improvement of the error, since the analyzer vector positions of the 6-output device are closer to being optimal (Fig. 3.11d). It is therefore expected that error will decrease with the condition number (chapter 3). Figure 4.18 shows the result of a number of polarization measurements of 4-output and 6-output devices measured in in-plane as well as out-of-plane configurations. Despite the variation in intensity noise and deviation in analyzer vectors (see Figs. 4.12 and 4.13), it is obvious that the RMSE decreases with the condition number. The 6-output devices have lower condition number than the 4-output devices in in-plane as well as out-of-plane configurations.

Actual wl: 1550.3 nm, Perceived wl: 1550 nm			
Polarization for max. error on S_0			
	S_1	S_2	S_3
Numerical	0.97	0.14	-0.20
Analytical	0.98	0.09	-0.19
Polarization for max. error on S_1			
	S_1	S_2	S_3
Numerical	-0.83	-0.25	0.50
Analytical	-0.83	-0.24	0.51
Polarization for max. error on S_2			
	S_1	S_2	S_3
Numerical	-0.83	-0.25	0.50
Analytical	-0.84	-0.25	0.46
Polarization for max. error on S_3			
	S_1	S_2	S_3
Numerical	0.96	0.01	0.27
Analytical	0.95	-0.00	0.31

Table 4.1. Numerical and analytical predictions for the polarization with maximum systematic error, when using 1550 nm calibration data to construct the perceived analyzer matrix and 1550.3 nm calibration data to construct the actual analyzer matrix. The deviation between numerical and analytical results are mainly due to sampling resolution. If the number of sampling points is increased one hundred times (to 80000), then the numerical and analytical results are the same to second decimal.

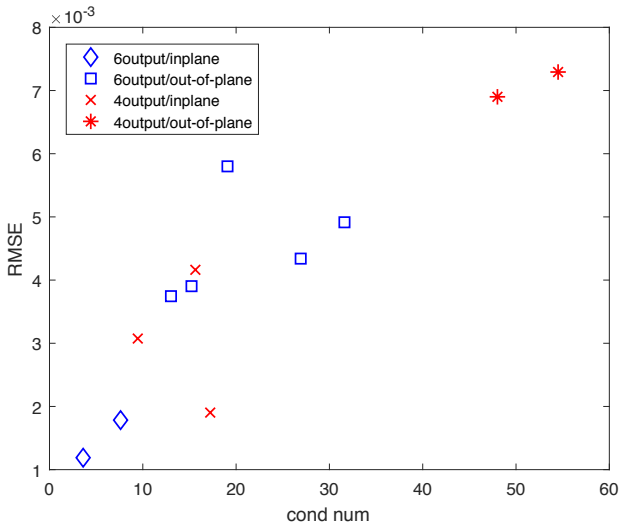

Figure 4.18. Root-mean-square error vs condition number for polarization measurements on 4-output and 6-output metasurface polarimeters corresponding to different sets of analyzer vectors measured both in in-plane and out-of-plane configurations.

The in-plane devices have generally a lower condition number because of the better signal contrast and because the metasurfaces were designed for in-plane measurements. The analyzer vectors of the out-of-plane devices are therefore closer to the equator of the Poincaré sphere (Fig. 4.13) and the polarimeters are less sensitive to the helicity of the incoming polarizations. All data points in Fig. 4.18 are made using devices where the metasurfaces are not superimposed but split in two or three separated metasurfaces. One exception is the 6-output in-plane measurements (see Fig. 4.19), where the position of the analyzer vectors are quite close to the designed positions and not very sensitive to change in fiber position. If this result turns out to be repeatable, it suggests that the fact that the long axis of all antennas are never parallel to the propagation direction of the scattered field greatly reduces the effect of rescattering and absorption by neighboring antennas. Also it could be hypothesized that the symmetry of the metasurface alleviates some of the deviations caused by superimposed metasurface antenneas (Fig. 3.11). The uncertainty of the DOP is calculated from the uncertainty of the Stokes parameters and

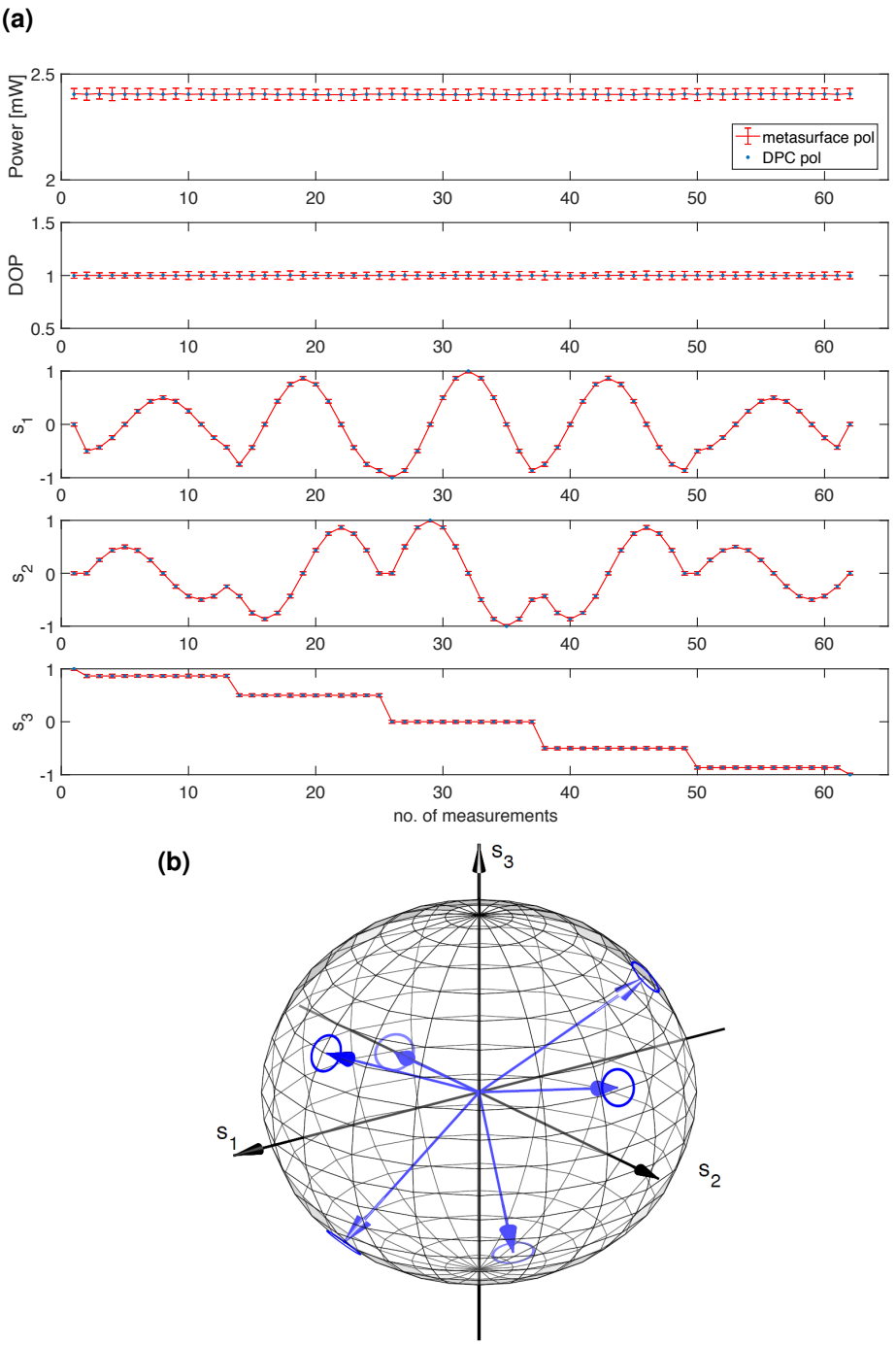

Figure 4.19. 6-output device with 3 superimposed metasurface in a single layer measured in in-plane configuration. (a) Polarization measurements showing all polarization parameters. (b) Analyzer vector positions on Poincaré sphere

6-output in-plane device			
RMSE Power	RMSE s1	RMSE s2	RMSE s3
0.0013mW	0.0012	0.0012	0.0012
RMSE DOP	Max abs azimuth error	Max abs ellipt. error	Max abs DOP error
0.0018	0.13°	0.11°	0.45%

Table 4.2. Root-mean-square error and maximum absolute error of the 6-output measurements shown in Fig. 4.19

Eq. (2.10) using the standard error propagation formula [120]

$$\begin{aligned}\sigma(p)^2 = &\frac{\sigma(S_0)^2(S_1^2+S_2^2+S_3^2)}{S_0^4} + \sum_i \frac{\sigma(S_i)^2 S_i^2}{S_0^2(S_1^2+S_2^2+S_3^2)} \\ &- 2\sum_i \frac{cov(S_0,S_i)S_i}{S_0^3} + 2\sum_{i\neq j} \frac{cov(S_i,S_j)S_iS_j}{S_0^2(S_1^2+S_2^2+S_3^2)}\end{aligned} \tag{4.10}$$

where $i \wedge j \in [1,3]$. The RMSE of individual parameters and maximum measured errors in form of angles on the Poincaré sphere is shown in table 4.2. All RMSE values are lower than the stated accuracy of the state-of-the-art inline polarimeter (IPM5300) from Thorlabs (SOP: $\pm 0.25°$, DOP: 0.25 %). It should be noted, however, that Thorlabs doesn't supply information about the power range within which the accuracy of the IPM5300 is valid, the fraction of incident intensity that is scattered to the detectors, nor details about data acquisition.

4.4 Metasurface polarimeters integrated on a fiber tip

Integration of nanostructures onto optical fiber facets has the potential of opening new applications for highly miniaturized optical devices, such as surface-enhanced Raman scattering sensors, surface-plasmon-resonance sensors, beam steering structures, fiber optical tweezers, polarization state generators, and devices for polarization monitoring in telecommunications networks [59, 121, 122]. Fabricating nanoscale structures on a fiber tip is a challenging task. The large aspect ratio and microscopic cross-section of the fiber are not compatible with conventional wafer-based processing platforms, originating

from the semiconductor industry. Instead, many different approaches have been demonstrated, employing technologies such as focused ion beam milling, nanoimprinting, two-photon polymerization, and transfer lithography [123–125].

Transfer lithography techniques offer convenient methods of high-resolution optical fiber tip patterning suitable for parallel processing. Many of the reported methods, however, require complicated processing like mold preparation, manual transfer by mechanical contact, or multiple film delamination [126–128]. Here, a simple nano-transfer technique that is used to define patterns of metallic nanoantennas on fiber facets is demonstrated. The method involves only a few simple processing steps, easy alignment and potential for low-cost production.

An in-line metasurface polarimeter was patterned on a 1550 nm single-mode fiber facet using this technique, demonstrating the capacity of the miniaturization of the metasurface polarimeter. Current commercially available in-line fiber-based polarimeters are constructed with multiple optical components in series [20]. Since a metasurface polarimeter requires only one ultrathin surface of nanoantennas [11], the fiber-based in-line metasurface polarimeter represents a reduction in size and potentially an improvement in stability while matching state-of-the-art fiber-based in-line polarimeters in terms of speed, accuracy and precision. In-line polarimeters play a critical role in monitoring and controlling the polarization in optical communication networks. Integrating the metasurface polarimeter on an optical fiber would therefore not only represent an important step towards the ultimate miniaturization of the polarimeter but could also be very useful in applications like optical networks.

4.5 Fabrication of metasurface polarimeters integrated on fiber facet

The principle of the template stripping transfer processes is illustrated in Fig. 4.20. The metasurface pattern was initially written into an approximately 100 nm thick layer of PMMA (950 PMMA A, 2% in Anisole from MicroChem) on a silicon wafer using electron-beam lithography and developed for 50 s in MIBK:IPA 1:3. The thickness of the PMMA was measured in an ellipsometer. A 20 nm thick gold layer was subsequently deposited on the resist using electron-beam evaporation and patterned in a lift-off process.

The setup for the template stripping transfer lithography process consists of a fiber

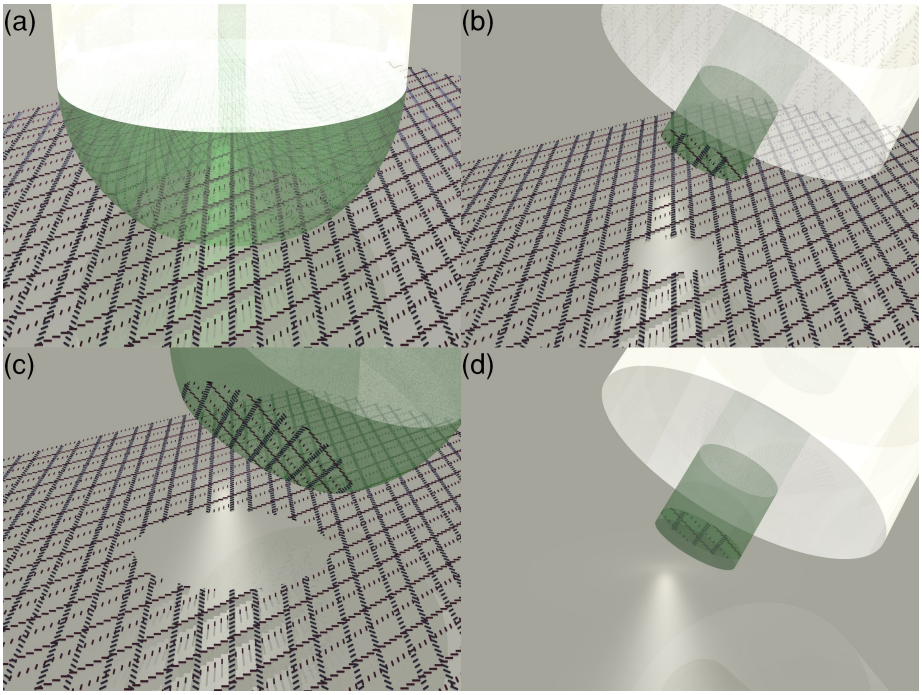

Figure 4.20. (a) An optical fiber (white cylinder) with a drop of polymer (green hemisphere) on the tip in proximity to a metasurface consisting of arrays of gold nanoantennas. The metasurface is made of two superimposed gratings of antenna columns arranged in a pattern where the antennas in each column are rotated 90° relative to antennas in the neighboring column. (b) The polymer is UV-cured through the fiber core resulting in only the antennas under the center of the fiber being released from the wafer. (c) The polymer is UV-cured using flood exposure resulting in a larger metasurface area being released from the surface. (d) A second layer of polymer is cured on top of the existing polymer. The polymer is cured while in contact with an unstructured surface to ensure a flat end face.

mount (a bare fiber rotator), an xyz stage, and a fiber-coupled UV-diode, see Fig. 4.21. A 1550-nm single-mode fiber was mechanically cleaved and placed in the setup. The fiber tip was dipped in a UV-curable hybrid organic/inorganic polymer (OrmoComp®, micro resist technology GmbH) that had been prebaked at 80 °C for 2 minutes, leaving a droplet of polymer on the fiber tip. The fiber tip was then brought into near proximity to the patterned silicon wafer bringing the droplet in contact with the sample (Fig. 4.20a). The total size of the pattern is 100 µm × 100 µm. The xyz stage was used to align the fiber tip over the nano-patterned area by the help of optical lenses. The polymer was then cured with 365-nm ultraviolet light using one of two approaches. With the fiber exposure approach the UV-light was transmitted through the fiber itself, thus forming a cylindrical polymer rod between the fiber and the wafer as a result of confinement within the fiber and a self-guiding phenomenon within the optically-cured polymer. After UV exposure, the fiber was retracted, delaminating the gold from the wafer and transferring it to the surface of the cured polymer rod, as a result of low adhesion between gold and silicon. This simple delamination process is known as template stripping [129, 130]. Template stripping uses the fact that some metals, gold included, have low adhesion when deposited directly on silicon. The adhesion is high enough that structures do not delaminate during the liftoff process, but low enough that stripping from the wafer is straightforward. The adhesion experienced with the present procedure and equipment was very suitable for template stripping. However, if adhesion between gold and silicon needs to be improved due to delamination during liftoff, the silicon can be primed with a thin layer of sputtered gold [131]. UV-curing through the fiber ensures that the nanostructure is automatically transferred only to the area corresponding to the fiber-core (Fig. 4.20b). Uncured polymer was removed with a developer (OrmoDev®, micro resist technology GmbH) for 50 s. Figure 4.20c illustrates an alternative flood-exposure approach where the polymer was cured from outside the fiber, thus curing the entire droplet of polymer on the fiber tip. After a rinse in IPA, the metasurfaces transferred to the polymer rod can subsequently be fully embedded in polymer by repeating the process using a clean silicon wafer without nanoantennas. This is illustrated in Fig. 4.20d with the fiber exposure approach. Simulations (Fig. 3.12) and experiments show that the performance of the polarimeter is degraded if the antennas are not fully embedded in polymer.

Electron micrograph images of the patterned fibers are shown in Fig. 4.22. The diameter of the polymer rod in Fig. 4.22a is 10 – 10.5 µm corresponding well to the core size of the SMF-28 optical fiber. Figure 4.22d shows a micrograph of the silicon

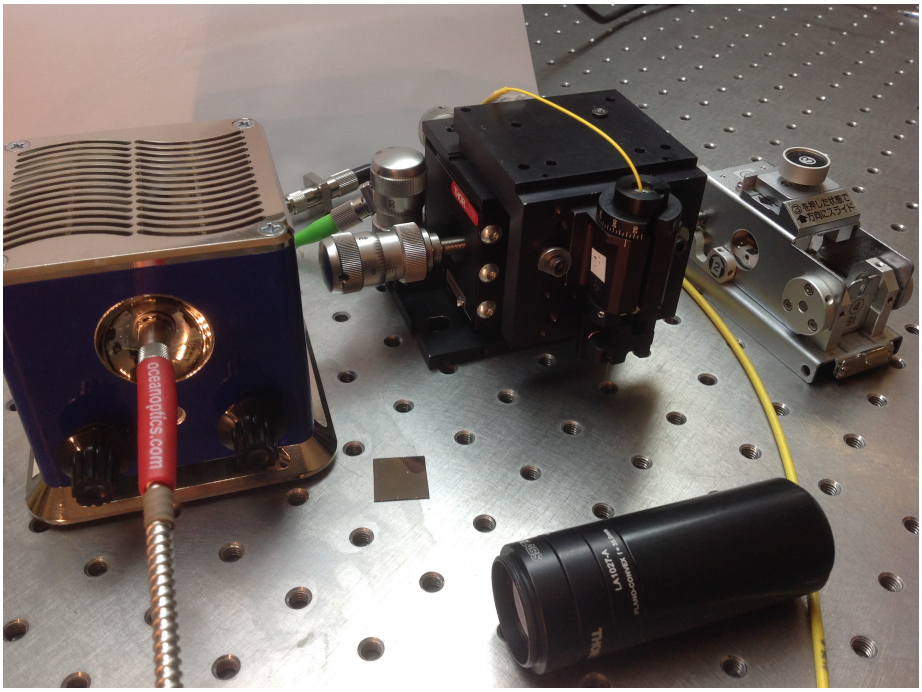

Figure 4.21. The setup for template stripping transfer lithography. The blue box to the left contains a 365 nm UV-diode which couples light, via a $\varnothing 600\,\mu m$ multimode fiber into a single mode SMF-28 fiber with a cleaved facet. The bare fiber is positioned in the fiber mount, which is fixed in vertical position on an xyz stage that allows for positioning of the fiber facet in all three dimensions. A patterned silicon sample is shown in the middle of the image. Optical lenses to assist alignment is shown in the front and the mechanical fiber cleaver is shown to the far right.

wafer after transfer lithography with the fiber exposure approach. It is observed that all antennas in a circular area are successfully detached from the sample.

4.6 Performance of metasurface polarimeters integrated on fiber tip

4.6.1 Metasurface design

The metasurface pattern transferred onto an optical fiber facet consisted of identical gold nanorods (250 nm × 50 nm × 20 nm) arranged with subwavelength-spacing in parallel arrays, as presented in chapter 3. The fiber-based metasurface polarimeter is, like the wafer-based polarimeter in sections 4.1 to 4.2, designed for near-infrared light (C-band wavelengths), which when normally incident on the metasurface will scatter a fraction of the intensity in polarization-dependent in-plane and out-of-plane meta-grating orders; each order serving as a polarization analyzer. The in-plane grating orders stay in the plane of the metasurface, whereas light in the out-of-plane orders is scattered at an angle close to 45° from the metasurface plane after refraction at the polymer/air interface. Only out-of-plane orders are used for intensity measurements, since in-plane orders suffer from lensing and scattering from imperfections at the edge of the structure when the transfer lithography method is used. The rescattering of the in-plane orders at the fiber-cladding/air interface is observed in images in Fig. 4.23 using an infrared camera and a reflective microscope objective from Ealing. Aside from mapping the fiber facet to the image plane, the reflective objective serves to block most of the light from the fiber to avoid overexposing the image. The images of the rescattering demonstrate the polarization-dependent light scattered by the metasurface.

To achieve optimum polarization response and scattered light intensity, the metasurface was designed for measuring in out-of-plane configuration, where the distance between the two columns of perpendicularly oriented antennas is $\lambda(1+1/4)$ and the column-pairs are spaced 2λ, where λ is the design wavelength in the polymer material, corresponding also roughly to the resonance wavelength of the individual antennas. The 4-output design was chosen for simplicity.

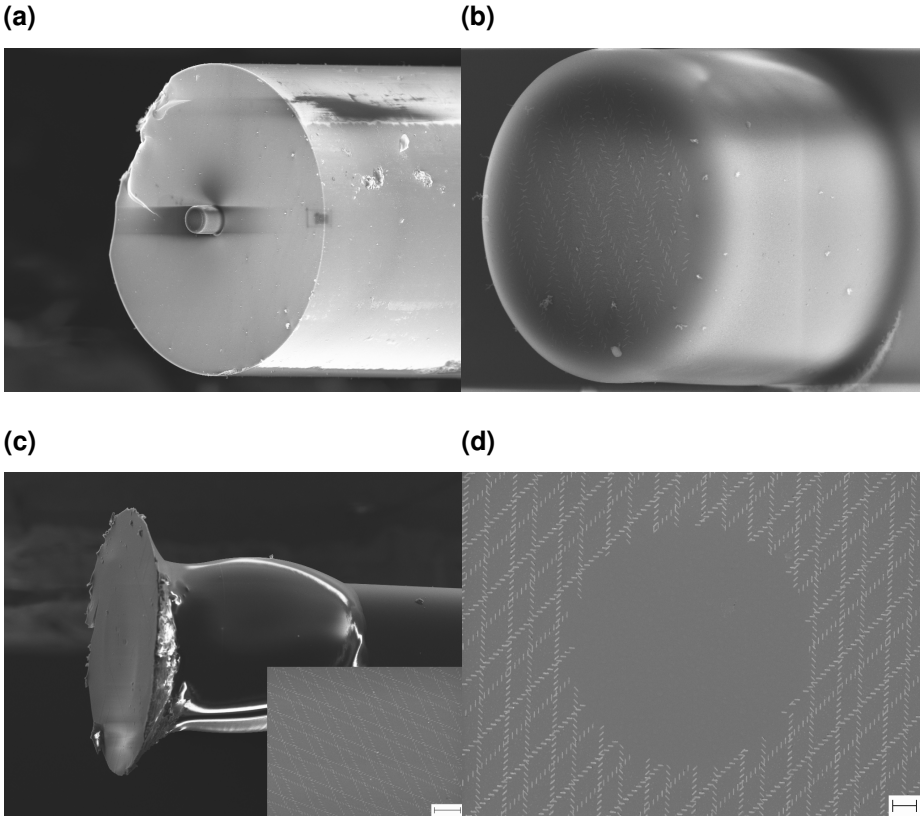

Figure 4.22. Electron micrograph images of patterned fiber facets. (a) Image of a processed 125 µm diameter bare fiber fabricated with the fiber exposure approach, showing the 10 µm-diameter polymer rod in the center of the the fiber facet. (b) A zoom-in of the polymer rod showing the transferred gold nanoantennas. (c) Image of a patterned fiber facet using the flood exposure approach, where a much larger area of nanoantennas arrays is transferred. The inset shows a zoom-in of the transferred nanoantenna arrays (the scale bar represents a length of 2 µm). (d) Micrograph of metasurface on a silicon wafer after stripping. In the middle of the image is a circle with a diameter of about 10 µm, where the gold nanoantennas have been transferred to the fiber tip. The scale bar represents a length of 1 µm.

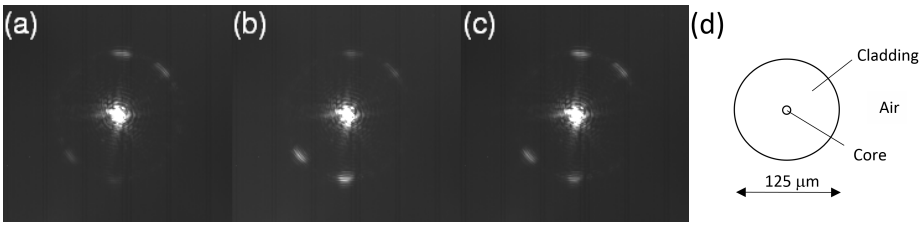

Figure 4.23. Fiber-cladding images of an optical fiber facet patterned with a flood exposure metasurface polarimeter design. In-plane orders are seen rescattered out of plane at the fiber-cladding/air interface. The bright spot in the middle is the light emitted from the fiber that escapes being blocked by the reflective objective. The relative intensity of scattered orders varies with the polarization of the incoming light. (a) Right-hand circular polarization. (b) Left-hand circular polarization. (c) Horizontal linear polarization. (d) Schematic of fiber facet showing the dimensions of the cladding.

4.6.2 Optical setup

The patterned optical fiber was connected to a fiber laser at a wavelength of 1550 nm, followed by a deterministic polarization controller (DPC). The intensity of four out-of-plane orders was measured to obtain information about the polarization of the incoming light. Four InGaAs photodiodes were fitted in a 3D printed holder and aligned to the scattered light from the grating orders with the help of an xyz stage. The out-of-plane grating orders can be observed in Fig. 4.24. The images were recorded by placing the

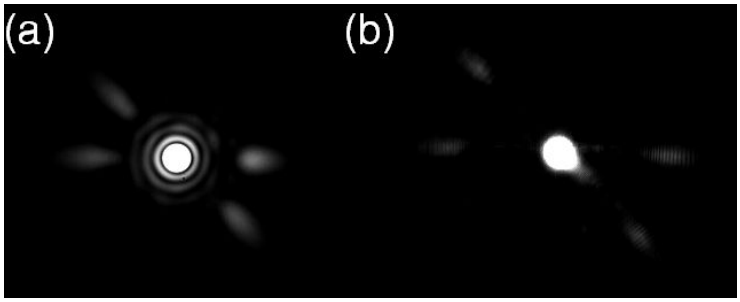

Figure 4.24. Images of the out-of-plane orders for (a) fiber exposure design and (b) flood exposure design.

structured fiber directly in front of the infrared camera. The signal from the diodes

was amplified and sampled using a microcontroller. The transmitted light was coupled back into a second fiber, which was attached to another xyz stage and positioned approximately 100 µm from the metasurface, resulting in a coupling efficiency of about 50 % (-3 dB) where about 3 % can be related to reflection losses. A photo of the setup, showing the two fibers attached to two xyz stages and aligned to each other inside the photodiode holder, is seen in Fig. 4.25. The unstructured fiber was connected to a commercial in-line polarimeter (IPL). Since transmission through the optical fibers affects the polarization of the light, the polarization at the metasurface polarimeter and the in-line polarimeter were calibrated to the polarization set by the DPC using a commercial free-space polarimeter (POL) and two manual polarization controllers (MPC), which were placed on the fibers before and after the metasurface polarimeter. First the MPC on the metasurface fiber was employed to calibrate the polarization at the position of the metasurface to the DPC by removing the fiber attached to the IPL and measuring the output polarization with the POL. Then the unstructured fiber was aligned to the metasurface fiber and the polarization of the IPL was calibrated to the DPC using the MPC on the unstructured fiber. A schematic of the measurement setup are shown in Fig. 4.26 together with an illustration of the detector configuration.

4.7 Characterization of metasurface polarimeters integrated on fiber facet

The Stokes vector of the incoming light was reconstructed using a linear transformation, as described in chapter 2. The results are presented in Fig. 4.27, which shows the polarization states measured by the metasurface fiber polarimeter, reference polarizations measured by the deterministic polarization controller, and polarization measurements using the in-line polarimeter; all represented on the same Poincaré sphere, viewed from opposing angles. The discrepancy between the DPC and the IPL polarization measurements is caused by inaccuracy in correction of polarization changes in the fiber (a 3-dimensional rotation on the Poincaré sphere) and polarization-dependent losses between the DPC and the IPL that causes a slight asymmetry of the polarization measurements on the Poincaré sphere (stretched towards the polarization state with the highest transmission [10, 32]). The root-mean-square error (RMSE) between measured and reference polarizations on all state-of-polarization parameters was around 0.006. Conversely, the RMSE for the device made using the flood exposure method

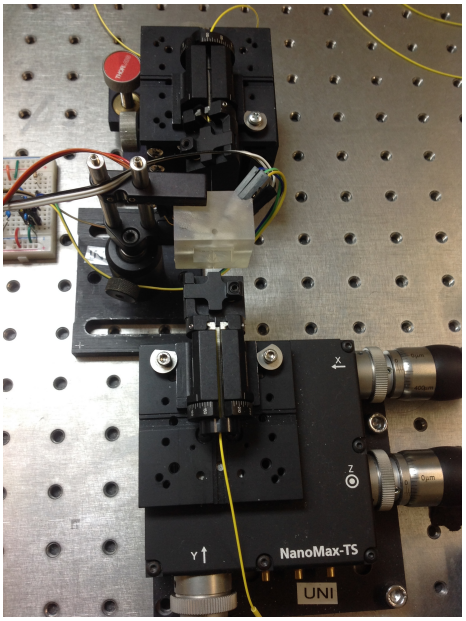

Figure 4.25. Photo of the setup for polarization measurements with the fiber-based metasurface polarimeter. The fibers (structured in bottom of image and unstructured in the top of the image) are placed in fiber mounts and fastened on xyz stages. The two fibers are aligned to another inside the 3D printed holder for the photodetectors.

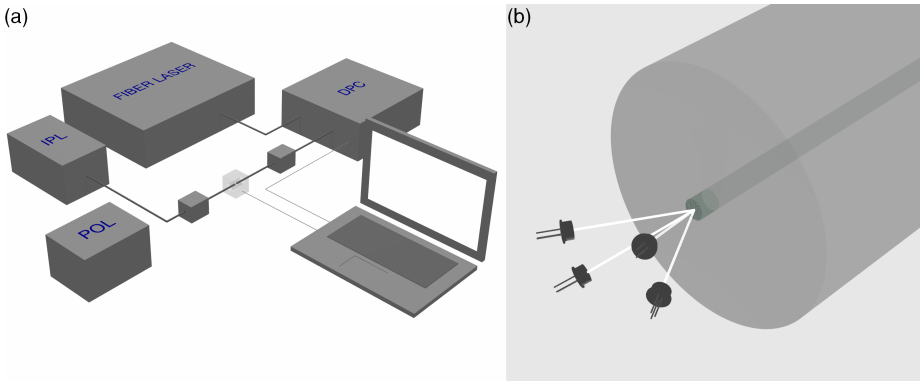

Figure 4.26. (a) A schematic of the measurement setup showing a fiber laser connected to a deterministic polarization controller (DPC) with a 1550 nm single mode fiber. The nanostructured fiber is connected to the output of the DPC and aligned to four photodiodes using a 3D-printed holder (the semitransparent box). An optical fiber with an unstructured tip is aligned to the nanostructured fiber to couple the signal into a commercial in-line polarimeter (IPL). The commercial free-space polarimeter (POL) and the manual polarization controllers (the two small boxes on the fibers) are used to ensure that all polarimeters are measuring the same polarization state. (b) The configuration of the photodetectors is illustrated. The diodes are scaled down in size relative to the fiber.

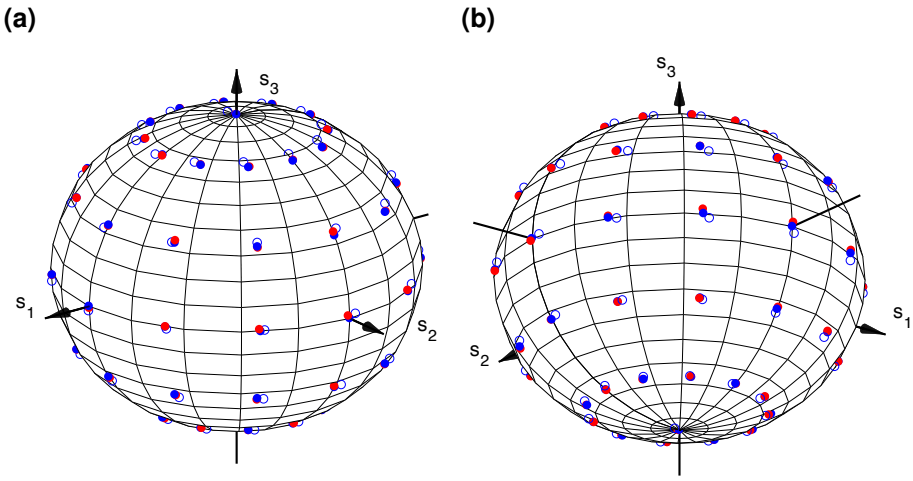

Figure 4.27. Measurements of the polarization state depicted on a Poincaré sphere, viewed from two opposite angles. Red dots are measurements using the metasurface polarimeter with the fiber exposure design, blue dots are reference polarization states measured by the DPC. The open blue circles are polarization states measured by the IPL.

was around 0.004. The lower error with the flood exposure approach is expected, due to an increased signal to the detectors. The improvement in error is, however, to a certain degree compensated by an improved polarization sensitivity of the polarization analyzers belonging to the device using the fiber exposure method. The RMSE obtained with the fiber-based metasurface polarimeters corresponds to the same level of precision that was obtained with 4-output metasurface polarimeters fabricated on fused silica wafers (see appendix A7), implying that transferring the metasurface to the tip of a fiber does not deteriorate the performance of the polarimeter. Furthermore, the presented accuracy is obtained with a power at each photodetector of less than 1 % of the input signal. These results show that the template stripping transfer lithography method is an effective method for fabricating high quality optical componts and they suggest that a fiber-based metasurface in-line polarimeter is a viable alternative to in-line polarimeters based on, e.g., pairs of tilted fiber Bragg gratings separated by birefringent fiber sections. The presented transfer technique may be useful for sensor applications, such as fiber-based surface-enhanced Raman scattering probes and surface-plasmon-resonance sensors. By including active alignment of the silicon wafer base, the future prospect of the technique also includes integration of wavefront shaping elements like flat lenses and q-plates (spin-to-orbital angular momentum converters) directly onto the fiber facet. Furthermore, the demonstration of multiple-layer hybrid polymer structures opens for fiber-based devices with several consecutive layers of metasurfaces.

Chapter 5

Conclusion and future aspects

An in-line metasurface polarimeter that relies on a simple and compact design consisting of an ultrathin polarization-analyzing element and four or six photodetectors has been demonstrated. As there is no need for optical elements between the metasurface and the photodetectors, low-cost fabrication of extremely compact polarimeter devices or device arrays is made possible. The accuracy of the metasurface polarimeter in the current design was shown to be close to commercial in-line polarimeters, establishing the metasurface polarimeter as a fully viable alternative to existing solutions. The current polarimeter design was demonstrated to work in the wavelength range 1510 – 1610 nm for both the in-plane and the out-of-plane designs. Experiments and simulations suggest that the out-of-plane design has a larger bandwidth. Also, it is better suited for practical applications because a larger metasurface area solves alignment problems without causing additional rescattering and absorption losses. The in-plane design, however, offers a lower error, especially on the SOP. Sources of error in the polarization response of the metasurfaces were analyzed and it was shown that the improvement of analyzer vector position of the 6-output device provides an improvement in the accuracy of the polarimeter. An analytical model for prediction of the polarization with maximum systematic error for a known error source was presented and compared with good accuracy to numerical simulations. In summary, the new polarimeter design promises excellent accuracy, compact design, potential for low-cost mass production, and the possibility of modifying the structure (in conjunction with suitable photodetectors) to address wavelength ranges well beyond the one presently investigated. A future project may include the fabrication of large area metasurfaces to study the influence of geometric variations of nanoantennas on the polarization response and sensitivity of the polarimeter to angle deviation. Another project could be integration of the photodetectors and metasurface on the same chip. The deep learning approach to

improving the metasurface polarimeter was very promising, and is not limited to polarimeters. These results indicate that prospects of creating new optical devices or improving the functionality of existing devices using machine learning are very good and optical solutions based on machine learning are worth pursuing further.

A new transfer-lithography process based on template stripping for nanostructuring of optical fiber facets has been presented. The applicability of this novel approach has been demonstrated by transferring a 4-output metasurface polarimeter onto the facet of a single-mode telecom fiber. The results show that the performance of the metasurface polarimeter is not negatively affected by the transfer from a wafer to an optical fiber. The template stripping transfer lithography method is therefore a comprehensively applicable method for the fabrication of high quality optical elements and devices. The metasurface polarimeter-on-a-fiber is an excellent candidate for telecommunication applications with exceptional stability and compactness and no subsequent pigtailing requirements. The presented transfer technique may also be useful for sensor applications, such as fiber-based surface-enhanced Raman scattering probes and surface-plasmon-resonance sensors. By including active alignment of the silicon wafer base, the future prospect of the technique also include integration of wavefront shaping elements like flat lenses and q-plates directly onto the fiber facet. Furthermore, the demonstration of multiple-layer structures opens for fiber-based devices with several consecutive layers of metasurfaces, like wavelength filters. A future experiment that could be interesting to explore, especially for the flood exposure method, is the replacement of the template stripping of gold with a sacrificial layer, e.g. aluminium, which is etched away to release the nanopattern. Another interesting future endeavor could be the joining of the patterned fiber with the receiving fiber end-to-end. This is a process that could easily be performed with the UV-curable hybrid organic/inorganic polymer used in the present work. It would, however, require a solution where the detectors are integrated either on the metasurface or the fiber.

Appendix

A1 Finite-difference time-domain simulations in FDTD Solutions

FDTD simulations of the scattered field from gold nanorods are performed in the photonic simulation software "FDTD Solutions" from Lumerical using a "Total field scattered field" (TFSF) source. An example of a setup in FDTD Solutions is shown in Fig. A1.1. The simulated structure (a single gold nanorod) is shown in the center. The source is a plane on one side of the rod, depicted by a set of arrows, from which a plane wave propagates. The purple arrow illustrates the direction of propagation and the blue arrow shows the polarization of the wave. The grey box, which is also related to the source, defines the TFSF region. Inside the box, there is the total field, i.e. the incoming wave and the scattered field. Outside the box, the incident wave is subtracted from the total field so that only the scattered field remains. Therefore, to measure the power of the scattered field a monitor must be placed outside the grey box. The monitors are the yellow boxes and rectangles. In the example of Fig. A1.1 two simulation boxes are placed outside the TFSF region: a scattering box and transmission box. The scattering box measures the scattering cross section, which is the scattered power divided by the source intensity. The transmission measures the normalized total power in the scattered field. The simulation region, which is the orange frame, is surrounded by non-reflecting boundary conditions (PML). Since, in experiments the antennas are completely embedded in BCB, the background refractive index is defined as 1.535. A commonly used model of the gold properties is built on data from Johnson and Christy [132]. However, many of the simulations presented in this work use data from E. Palik [133], since it is more precise at near-infrared wavelengths.

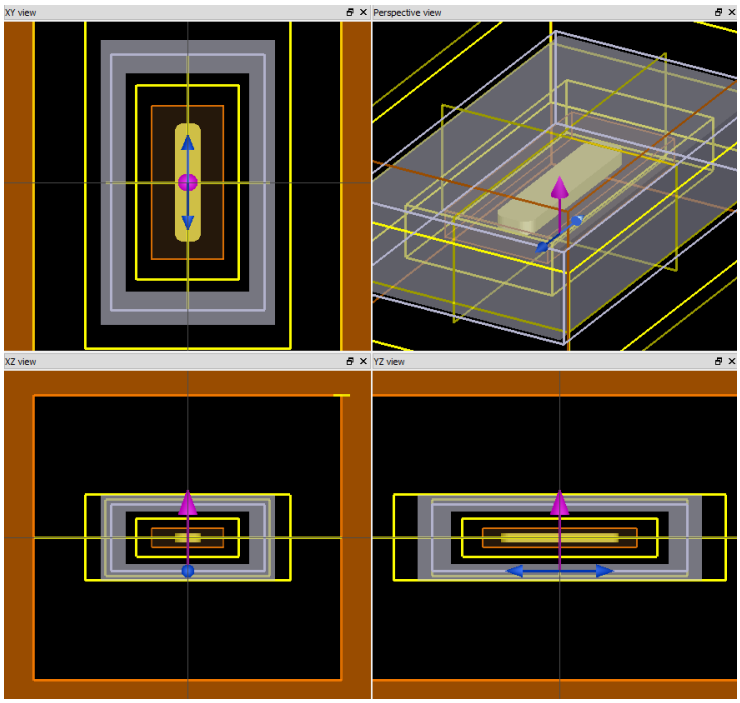

Figure A1.1. Setup of a simulation of a single nanorod in FDTD Solutions. The red area illustrates the fully absorbing boundary conditions, the yellow boxes and lines are the monitors, the grey box sets the source plane and the region for the total field (and scattered field), the magenta arrow is the direction of the source wave, the blue arrows shows the polarization of the wave, and the red box is the region where the mesh size is set manually.

A2 Nearfield coupling versus row distance

The analytical model presented in Chapter 2 does not take into account nearfield coupling between antennas. Nearfield coupling may however affect the polarization response of a real-life polarimeter. There is no nearfield coupling between columns, since the minimum column distance of the metasurfaces fabricated in this work is $3/4\lambda$ (the out-of-plane design). The nearfield coupling is negligible at these distances. However, there is nearfield coupling between rows as seen in Fig. A2.1, where the electric field scattered from two antennas with varying row distances is simulated in lumerical (red dashed curve). These simulations are compared with the sum of the electric field for two simulations, where the antennas are simulated one at the time (blue curve). It is seen that in Fig. A2.1a and b, there is a difference in the amplitude as well as the phase. The row distance needs to exceed $\lambda/2$ for the nearfield coupling to completely disappear. However, a phase change on both columns will not affect the polarization response of the polarimeter and row distance of the polarimeters fabricated in this work was therefore kept at $\lambda/4$ to increase the intensity of the scattered light relative to larger row distances.

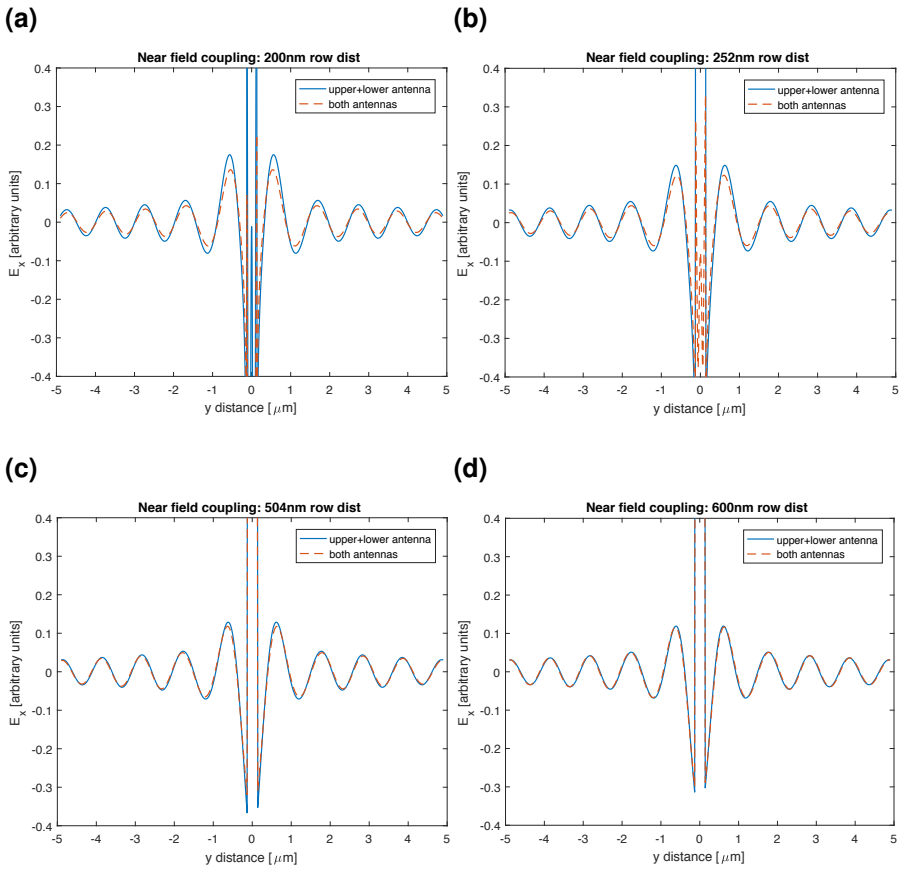

Figure A2.1. FDTD simulations of the scattered electric field (E_x), from a "column" consisting of two antennas rotated 45° from the x-axis (parallel to the column), propagating in the direction of the y-axis (in the plane of the metasurface perpendicular to the antenna column). The blue lines are the results of the sum of two simulations, each simulation containing only one of the two antennas. The red dashed lines are simulations containing both antennas. (a) The row distance between the antennas is 200 nm. (b) The row distance is 252 nm corresponding to $\lambda/4$ in BCB, where $\lambda_0 = \lambda n_{BCB} = 1550$ nm is the design wavelength. (c) Row distance is 504 nm corresponding to $\lambda/2$. (d) Row distance is 600 nm.

A3 Angle Dependence

The polarization response of the metasurface polarimeter is dependent on angle of incidence. Consider a plane wave propagating towards a metasurface consisting of antenna arrays arranged in a fishbone pattern as presented in chapter 3. If the angle (v) of the incoming wave deviates from normal incidence as shown in Fig. A3.1, the wavefront will reach the left antenna column before it reaches the right antenna column. This means that the effective distance between antenna columns will be larger than the physical distance (S) for the scattered field travelling to the left whereas the effective distance between antenna columns will be smaller than the physical distance for the scattered field travelling to the right. The effective distance is given by $S \pm sin(v)$. Therefore, both the wavelength and polarization response will change with the angle of incidence as illustrated with FDTD simulations shown in Fig. A3.2.

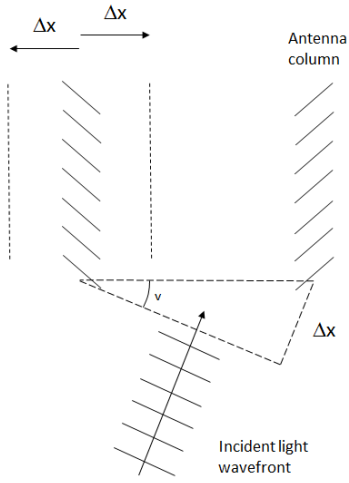

Figure A3.1. Schematic of incident light at an angle. The dashed lines illustrate the distance the scattered light from the left antenna column has travelled when the wavefront reaches the right antenna column.

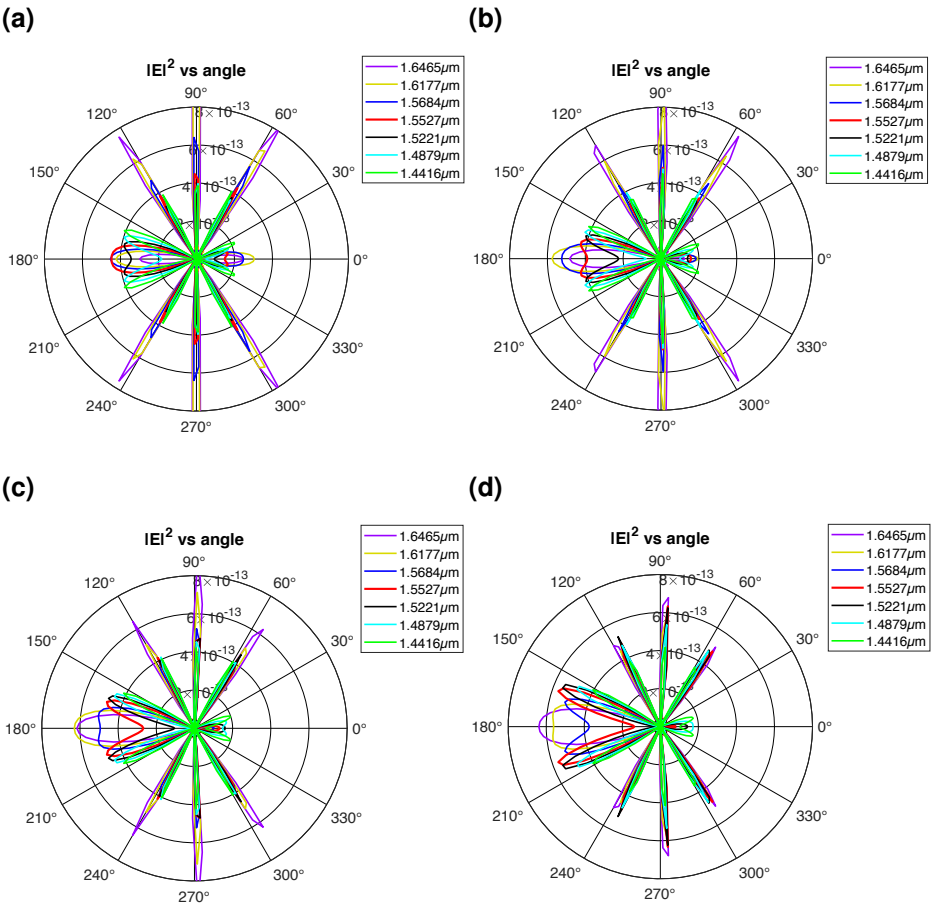

Figure A3.2. Radiation patterns of a 5-column metasurface with elliptically polarized light, $(\psi, \delta) = (\pi/4, \pi/4)$, with a deviation (counterclockwise) from normal incidence of (a) 0°, (b) 1° (c) 2° (d) 3°. When the angled patterns (b)-(d) are compared to the pattern with normal incidence (a) or Fig. 3.7a, it is seen that the left lobe (at 180°) of the angled patterns at 1550 nm (red curve) behaves like low wavelength patterns in (a) whereas the right lobe (at 0°) behaves as long wavelength patterns.

A4 3D printing

For the fabrication of wafer-based metasurface polarimeters, holders were 3D printed to align together the sample, detectors, and fiber connector in a compact package, see section 4.1. The holders were drawn in Inventor from AutoDesk. Four different designs were made, for four and six outputs, both for in-plane and out-of-plane configurations, see Fig. A4.1. The shape of the out-of-plane samples are not critical and they are cut to 12 mm $\times$ 12 mm or 15 mm $\times$ 15 mm squares. The in-plane samples must be cut perpendicular to the direction of the scattered light and the holders are therefore shaped to fit the more irregular shapes of the in-plane samples. Figure A4.2 illustrates a sample with a 4-output metasurface fitted in a holder. The 3D printing was performed using a Form 1+ 3D printer from Formlabs, which uses the *stereolithography* method. In stereoligraphy a UV-sensitive liquid resin is polymerized by a laser that scans the resin basin and selectively hardens the material, one cross section at a time, to build the 3D structure from the bottom to the top. The stereolithography method is more expensive than the traditional *fused filament fabrication* where a movable extruder heats a filament and turns the flow on and off, but the advantage of the stereolithography method is that it is more accurate and therefore better suited for the fine alignment of optical equipment.

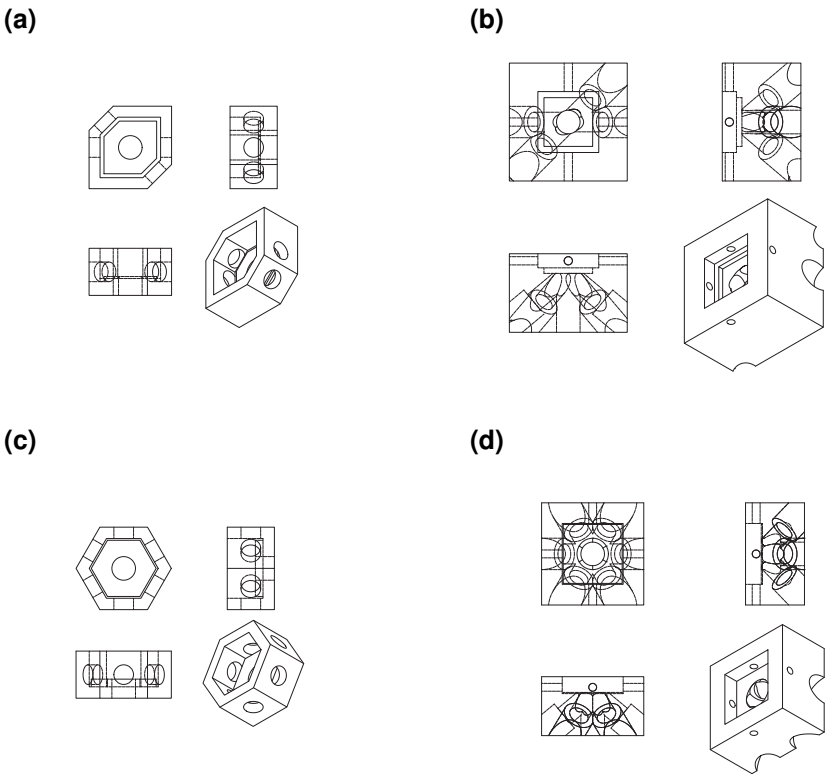

Figure A4.1. 3D Inventor drawings of the polarimeter holders, shown in .dwg (AutoCad) format. (a) 4-output, in-plane. (b) 4-output, out-of-plane. (c) 6-output, in-plane. (d) 6-output, out-of-plane.

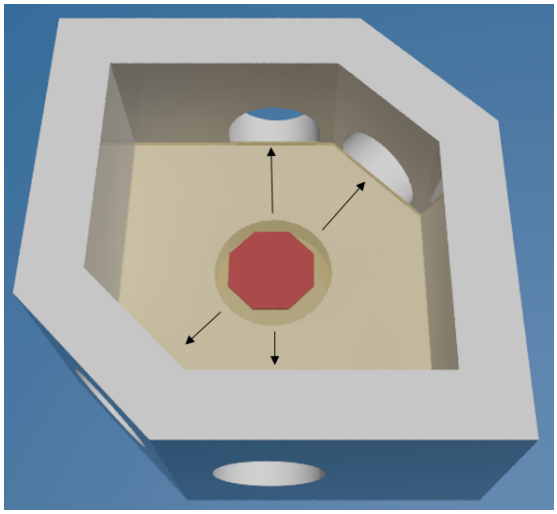

Figure A4.2. Illustration of a fused silica sample in a 4-output 3D printed holder. Arrows illustrate direction of scattered light and the red structure illustrates an (oversized) metasurface on a diced chip.

A5 Analyzer matrix dependence of wavelength

The sensitivity of the metasurface polarimeter to wavelength variations is shown in Fig. 4.7 as normalized analyzer vector positions on a Poincaré sphere and polarization ellipses. The corresponding 2D plots of individual normalized SOP parameters are shown in Fig. A5.1.

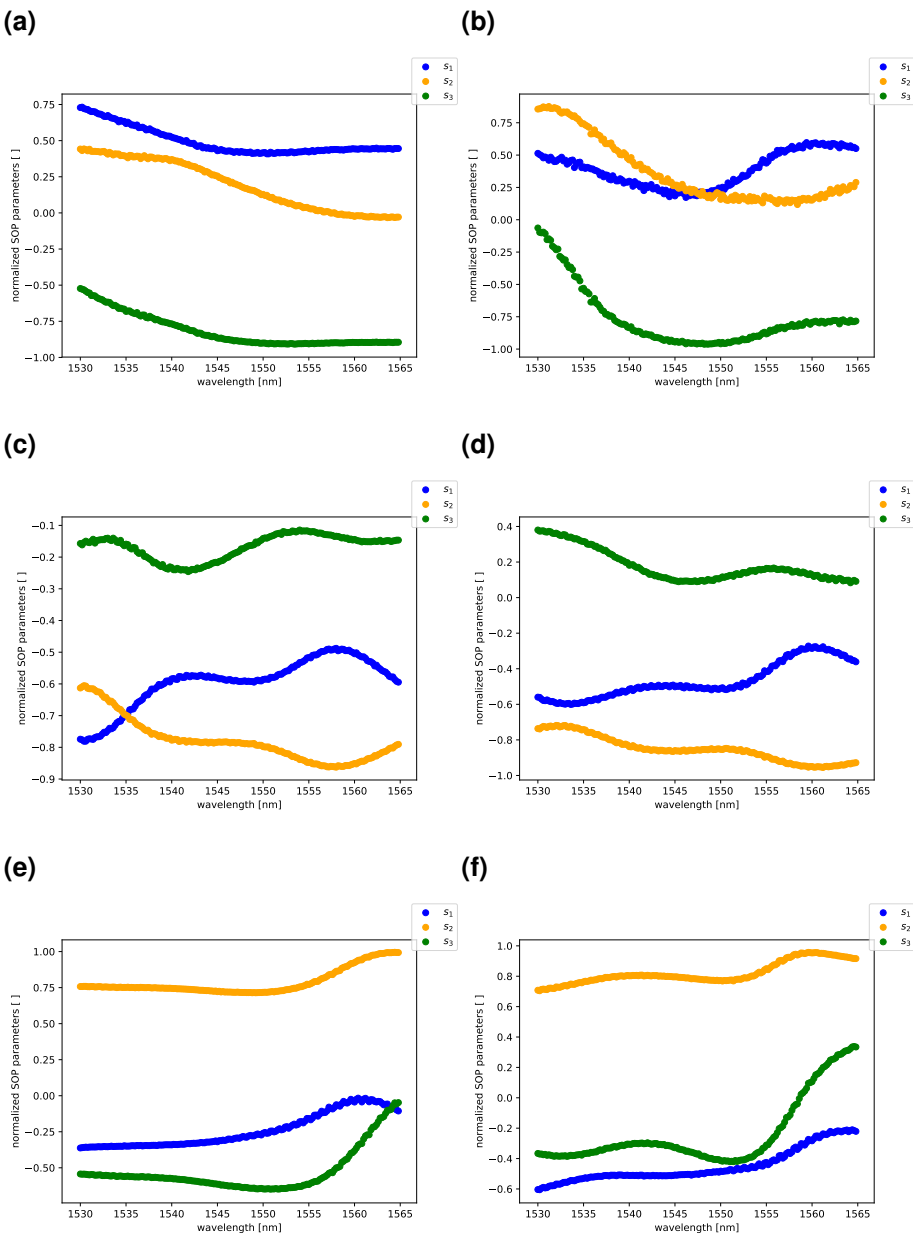

Figure A5.1. Analyzer vector wavelength dependence of a 6-output metasurface polarimeter measured in out-of-plane configuration from 1530 – 1565 nm in steps of 0.2 nm. The analyzer vector polarizations are shown as 2D plots of the normalized state of polarization (SOP) parameters versus wavelength. (a) Polarization states corresponding to the red circles in Fig. 4.7a and the top/left polarization ellipses in Fig. 4.7b, (b) yellow circles in Fig. 4.7a and bottom/left in Fig. 4.7b, (c) green circles in Fig. 4.7a and the top/middle in Fig. 4.7b. (d) Cyan circles in Fig. 4.7a and the bottom/middle in Fig. 4.7b, (e) blue circles in Fig. 4.7a and the top/right in Fig. 4.7b, (f) black circles in Fig. 4.7a and the bottom/right in Fig. 4.7b.

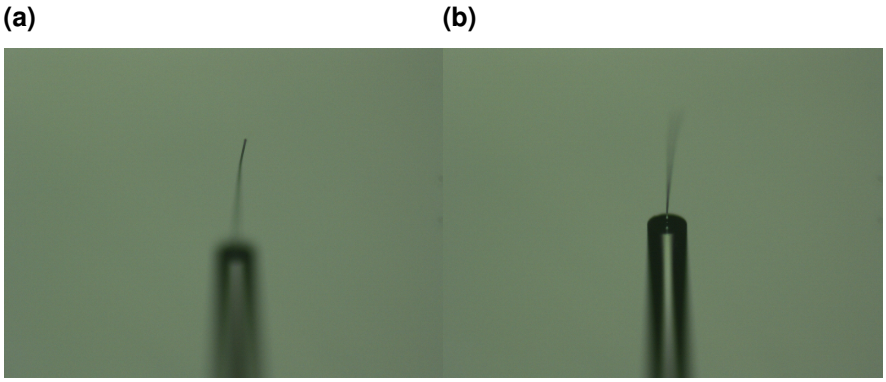

Figure A6.1. Optical microscope images of cured OrmoClear polymer large aspect-ratio core-extensions on the facet of a single-mode optical fiber.

A6 Hybrid Polymer on Fiber

In chapter 4 a UV-curable organic/inorganic hybrid polymer (OrmoComp) was used as a means to transfer the metasurface to a fiber facet. With the fiber exposure method a polymer rod was formed from the core of the fiber to the surface of the sample. This technique could be used in many other applications than transfer lithography. For example, if the tip is immersed in a hybrid polymer drop of relatively large volume keeping the tip far from the surface and exposed with UV-light through the fiber, then the result is a very long thread of cured polymer. The best results are obtained with another hybrid polymer, OrmoClear®, from the portfolio of UV-curable hybrid polymers from micro resist technology, see Fig. A6.1. The images show the strength of the self-guiding effects in the cured polymer rod. The cured polymer fiber seems to have a quite homogeneous diameter and an application for this technique could be waveguides that connects the signal from an optical fiber to waveguides on a wafer for integrated optics.

In the transfer process the growth of the cured polymer rod is terminated at the silicon sample. Therefore, the end of the rod is flat. Figure A6.2 shows the case when the curing is stopped before the rod reaches a surface. The end of the polymer rod is now a rounded tip. Furthermore, it is seen that when gold is deposited on the polymer, gold nanowires are self-assembled on the polymer tip. The same phenomenon can be observed in Fig. 4.22b. This effect could be optimized for use in applications like SNOM (scanning near-field optical microscopy) tips or surface-enhanced Raman spectroscopy.

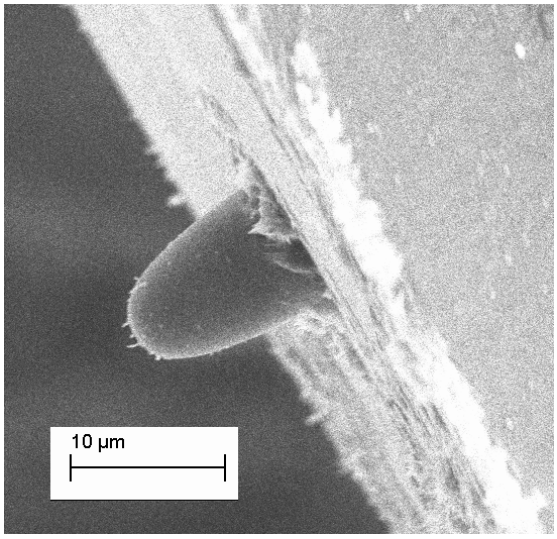

Figure A6.2. Electron micrograph of short OrmoClear polymer rod on a fiber facet with a 20 nm layer of gold.

A7 Polarization measurements to compare performance of fiber-based polarimeter with wafer-based polarimeter

In section 4.7 it is stated that the precision of the fiber-based polarimeter were on the same level as the precision of the wafer-based polarimeter. Figures A7.1 and A7.2 shows 2D plots of polarization measurement of a 4-output wafer-based polarimeter measured in out-of-plane configuration and fiber-based polarimeter measurements for comparison. The root-mean-square error (RMSE) between polarization states measured by the wafer-based metasurface polarimeter and reference polarization states for the wafer-based polarimeter is 0.005. This is the same level of precision as with the fiber-based polarimeter, which is 0.004-0.006. It should be noted, however, that the variation in the position of the analyzer vectors between the three devices affects the error. Also the variance of the measured intensities, caused by electronic noise, is higher for the wafer-based metasurface polarimeter.

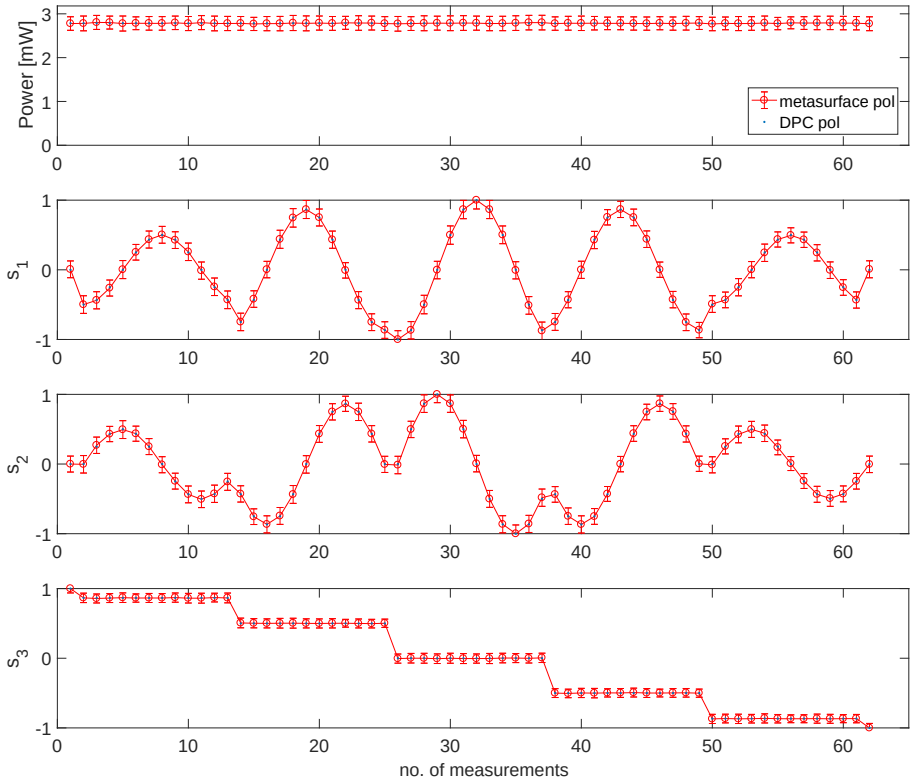

Figure A7.1. Polarization measurements at a wavelength of 1550 nm using a wafer-based 4-output metasurface polarimeter measured in out-of-plane configuration. Each subplot contains one element in the Stokes vector. The first subplot is the power of the incident light, which is proportional to S_0. The three last subplots are the parameters characterizing the state of polarization (SOP), $s_1 - s_3$. The red circles are the polarization measurements of the metasurface polarimeter, the blue dots are the reference polarizations set by the deterministic polarization controller (DPC). Error on the reference polarization measurements is not depicted on the plot, since the size of the error bars would be smaller than the size of the marker.

(a)

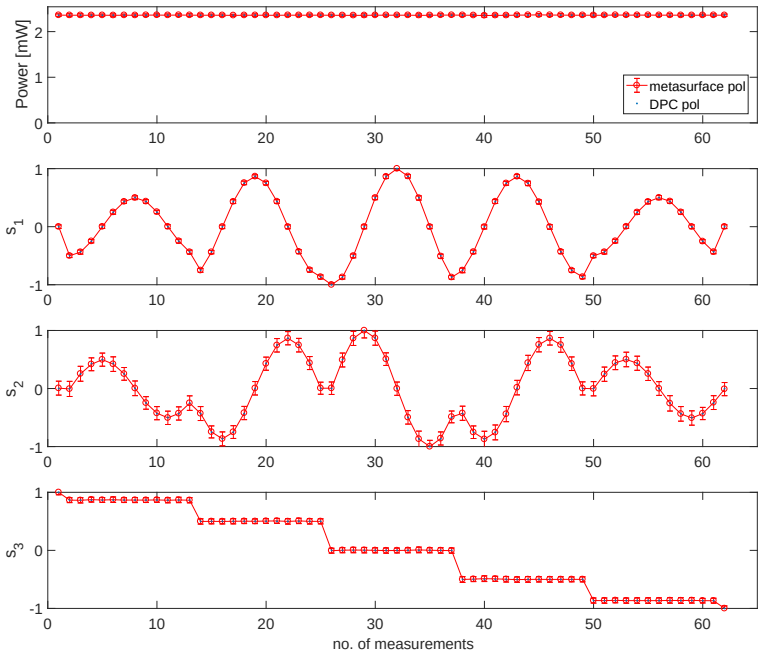

(b)

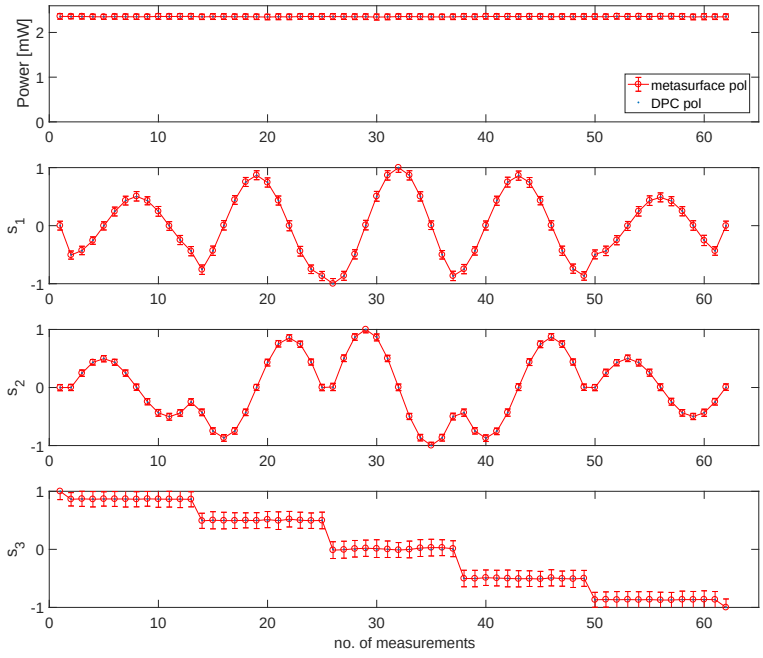

Figure A7.2. Polarization measurements at 1550 nm using (a) the fiber-based flood exposure metasurface polarimeter and (b) the fiber-based fiber exposure metasurface polarimeter.

Bibliography

[1] R. P. Feynman, "There's plenty of room at the bottom," *Engineering and Science*, vol. 23, no. 5, pp. 22–36, 1960.

[2] B. Bharat, *Springer handbook of nanotechnology*. 2007.

[3] A. ten Wolde, *Nanotechnology: Towards a molecular construction kit*. Netherlands Study Centre for Technology Trends (STT), 1998.

[4] W. Cai and V. Shalaev, *Optical Metamaterials, Fundamentals and Applications*. New York, Springer, 2010.

[5] N. Yu and F. Capasso, "Flat optics with designer metasurfaces," *Nature Materials*, vol. 13, 2014.

[6] A. V. Kildishev, A. Boltasseva, and V. M. Shalaev, "Planar photonics with metasurfaces," *Science*, vol. 339, no. 6125, 2013.

[7] P. Genevet, F. Capasso, F. Aieta, M. Khorasaninejad, and R. Devlin, "Recent advances in planar optics: From plasmonic to dielectric metasurfaces," *Optica*, vol. 4, no. 1, pp. 139–152, 2017.

[8] G. Ropars, G. Gorre, A. Le Floch, J. Enoch, and V. Lakshminarayanan, "A depolarizer as a possible precise sunstone for viking navigation by polarized skylight," *Proceedings of the Royal Society of London A: Mathematical, Physical and Engineering Sciences*, vol. 468, no. 2139, pp. 671–684, 2012.

[9] R. Bartholin, *Experimenta Crystalli Islandici disdiaclastici, quibus mira et insolita refractio detegitur*. Daniel Paulli, Copenhagen, 1669.

[10] N. Rubin, A. Zaidi, M. Juhl, R. Li, J. P. B. Mueller, R. Devlin, K. Leosson, and F. Capasso, "Polarization state generation and measurement with a single metasurface," *Optics Express*, vol. 26, pp. 21 455–21 478, 2018.

[11] J. P. B. Mueller, K. Leosson, and F. Capasso, "Ultracompact metasurface in-line polarimeter," *Optica*, vol. 3, no. 1, pp. 42–47, 2016.

[12] A. Pors, M. G. Nielsen, and S. I. Bozhevolnyi, "Plasmonic metagratings for simultaneous determination of Stokes parameters," *Optica*, vol. 2, no. 8, pp. 716–723, 2015.

[13] M. Khorasaninejad and F. Capasso, "Metalenses: Versatile multifunctional photonic components," *Science*, vol. 358, no. 6367, 2017.

[14] W. T. Chen, A. Y. Zhu, V. Sanjeev, M. Khorasaninejad, Z. Shi, E. Lee, and F. Capasso, "A broadband achromatic metalens for focusing and imaging in the visible," *Nature nanotechnology*, vol. 13, pp. 220–226, 2018.

[15] A. Arbabi, E. Arbabi, S. M. Kamali, Y. Horie, S. Han, and A. Faraon, "Miniature optical planar camera based on a wide-angle metasurface doublet corrected for monochromatic aberrations," *Nature communications*, vol. 7, p. 13 682, 2016.

[16] A. Y. Zhu, W.-T. Chen, M. Khorasaninejad, J. Oh, A. Zaidi, I. Mishra, R. C. Devlin, and F. Capasso, "Ultra-compact visible chiral spectrometer with metalenses," *APL Photonics*, vol. 2, no. 3, p. 036 103, 2017.

[17] L. Kristjánsson, *Silfurberg og þáttur þess í þróun raunvísinda og ýmissar tækni, einkum á 19. öld: minnisblöð og heimildaskrá*. University of Iceland, 2007.

[18] J. Biot, "Phénomènes de polarisation successive, observés dans des fluides homogènes," *Bull. Soc. Philomath*, vol. 190, p. 1815, 1815.

[19] R. M. A. Azzam, "The intertwined history of polarimetry and ellipsometry," *Thin Solid Films*, vol. 519, no. 9, pp. 2584–2588, 2011, 5th International Conference on Spectroscopic Ellipsometry (ICSE-V).

[20] P. S. Westbrook, T. A. Strasser, and T. Erdogan, "In-line polarimeter using blazed fiber gratings," *IEEE Photonics Technology Letters*, vol. 12, no. 10, pp. 1352–1354, 2000.

[21] A. Peinado, A. Lizana, J. Vidal, C. Iemmi, and J. Campos, "Optimization and performance criteria of a Stokes polarimeter based on two variable retarders," *Optics Express*, vol. 18, no. 10, pp. 9815–9830, 2010.

[22] G. E. Jellison and F. A. Modine, "Two-modulator generalized ellipsometry: Experiment and calibration," *Applied Optics*, vol. 36, no. 31, pp. 8184–8189, 1997.

[23] E. Arbabi, S. M. Kamali, A. Arbabi, and A. Faraon, "Full Stokes imaging polarimetry using dielectric metasurfaces," *arXiv preprint arXiv:1803.03384*, 2018.

[24] F. Ding, Y. Chen, and S. I. Bozhevolnyi, "Metasurface-based polarimeters," *Applied Sciences*, vol. 8, no. 4, 2018.

[25] H.-T. Chen, A. J. Taylor, and N. Yu, "A review of metasurfaces: Physics and applications," *Reports on Progress in Physics*, vol. 79, no. 7, p. 076 401, 2016.

[26] R. M. A. Azzam and N. M. Bashara, *Ellipsometry and Polarized Light*. Amsterdam: North-Holland, 1977.

[27] C. R. R. Menyuk and A. Galtarossa, *Polarization Mode Dispersion*. New York, Springer, 2005.

[28] J. R. Schott, *Fundamentals of Polarimetric Remote Sensing*. Bellingham, Washington, USA : SPIE Press, 2009.

[29] A. Hayat, J. P. B. Mueller, and F. Capasso, "Lateral chirality-sorting optical forces," *Proceedings of the National Academy of Sciences*, vol. 112, no. 43, pp. 13 190–13 194, 2015.

[30] A. Pierangelo *et al.*, "Ex-vivo characterization of human colon cancer by Mueller polarimetric imaging," *Optics Express*, vol. 19, no. 2, pp. 1582–1593, 2011.

[31] K. M. Twietmeyer, R. A. Chipman, A. E. Elsner, Y. Zhao, and D. VanNasdale, "Mueller matrix retinal imager with optimized polarization conditions," *Optics Express*, vol. 16, no. 26, pp. 21 339–21 354, 2008.

[32] J. N. Damask, *Polarization Optics in Telecommunication*. New York, Springer, 2005.

[33] M. Bass *et al.*, *Handbook of Optics*. New York, MGraw-Hill, 1995.

[34] J. S. Tyo, "Design of optimal polarimeters: Maximization of signal-to-noise ratio and minimization of systematic error," *Applied Optics*, vol. 41, no. 4, pp. 619–630, 2002.

[35] R. M. A. Azzam, I. M. Elminyawi, and A. M. El-Saba, "General analysis and optimization of the four-detector photopolarimeter," *Journal of the Optical Society of America A*, vol. 5, no. 5, pp. 681–689, 1988.

[36] R. M. A. Azzam and A. G. Lopez, "Accurate calibration of the four-detector photopolarimeter with imperfect polarizing optical elements," *JOSA A*, vol. 6, no. 10, pp. 1513–1521, 1989.

[37] C. Macias-Romero and P. Török, "Eigenvalue calibration methods for polarimetry," *Journal of the European Optical Society - Rapid publications*, vol. 7, 2012.

[38] B. Boulbry, J. C. Ramella-Roman, and T. A. Germer, "Improved method for calibrating a Stokes polarimeter," *Applied Optics*, vol. 46, no. 35, pp. 8533–8541, 2007.

[39] D. Layden, M. F. G. Wood, and I. A. Vitkin, "Optimum selection of input polarization states in determining the sample Mueller matrix: A dual photoelastic polarimeter approach," *Optics Express*, vol. 20, no. 18, pp. 466–481, 2012.

[40] A. A. Ramos and M. Collados, "Error propagation in polarimetric demodulation," *Applied Optics*, vol. 47, no. 14, pp. 2541–2549, 2008.

[41] R. M. A. Azzam, "Photopolarimetric measurement of the Mueller matrix by Fourier analysis of a single detected signal," *Optics Letters*, vol. 2, no. 6, pp. 148–150, 1978.

[42] D. H. Goldstein, "Mueller matrix dual-rotating retarder polarimeter," *Applied Optics*, vol. 31, no. 31, pp. 6676–6683, 1992.

[43] R. M. A. Azzam, "Division-of-amplitude photopolarimeter (DOAP) for the simultaneous measurement of all four Stokes parameters of light," *Optica Acta: International Journal of Optics*, vol. 29, no. 5, pp. 685–689, 1982.

[44] R. M. A. Azzam, "In-line light-saving photopolarimeter and its fiber-optic analog," *Optics Letters*, vol. 12, no. 8, pp. 558–560, 1987.

[45] G. Myhre, W.-L. Hsu, A. Peinado, C. LaCasse, N. Brock, R. A. Chipman, and S. Pau, "Liquid crystal polymer full-stokes division of focal plane polarimeter," *Opt. Express*, vol. 20, no. 25, pp. 27 393–27 409, 2012.

[46] J. S. Tyo, D. L. Goldstein, D. B. Chenault, and J. A. Shaw, "Review of passive imaging polarimetry for remote sensing applications," *Appl. Opt.*, vol. 45, no. 22, pp. 5453–5469, 2006.

[47] R. W. Wood, "On a remarkable case of uneven distribution of light in a diffraction grating spectrum," *Proceedings of the Physical Society of London*, vol. 18, no. 1, pp. 269–275, 1902.

[48] U. Fano, "The theory of anomalous diffraction gratings and of quasi-stationary waves on metallic surfaces (Sommerfeld's waves)," *Journal of the Optical Society of America*, vol. 31, no. 3, pp. 213–222, 1941.

[49] T. B. A. Senior, "Approximate boundary conditions," *IEEE Transactions on Antennas and Propagation*, vol. 29, no. 5, pp. 826–829, 1981.

[50] D. R. Smith, W. J. Padilla, D. C. Vier, S. C. Nemat-Nasser, and S. Schultz, "Composite medium with simultaneously negative permeability and permittivity," *Phys. Rev. Lett.*, vol. 84, pp. 4184–4187, 2000.

[51] J. B. Pendry, "Negative refraction makes a perfect lens," *Phys. Rev. Lett.*, vol. 85, pp. 3966–3969, 2000.

[52] N. Yu, P. Genevet, M. A. Kats, F. Aieta, J.-P. Tetienne, F. Capasso, and Z. Gaburro, "Light propagation with phase discontinuities: Generalized laws of reflection and refraction," *Science*, vol. 334, no. 6054, pp. 333–337, 2011.

[53] N. Yu, F. Aieta, P. Genevet, M. A. Kats, Z. Gaburro, and F. Capasso, "A broadband, background-free quarter-wave plate based on plasmonic metasurfaces," *Nano Letters*, vol. 12, no. 12, pp. 6328–6333, 2012.

[54] A. Pors and S. I. Bozhevolnyi, "Plasmonic metasurfaces for efficient phase control in reflection," *Opt. Express*, vol. 21, no. 22, pp. 27 438–27 451, 2013.

[55] H.-H. Hsiao, C. H. Chu, and D. P. Tsai, "Fundamentals and applications of metasurfaces," *Small Methods*, vol. 1, no. 4, p. 1 600 064, 2017.

[56] X. Luo, "Subwavelength optical engineering with metasurface waves," *Advanced Optical Materials*, p. 1 701 201, 2018.

[57] V. M. Shalaev, "Optical negative-index metamaterials," *Nature photonics*, vol. 1, no. 1, p. 41, 2007.

[58] H. Galinski, G. Favraud, H. Dong, J. Gongora, F. Favaro, M. Döbeli, R. Spolenak, A. Fratalocchi, and F. Capasso, "Scalable, ultra-resistant structural colors based on network metamaterials," *Light: Science & Applications*, 2016.

[59] N. Yu and F. Capasso, "Optical metasurfaces and prospect of their applications including fiber optics," *Journal of Lightwave Technology*, vol. 33, no. 12, 2015.

[60] M. Khorasaninejad, W. T. Chen, R. C. Devlin, J. Oh, A. Y. Zhu, and F. Capasso, "Metalenses at visible wavelengths: Diffraction-limited focusing and subwavelength resolution imaging," *Science*, vol. 352, pp. 1190–1194, 2016.

[61] V.-C. Su, C. H. Chu, G. Sun, and D. P. Tsai, "Advances in optical metasurfaces: Fabrication and applications," *Opt. Express*, vol. 26, no. 10, pp. 13 148–13 182, 2018.

[62] C. Huygens, *Treatise on light*. Leyden, 1690.

[63] A. Pors, O. Albrektsen, I. P. Radko, and S. I. Bozhevolnyi, "Gap plasmon-based metasurfaces for total control of reflected light," *Scientific reports*, vol. 3, p. 2155, 2013.

[64] A. Pors, M. G. Nielsen, R. L. Eriksen, and S. I. Bozhevolnyi, "Broadband focusing flat mirrors based on plasmonic gradient metasurfaces," *Nano letters*, vol. 13, no. 2, pp. 829–834, 2013.

[65] A. E. Krasnok, A. E. Miroshnichenko, P. A. Belov, and Y. S. Kivshar, "All-dielectric optical nanoantennas," *Opt. Express*, vol. 20, no. 18, pp. 20 599–20 604, 2012.

[66] A. I. Kuznetsov, A. E. Miroshnichenko, M. L. Brongersma, Y. S. Kivshar, and B. Luk'yanchuk, "Optically resonant dielectric nanostructures," *Science*, vol. 354, no. 6314, 2016.

[67] R. C. Devlin, M. Khorasaninejad, W. T. Chen, J. Oh, and F. Capasso, "Broadband high-efficiency dielectric metasurfaces for the visible spectrum," *Proceedings of the National Academy of Sciences*, vol. 113, no. 38, pp. 10 473–10 478, 2016.

[68] C. Pfeiffer and A. Grbic, "Metamaterial Huygens' surfaces: Tailoring wave fronts with reflectionless sheets," *Phys. Rev. Lett.*, vol. 110, p. 197 401, 19 2013.

[69] A. Epstein and G. V. Eleftheriades, "Huygens' metasurfaces via the equivalence principle: Design and applications," *JOSA B*, vol. 33, no. 2, A31–A50, 2016.

[70] S. Kruk, B. Hopkins, I. I. Kravchenko, A. Miroshnichenko, D. N. Neshev, and Y. S. Kivshar, "Invited article: Broadband highly efficient dielectric metadevices for polarization control," *APL Photonics*, vol. 1, no. 3, p. 030 801, 2016.

[71] L. Huang, X. Chen, H. Muehlenbernd, G. Li, B. Bai, Q. Tan, G. Jin, T. Zentgraf, and S. Zhang, "Dispersionless phase discontinuities for controlling light propagation," *Nano letters*, vol. 12, no. 11, pp. 5750–5755, 2012.

[72] L. Wang, S. Kruk, H. Tang, T. Li, I. Kravchenko, D. N. Neshev, and Y. S. Kivshar, "Grayscale transparent metasurface holograms," *Optica*, vol. 3, no. 12, pp. 1504–1505, 2016.

[73] S. Pancharatnam, "Generalized theory of interference and its applications," in *Proceedings of the Indian Academy of Sciences-Section A*, Springer, vol. 44, 1956, pp. 398–417.

[74] A. A. High, R. C. Devlin, A. Dibos, M. Polking, D. S. Wild, J. Perczel, N. P. de Leon, M. D. Lukin, and H. Park, "Visible-frequency hyperbolic metasurface," *Nature*, vol. 522, no. 7555, p. 192, 2015.

[75] M. A. Kats, R. Blanchard, P. Genevet, and F. Capasso, "Nanometre optical coatings based on strong interference effects in highly absorbing media," *Nature materials*, vol. 12, no. 1, p. 20, 2013.

[76] N. I. Zheludev and Y. S. Kivshar, "From metamaterials to metadevices," *Nature materials*, vol. 11, no. 11, p. 917, 2012.

[77] A. She, S. Zhang, S. Shian, D. R. Clarke, and F. Capasso, "Adaptive metalenses with simultaneous electrical control of focal length, astigmatism, and shift," *Science Advances*, vol. 4, no. 2, 2018.

[78] T. Roy, S. Zhang, I. W. Jung, M. Troccoli, F. Capasso, and D. Lopez, "Dynamic metasurface lens based on mems technology," *APL Photonics*, vol. 3, no. 2, 2018.

[79] W. T. Chen, A. Y. Zhu, M. Khorasaninejad, Z. Shi, V. Sanjeev, and F. Capasso, "Immersion meta-lenses at visible wavelengths for nanoscale imaging," *Nano letters*, vol. 17, no. 5, pp. 3188–3194, 2017.

[80] N. K. Grady, J. E. Heyes, D. R. Chowdhury, Y. Zeng, M. T. Reiten, A. K. Azad, A. J. Taylor, D. A. R. Dalvit, and H.-T. Chen, "Terahertz metamaterials for linear polarization conversion and anomalous refraction," *Science*, vol. 340, no. 6138, pp. 1304–1307, 2013.

[81] X. Gao, L. Singh, W. Yang, J. Zheng, H. Li, and W. Zhang, "Bandwidth broadening of a linear polarization converter by near-field metasurface coupling," *Scientific reports*, vol. 7, no. 1, p. 6817, 2017.

[82] Y. Chen, F. Ding, V. Coello, and S. I. Bozhevolnyi, "On-chip spectropolarimetry by fingerprinting with random surface arrays of nanoparticles," *Acs Photonics*, vol. 5, no. 5, pp. 1703–1710, 2018.

[83] F. Afshinmanesh, J. S. White, W. Cai, and M. L. Brongersma, "Measurement of the polarization state of light using an integrated plasmonic polarimeter," *Nanophotonics*, vol. 1, no. 2, pp. 125–129, 2012.

[84] M. Juhl, C. Mendoza, J. P. B. Mueller, F. Capasso, and K. Leosson, "Performance characteristics of 4-port in-plane and out-of-plane in-line metasurface polarimeters," *Opt. Express*, vol. 25, no. 23, pp. 28 697–28 709, 2017.

[85] E. Arbabi, A. Arbabi, S. M. Kamali, Y. Horie, and A. Faraon, "Multiwavelength polarization-insensitive lenses based on dielectric metasurfaces with meta-molecules," *Optica*, vol. 3, no. 6, pp. 628–633, 2016.

[86] A. She, S. Zhang, S. Shian, D. R. Clarke, and F. Capasso, "Large area metalenses: Design, characterization, and mass manufacturing," *Optics Express*, vol. 26, no. 2, pp. 1573–1585, 2018.

[87] X. Ni, A. V. Kildishev, and V. M. Shalaev, "Metasurface holograms for visible light," *Nature communications*, vol. 4, p. 2807, 2013.

[88] J. B. Mueller, N. A. Rubin, R. C. Devlin, B. Groever, and F. Capasso, "Metasurface polarization optics: Independent phase control of arbitrary orthogonal states of polarization," *Physical review letters*, vol. 118, no. 11, p. 113 901, 2017.

[89] R. C. Devlin, A. Ambrosio, N. A. Rubin, J. P. B. Mueller, and F. Capasso, "Arbitrary spin-to–orbital angular momentum conversion of light," *Science*, vol. 358, no. 6365, pp. 896–901, 2017.

[90] G. Biener, A. Niv, V. Kleiner, and E. Hasman, "Formation of helical beams by use of Pancharatnam–Berry phase optical elements," *Optics letters*, vol. 27, no. 21, pp. 1875–1877, 2002.

[91] T. Lee, J. Jang, H. Jeong, and J. Rho, "Plasmonic-and dielectric-based structural coloring: From fundamentals to practical applications," *Nano Convergence*, vol. 5, no. 1, p. 1, 2018.

[92] N. I. Landy, S. Sajuyigbe, J. J. Mock, D. Smith, and W. J. Padilla, "Perfect metamaterial absorber," *Physical review letters*, vol. 100, no. 20, p. 207 402, 2008.

[93] J. Hao, J. Wang, X. Liu, W. J. Padilla, L. Zhou, and M. Qiu, "High performance optical absorber based on a plasmonic metamaterial," *Applied Physics Letters*, vol. 96, no. 25, p. 251 104, 2010.

[94] P. Spinelli, M. A. Verschuuren, and A. Polman, "Broadband omnidirectional antireflection coating based on subwavelength surface mie resonators," *Nature communications*, vol. 3, p. 692, 2012.

[95] S. D. Senturia, *Microsystem design*. Kluwer Academic Publishers, 2001.

[96] M. Totzeck, W. Ulrich, A. Göhnermeier, and W. Kaiser, "Semiconductor fabrication: Pushing deep ultraviolet lithography to its limits," *Nature Photonics*, vol. 1, no. 11, pp. 629–631, 2007.

[97] S. K. Moore, "EUV lithography finally ready for fabs," *IEEE Spectrum*, vol. 55, no. 1, pp. 46–48, 2018.

[98] S.-J. Jeong, J. Y. Kim, B. H. Kim, H.-S. Moon, and S. O. Kim, "Directed self-assembly of block copolymers for next generation nanolithography," *Materials Today*, vol. 16, no. 12, pp. 468–476, 2013.

[99] S. Y. Chou, P. R. Krauss, and P. J. Renstrom, "Imprint lithography with 25-nanometer resolution," *Science*, vol. 272, pp. 85–87, 1996.

[100] K.-S. Lee, R. H. Kim, D.-Y. Yang, and S. H. Park, "Advances in 3D nano/microfabrication using two-photon initiated polymerization," *Progress in Polymer Science*, vol. 33, no. 6, pp. 631–681, 2008.

[101] S. A. Maier, *Plasmonics: fundamentals and applications*. Springer Science & Business Media, 2007.

[102] J. Lin, J. P. B. Mueller, Q. Wang, G. Yuan, N. Antoniou, X.-C. Yuan, and F. Capasso, "Polarization-controlled tunable directional coupling of surface plasmon polaritons," *Science*, vol. 340, no. 6130, pp. 331–334, 2013.

[103] J. P. B. Mueller, K. Leosson, and F. Capasso, "Polarization-selective coupling to long-range surface plasmon polariton waveguides," *Nanoletters*, vol. 14, no. 10, pp. 5524–5527, 2014.

[104] F. Falcone, T. Lopetegi, M. Laso, J. Baena, J. Bonache, M. Beruete, R. Marques, F. Martin, and M. Sorolla, "Babinet principle applied to the design of metasurfaces and metamaterials," *Physical Review Letters*, vol. 93, no. 19, 2004.

[105] M. Juhl, C. Mendoza, J. B. Mueller, F. Capasso, and K. Leósson, "Packaged inline metasurface polarimeters with in-plane and out-of-plane detection," in *The European Conference on Lasers and Electro-Optics*, Optical Society of America, 2017, CK_4_2.

[106] E. B. Magnusson, J. P. B. Mueller, M. Juhl, C. Mendoza, and K. Leosson, "Neural polarimeter and wavemeter," *ACS Photonics*, vol. 5, no. 7, pp. 2682–2687, 2018.

[107] M. Juhl, C. Mendoza, J. P. B. Mueller, F. Capasso, and K. Leósson, "Self-aligned nano-transfer of metasurface polarimeter to an optical fiber tip using UV-curable hybrid polymer," in *Conference on Lasers and Electro-Optics*, Optical Society of America, 2018, SF1J.8.

[108] M. Juhl, J. P. B. Mueller, and K. Leosson, "Metasurface polarimeter on optical fiber facet by nano-transfer to UV-curable hybrid polymer," *Submitted for publication*, 2018.

[109] G. Spektor, A. David, B. Gjonaj, G. Bartal, and M. Orenstein, "Metafocusing by a metaspiral plasmonic lens," *Nano Letters*, vol. 15, no. 9, pp. 5739–5743, 2015.

[110] G. Spektor, D. Kilbane, A. Mahro, M. Hartelt, E. Prinz, M. Aeschlimann, and M. Orenstein, "Metasurfaces and ultrafast dynamics for high angular momentum compound optical fields," in *Conference on Lasers and Electro-Optics*, Optical Society of America, 2018, FTh3M.3.

[111] F. L. Pedrotti and L. S. Pedrotti, *Introduction to Optics*. Pearson Education, 2008.

[112] P. Biagioni, J.-S. Huang, and B. Hecht, "Nanoantennas for visible and infrared radiation," *Reports on Progress in Physics*, vol. 75, no. 2, p. 024 402, 2012.

[113] S. J. Orfanidis, *Electromagnetic waves and antennas*. Rutgers University New Brunswick, NJ, 2002.

[114] J. N. Sahalos, *Orthogonal Methods for Array Synthesis: Theory and the ORAMA Computer Tool*. Chichester UK, John Wiley & Sons, Ltd, 2006.

[115] M. R. Foreman, A. Favaro, and A. Aiello, "Optimal frames for polarization state reconstruction," *Phys. Rev. Lett.*, vol. 115, p. 263 901, 26 2015.

[116] A. Peinado Capdevila, J. Campos Coloma, and A. Lizana Tutusaus, "Design of polarimeters based on liquid crystals and biaxial crystals for polarization metrology," PhD thesis, Universitat Autònoma de Barcelona, Bellaterra, Barcelona, 2015.

[117] D. Lara and C. Paterson, "Stokes polarimeter optimization in the presence of shot and Gaussian noise," *Optics Express*, vol. 17, no. 23, pp. 21 240–21 249, 2009.

[118] J. Jahn, *Introduction to the Theory of Nonlinear Optimization*. Springer-Verlag Berlin Heidelberg, 2007.

[119] D. S. Sabatke, M. R. Descour, E. L. Dereniak, W. C. Sweatt, S. A. Kemme, and G. S. Phipps, "Optimization of retardance for a complete Stokes polarimeter," *Opt. Lett.*, vol. 25, no. 11, pp. 802–804, 2000.

[120] J. Taylor, *An introduction to error analysis, the study of uncertainties in physical measurements*. University Science Books, 1997.

[121] G. Kostovski, P. R. Stoddart, and A. Mitchell, "The optical fiber tip: An inherently light-coupled microscopic platform for micro-and nanotechnologies," *Advanced Materials*, vol. 26, no. 23, pp. 3798–3820, 2014.

[122] J. P. B. Müller, "Polarization in nanophotonics," PhD thesis, Dissertation from Harvard University, Cambridge, Massachusetts, 2016.

[123] M. Principe, M. Consales, A. Micco, A. Crescitelli, G. Castaldi, E. Esposito, V. La Ferrara, A. Cutolo, V. Galdi, and A. Cusano, "Optical fiber meta-tips," *Light: Science & Applications*, vol. 6, no. 3, e16226, 2017.

[124] G. Calafiore, A. Koshelev, F. I. Allen, S. Dhuey, S. Sassolini, E. Wong, P. Lum, K. Munechika, and S. Cabrini, "Nanoimprint of a 3D structure on an optical fiber for light wavefront manipulation," *Nanotechnology*, vol. 27, no. 37, p. 375 301, 2016.

[125] H. E. Williams, D. J. Freppon, S. M. Kuebler, R. C. Rumpf, and M. A. Melino, "Fabrication of three-dimensional micro-photonic structures on the tip of optical fibers using SU-8," *Opt. Express*, vol. 19, no. 23, pp. 22 910–22 922, 2011.

[126] S. Scheerlinck, P. Dubruel, P. Bienstman, E. Schacht, D. V. Thourhout, and R. Baets, "Metal grating patterning on fiber facets by UV-based nano imprint and transfer lithography using optical alignment," *J. Lightwave Technol.*, vol. 27, no. 10, pp. 1415–1420, 2009.

[127] B. Wang, T. Siahaan, M. A. Dündar, R. Nötzel, M. J. van der Hoek, S. He, and R. W. van der Heijden, "Photonic crystal cavity on optical fiber facet for refractive index sensing," *Optics letters*, vol. 37, no. 5, pp. 833–835, 2012.

[128] E. J. Smythe, M. D. Dickey, G. M. Whitesides, and F. Capasso, "A technique to transfer metallic nanoscale patterns to small and non-planar surfaces," *ACS nano*, vol. 3, no. 1, pp. 59–65, 2008.

[129] P. Nagpal, N. C. Lindquist, S.-H. Oh, and D. J. Norris, "Ultrasmooth patterned metals for plasmonics and metamaterials," *Science*, vol. 325, no. 5940, pp. 594–597, 2009.

[130] N. Vogel, J. Zieleniecki, and I. Köper, "As flat as it gets: Ultrasmooth surfaces from template-stripping procedures," *Nanoscale*, vol. 4, no. 13, pp. 3820–3832, 2012.

[131] W. T. Chen, P. C. Wu, C. J. Chen, H.-Y. Chung, Y.-F. Chau, C.-H. Kuan, and D. P. Tsai, "Electromagnetic energy vortex associated with sub-wavelength plasmonic taiji marks," *Optics Express*, vol. 18, no. 19, pp. 19 665–19 671, 2010.

[132] P. B. Johnson and R.-W. Christy, "Optical constants of the noble metals," *Physical review B*, vol. 6, no. 12, p. 4370, 1972.

[133] E. Palik, *Handbook of Optical Constants of Solids vol 1*. New York: Academic, 1998.

Paper I

Performance characteristics of 4-port in-plane and out-of-plane in-line metasurface polarimeters

Michael Juhl, Carlos Mendoza, J. P. Balthasar Mueller, Federico Capasso, and Kristjan Leosson

Optics Express, 25, 23

Research Article | Vol. 25, No. 23 | 13 Nov 2017 | OPTICS EXPRESS 28697

Optics EXPRESS

Performance characteristics of 4-port in-plane and out-of-plane in-line metasurface polarimeters

MICHAEL JUHL,[1,2] CARLOS MENDOZA,[1] J. P. BALTHASAR MUELLER,[3] FEDERICO CAPASSO,[3] AND KRISTJAN LEOSSON[1,2,*]

[1]*Innovation Center Iceland, 112 Reykjavík, Iceland*
[2]*University of Iceland, 101 Reykjavík, Iceland*
[3]*Harvard John A. Paulson School of Engineering and Applied Sciences, Harvard University, Cambridge, Massachusetts 02138, USA*
**kristjan.leosson@nmi.is*

Abstract: In-line polarimeters perform nonterminating measurements of the polarization state of light by sampling only a small part of the total light intensity. In-line polarimeters are used in applications such as polarization state generators and in optical communications. Current polarimeters use multiple optical components in sequence for polarization analysis and therefore often become bulky and expensive. Here, we experimentally demonstrate the operation of compact fiber-coupled polarimeters with high sampling rates, operating at telecom wavelengths, each polarimeter comprising a single ultra-thin metasurface aligned to four photodetectors. We compare two configurations of such metasurface polarimeters, with in-plane and out-of-plane detection, respectively. The metasurface polarimeters reported here show excellent agreement with commercial polarimeters and cover a bandwidth of at least 100 nm.

OCIS codes: (050.6624) Subwavelength structures; (120.5410) Polarimetry; (220.4241) Nanostructure fabrication; (230.0230) Optical devices; (260.5430) Polarization.

References and links

1. R. M. A. Azzam and N. M. Bashara, *Ellipsometry and Polarized Light* (North-Holland, 1977).
2. C. R. Menyuk and A. Galtarossa, *Polarization Mode Dispersion* (Springer, 2005).
3. J. R. Schott, *Fundamentals of Polarimetric Remote Sensing* (SPIE, 2009).
4. A. Hayat, J. P. B. Mueller, and F. Capasso, "Lateral chirality-sorting optical forces," Proc. Natl. Acad. Sci. U.S.A. **112**(43), 13190–13194 (2015).
5. A. Pierangelo, A. Benali, M. R. Antonelli, T. Novikova, P. Validire, B. Gayet, and A. De Martino, "Ex-vivo characterization of human colon cancer by Mueller polarimetric imaging," Opt. Express **19**(2), 1582–1593 (2011).
6. K. M. Twietmeyer, R. A. Chipman, A. E. Elsner, Y. Zhao, and D. VanNasdale, "Mueller matrix retinal imager with optimized polarization conditions," Opt. Express **16**(26), 21339–21354 (2008).
7. R. M. A. Azzam, "Photopolarimetric measurement of the Mueller matrix by Fourier analysis of a single detected signal," Opt. Lett. **2**(6), 148–150 (1978).
8. D. H. Goldstein, "Mueller matrix dual-rotating retarder polarimeter," Appl. Opt. **31**(31), 6676–6683 (1992).
9. A. Peinado, A. Lizana, J. Vidal, C. Iemmi, and J. Campos, "Optimization and performance criteria of a Stokes polarimeter based on two variable retarders," Opt. Express **18**(10), 9815–9830 (2010).
10. G. E. Jellison and F. A. Modine, "Two-modulator generalized ellipsometry: experiment and calibration," Appl. Opt. **36**(31), 8184–8189 (1997).
11. R. M. A. Azzam, "Division-of-amplitude photopolarimeter (DOAP) for the simultaneous measurement of all four stokes parameters of light," Opt. Acta (Lond.) **29**(5), 685–689 (1982).
12. R. M. A. Azzam, I. M. Elminyawi, and A. M. El-Saba, "General analysis and optimization of the four-detector photopolarimeter," J. Opt. Soc. Am. A **5**(5), 681–689 (1988).
13. R. M. A. Azzam, "In-line light-saving photopolarimeter and its fiber-optic analog," Opt. Lett. **12**(8), 558–560 (1987).
14. P. S. Westbrook, T. A. Strasser, and T. Erdogan, "In-line polarimeter using blazed fiber gratings," IEEE Photonics Technol. Lett. **12**(10), 1352–1354 (2000).
15. N. Yu and F. Capasso, "Flat optics with designer metasurfaces," Nat. Mater. **13**(2), 139–150 (2014).

#303696 https://doi.org/10.1364/OE.25.028697
Journal © 2017 Received 2 Aug 2017; revised 18 Oct 2017; accepted 30 Oct 2017; published 3 Nov 2017

Optics EXPRESS

16. D. R. Smith, W. J. Padilla, D. C. Vier, S. C. Nemat-Nasser, and S. Schultz, "Composite medium with simultaneously negative permeability and permittivity," Phys. Rev. Lett. **84**(18), 4184–4187 (2000).
17. H. Galinski, G. Favraud, H. Dong, J. S. T. Gongora, F. Favaro, M. Döbeli, R. Spolenak, A. Fratalocchi, and F. Capasso, "Scalable, ultra-resistant structural colors based on network metamaterials," Light Sci. Appl. **6**, 16233 (2016).
18. N. Yu and F. Capasso, "Optical metasurfaces and prospect of their applications including fiber optics," J. Lightwave Technol. **33**(12), 2344–2358 (2015).
19. M. Khorasaninejad, W. T. Chen, R. C. Devlin, J. Oh, A. Y. Zhu, and F. Capasso, "Metalenses at visible wavelengths: diffraction-limited focusing and subwavelength resolution imaging," Science **352**(6290), 1190–1194 (2016).
20. J. P. B. Mueller, K. Leosson, and F. Capasso, "Ultracompact metasurface in-line polarimeter," Optica **3**(1), 42–47 (2016).
21. R. A. Chipman, *Handbook of Optics* (MGraw-Hill, 1995), Chap. 22.
22. B. Boulbry, J. C. Ramella-Roman, and T. A. Germer, "Improved method for calibrating a Stokes polarimeter," Appl. Opt. **46**(35), 8533–8541 (2007).
23. J. Lin, J. P. B. Mueller, Q. Wang, G. Yuan, N. Antoniou, X. C. Yuan, and F. Capasso, "Polarization-controlled tunable directional coupling of surface plasmon polaritons," Science **340**(6130), 331–334 (2013).
24. M. Skolnik, *Radar Handbook* (McGraw-Hill, 1970).
25. J. N. Sahalos, *Orthogonal Methods for Array Synthesis: Theory and the ORAMA Computer Tool* (John Wiley & Sons, 2006).
26. J. P. B. Mueller, K. Leosson, and F. Capasso, "Polarization-selective coupling to long-range surface plasmon polariton waveguides," Nano Lett. **14**(10), 5524–5527 (2014).

1. Introduction

Polarization is a property of light that describes the vectorial nature of its electric field oscillations. Stokes polarimeters are devices that measure the four Stokes parameters describing the state and degree of polarization of a light beam. The polarimetric information is crucial in a large number of applications. In materials characterization the measurement of polarization is used, e.g., to determine film thickness and refractive index [1]; in telecommunication it is used to monitor effects such as polarization-mode dispersion, polarization-dependent loss, and polarization dependent properties of optical devices [2]; in remote sensing the polarization information allows to distinguish between surfaces of different structures, remove clutter and image through dust and clouds [3]; in chemistry and biotechnology, polarization is used to measure the concentration and/or purity of optically active substances (such as sugars and antibiotics) using angle of rotation or evanescent chiral sensing [4], or to detect cancer or glaucoma in the human eye [5,6], to name a few examples. Due to the 4-dimensional nature of the Stokes vector, a complete Stokes polarimeter performs at least four intensity measurements. This can be realized in a number of different ways. One of the most common methods is the time-sequential approach, where measurements are separated over time, generally employing a single detector. Such polarization analysis can be carried out using mechanically rotating [7,8] or oscillating waveplates [9], or photoelastic modulators [10]. Products based on all three different approaches are available on the market. None of these configurations are signal-saving and, since the measurement is spread over time, such devices have a limited sampling rate. Another method is division-of-amplitude, where the beam is split up and measured simultaneously using several detectors, e.g. by employing a sequence of beamsplitters and waveplates [11,12]. Signal saving polarimeter designs using the division-of-amplitude method can be realized by employing polarization state analyzers that use only a small fraction of the incident light intensity to measure its polarization [13]. A modern-day example of this configuration is the in-line fiber polarimeter, where two or more polarization-dependent tilted fiber Bragg gratings, separated by a fiber quarter-wave plate, split off a small proportion of the transmitted optical power to four photodetectors [14]. The in-line fiber polarimeter offers a higher sampling rate than the time-sequential method. Some of the measurement accuracy is sacrificed by only measuring a fraction of the signal intensity. However, the accuracy of most commercial in-line fiber polarimeters still lies in the same range as their signal-terminating counterparts. Due to cost, speed or space limitations, the abovementioned solutions are inappropriate for many

Optics EXPRESS

applications such as parallel monitoring of polarization of a large number of channels in optical networks. Furthermore, none of the in-line polarimeters preserves the polarization of the incident light.

Metasurfaces are two-dimensional optical nano-structures that enable the tailoring of the amplitude, phase or polarization of light using dense arrays of sub-wavelength scale optical antennas [15]. In addition to displaying interesting optical phenomena, such as negative refraction and near-zero permittivity or permeability [16,17], metasurfaces also provide a promising platform for simplifying and miniaturizing existing optical components [15,18,19]. In 2016, we presented the concept of a metasurface-based in-line polarimeter [20]. Using a laboratory setup, we demonstrated that all four polarization state analyzers of a Stokes polarimeter could be combined in a single-layered array of sub-wavelength nanoantennas. The ultra-compact design of the metasurface polarimeter, combined with its non-destructive, polarization-preserving features, allows for applications such as feedback-driven polarization generation and large-scale online polarization monitoring in optical communication. In addition to the ultra-compact design that allows for planar integration, the benefits of the metasurface polarimeter include a detection-limited response time, simple and versatile design that can be tailored for operation across a wide range of wavelengths simply by changing the dimensions of the metasurface structure, increased robustness and reduced costs due to the replacement of moving parts and optical components like waveplates with structures produced by conventional lithographic process technology. In the present paper, we provide analysis and comparison of two configurations of packaged fiber-coupled polarimeter devices based on the metasurface principle.

2. Polarimeter design

The four-port metasurface polarimeter is described using the mathematical formalism of the polarimetric measurement and analysis of a standard Stokes polarimeter, see [12,20], where the four power measurements and the incident polarization are related by the *analyzer matrix*

$$\mathbf{P} = \mathbf{MS} \tag{1}$$

where **P** is the measured power from each of the output channels and **M** is a 4x4 matrix with each row containing an *analyzer vector* that characterizes one polarization analyzer [21]. **S** is the Stokes vector of the incoming light given by

$$\mathbf{S} = \begin{pmatrix} S_0 \\ S_1 \\ S_2 \\ S_3 \end{pmatrix} = \begin{pmatrix} I \\ pIs_1 \\ pIs_2 \\ pIs_3 \end{pmatrix} \tag{2}$$

where I is the incident light intensity, p is the degree of polarization (DOP), and s_1-s_3 is the state of polarization (SOP) represented as a point on the surface of the Poincaré sphere.

Calibration of the polarimeter devices was carried out by determining the analyzer matrix from a set of (usually 80) individual reference measurements, using the method described in [22].

The metasurface described in this section consists of arrays of metallic nanorods. A graphical representation of the metasurface design is seen in Fig. 1(a).

Optics EXPRESS

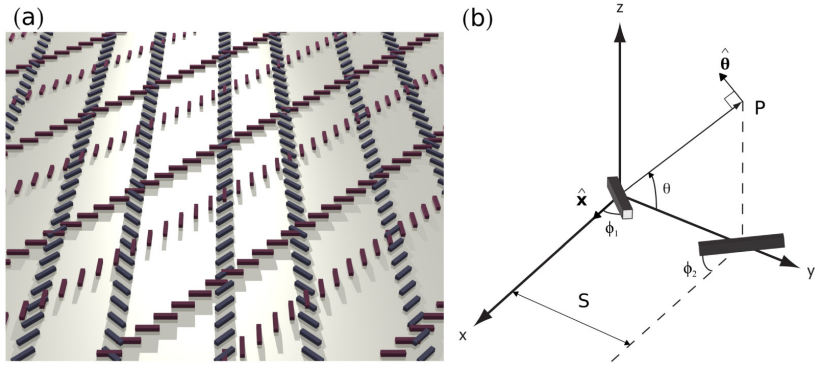

Fig. 1. (a) Graphical representation of the metasurface design. The metasurface consists of columns of sub-wavelength spaced nano-antennas. The antennas in each column are rotated 90° relative to the antennas in the neighboring column. The distance between every second column is twice the resonance wavelength, $2\lambda_0$, and the distance between two column-pairs is $\lambda_0(1 + 1/8)$. The red antenna columns are arranged in a pattern identical to the blue design except from a 45° rotation relative to the blue antenna columns. The height of the antennas are 2 times larger than their designed proportions for visual purposes. (b) Geometry of a phased array with two elements with individual orientation (ϕ_1 and ϕ_2) in the xy-plane. The point of observation (P) is established by the angle θ. One antenna (n = 1) is placed in origo and the other antenna (n = 2) is positioned at (0, S, 0). The direction of the unit vectors in Eq. (3) is shown on the figure. Incident light is parallel to the z-axis.

A metallic nanorod can be modelled as a thin optical dipole antenna. Consider electromagnetic radiation that has a wavelength corresponding to the resonance wavelength of the nanoantennas and is normally incident on the antenna. The antenna then emits radiation as long as the incoming light contains a component of polarization along the long axis of the rod. The far-field radiation pattern of a nanoantenna with length less than a wavelength can be modelled reasonably well as a short dipole. If identical antennas are placed in a subwavelength-spaced 1-dimensional array, the azimuthal radiation pattern is constant along the array. Two parallel columns having antennas rotated ± 45° from their column axis in a fishbone pattern will scatter most efficiently two orthogonal linear polarization components of an incident electromagnetic field [23]. Therefore, the antennas will emit an interference pattern similar to the radiation pattern of a phased array with two elements. The interference pattern depends on the polarization of the incoming wave and the distance between the two columns. The distance between the two columns can be tuned to fit the phase difference between the two orthogonal components of a preferred incoming polarization to obtain a maximum of scattered field intensity in the directions of interest for that particular (generally elliptical) polarization state. The array factor of a two-pair column is given by [20,24,25]

$$\mathbf{A} = \Phi_1 I_1 + \Phi_2 I_2 = \left[\cos(\phi_1)\hat{\mathbf{x}} - \sin(\phi_1)\sin(\theta)\hat{\boldsymbol{\theta}}\right]\cos(\psi) + \left[\cos(\phi_2)\hat{\mathbf{x}} - \sin(\phi_2)\sin(\theta)\hat{\boldsymbol{\theta}}\right]\sin(\psi)e^{i(\delta - kS\cos(\theta))} \tag{3}$$

where

$$I_1 = \cos(\psi), I_2 = \sin(\psi)e^{i\delta}$$

are the excitation currents for each antenna and

$$\Phi_n = \left[\cos(\phi_n)\hat{\mathbf{x}} - \sin(\phi_n)\sin(\theta)\hat{\boldsymbol{\theta}}\right]e^{-i(n-1)kS\cos(\theta)}$$

Optics EXPRESS

is a vector that describes the radiation as a function of the spatial orientation of the n^{th} dipole for n = 1, 2. ψ and δ describe the polarization of the incoming light using the Jones vector model of polarization in complex number representation. ψ is related to the amplitudes $\psi = \arctan(E_y/E_x)$ and δ is the relative phase difference. $k = 2\pi/\lambda$ is the angular wavenumber of the incoming wave. The position of the first dipole (n = 1) is in origo. S is the distance between columns and the azimuthal angle θ is the angle in the yz-plane between y-axis in the sample plane and the axis from origo to the point of measurement P. The x-axis is parallel to the column axes and ϕ_n is the rotation of the n^{th} dipole away from the x axis in the xy-plane normal to the incident light. $\hat{\mathbf{x}}$ is a unit vector parallel to the x-axis, and $\hat{\boldsymbol{\theta}}$ is a unit vector in the angular tangential direction associated to the rotation of θ. The choice of excitation current restricts the dipoles to be perpendicular to each other, i.e. $|\phi_2 - \phi_1| = 90°$. A sketch of the geometry of an individually rotated two-element array is shown in Fig. 1(b) and radiation patterns for 4 different input polarizations are shown in Fig. 2, with $S = \lambda_0(1 + 1/8)$ and $\phi_n = \pm 45°$. λ_0 is the resonance wavelength of the dipole antennas.

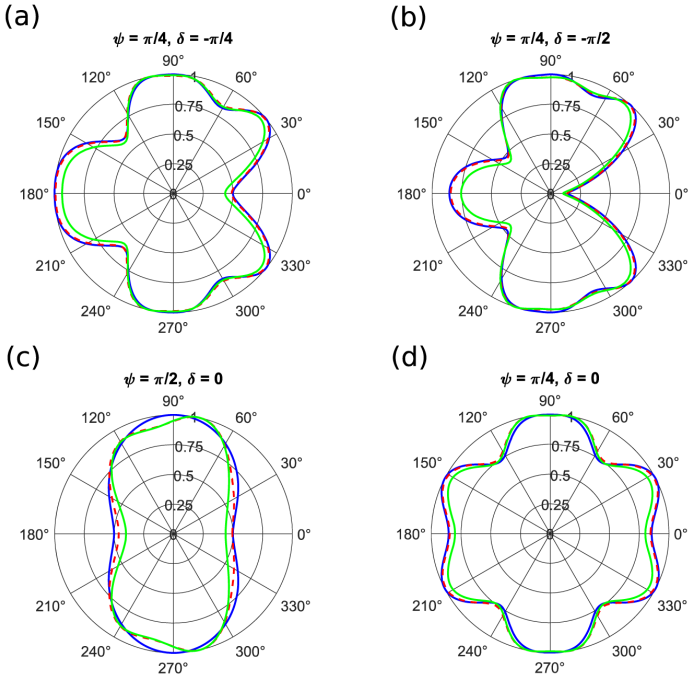

Fig. 2. Radiation patterns of two nanoantennas oriented perpendicularly to each other (± 45°) for different polarizations of the incoming light. The blue line is $|A|^2$ vs θ in the yz-plane (see Fig. 1(b)) normalized to unity using the analytical model Eq. (3), the red dashed line corrects the analytical model for mutual coupling and the green line is $|E|^2$ vs θ normalized to unity using a finite-difference time-domain (FDTD) simulation. (a) is elliptically polarized light with (ψ, δ) = (π/4, -π/4), (b) is circularly polarized light, (c) is linearly polarized light at 45°, and (d) is vertically polarized light.

The inter-antenna distance $S = \lambda_0(1 + 1/8)$ is designed to maximize the array factor Eq. (3) at θ = 0° and θ = 180° (in-plane output) for elliptically polarized light with ψ = π/4 and δ = ± π/4. It is seen that the analytical model fits very well to a finite-difference time-domain

Optics EXPRESS

(FDTD) simulation of two gold antennas with dimensions of 250 nm × 50 nm × 20 nm. Correcting the analytical model for mutual coupling improves the fit even further. The radiation pattern is left/right asymmetric for all elliptical/circular polarizations, as a result of the difference in phase between the two linear orthogonal components of the incoming light's polarization state. The polarization for which the measured power of the scattered field in a given direction (proportional to $|\mathbf{A}|^2$) is maximal corresponds to the analyzer vector. At $\theta = 0°$ or $\theta = 180°$ the second term in Φ_n vanishes and a signal contrast of 100% on each detector is possible. In the case where θ is 60° or 120°, Φ_1 and Φ_2 will no longer be equal and a theoretical polarization-dependent contrast of only 25% of the overall signal is possible.

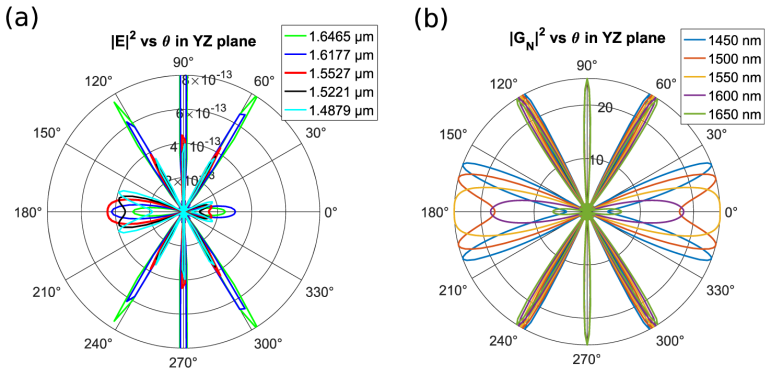

Fig. 3. (a) Wavelength dependence of the finite-difference time-domain (FDTD) simulated radiation pattern, $|E|^2$ versus θ in the yz-plane, of a metasurface consisting of five column-pairs of ± 45°-oriented antennas. Incoming light is elliptically polarized with $(\psi, \delta) = (\pi/4, -\pi/4)$. (b) Diffraction pattern of a meta-grating with N = 2 and $d = 2\lambda_0$ using Eq. (4), $|G_N|^2$ versus θ in the yz-plane, plotted versus different wavelengths. Equation (4) isolates the meta-grating's contribution to the array factor. The plot illustrates that the meta-grating is responsible for the difference in sensitivity to wavelength fluctuations between the in-plane and the out-of-plane design.

Repeating the column-pairs in an array of 2N + 1 elements with a period of $d = 2\lambda_0$ will form a meta-grating that covers a larger area and results in a highly directional intensity distribution. To account for the repeated column-pairs the array factor is multiplied with [20]

$$G_N = \sum_{n=-N}^{N} e^{i n k d \cos(\theta)} \tag{4}$$

In our case, the interesting angles for measurement are the first and second orders of the grating, corresponding to azimuthal angles θ in the yz-plane (see Fig. 1) of 0°, 180° and 60°, 120°, as illustrated in Fig. 3. Figure 3(a) is a plot that shows FDTD simulations of a full metasurface containing five column-pairs and the same S and antenna dimensions as in Fig. 2. Equation (4) is plotted in Fig. 3(b) at different wavelengths and shows the effect of the meta-grating alone.

Optics EXPRESS

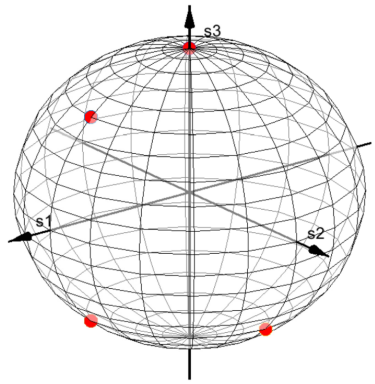

Fig. 4. The four analyzer vectors of a complete Stokes polarimeter depicted on the Poincaré sphere. It is seen that the four polarizations span a volume in SOP space and it is therefore possible to distinguish between the intensity and the DOP.

The four analyzer vectors in the analyzer matrix are defined in a manner analogous to Stokes vectors and they form a basis for the SOP space. If using the four angles of the two grating orders mentioned above the basis will be incomplete and it will not be possible to measure the full SOP. Furthermore, a complete polarimeter that measures the intensity and SOP as well as the DOP needs to have analyzer vectors that span a volume in SOP space [20]. These problems are solved by superimposing another column-pair grating at a 45° angle relative to the first. A distance of $S = \lambda_0(1 + 1/4)$ and an out-of-plane measurement of the first column-pair grating would theoretically result in an analyzer vector with two elliptically polarized states, $(\psi, \delta) = (\pi/4, \pm 3\pi/4)$. Measuring the second column-pair at 0° and 60° would produce an analyzer vector with a circularly polarized state $(\psi, \delta) = (\pi/4, \pi/2)$, and another with an elliptically polarized state $(\psi, \delta) = (\pi/4, -3\pi/4)$, see Fig. 4. However, out-of-plane and in-plane measurement comes with different traits, so here we will focus only on purely in-plane or out-of-plane designs. The in-plane metasurface polarimeter is designed with two 45° superimposed column-pair gratings and distances of $S = \lambda_0(1 + 1/8)$ to obtain (ideally) the best basis for a four-output polarimeter with the constraint that the analyzer vectors consists of two pairs of vectors mirrored about the equator of the Poincaré sphere [12]. Figure 5 shows schematics of a full metasurface, with two superimposed columns-pair gratings, each grating consisting of 5 column-pairs. The arrows illustrate the direction of the incoming light and direction of the scattered light of interest for in-plane and out-of-plane measurements. Figure 5(a) shows the in-plane design and Fig. 5(b) illustrates the out-of-plane design. Theoretically, the analyzer vectors of these two designs do not span a volume in SOP space, but deviations of the analyzer vectors caused by antenna interactions, geometric deviation, internal reflections and/or wavelength dependence are nevertheless large enough to distinguish between changes in DOP and intensity. The in-plane design is well suited for coupling the scattered radiation directly to planar waveguides and could therefore be advantageous in an on-chip polarimeter array design. Furthermore, the signal contrast Eq. (3) and the maximum power to the detector at the designed wavelength (Fig. 3(a)) are larger. The out-of-plane design shows less wavelength dependence, which is mainly an effect of the meta-grating as seen in Fig. 3(b). Furthermore, there are no rescattering or absorption losses in the out-of-plane design, since the scattered field does not propagate along the plane of the metasurface. There is therefore no limit to the overall size of the metasurface, making alignment with the incoming light beam a simpler task.

Optics EXPRESS

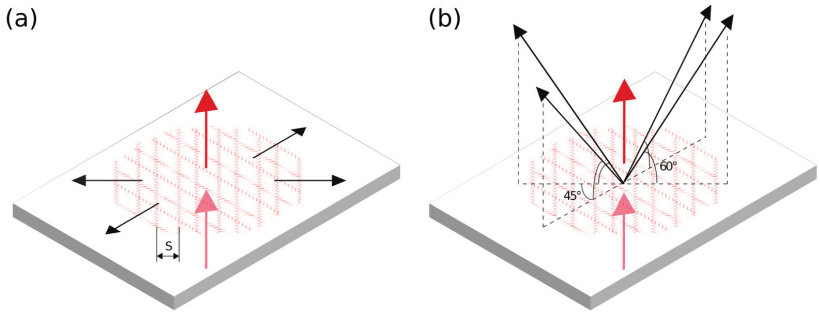

Fig. 5. Schematics of a metasurface polarimeter showing the geometry of the antenna structure placed onto a transparent substrate. (a) The black arrows represent the directions of scattered light, propagating in the plane of the sample surface. (b) The black arrows indicate the angles that can be used for out-of-plane measurements. The scattered field intensity is measured behind the sample (seen from the perspective of the light source). The red arrows illustrate the incident light beam and the light transmitted through the sample.

3. Experiments and results

The arrays of nanoantennas forming the metasurface were fabricated on fused silica substrates. The metasurface structures were patterned using electron beam lithography, gold deposition and lift-off. The resulting nanorods have a thickness of 25 nm, width of approximately 50 nm and a length of 250 nm (approximately 1/4 of a wavelength) and are embedded within a 25 μm layer of dielectric (BCB polymer) for protection. The full metasurface covers an area of 100 μm × 100 μm. Scanning electron micrograph (SEM) images of the metasurface is seen in Fig. 6. In the case of in-plane detection, the substrate was diced such that the substrate edges were perpendicular to the direction of the four scattered light directions. The substrates were fitted into a 3D-printed holder that aligned the sample with four individual TO-canned PIN photodiodes. Another 3D-printed holder was made for the different positions of the detectors in the out-of-plane design. One half of a fiber mating sleeve was used to align a fiber connector to the metasurface, as shown in Fig. 7. This compact polarimeter, consisting of the metasurface chip, a 3D-printed holder, four photodetectors, and one half of a mating sleeve, demonstrates that the polarimeter can be realized without any optical elements between the metasurface and the detectors. This is an important step towards extremely compact polarimeters that integrates detectors on the metasurface chip. A schematic of the setup is seen in Fig. 8. 1510 nm – 1610 nm light from a tunable laser was coupled into a deterministic polarization controller (DPC) and directed to the metasurface. The optical fiber between the DPC and the sample inevitably changes the polarization of the light. Therefore, the polarization of the light transmitted through the sample was additionally measured using a commercial free-space rotating-wave-plate polarimeter. A manual polarization controller was used to ensure that the DPC and the rotating-waveplate polarimeter registered the same polarization state. The output signals from the four detectors on the metasurface polarimeter were fed through an amplification circuit and measured in photoconductive mode. A microcontroller collected a 300-sample set from the four photo-detectors at a rate of 1 kHz. This sampling rate is limited only by the electronics. Approximately 25% of the input power is lost in the metasurface at 1550 nm due to absorption and scattering. A maximum of 0.4% of the total incoming power is scattered to each photodetector.

Optics EXPRESS

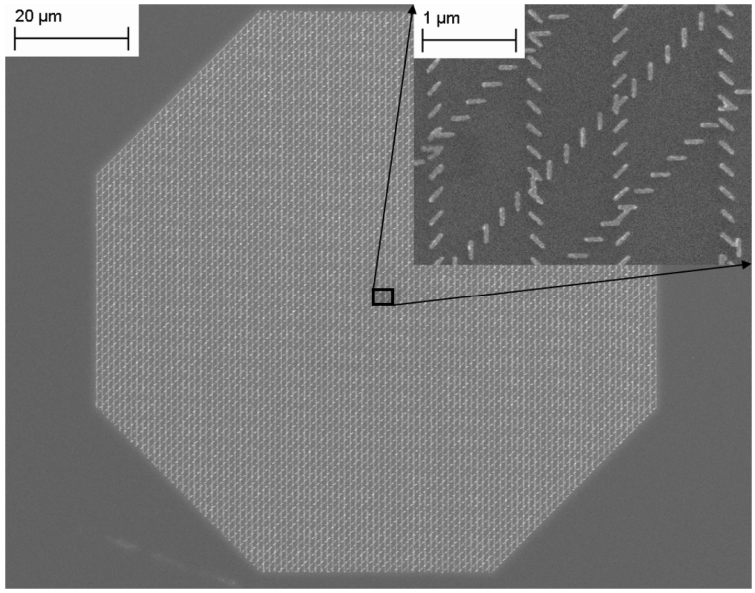

Fig. 6. Scanning electron micrograph (SEM) images of the fabricated metasurface showing the total metasurface structure. Inset: zoom-in of the metasurface displaying the individual antennas of the array.

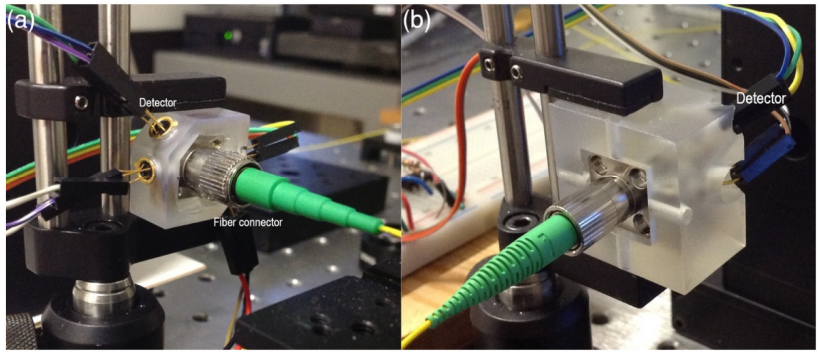

Fig. 7. Images of the in-plane metasurface polarimeter (a) and the out-of-plane polarimeter (b). The incident light enters each device through the optical fiber which is placed in contact with the sample perpendicular to the metasurface. The transmitted light exits through a hole in the back of the 3D holder. Four TO-canned photodiodes are glued into each holder.

Optics EXPRESS

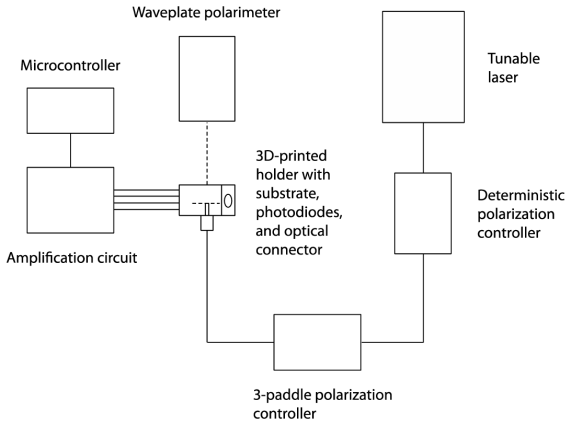

Fig. 8. A sketch of the experimental setup. Light from a tunable fiber laser is coupled through a standard single mode fiber to a deterministic polarization controller. A 3-paddle polarization controller corrects for polarization changes caused by the fiber. The optical connector is placed in contact with the sample by using half of a mating sleeve. A commercial polarimeter is placed behind the sample. Four photodiodes are fitted onto the sample holder and the measured signal is picked up by a microcontroller.

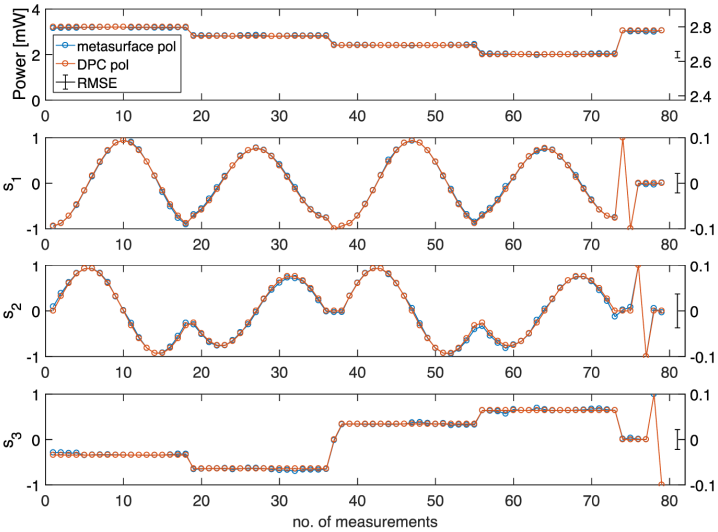

Fig. 9. Polarization measurements at 1550 nm using a device with in-plane design. Each subplot contains one element in the Stokes vector. The first subplot is the power of the incident light, which is proportional to S_0. The next three subplots are the parameters characterizing the state of polarization (SOP), s_1-s_3. The blue dots are the polarization measurements of the metasurface polarimeter, the red dots are the measurements of the deterministic polarization controller (DPC) for comparison. The error bar is the root mean square error (RMSE) giving a measure of the deviation between the two data set, note the 10x change in scale on the y-axes.

Optics EXPRESS

A number of polarization measurements were performed and the results were compared to the polarization state specified by the DPC, using the calibration procedure mentioned in Section 2 [22]. Each metasurface polarimeter was tested at several wavelengths. One set of measurements performed at a wavelength of 1550 nm is shown in Fig. 9 using a device with the in-plane design. Figure 10 shows the root-mean-square-error (RMSE) for both the in-plane and out-of-plane design at several wavelengths. In both cases, a design with antenna column spacing of $\lambda_0(1 + 1/8)$ was used. The device calibration was repeated for each wavelength, since the polarimeter response is substantially wavelength-dependent, as shown in Fig. 3. The same metasurface polarimeter design can therefore be applied across a wide range of wavelengths as long as the spectral information of the incident light source is known *a priori*. As seen in Fig. 11 the wavelength-dependence is quite strong indicating that broadband signals will be affected. Based on these measurements it will be necessary to include wavelength calibration of the polarimeter when wavelength and linewidth is not accurately known. Excellent agreement between the metasurface polarimeter and the DPC is observed. The deviations shown in the figures are not far from the stated accuracy of the state-of-the-art inline polarimeter (IPM5300) from Thorlabs (SOP: ± 0.25° from 1510 nm – 1640 nm). For comparison, Table 1 shows RMSE of the SOP in spherical coordinates for both in-plane and out-of-plane devices.

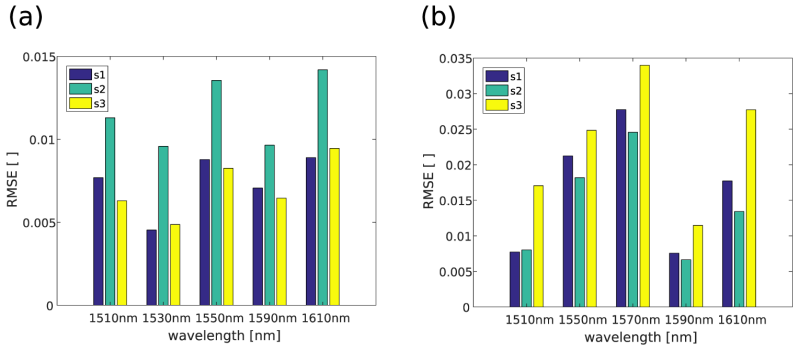

Fig. 10. Root-mean-square-error (RMSE) at wavelengths between 1510 nm and 1610 nm for the in-plane device (a) and the out-of-plane device (b). Each of the columns represents one state of polarization (SOP) parameter.

Table 1. Root-mean-square-error (RMSE) of state of polarization (SOP) parameters

In-Plane device		
λ (nm)	Azimuth error	Ellipticity error
1510	0.44°	0.23°
1550	0.48°	0.29°
1590	0.38°	0.23°
1610	0.54°	0.32°
Out-of-plane device		
1510	0.19°	0.56°
1550	0.81°	0.80°
1590	0.24°	0.39°
1610	0.58°	0.91°

Optics EXPRESS

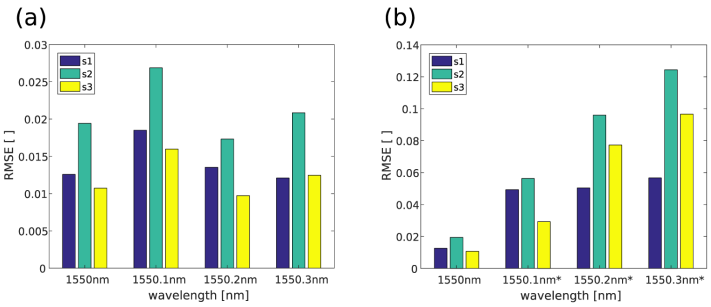

Fig. 11. Root-mean-square-error (RMSE) of each state of polarization (SOP) parameter at wavelengths between 1550.0 nm and 1550.3 nm for the in-plane device. In (a) the data of each wavelength is calibrated individually. (b) shows the same measurements with the difference that the calibration at 1550 nm is used on all four data set (the asterisks indicate the data set that are not calibrated individually).

For the out-of-plane device, about 75% of the scattered light intensity is insensitive to the incoming polarization. Therefore, this configuration is more sensitive to intensity than state of polarization. In other words, the S_0 parameter is more accurate than the s_1-s_3 parameters due to the fact that the intensity element in the analyzer vectors are larger than the SOP elements. Conversely, the in-plane device generally has a lower error on the SOP than the out-of-plane device, because of the better polarization-dependent contrast and the larger power to the detectors. The variation in error between measurements at different wavelengths is mainly caused by wavelength variations of the analyzer vectors.

In [26], the deviation of the analyzer vectors from the theoretically predicted values are very small. The four-output metasurface design, on the other hand, introduces much larger deviations, as seen in Fig. 12. Especially deviations caused by antenna interactions are expected to increase, due to the overlapping of multiple rows of nanoantennas. In order to eliminate this effect, it might be necessary to place two (or more) superimposed metasurfaces in different layers with a vertical spacing larger than the near-field interaction distance. As seen in Fig. 12, the actual analyzer vectors of the in-plane device are very close to each other on the Poincaré sphere. It is clear that a device with a basis for SOP space closer to the theoretically predicted values will yield a lower measurement error. Therefore, it is expected that with future design improvements, the accuracy of the metasurface polarimeter can be made substantially better.

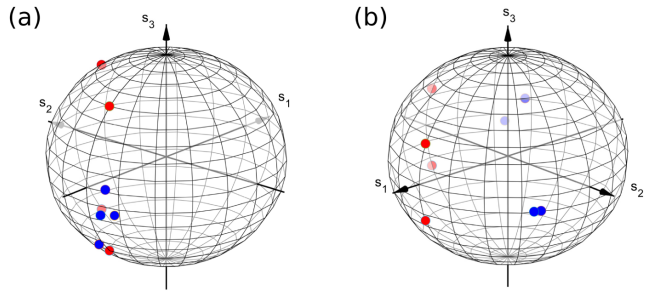

Fig. 12. Analyzer vector position on the Poincaré sphere for a device with (a) in-plane design and (b) out-of-plane design. The analyzer vectors are normalized to unit length. Red dots are the theoretically predicted positions. Blue dots are the measured positions.

Optics EXPRESS

4. Conclusion

We have demonstrated an in-line metasurface polarimeter design that relies on a simple and compact design consisting of only a single polarization-analyzing element and four photodetectors. As there is no need for optical elements between the metasurface and the photodetectors, low-cost fabrication of extremely compact polarimeter devices or device arrays is made possible. The accuracy of the metasurface polarimeter in the current design was shown to be close to commercial in-line polarimeters and further improvement of SOP accuracy is certainly possible, establishing the metasurface polarimeter as a fully viable alternative to existing solutions.

The current polarimeter design was demonstrated to work in the wavelength range 1510 nm – 1610 nm for both the in-plane and the out-of-plane designs. Experiments and simulations suggest that the out-of-plane design has a larger bandwidth. Also, it is better suited for practical applications because a larger metasurface area solves alignment problems without causing additional rescattering and absorption losses. The in-plane design offers a lower error, especially on the SOP.

In summary, our new polarimeter design promises excellent accuracy, compact design, potential for low-cost mass production, and the possibility of modifying the structure (in conjunction with suitable photodetectors) to address a wavelength range well beyond the one presently investigated.

Funding

Icelandic Research Fund (152098051); Air Force Office for Scientific Research (AFOSR) MURI Grant (FA9550-14-1-0389).

Paper II

Neural polarimeter and wavemeter

Einar B. Magnusson, J. P. Balthasar Mueller, Michael Juhl, Carlos Mendoza, and Kristjan Leosson

ACS Photonics, 5

ACS Photonics

Letter

Cite This: ACS Photonics 2018, 5, 2682−2687

Neural Polarimeter and Wavemeter

Einar B. Magnusson,[†,§] J. P. Balthasar Mueller,[†,‡,§] Michael Juhl,[†,∥] Carlos Mendoza,[†] and Kristjan Leosson*[,†,∥]

[†]Innovation Center Iceland, Arleynir 2-8, Reykjavik, Iceland

[‡]Harvard School of Engineering and Applied Science, Cambridge, Massachusetts 02138, United States

[∥]Science Institute, University of Iceland, Dunhagi 5, Reykjavik, Iceland

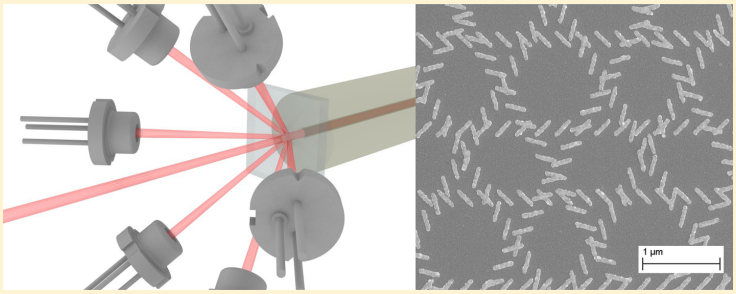

ABSTRACT: Numerous optical devices can be conveniently described in terms of a transfer function matrix formalism. An important example is the intensity-division Stokes polarimeter where four device outputs can be related to the four parameters of the Stokes vector using a linear 4 × 4 matrix transformation. In the present paper, we demonstrate how the functionality of such devices can be substantially enhanced by increasing the number of outputs and employing deep neural networks instead of the traditional linear algebra approach to establish correlations between device outputs and inputs. Specifically, we employ a neural network calibration of a metasurface-based intensity-division Stokes polarimeter with six outputs to accurately measure the four parameters of the Stokes vector of the input light across a much wider wavelength range than is afforded by a canonical linear transfer matrix model. Furthermore, the neural network model allows the device to determine the input wavelength from the measured data. We argue that nonlinear machine learning models used to fit calibration functions in this way are able to capture physical parameters that cannot be easily described using analytically derived models and that this approach is thus poised to improve the performance of a broad variety of optical sensors.

KEYWORDS: *Polarimetry, Integrated optics devices, Metamaterials, Neural networks*

Recent breakthroughs in machine learning (ML) techniques based on deep neural networks (DNNs) are transforming many information processing tasks, including unprecedented advances in game playing, computer vision and natural language translation.[1,2] At the same time, the basic concept of neural networks has found its way into optical technology two or three decades ago, with particularly striking applications falling into the realm of optical information processing (via an optical, rather than software, implementation of neural networks),[3,4] as well as into communications, imaging and spectroscopy.[5−7]

Artificial neural networks represent a subclass of computational architectures that include a large variety of nonlinear statistical models and learning methods, first originating in attempts to simulate the human brain.[8−10] The most widely used neural networks define a mapping between a set of input variables and a set of output variables, based on a sequence of linear transformations followed by nonlinear activation functions that form the layers of a network. It has been shown that neural networks with a single hidden layer are universal function approximators, i.e. they can approximate continuous functions on a compact space. How to learn this representation from data is a nontrivial subject and currently an active area of research. In the case of regression, where the task is to learn a functional mapping to a space of continuous target variables, the general approach is to define a cost function (most commonly mean squared error), and work toward minimizing the cost while at the same time controlling for overfitting. This is most often done using gradient descent algorithms, which in the context of artificial neural networks is known as backpropagation. Although neural networks and backpropagation methods have been studied for decades,[11] they have recently shown great success and potential due to increases in computing power and new techniques to make the model learning tractable, notably when the number of hidden layers is increased ("deep learning"). Previously, neural networks have been used for a variety of signal processing tasks

Received: March 5, 2018
Published: May 14, 2018

DOI: 10.1021/acsphotonics.8b00295
ACS Photonics 2018, 5, 2682−2687

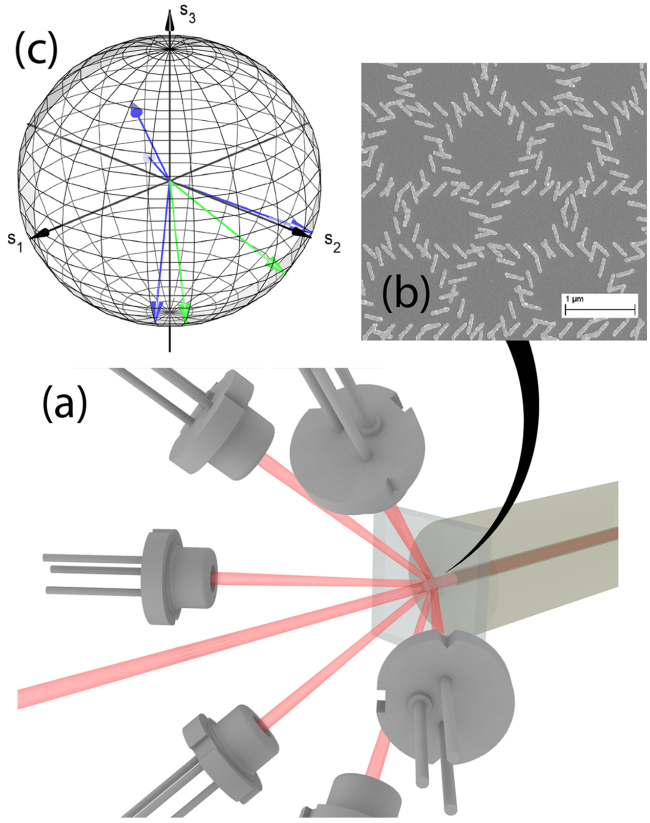

Figure 1. (a) Configuration of a 6-port metasurface polarimeter. Light exiting from the fiber passes through the metasurface layer where polarization-dependent scattering takes place into six out-of-plane directions. (b) The configuration of gold nanoantennas for realizing a 6-output metasurface polarimeter. (c) Orientation of the six experimentally determined device vectors depicted on the Poincaré sphere. The device vectors shown in blue were used for operating the device as a 4-output polarimeter.

based on sensor and imaging data,[12,13] including object recognition through diffuse media using speckle patterns.[14]

Traditionally in optical measurements, the reconstruction of relevant information in the input light field has frequently been carried out by determining the inverse of a transfer matrix **T** (also referred to as the device matrix, instrument matrix, analysis matrix or transmission matrix) that maps an input vector **S** to an output vector **I**, where the latter typically consists of a set of intensity measurements, i.e. $\mathbf{I} = \mathbf{TS}$.[15] The determination of the matrix inverse is nontrivial in the presence of experimental noise and the accuracy of the recovery of the original signal depends on the properties of the device vectors (rows of the device matrix).[16,17] Numerous examples of such transfer-matrix projections can be found in the literature.[16,18−25] Here, we will focus on intensity-division polarimeters as a convenient example of such projective optical devices.

Recently, we have developed a novel in-line fiber-coupled Stokes polarimeter that uses polarization-dependent scattering from a single metasurface to cast the Stokes vector of the input light into a number of intensity measurements.[26,27] Metasurfaces are essentially two-dimensional optical nanostructures that enable the tailoring of the amplitude, phase or polarization of light,[28] providing a promising platform for simplifying and miniaturizing existing optical components.[29,30] Generally speaking, a full Stokes polarimeter is a device that performs measurements of all four Stokes parameters describing the state and degree of polarization of electromagnetic waves as well as their intensity. This is achieved using either a wavefront-division, time-division or intensity-division approach.[31] An in-line polarimeter performs such measurements by using only a fraction of the light intensity to measure the full state of polarization, preferably without significantly perturbing the input polarization. In-line intensity-division polarimeters are especially important for polarization generation and polarization management in optical telecommunications. In order to demonstrate the capability of our neural network calibration model, we designed and fabricated a version of the metasurface polarimeter having six intensity outputs, thus creating a system where the dimensionality of the output vector exceeds the dimensionality of the input vector.

In our previous reports, a linear transformation was used to map four intensity measurements of a metasurface polarimeter back to the Stokes vector of the incoming light.[26] A distinct

DOI: 10.1021/acsphotonics.8b00295
ACS Photonics 2018, 5, 2682−2687

limitation of this approach is that the device matrix is highly wavelength-dependent.[27] Hence, polarization can only be accurately determined if the input wavelength is within approximately 0.1 nm of the calibration wavelength. This limitation can, in principle, be addressed by deploying a highly resolved look-up table containing device matrices for each wavelength, provided also that the input wavelength is known with sufficient accuracy. Given the potential size of such a table, and that wavelength information may not be available, a calibration method that enables wavelength-independent polarimetry within a given range is highly desirable. In the present paper we show that the combination of six-output measurement in a metasurface polarimeter and the use of DNNs can provide for such wavelength-independent measurements across our chosen range of 1530−1565 nm (telecom C-band). The DNN-calibrated device simultaneously provides a measurement of the polarization *and* the wavelength of the incident laser light, with a wavelength prediction accuracy matching the wavelength resolution of the training data set.

The fiber-coupled metasurface polarimeter (Figure 1(a)), consisting of an array of metal nanoantennas, was fabricated on a transparent substrate using a procedure described elsewhere.[27] An antenna configuration providing polarization-dependent scattering into six out-of-plane directions (Figure 1(b)) was used, yielding six device vectors. The orientation of the device vectors can be depicted on the Poincaré sphere as shown in Figure 1(c). The measurement setup (Figure 2)

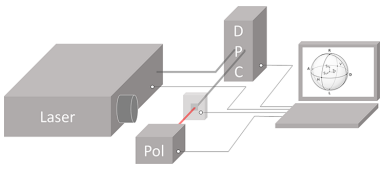

Figure 2. Measurement setup, including tunable laser, deterministic polarization controller, metasurface polarimeter and reference rotating waveplate polarimeter.

consisted of a tunable fiber-coupled laser, combined with a deterministic polarization controller (Thorlabs), producing light with tunable input polarization, power and wavelength. The metasurface was positioned at the output end of the fiber and surrounded by photodetectors, as illustrated schematically in Figure 1(a). The signal from the diodes was amplified and simultaneously sampled from all detectors, using a microcontroller. The device is signal-preserving in the sense that each photodetector samples less than 1% of the input signal and no internal manipulation of the input polarization is required. For reference, the light transmitted through the device was measured using a conventional time-division rotating-waveplate polarimeter (Thorlabs). The investigated wavelength range covered the full telecom C-band (1530−1565 nm) in steps of 0.2 nm. For each value of the incident wavelength, a set of 100 polarization measurements was collected; each corresponding to a random polarization state. In order to eliminate artificial correlations arising e.g. from polarization-dependent insertion loss to the fibers, or depolarization in the system, the laser power in the training set was randomized, varying between 1−3 mW. The setup was automated to allow rapid collection of the large data sets required for neural network training with the desired variation of input parameters. The full data set of 17,500 points was randomly split into training/validation/test sets in the ratio 3:1:1.

At a particular input wavelength, the underlying optical physics determines that the relationship between the Stokes vector and the metasurface outputs is given by a simple projection, which is a linear transformation. We therefore consider the accuracy of the polarization measurement obtained using the device matrix for a given wavelength to represent a benchmark of the irreducible error of the polarimeter device at that wavelength. This error is related to instrument noise and the configuration of the device vectors. We determine the reference device matrices from the full sets of measured polarization states at each input wavelength using standard methods.[27] For our neural network calibration we use neural networks with one or more hidden layers where each layer is fully connected, i.e. each node in a layer is defined by a linear combination of all the nodes in the previous layer. Every node in the hidden layers is activated with a nonlinear activation function. In our case, we empirically chose the exponential-linear unit (ELU), defined as[32]

$$\mathrm{ELU}(x) = \begin{cases} \alpha(e^x - 1), & \text{if } x < 0 \\ x, & \text{otherwise,} \end{cases} \quad (1)$$

with $\alpha = 1$, as this resulted in less noisy training curves than other commonly used activation functions. The models were trained using the ADAM optimization algorithm.[33]

The accuracy of Stokes vector predictions from the metasurface polarimeter using different calibration models is summarized in Figure 3. It shows the angular error of a single

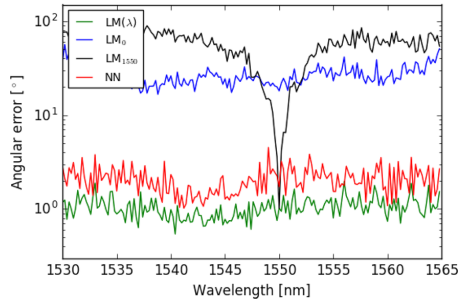

Figure 3. Comparison of the angular error of Stokes vector prediction using a linear transformation at each wavelength (LM(λ), green curve), a linear transformation without knowledge of wavelength (LM_0, blue curve), a linear model fitted at $\lambda = 1550$ nm (LM_{1550}, black curve), and a neural network with 7 hidden layers of 32 units each (NN, red curve).

linear model applied to data from the full wavelength range (blue curve) as well as a model where the device is calibrated only at $\lambda = 1550$ nm (black curve), compared to the result of using a separate linear model for each wavelength (green curve). Calibrating the device at a single wavelength only yields reliable results in a very narrow wavelength interval, while trying to generalize a single device matrix to the full wavelength range results in essentially random Stokes vector predictions from the measured data. The angular error obtained when a device matrix determined for each measured wavelength, on the other hand, is around 1°, representing the irreducible error for this particular metasurface, detector configuration, and

DOI: 10.1021/acsphotonics.8b00295
ACS Photonics 2018, 5, 2682−2687

measurement method. It should be noted that the present measurements were set up to allow rapid data collection. It is possible to realize a lower absolute error by using lower data sampling rates. The minimum absolute error of the metasurface polarimeter for slower sampling was observed to be about 50% lower than for the configuration used above and comparable to the minimum error of commercial in-line polarimeters (±0.25°).[27] Considering the large number of measurements required for the present study, a higher sampling rate was, however, preferred to avoid unsuitably long data collection times. This does not affect the relative comparison of accuracy in Stokes vector predictions between the different calibration methods.

For the neural-network-based calibration, we trained a neural network with 7 hidden layers of 32 units each, using data from the full wavelength range. This choice of parameters was based on an investigation of the hyperparameter space, as discussed below. The angular error obtained when applying the neural model to the test data is shown in Figure 3 (red curve). The average error in this case is about 2.1°, which is only a factor of 2 higher than the benchmark error. For simplicity, we restricted optimization to modifying only the number of hidden layers and number of units per layer of the network, even though a wide array of improvement techniques are known to the community.[10] The results obtained from each neural network configuration are compared in Figure 4. As the networks grow

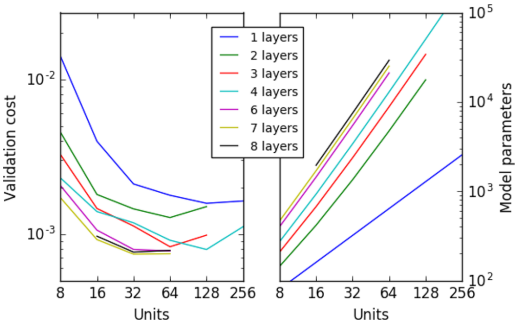

Figure 4. Optimizing neural network hyperparameters. Early stopping helps to avoid overfitting with high variance models, but the model performance saturates at around 7 hidden layers, 32 units per layer.

in layers and units, the models begin to overfit the training data. We address this by aborting the training process as soon as the loss on the validation set begins to increase with respect to the loss on the training set (known as "early stopping") . Between choosing a model with a reasonable amount of free parameters and good prediction performance, a model consisting of 7 hidden layers of 32 units was selected.

Although the metasurface polarimeter devices were designed to measure polarization only, we considered also whether their inherent wavelength dependence would allow a neural network to determine the wavelength of the incoming (monochromatic) light from the measured data, thus adding a wavemeter functionality to the polarimeter device. Similarly to before, we fitted a linear model and trained a neural network on the 6-port metasurface polarimeter data for this task. Results are shown in Figure 5, where a neural network with 3 hidden layers and 32 units per layer was used. The linear model (blue curve) can be seen to have an RMS error in wavelength prediction of 1−3

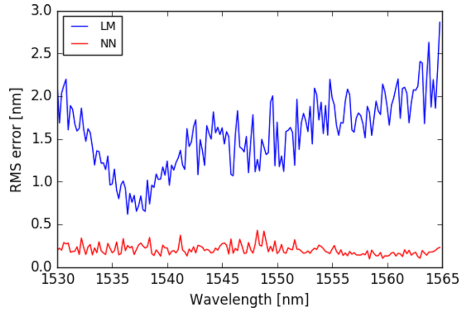

Figure 5. Comparison of wavelength modeling using a linear model (LM, blue curve) and a neural network (NN, red curve).

nm. The neural network model (red curve), on the other hand, performs an order of magnitude better, with an RMS error of 0.1−0.3 nm. It is worth mentioning that this error value is close to the wavelength spacing used in the training set (0.2 nm).

As mentioned before, one way of accurately calibrating the metasurface for a given wavelength range is to use a lookup table of linear calibrations at closely spaced wavelengths. This is, however, only useful when the wavelength of the measured light is known. Given that we can accurately determine the wavelength with a neural network model, this implies that we can also create a hybrid model by using the wavelength determined by the neural network to look up the corresponding linear calibration. The comparison of this hybrid model to the full neural network model and the linear calibration benchmark error is shown in Figure 6. The hybrid model, in fact, performs nearly as well as the full neural network model, with an average error of about 2.6°.

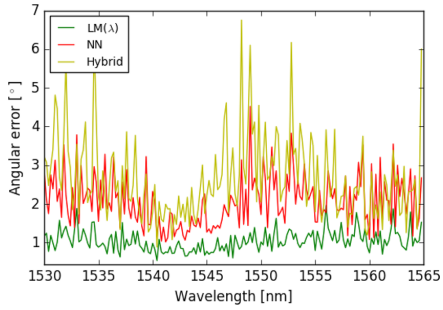

Figure 6. Comparison of Stokes vector modeling using a full neural network model (NN, red curve) and a hybrid one where the output of the wavelength neural network is used to look up the correct linear calibration (Hybrid, yellow curve). The irreducible error (LM(λ), green curve) from Figure 3 is shown for reference.

Our results show that 6-port metasurface polarimeters, calibrated using deep neural networks, provide an accuracy in the Stokes vector measurement close to the minimum device error *without a priori knowledge of the input wavelength*, in addition to accurately predicting the input wavelength (presupposing, in this case, a monochromatic input). In our previous work[26,27] we focused on the traditional four-output approach, where the four parameters of the Stokes vector are projected onto an output space of equal dimensionality, as

DOI: 10.1021/acsphotonics.8b00295
ACS Photonics 2018, 5, 2682−2687

mentioned above. In order to compare the neural network calibration approach on such devices with the performance of the 6-port devices reported here, we also tried limiting our neural network training to the 4 ports of the present device that gave the most precise linear calibration (blue arrows in Figure 1(c)), which is equivalent to training a neural network on the output of a 4-port device. We were not able to train a well-performing neural network for Stokes vector prediction in this case, but were in fact able to accurately measure input wavelength with a neural network calibration (albeit with significantly longer training time than for the 6-port data). This suggests that it could also be possible to accurately determine the Stokes vector using a neural network calibration with fewer than six intensity measurements, without knowledge of the incident wavelength. However, it is clear that using six (or possibly more) sufficiently independent outputs makes it significantly easier to train well-performing models.

In summary, we maintain that machine learning models, provided with a sufficient amount of calibration data, can be brought to interpret the input signals of an optical sensor in terms of functions that would be difficult or impossible to derive by hand. This can produce a much better approximation to the physics that determines the relationship between sensor input and output, but sacrifices an interpretable link between the physics and the calibration function. In case of the metasurface polarimeter, neural network models enabled us to ameliorate the high sensitivity of the polarimeter to discrepancies between the input and the calibration wavelength, and also to extend its functionality to act as a wavemeter. Our results demonstrate the potential for this type of machine learning in producing substantial performance improvements of even relatively simple optical systems that have previously been treated in terms of transfer function matrix formalism.

AUTHOR INFORMATION

Corresponding Author

*E-mail: kristjan.leosson@nmi.is. Phone: +354 5229000.

ORCID

Kristjan Leosson: 0000-0002-7897-5911

Author Contributions

§These authors contributed equally to this work. The manuscript was written through contributions of all authors. All authors have given approval to the final version of the manuscript. J.P.B.M. proposed the idea developed in this work. E.B.M. and J.P.B.M. developed the neural network algorithms. M.J. carried out the sample fabrication. E.B.M., C.M., and M.J. designed the setup for data collection and E.B.M. performed the optical characterization of the samples. E.B.M., J.P.B.M., and K.L. wrote the paper. K.L. supervised this work.

Notes

The authors declare no competing financial interest.

ACKNOWLEDGMENTS

The project was supported by the Icelandic Research Fund (152098-051) and the U.S. Air Force Office of Scientific Research (AFOSR) under MURI: FA9550-14-1-0389 and FA9550-16-1-0136.

REFERENCES

(1) Silver, D.; et al. Mastering the game of Go without human knowledge. *Nature* **2017**, *550*, 354−359.

(2) LeCun, Y.; Bengio, Y.; Hinton, G. Deep learning. *Nature* **2015**, *521*, 436−444.

(3) Yu, F. T.; Jutamulia, S. *Optical Signal Processing, Computing, And Neural Networks*; John Wiley and Sons, Inc., 1992.

(4) Woods, D.; Naughton, T. J. Optical computing: Photonic neural networks. *Nat. Phys.* **2012**, *8*, 257−259.

(5) Jun, J.; Kim, C. Robust camera calibration using neural network. *TENCON 99, Proceedings of the IEEE Region 10 Conference*; IEEE, 1999; pp 694−697.

(6) Long, J. R.; Gregoriou, V. G.; Gemperline, P. J. Spectroscopic calibration and quantitation using artificial neural networks. *Anal. Chem.* **1990**, *62*, 1791−1797.

(7) Giles, C. L.; Goudreau, M. W. Routing in optical multistage interconnection networks: A neural network solution. *J. Lightwave Technol.* **1995**, *13*, 1111−1115.

(8) Hastie, T.; Tibshirani, R.; Friedman, J. H. *The Elements of Statistical Learning: Data Mining, Inference, and Prediction*, 2nd ed.; Springer: New York, 2009; p 745.

(9) Friedman, J.; Hastie, T.; Tibshirani, R. *The Elements of Statistical Learning*, Springer Series in Statistics; Springer: New York, 2001; Vol. *1*.

(10) Goodfellow, I.; Bengio, Y.; Courville, A. *Deep Learning*; The MIT Press: Cambridge MA, 2016.

(11) Schmidhuber, J. Deep learning in neural networks: An overview. *Neural net.* **2015**, *61*, 85−117.

(12) Moraru, A.; Pesko, M.; Porcius, M.; Fortuna, C.; Mladenic, D. Using Machine Learning on Sensor Data. *J. Comput. Inf. Technol.* **2010**, *18*, 341.

(13) Xuan, J.; Klimach, U.; Zhao, H.; Chen, Q.; Zou, Y.; Wang, Y. Improved diagnostics using polarization imaging and artificial neural networks. *Int. J. Biomed. Imaging* **2007**, *2007*, 74143.

(14) Ando, T.; Horisaki, R.; Tanida, J. Speckle-learning-based object recognition through scattering media. *Opt. Express* **2015**, *23*, 33902.

(15) Azzam, R. Instrument matrix of the four-detector photopolarimeter: physical meaning of its rows and columns and constraints on its elements. *J. Opt. Soc. Am. A* **1990**, *7*, 87−91.

(16) Popoff, S. M.; Lerosey, G.; Fink, M.; Boccara, A. C.; Gigan, S. Controlling light through optical disordered media: Transmission matrix approach. *New J. Phys.* **2011**, *13*, 123021.

(17) Azzam, R. M. A.; De, A. Optimal beam splitters for the division-of-amplitude photopolarimeter. *J. Opt. Soc. Am. A* **2003**, *20*, 955−958.

(18) Choi, Y.; Yoon, C.; Kim, M.; Yang, T. D.; Fang-Yen, C.; Dasari, R. R.; Lee, K. J.; Choi, W. Scanner-free and wide-field endoscopic imaging by using a single multimode optical fiber. *Phys. Rev. Lett.* **2012**, *109*, 203901.

(19) Čižmár, T.; Dholakia, K. Exploiting multimode waveguides for pure fibre-based imaging. *Nat. Commun.* **2012**, *3*, 1027.

(20) Redding, B.; Liew, S. F.; Sarma, R.; Cao, H. Compact spectrometer based on a disordered photonic chip. *Nat. Photonics* **2013**, *7*, 746−751.

(21) Redding, B.; Popoff, S. M.; Cao, H. All-fiber spectrometer based on speckle pattern reconstruction. *Opt. Express* **2013**, *21*, 6584.

(22) Kolenderska, S. M.; Katz, O.; Fink, M.; Gigan, S. Scanning-free imaging through a single fiber by random spatio-spectral encoding. *Opt. Lett.* **2015**, *40*, 534.

(23) Morales-Delgado, E. E.; Farahi, S.; Papadopoulos, I. N.; Psaltis, D.; Moser, C. Delivery of focused short pulses through a multimode fiber. *Opt. Express* **2015**, *23*, 9109.

(24) Caravaca-Aguirre, A. M.; Piestun, R. Single multimode fiber endoscope. *Opt. Express* **2017**, *25*, 1656.

(25) Peinado, A.; Campos, J.; Lizana, A. Design of polarimeters based on liquid crystals and biaxial crystals for polarization metrology. *Opt. Pura Apl.* **2016**, *49*, 167−177.

(26) Mueller, J. P. B.; Leosson, K.; Capasso, F. Ultracompact metasurface in-line polarimeter. *Optica* **2016**, *3*, 42−47.

(27) Juhl, M.; Mendoza, C.; Mueller, J. P. B.; Capasso, F.; Leosson, K. Performance characteristics of 4-port in-plane and out-of-plane in-line metasurface polarimeters. *Opt. Express* **2017**, *25*, 28697.

DOI: 10.1021/acsphotonics.8b00295
ACS Photonics 2018, 5, 2682−2687

(28) Yu, N.; Capasso, F. Flat optics with designer metasurfaces. *Nat. Mater.* **2014**, *13*, 139−150.
(29) Yu, N.; Capasso, F. Optical metasurfaces and prospect of their applications including fiber optics. *J. Lightwave Technol.* **2015**, *33*, 2344−2358.
(30) Khorasaninejad, M.; Chen, W. T.; Devlin, R. C.; Oh, J.; Zhu, A. Y.; Capasso, F. Metalenses at visible wavelengths: Diffraction-limited focusing and subwavelength resolution imaging. *Science* **2016**, *352*, 1190−1194.
(31) Tyo, J. S.; Goldstein, D. L.; Chenault, D. B.; Shaw, J. A. Review of passive imaging polarimetry for remote sensing applications. *Appl. Opt.* **2006**, *45*, 5453−5469.
(32) Clevert, D.-A.; Unterthiner, T.; Hochreiter, S. Fast and Accurate Deep Network Learning by Exponential Linear Units (ELUs). *arXiv preprint arXiv:1511.07289* **2015**.
(33) Kingma, D. P.; Ba, J. L. Adam: a Method for Stochastic Optimization. *International Conference on Learning Representations 2015*; 2015, 1412.6980.

DOI: 10.1021/acsphotonics.8b00295
ACS Photonics 2018, 5, 2682−2687

Paper III

Polarization state generation and measurement with a single metasurface

Noah A. Rubin, Aun Zaidi, Michael Juhl, Ruo Ping Li, J.P. Balthasar Mueller, Robert C. Devlin, Kristján Leósson, and Federico Capasso

Optics Express, 26, 17

Research Article | Vol. 26, No. 17 | 20 Aug 2018 | OPTICS EXPRESS 21455

Optics EXPRESS

Polarization state generation and measurement with a single metasurface

NOAH A. RUBIN,[1] AUN ZAIDI,[2,3] MICHAEL JUHL,[4,5] RUO PING LI,[6] J.P. BALTHASAR MUELLER,[1] ROBERT C. DEVLIN,[1] KRISTJÁN LEÓSSON,[4,5] AND FEDERICO CAPASSO[1,*]

[1]*Harvard John A. Paulson School of Engineering and Applied Sciences, Harvard University, Cambridge, MA 02138, USA*
[2]*Harvard College, Cambridge, MA 02138, USA*
[3]*Department of Electrical Engineering and Computer Science, Massachusetts Institute of Technology, Cambridge, MA 02139, USA*
[4]*University of Iceland, 101 Reykjavik, Iceland*
[5]*Innovation Center Iceland, 112 Reykjavik, Iceland*
[6]*Department of Physics and Astronomy, University of Waterloo, Waterloo, ON N2L 3G1, Canada*
[*]*capasso@seas.harvard.edu*

Abstract: The constituent elements of metasurfaces may be designed with explicit polarization dependence, making metasurfaces a fascinating platform for new polarization optics. In this work we show that a metasurface grating can be designed to produce arbitrarily specified polarization states on a set of defined diffraction orders given that the polarization of the incident beam is known. We also demonstrate that, when used in a reverse configuration, the same grating may be used as a parallel snapshot polarimeter, requiring a minimum of bulk polarization optics. We demonstrate its use in measuring partially polarized light, and show that it performs favorably in comparison to a commercial polarimeter. This work is of consequence in any application requiring lightweight, compact, and low-cost polarization optics, polarimetry, or polarization imaging.

OCIS codes: (260.5430) Polarization; (230.5440) Polarization-selective devices; (160.3918) Metamaterials; (050.2555) Form birefringence; (050.2770) Gratings.

References and links

1. M. Born and E. Wolf, *Principles of Optics* (Cambridge University, 1999).
2. J. N. Damask, *Polarization Optics in Telecommunications* (Springer, 2005).
3. A. Yariv and P. Yeh, *Photonics: Optical Electronics in Modern Communications* (Oxford University, 2006).
4. J. S. Tyo, D. L. Goldstein, D. B. Chenault, and J. A. Shaw, "Review of passive imaging polarimetry for remote sensing applications." Appl. Opt. **45**, 5453–5469 (2006).
5. F. Snik, J. Craven-Jones, M. Escuti, S. Fineschi, D. Harrington, A. De Martino, D. Mawet, J. Riedi, and J. S. Tyo, "An overview of polarimetric sensing techniques and technology with applications to different research fields," Proc. SPIE **9099**, 90990B (2014).
6. P. Y. Deschamps, J. C. Buriez, F. M. Bréon, M. Leroy, A. Podaire, A. Bricaud, and G. Sèze, "The POLDER mission: instrument characteristics and scientific objectives," IEEE Trans. Geosci. Remote Sens. **32**, 598–615 (1994).
7. T. Novikova, A. Pierangelo, and A. De Martino, "Polarimetric imaging for cancer diagnosis and staging," Opt. Photonics News **23**, 26–33 (2012).
8. A. Pierangelo, A. Nazac, A. Benali, P. Validire, H. Cohen, T. Novikova, B. H. Ibrahim, S. Manhas, C. Fallet, M.-R. Antonelli, and A.-D. Martino, "Polarimetric imaging of uterine cervix: a case study," Opt. Express **21**, 14120–14130 (2013).
9. J. Trujillo-Bueno, F. Moreno-Insertis, F. Sanchez, E. Landi Degl'Innocenti, J. O. Stenflo, G. Mathys, R. Antonucci, R. Blandford, E. Agol, A. Broderick, J. Heyl, L. Koopmans, H.-W. Lee, M. Elitzur, R. H. Hildebrand, and C. U. Keller, *Astrophysical Spectropolarimetry* (Cambridge University, 2002).
10. S. J. Wiktorowicz and G. P. Laughlin, "Toward the detection of exoplanet transits with polarimetry," Astrophys. J. **795**, 12 (2014).
11. J. O. Stenflo, *Instrumentation for Solar Polarimetry* (Springer Netherlands, Dordrecht, 1994), pp. 312–350.
12. R. M. A. Azzam, "Stokes-vector and Mueller-matrix polarimetry," J. Opt. Soc. Am. A **33**, 1396–1408 (2016).

#327946 https://doi.org/10.1364/OE.26.021466
Journal © 2018 Received 20 Apr 2018; revised 15 Jul 2018; accepted 16 Jul 2018; published 6 Aug 2018

Optics EXPRESS

13. R. M. A. Azzam, "Division-of-amplitude photopolarimeter (DOAP) for the simultaneous measurement of all four Stokes parameters of light," J. Mod. Opt. **29**, 685–689 (1982).
14. R. M. A. Azzam and K. A. Giardina, "Photopolarimeter based on planar grating diffraction," J. Opt. Soc. Am. A **10**, 1190–1196 (1993).
15. Y. Cui and R. M. A. Azzam, "Sixteen-beam grating-based division-of-amplitude photopolarimeter," Opt. Lett. **21**, 89–91 (1996).
16. W. Shurcliff, *Polarized Light: Production and Use* (Harvard University, 1962).
17. N. Yu, P. Genevet, M. A. Kats, F. Aieta, J. P. Tetienne, F. Capasso, and Z. Gaburro, "Light propagation with phase discontinuities: generalized laws of reflection and refraction," Science **334**, 333–337 (2011).
18. A. Arbabi, Y. Horie, M. Bagheri, and A. Faraon, "Dielectric metasurfaces for complete control of phase and polarization with subwavelength spatial resolution and high transmission," Nat. Nanotechnol. **10**, 937–943 (2015).
19. J. P. B. Mueller, N. A. Rubin, R. C. Devlin, B. Groever, and F. Capasso, "Metasurface polarization optics: independent phase control of arbitrary orthogonal states of polarization," Phys. Rev. Lett. **118**, 113901 (2017).
20. J. P. B. Mueller, K. Leosson, and F. Capasso, "Ultracompact metasurface in-line polarimeter," Optica **3**, 42–47 (2016).
21. M. Juhl, C. Mendoza, J. P. B. Mueller, F. Capasso, and K. Leosson, "Performance characteristics of 4-port in-plane and out-of-plane in-line metasurface polarimeters," Opt. Express **25**, 28697–28709 (2017).
22. A. Pors, M. G. Nielsen, and S. I. Bolzhevolnyi, "Plasmonic metagratings for simultaneous determination of Stokes parameters," Optica **2**, 716–723 (2015).
23. A. Pors and S. I. Bozhevolnyi, "Waveguide metacouplers for in-plane polarimetry," Phys. Rev. Appl. **5**, 1–9 (2016).
24. W. T. Chen, P. Török, M. R. Foreman, C. Y. Liao, W.-Y. Tsai, P. R. Wu, and D. P. Tsai, "Integrated plasmonic metasurfaces for spectropolarimetry," Nanotechnology **27**, 224002 (2016).
25. F. Ding, A. Pors, Y. Chen, V. A. Zenin, and S. I. Bozhevolnyi, "Beam-size-invariant spectropolarimeters using gap-plasmon metasurfaces," ACS Photonics **4**, 943–949 (2017).
26. S. Wei, Z. Yang, and M. Zhao, "Design of ultracompact polarimeters based on dielectric metasurfaces," Opt. Lett. **42**, 1580–1583 (2017).
27. F. Afshinmanesh, J. S. White, W. Cai, and M. L. Brongersma, "Measurement of the polarization state of light using an integrated plasmonic polarimeter," Nanophotonics **1**, 125–129 (2012).
28. F. Gori, "Measuring Stokes parameters by means of a polarization grating," Opt. Lett. **24**, 584–586 (1999).
29. G. Cincotti, "Polarization gratings: design and applications," IEEE J. Quantum Electron. **39**, 1645–1652 (2003).
30. F. Xu, J. E. Ford, and Y. Fainman, "Polarization-selective computer-generated holograms: design, fabrication, and applications," Appl. Opt. **34**, 256–266 (1995).
31. J. Tervo and J. Turunen, "Paraxial-domain diffractive elements with 100% efficiency based on polarization gratings," Opt. Lett. **25**, 785–786 (2000).
32. J. A. Davis, J. Adachi, C. R. Fernández-Pousa, and I. Moreno, "Polarization beam splitters using polarization diffraction gratings." Opt. Lett. **26**, 587–589 (2001).
33. C. Menzel, C. Rockstuhl, and F. Lederer, "Advanced Jones calculus for the classification of periodic metamaterials," Phys. Rev. A **82**, 053811 (2010).
34. L. A. Romero and F. M. Dickey, "Theory of optimal beam splitting by phase gratings. I. One-dimensional gratings," J. Opt. Soc. Am. A **24**, 2296–2312 (2007).
35. R. C. Devlin, M. Khorasaninejad, W.-T. Chen, J. Oh, and F. Capasso, "Broadband high-efficiency dielectric metasurfaces for the visible spectrum," Proc. Natl. Acad. Sci. **113**, 10473–10478 (2016).
36. D. S. Sabatke, M. R. Descour, E. L. Dereniak, W. C. Sweatt, S. A. Kemme, and G. S. Phipps, "Optimization of retardance for a complete Stokes polarimeter," Opt. Lett. **25**, 802–804 (2000).
37. J. S. Tyo, "Design of optimal polarimeters: maximization of signal-to-noise ratio and minimization of systematic error." Appl. Opt. **41**, 619–630 (2002).
38. R. M. A. Azzam and A. G. Lopez, "Accurate calibration of the four-detector photopolarimeter with imperfect polarizing optical elements," J. Opt. Soc. Am. A **6**, 1513–1521 (1989).
39. R. M. A. Azzam, "Arrangement of four photodetectors for measuring the state of polarization of light." Opt. Lett. **10**, 309–311 (1985).
40. A. Asensio Ramos and M. Collados, "Error propagation in polarimetric demodulation," Appl. Opt. **47**, 2541–2549 (2008).
41. E. Wolf, *Introduction to the Theory of Coherence and Polarization of Light* (Cambridge University, 2007).
42. A. Lizana, I. Estévez, F. A. Torres-Ruiz, A. Peinado, C. Ramirez, and J. Campos, "Arbitrary state of polarization with customized degree of polarization generator," Opt. Lett. **40**, 3790–3793 (2015).
43. H. G. Berry, G. Gabrielse, and A. E. Livingston, "Measurement of the Stokes parameters of light." Appl. Opt. **16**, 3200–3205 (1977).
44. L. A. Romero and F. M. Dickey, "The mathematical theory of laser beam-splitting gratings," Prog. Opt. **54**, 319–386 (2009).
45. J. S. Jensen and O. Sigmund, "Topology optimization for nano-photonics," Laser Photonics Rev. **5**, 308–321 (2011).
46. D. Sell, J. Yang, S. Doshay, R. Yang, and J. A. Fan, "Large-angle, multifunctional metagratings based on freeform multimode geometries," Nano Lett. **17**, 3752–3757 (2017).
47. J. Yang and J. A. Fan, "Topology-optimized metasurfaces: impact of initial geometric layout," Opt. Lett. **42**, 3161–3164

Optics EXPRESS

(2017).
48. Z. Lin, B. Groever, F. Capasso, A. W. Rodriguez, and M. Lončar, "Topology-optimized multilayered metaoptics," Phys. Rev. Appl. **9**, 044030 (2018).
49. T. Todorov, L. Nikolova, and N. Tomova, "Polarization holography. 1: A new high-efficiency organic material with reversible photoinduced birefringence." Appl. Opt. **23**, 4309–4312 (1984).
50. L. Nikolova and P. Ramanujam, *Polarization Holography* (Cambridge University, 2009).
51. Z. Bomzon, G. Biener, V. Kleiner, and E. Hasman, "Spatial Fourier-transform polarimetry using space-variant subwavelength metal-stripe polarizers," Opt. Lett. **26**, 1711–1713 (2001).
52. Z. Bomzon, G. Biener, V. Kleiner, and E. Hasman, "Real-time analysis of partially polarized light with a space-variant subwavelength dielectric grating." Opt. Lett. **27**, 188–190 (2002).
53. T. Todorov and L. Nikolova, "Spectrophotopolarimeter: fast simultaneous real-time measurement of light parameters," Opt. Lett. **17**, 358–359 (1992).
54. Z. Bomzon, V. Kleiner, and E. Hasman, "Pancharatnam-Berry phase in space-variant polarization-state manipulations with subwavelength gratings." Opt. Lett. **26**, 1424–1426 (2001).
55. E. Hasman, Z. Bomzon, A. Niv, G. Biener, and V. Kleiner, "Polarization beam-splitters and optical switches based on space-variant computer-generated subwavelength quasi-periodic structures," Opt. Commun. **209**, 45–54 (2002).
56. E. Hasman, G. Biener, A. Niv, and V. Kleiner, "Space-variant polarization manipulation," Prog. Opt. **47**, 215–289 (2005).
57. J. A. Davis, I. Moreno, M. M. Sánchez-López, K. Badham, J. Albero, and D. M. Cottrell, "Diffraction gratings generating orders with selective states of polarization," Opt. Express **24**, 907–917 (2016).
58. A. Cofré, A. Vargas, F. A. Torres-Ruiz, J. Campos, A. Lizana, M. del Mar Sánchez-López, and I. Moreno, "Quantitative performance of a polarization diffraction grating polarimeter encoded onto two liquid-crystal-on-silicon displays," Opt. Laser Technol. **96**, 219–226 (2017).
59. A. G. Andreou and Z. K. Kalayjian, "Polarization imaging: Principles and integrated polarimeters," IEEE Sens. J. **2**, 566–576 (2002).
60. G. P. Nordin, J. T. Meier, P. C. Deguzman, and M. W. Jones, "Micropolarizer array for infrared imaging polarimetry," J. Opt. Soc. Am. A **16**, 1168–1174 (1999).
61. D. A. LeMaster and K. Hirakawa, "Improved microgrid arrangement for integrated imaging polarimeters." Opt. Lett. **39**, 1811–1814 (2014).
62. I. J. Vaughn, A. S. Alenin, and J. Scott Tyo, "Focal plane filter array engineering I: rectangular lattices," Opt. Express **25**, 11954–11968 (2017).
63. W.-L. Hsu, G. Myhre, K. Balakrishnan, N. Brock, M. Ibn-Elhaj, S. Pau, K. M. Twietmeyer, R. A. Chipman, A. E. Elsner, Y. Zhao, and D. VanNasdale, "Full-Stokes imaging polarimeter using an array of elliptical polarizer," Opt. Express **22**, 3063–3074 (2014).
64. C. Oh and M. J. Escuti, "Achromatic diffraction from polarization gratings with high efficiency." Opt. Lett. **33**, 2287–2289 (2008).
65. J. Kim, Y. Li, M. N. Miskiewicz, C. Oh, M. W. Kudenov, and M. J. Escuti, "Fabrication of ideal geometric-phase holograms with arbitrary wavefronts," Optica **2**, 958–964 (2015).
66. M. W. Kudenov, M. J. Escuti, E. L. Dereniak, and K. Oka, "White-light channeled imaging polarimeter using broadband polarization gratings," Appl. Opt. **50**, 2283–2293 (2011).
67. M. W. Kudenov, M. J. Escuti, N. Hagen, E. L. Dereniak, and K. Oka, "Snapshot imaging Mueller matrix polarimeter using polarization gratings," Opt. Lett. **37**, 1367–1369 (2012).
68. C. F. LaCasse, B. J. Redman, M. W. Kudenov, and J. M. Craven, "Maximum bandwidth snapshot channeled imaging polarimeter with polarization gratings," Proc. SPIE **9853**, 98530U (2016).
69. R. A. Chipman, *Handbook of Optics: Volume I: Geometrical and Physical Optics, Polarized Light, Components and Instruments* (McGraw-Hill, 2010), chap. 15.

1. Introduction

Polarization holds a role of paramount importance in countless areas of science and technology, in areas as diverse as atomic physics and fundamental light/matter interaction [1], fiber-optic telecommunications [2, 3], and polarization-resolved imaging [4, 5]. The latter has found application in remote sensing [4], aerosol characterization [6], non-invasive cancer pathology [7,8], and astrophysics [9–11]. Methods of producing and measuring polarized light, then, are of significant scientific and technological interest.

Polarization measurement is known as polarimetry [12]. Stokes polarimetry in particular refers to the determination of the full, four-component polarization Stokes vector $\vec{S} = \begin{pmatrix} S_0 & S_1 & S_2 & S_3 \end{pmatrix}^T$, which quantifies the shape and orientation of the polarization ellipse as well as the beam's intensity and degree of polarization. Polarization generation and analysis are conjugate — any configuration of polarization optics serving as a polarization state

Optics EXPRESS

generator may be an analyzer, if used in reverse. If an unknown Stokes vector $\vec{S}_{\text{inc}}$ is incident on an analyzer, a detector would observe, as a consequence of this symmetry, $I_{\text{meas}} \propto \vec{S}_a \cdot \vec{S}_{\text{inc}}$, where $\vec{S}_a$ is the characteristic polarization of the analyzer. Polarimetry amounts to several such projective measurements of the Stokes vector (Fig. 1(f)). This is formalized in the matrix equation

$$A\vec{S}_{\text{inc}} = \vec{I}. \tag{1}$$

A is an $N \times 4$ matrix known as the instrument matrix, $\vec{S}_{\text{inc}}$ is an incident Stokes vector, and $\vec{I}$ is a list of N measured intensities. A links the Stokes vector to N measured intensities $\vec{I}$ on N analyzer channels. In the special case where $N = 4$ we can write $\vec{S}_{\text{inc}} = A^{-1}\vec{I}$ (in the over-determined case $N > 4$, one finds a least-squares solution for $\vec{S}_{\text{inc}}$) [12].

Several broad categories of Stokes polarimeters exist, varying in how these N projective measurements are implemented. In the division-of-time approach, measurements are taken sequentially as a configuration of polarization optics changes. While this reduces the number of necessary components, time resolution is limited by the speed at which the polarization optics may be readjusted, representing a handicap (especially in the case of mechanical rotation). Active polarization optics such as liquid-crystal variable retarders ameliorate this somewhat, though here too, time resolution is limited to the ms range at great expense [5]. In the division-of-amplitude (also known as parallel, or snapshot) approach, on the other hand, the beam is divided among N parallel channels each of which contains a different analyzer. This may be accomplished by the use of birefringent (e.g., Wollaston) prisms and beamsplitters [13] or by employing a diffraction grating to split the beam into N orders containing unique polarization optics and a detector [14,15]. Division-of-amplitude is desirable because its time-resolution is detector-limited with no moving parts. This, however, requires distinct polarization optics on each channel, increasing complexity and bulk.

The basic units of these polarization optics (in free space, at least) are polarizers and phase retarders (waveplates). Retarders most commonly take the form of bulk bi/uniaxial crystals whose birefringent properties allow for polarization conversion; these led to the original discovery of light's polarization. These plates are, however, difficult to manufacture and process and challenging to integrate [2,16].

Meanwhile, metasurfaces [17] — that is, subwavelength-spaced arrays of nanophotonic phase-shifting elements — have attracted significant interest and hold promise for miniaturization of a variety of bulk optics. The elements comprising a metasurface may possess tailored structural birefringence making metasurfaces a fascinating platform for new polarization optics [18,19].

Here, we present a scheme for the design of a metasurface grating that, when light of a known polarization is incident, may produce arbitrarily specified states of polarization in parallel on its orders (Fig. 1(a)) in the visible spectral region. We experimentally characterize two metasurface gratings designed with this scheme. The same grating, by the symmetry described above, may act as a parallel full-Stokes polarimeter requiring no bulk birefringent optics. We characterize such a polarimeter and compare its performance to a commercial rotating-waveplate instrument. In contrast to previous work by us [20,21] on terminating polarimeters and by others [22–27] on a variety of metasurface/metamaterial-based schemes, the present work allows for the generation and analysis of polarization on channels whose polarizations may themselves be arbitrarily specified, demonstrates *full*-Stokes vector determination (including partially polarized light), and provides a quantitative error analysis. As such, it is of consequence for any application requiring low-cost, easily integrated polarimetry or polarization imaging and is a testament to the flexibility of metasurfaces in the realm of polarization optics.

Optics EXPRESS

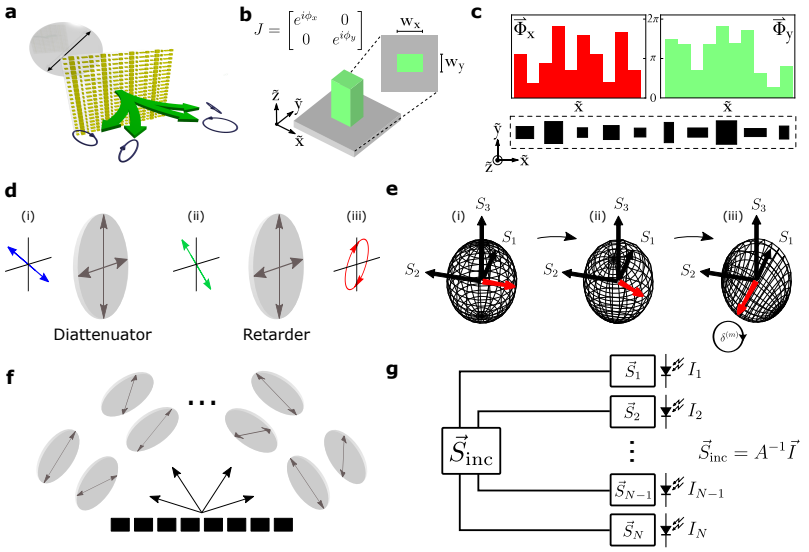

Fig. 1. **a**, Conceptual schematic: A metasurface diffraction grating can be designed to produce arbitrarily specified polarization states on its diffraction orders. The same device can also act as a parallel polarimeter. **b**, Such a metasurface is composed of pillar-like phase-shifting elements with two perpendicular mirror symmetry axes (e.g., rectangles) whose orthogonal dimensions w_x and w_y may be adjusted to allow for independent and tailorable phase delays ϕ_x and ϕ_y on x- and y-polarized light. **c**, If Q such elements of varying dimensions are arranged into a periodic unit cell along the $\tilde{x}$ direction, we form a 1D diffraction grating. At each point in the unit cell, constant phases are imparted on x- and y-polarized light. We may then describe the phase profiles experienced by these polarizations in the form of Q-vectors $\vec{\Phi}_x$ and $\vec{\Phi}_y$. **d**, The action of each diffraction order is equivalent to a bulk optic cascade of a diattenuator and a phase retarder, each oriented along x/y. **e**, The Poincaré sphere aids in understanding the behavior of the diffraction order for general input polarization. A standard Poincaré sphere (left) represents the set of all possible incident polarizations. After the beam passes through the diattenuator, the sphere is distorted along the S_1 axis according to the extinction ratio of the diattenuator (center). Finally, the phase retarder enacts a precession of the sphere along the S_1 axis by an angle equal to its retardance $\delta^{(m)}$ (right). The red arrows depict the corresponding polarization states in (d). Note also that the power of the output beam is polarization-dependent (not shown). **f**, The functionality contained in a single metasurface (c) would require, most generally, a two birefringent plates on each order in addition to a grating. **g**, Conceptually, polarimetry amounts to several projective measurements of an incident Stokes vector, $\vec{S}_{\text{inc}}$, onto a number of analysis Stokes vectors $\{\vec{S}_n\}$. If the analysis vectors are known and linearly independent, $\vec{S}_{\text{inc}}$ can be recovered.

2. Principle of operation

Space-variant polarization optics have long been a subject of investigation (as we discuss in Section 6.4) [28–32]. In the context of metasurfaces, a subwavelength element with two perpendicular symmetry axes [33] (e.g., a rectangle, but far from the only example) can function as a waveplate-like phase shifter, imparting independent phase shifts ϕ_x and ϕ_y on x- and y-polarized light [18, 19]. The values of ϕ_x and ϕ_y may be arbitrarily and independently adjusted

Optics EXPRESS

between 0 and 2π by changing the element's perpendicular dimensions w_x and w_y (Fig. 1(b)). If Q such birefringent phase shifters are arranged with subwavelength spacing in a 1D grating unit cell (Fig. 1(c)), we can denote the phase shift experienced by x-polarized light at the q^{th} position in the unit cell by $\phi_x^{(q)}$. That is, we may approximate the phase shift acquired by the wavefront at each position in the unit cell as constant. This discrete phase function $\phi_x(\tilde{x})$ experienced by x-polarized light, as a function of the spatial coordinate $\tilde{x}$ (not to be confused with x-polarized light), can be written as a vector, $\vec{\Phi}_x = \{\phi_x^{(1)}, ..., \phi_x^{(Q)}\}$ with $\vec{\Phi}_y$ holding an analogous meaning for y-polarized light. If the unit cell is tessellated we form a metasurface phase grating implementing independent and arbitrary periodic phase profiles for orthogonal x and y polarizations.

Being periodic, the grating's angular spectrum is discrete. Given the phase profiles $\phi_x(\tilde{x})$ and $\phi_y(\tilde{x})$ (which are contained in $\vec{\Phi}_x$ and $\vec{\Phi}_y$), we may compute the Fourier series of each phase grating. The projection onto grating order m is given by

$$c_x^{(m)} = \langle m|e^{i\phi_x(\tilde{x})}\rangle = \frac{1}{2\pi}\int_0^d e^{i\phi_x(\tilde{x})}e^{i\frac{2\pi m\tilde{x}}{d}}d\tilde{x} \tag{2}$$

and

$$c_y^{(m)} = \langle m|e^{i\phi_y(\tilde{x})}\rangle = \frac{1}{2\pi}\int_0^d e^{i\phi_y(\tilde{x})}e^{i\frac{2\pi m\tilde{x}}{d}}d\tilde{x} \tag{3}$$

where d is the length of the periodic unit cell and $\{c_x^{(m)}\}$ and $\{c_y^{(m)}\}$ are the Fourier coefficients of the gratings experienced by x and y polarizations, respectively.

Each coefficient is in general complex, so we may write $c_x^{(m)} = |c_x^{(m)}|e^{i\delta_x^{(m)}}$ and $c_y^{(m)} = |c_y^{(m)}|e^{i\delta_y^{(m)}}$. Then, we can ascribe to each order a Jones matrix $J^{(m)}$:

$$J^{(m)} = \begin{pmatrix} c_x^{(m)} & 0 \\ 0 & c_y^{(m)} \end{pmatrix} = \begin{pmatrix} |c_x^{(m)}| & 0 \\ 0 & |c_y^{(m)}| \end{pmatrix}\begin{pmatrix} e^{i\delta_x^{(m)}} & 0 \\ 0 & e^{i\delta_y^{(m)}} \end{pmatrix}. \tag{4}$$

The polarization properties of order m contained in $J^{(m)}$ may be seen as equivalent to a cascade of two bulk optical elements (Fig. 1(d)): the first Jones matrix in the product is that of a diattenuator—that is, an imperfect polarizing element selectively attenuating light along the x and y directions, while the second Jones matrix is that of a phase retarder — a waveplate — with retardance $\delta^{(m)} = \delta_x^{(m)} - \delta_y^{(m)}$. Both have their eigenaxes mutually oriented along x and y (Fig. 1(d)).

If, for instance, a beam linearly polarized at 45° with electric field amplitude E_0 is incident on the grating, the electric field on the m^{th} grating order will be

$$\vec{E}^{(m)} = \frac{E_0}{\sqrt{2}}\begin{pmatrix} c_x^{(m)} \\ c_y^{(m)} \end{pmatrix}. \tag{5}$$

In the special case of 45° polarized light, then, the complex grating coefficients $\{c_x^{(m)}\}$ and $\{c_y^{(m)}\}$ directly yield the polarization state of order m without any further transformation. For a general input polarization, the output polarization state on each order can be understood with aid of the Poincaré sphere (Fig. 1(e), see caption).

3. Optimization

Given a grating with known $\vec{\Phi}_x$ and $\vec{\Phi}_y$ and an incident beam of known polarization, the polarization state and power on each diffraction order m can be computed with simple Fourier optics. Conversely, can one deduce the $\vec{\Phi}_x$ and $\vec{\Phi}_y$ producing diffraction orders with specified states of polarization, for a given incident polarization? This would allow for the straightforward

Optics EXPRESS

engineering of such gratings, embedding in a single monolithically integrated metasurface a functionality that would otherwise require, in the most general case, an ordinary diffraction grating with $2P$ birefringent crystalline waveplates, where P is the number of diffraction orders to be controlled (Fig. 1(f)).

Suppose that for each diffraction order in a set $\{\ell\}$ we specify desired output polarization states. These polarizations directly dictate $\{c_x^m\}$ and $\{c_y^m\}$, the required Fourier coefficients. The requisite gratings for x and y polarizations could then be found by simply inverting the Fourier transform. However, being the sum of many spatial harmonics of the grating, this solution would require both amplitude and phase variation. In the realm of metasurfaces, this is undesirable. One generally hopes to obtain a range of phase-shifter geometries with nearly uniform amplitude transmission that yield phase shifts ranging between 0 and 2π [18]. It is generally difficult — at least, drawing from a limited set of possible geometries of simple design — to assemble a library of structures yielding arbitrarily shape-tunable phase shift *and* transmission. In the present case, we would require that this be achievable for both x and y polarizations, simultaneously and independent of one another. This is, without resorting to a very large range of simulated geometries, untenable. Moreover, an amplitude grating will inherently have lower transmission.

A phase-only grating addresses both issues. A phase-only grating, however, may only possess one or infinitely many diffraction orders, so the exact solution cannot in general be phase-only [34]. We must resort to optimization in order to concentrate as much diffracted light in the orders of interest while generating the desired polarization states.

More formally, we wish to design a grating that, when light linearly polarized at 45° is incident, produces desired polarization states on a set of grating orders $\{\ell\}$. The target Jones vector on each order $m \in \{\ell\}$ is given as

$$\vec{j}^{(m)} = \begin{pmatrix} \cos\chi^{(m)} \\ \sin\chi^{(m)} e^{i\phi^{(m)}} \end{pmatrix}. \tag{6}$$

Light will generally be diffracted into all orders, not just those in $\{\ell\}$. In order to direct as much of the incident power as possible into these desired orders, we seek to maximize

$$\eta(\vec{\Phi}_x, \vec{\Phi}_y) = \sum_{m\in\{\ell\}} \left(|c_x^{(m)}|^2 + |c_y^{(m)}|^2 \right) \tag{7}$$

under the constraints

$$\frac{|c_y^{(m)}|}{|c_x^{(m)}|} = \tan\chi^{(m)} \tag{8}$$

and

$$\delta_x^{(m)} - \delta_y^{(m)} = \phi^{(m)}. \tag{9}$$

The constraints provide for the desired polarization on each order, and the phase profile vectors $\vec{\Phi}_x$ and $\vec{\Phi}_y$ are the quantities to be optimized. If the grating has Q constituent elements, the optimization will involve $2Q$ parameters. Q and the inter-element separation dictate the grating period d which, along with the operating wavelength λ, specifies the angular separation of the grating orders. Once optimized $\vec{\Phi}_x$ and $\vec{\Phi}_y$ are obtained, the power in the desired orders and correspondence with the target polarization can be mathematically evaluated (cf. Eqns. (7), (8), and (9)).

We perform a simple gradient descent optimization of $\eta(\vec{\Phi}_x, \vec{\Phi}_y)$ under the above constraints with randomly generated initial conditions (Fig. 2(a)). This is a purely mathematical exercise and is independent of any particular material implementation or wavelength. Once optimized $\{\vec{\Phi}_x, \vec{\Phi}_y\}$ are found, the geometries of appropriate phase shifters can be located from a library of simulated structures, once the operating wavelength and desired material platform are specified.

Optics EXPRESS

While the essence of this work is wavelength-independent, in this work we use rectangular TiO_2 pillar structures for operation at $\lambda = 532$ nm, owing to the scientific and technological ubiquity of the visible range. The optimization scheme as presented above assumes that each phase shifter has a uniform amplitude transmission. In our library of simulated structures, the transmission does vary, an effect which compromises the results of the optimization. To address this, we add a second optimization step in which the result obtained from gradient descent (i.e., assuming uniform amplitude transmission) is used as an initial condition to a gradient-free scheme in which the Fourier transforms are computed using the transmission and phase shifts of actual structures drawn from our library; this two-step optimization, which explicitly acknowledges the properties of available phase-shifting structures, yielded improved results.

4. Polarization state generation

We designed two such gratings for operation at $\lambda = 532$ nm. For each element in the optimized $\vec{\Phi}_x$ and $\vec{\Phi}_y$, a rectangular TiO_2 pillar, 600 nm in height whose dimensions best impart the required phases on x and y polarized light is selected from a library of simulated structures. The designed gratings are then fabricated on a glass substrate with a process extensively detailed elsewhere that relies on electron beam lithography [35].

A first grating is designed to produce +45° linear, right-circular, left-circular, and −45° linear polarizations on the $m = -2, -1, +1$, and +2 diffraction orders, respectively, all with equalized intensities, when 45° linear polarized light is incident. These represent a set of polarizations commonly encountered in optics experiments and are thus of general interest. We refer to this as the "four polarization" grating. A second grating is designed to produce four polarization states on these same diffraction orders corresponding to the vertices of a tetrahedron inscribed in the Poincaré sphere, with equalized intensities, for incident 45° linear polarization. This set of polarizations is of significance in polarimetry (discussed below) [36, 37]. We refer to this as the "tetrahedron grating".

Both gratings contained $Q = 20$ individual elements, and thus each required the optimization of $2Q = 40$ parameters. This Q was found, heuristically, to produce results that achieve high efficiency η and good correspondence with the desired polarization ellipses — mathematically and from FDTD simulation — while minimizing the number of optimization parameters.

The unit cell geometries implementing the optimized phase profiles for each grating are shown in Fig 2c alongside corresponding electron micrographs. Each unit cell was tessellated into a bulk metasurface grating 250×250 μm in size.

Each grating was illuminated with laser light at $\lambda = 532$ nm linearly polarized at 45° relative to the axes of the grating. The polarization state on the diffraction orders of interest was then measured with a commercial rotating waveplate polarimeter.

In Fig. 2(b), for each grating, the measured polarization ellipses on each order are plotted alongside the desired target ellipses as well as the ellipses predicted by a finite-difference time-domain (FDTD) simulation of the grating geometry. We observe a qualitatively close correspondence between the desired target, simulated, and observed polarization states. Further data is tabulated in Appendix A.

5. Metasurface polarimetry

Each order of the metasurface polarization grating can be thought of as a diattenuator followed by a phase retarder, each oriented along x/y (Eqn. 4 and Fig. 1(d)). When light from a source passes through a polarizer oriented at 45°, a polarization state is produced on the grating order, ideally close to some target state (Fig. 3(a), top). When the grating is used in reverse — that is, with the grating followed by a linear polarizer oriented at 45° — each diffraction order may be seen as a polarization state analyzer for its characteristic Stokes vector (Fig. 3(a), bottom). The

Optics EXPRESS

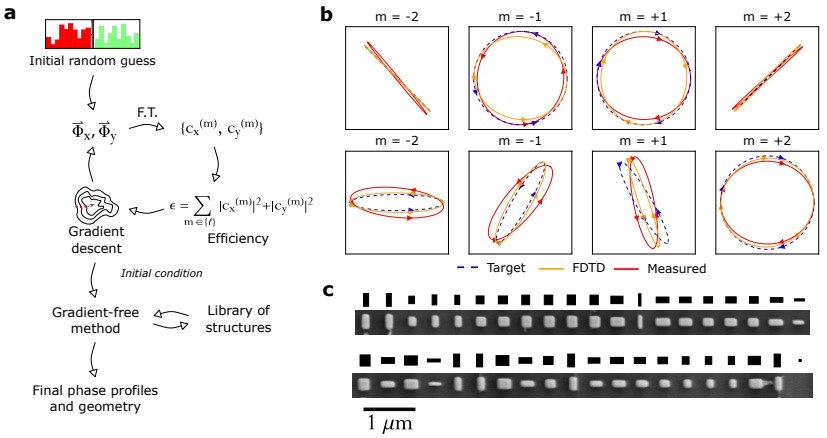

Fig. 2. **a**, Schematic of optimization routine used to design metasurface polarization gratings. A random initial guess for the phase profiles $\vec{\Phi}_x$ and $\vec{\Phi}_y$ is optimized to direct as much light as possible into the diffraction orders of interest using gradient descent under the constraints of the desired polarization states. This result is improved by a gradient-free method that accounts for simulated properties of the phase shifters used, and a final geometry is generated. These geometries are realized in TiO_2 for operation at $\lambda = 532$ nm. **b**, The scheme in (a) is used to generate two gratings, one for four polarizations of general interest (top) and one for a tetrahedron configuration of polarization states (bottom). Each grating generates four polarization states, and the target ellipse, expected result from FDTD simulation, and experimentally observed polarization ellipse on each grating order are shown. **c**, Design (black) and electron micrographs as-fabricated of the "four polarization" (top) and "tetrahedron" (bottom) gratings. In the tetrahedron grating, the small rightmost pillar has not survived fabrication.

characteristic analyzer Stokes vectors are the same as the generated polarizations with the chiral component S_3 reversed (owing to the symmetry of this particular system — see Appendix E).

The grating may then be used as a parallel full-Stokes polarimeter with no polarization optics (with the exception of a single polarizer, which could be easily integrated on top of the grating — the polarizer, even if it is imperfect, is indeed necessary for Stokes vector determination, as can be shown using simple Mueller calculus). This of course relies on a suitable choice of analyzer states, which must yield a non-singular instrument matrix; here, these states may be arbitrarily specified. The four polarization grating is not sufficient for full-Stokes polarimetry as its states are not linearly independent (in actuality, its imperfections break this and render it usable, though far from optimal, for polarimetry). For a polarimeter making $N = 4$ measurements, it has been extensively documented that, in the absence of calibration errors [37], a configuration of analyzers whose characteristic Stokes vectors correspond to (any) regular tetrahedron inscribed in the Poincaré sphere yields maximum signal-to-noise ratio in Stokes vector determination [36].

In acknowledgment of this, a larger version (1.5 mm × 1.5 mm) of the tetrahedron grating described above was fabricated. When laser light is incident, the four diffraction orders of interest diverge and pass through a polarizer oriented at 45°. Each beam then impinges on a standard silicon photodiode centimeters away, producing a photocurrent which is amplified and converted to digital form (Fig. 3(b), right side).

The instrument matrix A must be determined by calibration. Accordingly, we carry out

Optics EXPRESS

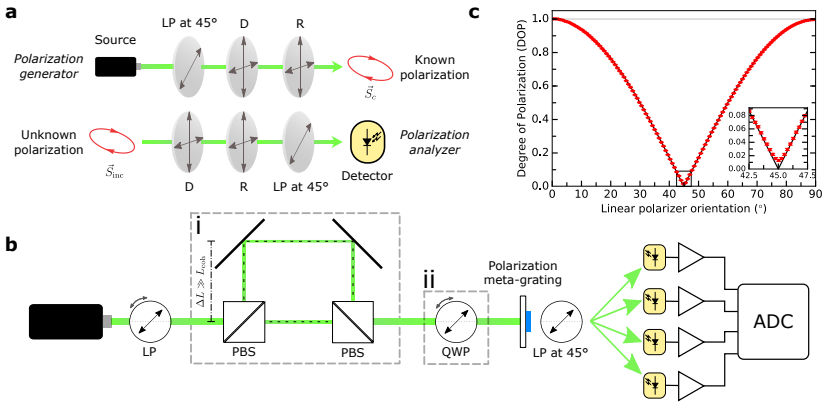

Fig. 3. **a**, As each diffraction order may be thought of as a cascade of a diattenuator and a retarder (Fig. 1d), when light from a source of known polarization (in this case, linearly polarized at 45°) is incident, a characteristic polarization $\vec{S}_c$ is produced. If light of unknown polarization $\vec{S}_{\text{inc}}$ is incident in the reverse direction and the source is replaced with a detector, the measured intensity $I \propto \vec{S}_{\text{inc}} \cdot \vec{S}'_c$, with $\vec{S}'_c$ identical to $\vec{S}_c$ with a change in the sign of the last component. **b**, This allows the meta-grating to function as a parallel polarimeter. Each of the four diffraction orders of the tetrahedron grating may be used as an analyzer. Light incident on the metasurface passes through a linear polarizer at 45° and diffracts onto four photodiodes whose photocurrents are amplified and digitized through an analog-to-digital converter (ADC). During testing and calibration, light passes through various polarization optics in front of the meta-grating. The role of the boxed components (i) and (ii) are described in the text. **c**, As the linear polarizer is rotated in front of a polarization Mach-Zehnder interferometer ((i) in (b)) whose path length difference is larger than the laser coherence length L_{coh}, the degree of polarization (DOP) varies. Plotted in red is the DOP measured by the meta-grating polarimeter which closely follows the theoretically expected curve (black). At 45° (inset) a DOP of $p = 0.12 \pm 0.018\%$ is measured.

a calibration scheme [38] developed for the well-known four-detector photopolarimeter of Azzam [39], applicable to any polarimeter with four intensity channels ($N = 4$) which explicitly accounts for imperfect quarterwave-plates. Each entry of the resultant instrument matrix A may be assigned error bounds which provide for the covariance matrix of any computed Stokes vector [40] allowing for the calculation of uncertainty bounds.

5.1. *Quantifying partially polarized light*

With the metasurface grating polarimeter thus calibrated, the Stokes vector of any incident beam may be determined from A and the measured intensities on the photodiodes. An interesting case is that of partially polarized light. Partially and un-polarized light, inherently a consequence of temporal coherence phenomena [2,41], are common in all non-laser light sources. The degree to which light is unpolarized is quantified by the degree of polarization (DOP), defined as

$$p = \frac{\sqrt{S_1^2 + S_2^2 + S_3^2}}{S_0} \tag{10}$$

where S_i denotes the i^{th} element of the Stokes vector. Fully polarized light corresponds to $p = 1$, totally unpolarized light to $p = 0$; in intermediate cases, p represents the ratio of the beam's

Optics EXPRESS

power which is polarized to that which is not.

To study the response of the metasurface-grating polarimeter to varying DOP, a deterministic means of producing partially polarized light is required. We employ a Mach-Zehnder-like setup with two polarization beamsplitters [2, 42]. This is depicted in Fig. 3(b), where the boxed components in (i) are included while (ii) is omitted (though (ii)'s presence would theoretically not affect the DOP). As a linear polarizer rotates in front of the interferometer, different fractions of incident light travel along each arm. When equal parts of the beam enter each path (when $\theta_{\mathrm{LP}} = 45°$) and the path-length difference of the interferometer is many coherence lengths L_{coh} of the laser source, the recombined beam will be totally unpolarized: The beam will be composed of half x-polarized light and half y-polarized light which no longer have phase-coherence. On the other hand, when $\theta_{\mathrm{LP}} = 0°$ or $90°$, all light goes along one path only and the beam is completely polarized. At intermediate angles, $p = |\cos\theta_{\mathrm{LP}}|$ [42].

A linear polarizer was rotated in front of the interferometer and the Stokes vector measured by the meta-grating computed. The corresponding DOPs (Eqn. 10) are plotted in Fig. 3(c). As shown in the inset, a minimum DOP of $1.2 \pm 0.018\%$ is observed.

5.2. *Comparison with a commercial rotating-waveplate polarimeter*

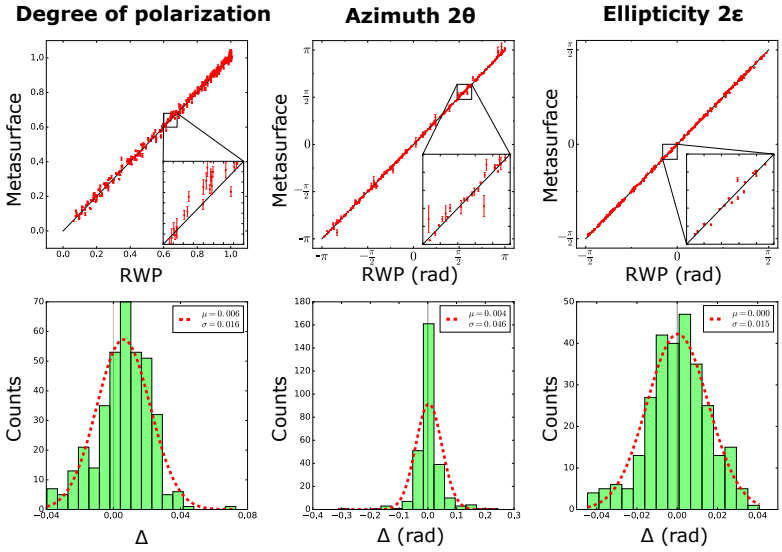

Fig. 4. In each column, the metasurface grating polarimeter (metasurface) and the commercial rotating waveplate polarimeter (RWP) are compared using different polarimetric quantities. In the top row of graphs, values measured by each polarimeter are plotted against one another (in the case of perfect correspondence all values would lie along the black 1:1 line). Insets of each plot are shown. Error bars are given only for the metasurface values since precision is not well-known for the commercial RWP. In the bottom row of plots, the differences between the values reported by each polarimeter are computed and plotted in a histogram. Each distribution is fitted with a normal distribution and the mean μ and variance σ are given for each. The quantities examined are the degree of polarization (DOP), the azimuth double angle 2θ, and the ellipticity double angle 2ϵ. The latter two are parameters of the polarization ellipse that give the spherical coordinates of the polarization state on the Poincaré sphere.

Optics EXPRESS

Finally, we compare the performance of the metasurface-grating polarimeter to a commercial and widely used visible-range rotating waveplate polarimeter (ThorLabs model PAX5710VIS-T). In a rotating waveplate polarimeter (RWP), a waveplate mechanically rotates in front of a linear polarizer and a detector. From the Fourier coefficients of the time-varying signal, the incident Stokes vector can be determined [12, 43].

An experiment was carried out using the setup depicted in Fig. 3(b) including boxed components (i) and (ii). A set of randomly selected linear polarizer (LP) and quarterwave-plate angles (QWP) were selected. In an automated measurement, the mounts holding the LP and QWP moved to these pre-determined angles and the polarization state produced at each of these configurations was deduced using the meta-grating polarimeter. Next, the commercial rotating waveplate polarimeter (RWP) was placed in the beampath in place of the metasurface-grating polarimeter. The QWP and LP revisited the same positions and the polarizations measured by the RWP were recorded.

The comparison is summarized in Fig. 4 with regards to the quantities of azimuth and ellipticity of the polarization ellipse (we plot the double azimuth and ellipticity angles 2θ and 2ϵ, since these are the angular coordinates on the Poincaré sphere) and DOP. The graphs in the top row of Fig. 4 plot the values measured by the metasurface-grating polarimeter along the vertical axis and the values measured by the RWP on the horizontal axis (an ideal 1:1 correspondence line is shown in black).

For each quantity, the difference in the values reported by the two polarimeters is calculated and plotted in a histogram in the bottom row of Fig. 4. Each is fitted with a normal distribution, whose means (μ) and standard deviations (σ) are shown.

6. Discussion

6.1. Optimization

In the literature of phase-only gratings, it has been shown using variational calculus that the optimum phase profile splitting light into a set of desired diffraction orders with maximal efficiency has an analytical optimum [34, 44]. Once the desired amplitude and phase relationship of light in these orders is specified, a finite set of coefficients may be optimized to find this optimum grating. The question of an analytical solution, not to mention uniqueness and local minima, in the present work, however, is complicated by the fact that this optimization couples two such phase gratings together, acknowledges their discrete nature, and is influenced by the properties of available phase-shifters from a library. An analytical and statistical examination of this optimization will form the basis for future work.

We stress the simplicity of the optimization scheme used here. Optimized structures are more generally of great interest in nanophotonics, including freeform geometries designed with the aid of topology optimization [45–48]. These schemes, however, are computationally expensive and require the repeated use of full-wave simulations. The gratings in the present work, on the other hand, are optimized using only the numerical evaluation of simple Fourier integrals. This method of course requires a considerable assumption about the physical nature of the problem, in that the transmission properties of the structures must be assumed to be of a certain mathematical form (cf. Eq. (4)). Additionally, the structures to be used are limited to those that have been previously simulated and may not take on arbitrary geometries. Nonetheless, this simple scheme enables arbitrary polarization control of the diffraction orders, and its success suggests that related polarization problems are an interesting application area for more sophisticated optimization.

6.2. Parallel polarization state generation

As illustrated in Fig. 2, for both the four polarization and tetrahedron gratings, the polarization ellipses observed on the diffraction orders compellingly match the desired target ellipses and those expected from FDTD simulation. A more quantitative view of this comparison is given in

Optics EXPRESS

Appendix A; there, we see that the average deviation in azimuth and ellipticity between target and measurement is 4.37% and 3.57%, respectively. Much of this difference is likely attributable to fabrication imperfections and unpredictability of the exact element dimensions. As the nominal dimensions of the fabricated geometries are slightly adjusted to compensate for overexposure and overetching, the measured polarization ellipses are observed to change smoothly in response (Appendix B). Given even ideal fabrication, the ellipses would not completely match the target states since the optimization will never achieve perfection. From the perspective of polarimetry, at least, any imperfection in the performance of the tetrahedron grating can be easily accounted for by the calibration (while the matrix condition number of A may only increase somewhat).

6.3. Parallel polarimetry

Above, we presented a characterization of the meta-grating's polarimeter functionality, specifically its ability to measure partially polarized light and its polarimetric performance in comparison with a commercial RWP.

We demonstrated that the meta-grating polarimeter can detect partially polarized light produced by a polarization Mach-Zehnder interferometer. The dependence of DOP on linear polarizer angle follows the expected theoretical trend. At 45°, we measure a minimum DOP of $1.2 \pm 0.18\%$. While the minimum DOP would ideally be 0%, the DOP aggregates error from all four Stokes components, and the minimum value achievable is in a sense a reflection of the accuracy of the polarimetric system as a whole. The exact significance this minimum value is not immediately clear — there are experimental subtleties to the production of partially polarized light with a polarization Mach-Zehnder interferometer, including the DOP varying over the profile of the output beam. The non-zero DOP observed at 45° could be a consequence of errors in the polarimeter, actual deviations of the beam's DOP from zero, or likely some combination of the two. The result, however, should be taken as a testament to the flexibility of the presented device — an integrated element in a completely parallel measurement can provide information about DOP, a coherence property.

Lastly, we compared the performance of the meta-grating polarimeter to that of a commercial rotating waveplate device. For the quantities of DOP, azimuth, and ellipticity — polarimetric parameters of common interest — we examined the difference in the values measured by the two polarimeters and treat these as statistical quantities. For DOP, we observe a standard deviation of $\sigma = 1.6\%$ and a mean difference of $\mu = 0.6\%$, a systematic error which could easily be attributed to one polarimeter being slightly misaligned. For azimuth χ and ellipticity ϵ, we observe $\sigma = 0.023$ rad $= 1.32°$ and $\sigma = 0.0075$ rad $= 0.43°$, respectively. This implicitly assumes that the RWP is an absolute polarization reference; any degree to which this is not true will increase the perceived error of the meta-grating polarimeter. Moreover, this error is itself polarization-dependent (see Appendices C and D). By sampling the error more or less uniformly over all possible polarizations, the values of σ for each parameter represent worst-case performance. Already, these are in the vicinity of the errors quoted for the RWP used (Appendix C). Notably, the performance of the RWP can be approached with a device having no moving parts, no bulk birefringent polarization optics, and detector-limited time resolution.

In Appendix D, we study angle-of-incidence effects and conclude that up to $\sim \pm 5°$ accidental misalignment, the meta-grating polarimeter could still be used with reasonable accuracy.

6.4. Context within diffractive optics and metasurfaces, and technological perspective

Diffractive optics has long been the subject of intensive investigation. Within diffractive optics, polarization gratings emerged from the realization that polarization had been largely overlooked [28, 31, 32]. As described in the review of Cincotti [29], polarization gratings (and their close cousins, polarization holograms [49, 50]) may be seen as a periodic modulation of diattenuation, retardance, angular orientation, or all three [29]. A parallel Stokes polarime-

Optics EXPRESS

ter may be constructed from cascades or a spatial interlacing (sometimes dubbed "spatial multiplexing") of such gratings [28, 29, 51–53]. More recently, metasurface-based diffractive polarimeters [22–24, 26] have appeared that, despite a higher spatial resolution of grating elements and new operating wavelengths, rest on a spatial multiplexing of the same unit cell designs conceived of with earlier polarization gratings.

Many diffractive optics works have examined periodic spatial modulation of retardance [29, 31, 51, 52, 54–56], but retardance itself is not all that counts. An overall phase may be added to both polarization components while keeping retardance constant, and this overall phase may vary spatially, too. This degree of freedom has largely not been exploited, and as a consequence, several discrete or spatially interlaced polarization gratings are necessary to generate (or measure) polarization in parallel [22, 24, 25, 28, 53] and the generated (or analyzed) states *cannot* be arbitrarily specified.

Explicit use of this phase freedom has interesting consequences [19], and it is the control of both retardance and overall phase that distinguishes this work. Notably, it allows for the generation of arbitrarily specified polarization states on the diffraction orders and equivalently, polarimetry with an arbitrarily specified set of basis polarizations. We note that a similar approach with similar functionality has been demonstrated using liquid crystal spatial light modulator technology [57, 58]. Owing to the constraints of these SLMs, however, a relatively complex double-pass architecture relying on a waveplate and a polarization beamsplitter must be employed in order to impart independent phase profiles on x and y polarized light independently, limiting the scope of potential applications.

In the present work, equivalent functionality has been embedded in a single, flat metasurface where the two phase profiles may be applied in the same plane, improving prospects for widescale application. Requiring only a linear polarizer (which may be easily integrated on top of the device as a wire grid), a single device may generate/measure polarization in parallel with no bulk birefringent optics or moving parts, permitting ease of integration and minizaturization. The device may be extended to spectroscopic polarimetry if linear arrays of detectors are used or to polarization imaging with imaging sensors. This may represent a far simpler solution to integrated full-Stokes polarimeters and polarization cameras which would not require bulk lithographic patterning of dichroic or birefringent material on top of a focal plane array [5, 59–63].

In diffractive optics, there exists an extensive body of work on geometric phase devices [51, 52, 55, 56, 64, 65]. In this approach, a phase profile may be imparted on circularly polarized light by spatially varying the angular orientation of a retarder. These retarders may take the form of, e.g., micro-fabricated dielectric [51] or liquid crystal [65] materials. The simplicity of this approach has numerous advantages, including achromatic phase (all wavelengths see the same angular orientation) and ease of fabrication, but the same simplicity is also a drawback. In contrast to the approach presented here, the spatially varying polarization in the plane of the grating cannot be arbitrarily engineered; the phase profile experienced by one circular polarization is constrained to be equal and opposite that experienced by the other [19]. Consequently, phase profiles *cannot* be imparted independently on an orthogonal basis of polarization states, and as such the polarization (and analysis) states of the diffraction orders cannot be arbitrarily specified as in this work. Nonetheless, geometric phase gratings have shown promise for use in a variety of polarization imaging systems [66–68]. However, owing to the constraint discussed above, multiple successive gratings [66] and other polarization optics are required for full-Stokes imaging polarimetry. The present work has the potential to significantly simplify these systems.

7. Conclusion

We have presented a method for the design of a metasurface diffraction grating with orders whose polarization states may be arbitrarily specified. We design and fabricate two such gratings and characterize the polarization states of the diffraction orders, finding close correspondence with

Optics EXPRESS

desired target polarization states. The grating, by time-reversal symmetry, may also function as a parallel polarization analyzer and permits for snapshot full-Stokes polarimetry. We demonstrate its ability to measure partially polarized light. Additionally, we compare its performance to a commercial RWP and present a statistical analysis showing comparable performance. The metasurface-based polarimeter has no moving parts and no bulk birefringent optics which facilitates its integration, and thus presents a significant simplification in polarimetric technology which may extend easily to polarization imaging if detector arrays are used instead. Being a grating, the chromatic dispersion of the orders may also be harnessed for use in spectroscopic polarimetry.

This work is a testament to the flexibility of metasurfaces in the realm of polarization optics and may have consequences for low-cost, lightweight, and significantly simplified polarimetry and polarization imaging systems.

Appendices

A. Tabulated data on measured polarization ellipses, design, and overall efficiency

Tabulated data detailing the measured polarization ellipses shown in main text Fig. 3 are given in Tables 1 and 2.

We note that there is an inherent issue with using the metrics in Tables 1 and 2 because certain azimuths (i.e., near the poles of the Poincaré sphere) are far more error prone. Even given this, the data are merely a supplement to the qualitative correspondence that is visually evident in Fig. 2.

In Table 3, we provide the optimized phase profiles $\{\vec{\Phi}_x, \vec{\Phi}_y\}$ for both gratings as well as the geometries of the 600 nm tall a-TiO_2 pillars that optimally impart these phase shifts (these geometries detail the schematics of each grating in Fig. 2(c)).

With any diffractive element, the question of efficiency naturally arises. In the present work, we stress that absolute efficiency is not the foremost concern, since in principle this work is independent of any particular material platform or wavelength regime. To provide order-of-magnitude type efficiency estimates, however, we characterized the tetrahedron grating described in the main text, with the results given in Table 4. In Table 4, the power in the innermost four diffraction orders (the four of interest) is given as a fraction of the power of the incident $\lambda = 532$ nm beam and as a fraction of the power in all diffraction orders. It can be seen that 63.4% of the incident power passes through the grating and diffracts into the orders. All of these orders and their energy are usable for polarimetry if extra detectors are employed, and indeed this would increase the accuracy of the polarimeter. It can also be seen, too, that the power in each of the four orders of interest is more-or-less uniform, as constrained by the optimization scheme.

For this grating, the optimized efficiency expected mathematically was $\eta = 73.1\%$. The fraction of the power in the four innermost orders with respect to all other diffraction orders, then, is off by about a factor of two from this prediction. This may have its origins in imperfections of the grating as-fabricated, or in the design assumption that the acquired phase is constant over the unit cell of one element. An optimization scheme that explicitly acknowledges the radiation pattern of the phase shifters may yield a better correspondence.

B. Effect of fabrication imperfection on observed polarization ellipses

Electron beam lithography yields size discrepancies between desired structures (as in a CAD layout file) and what is actually realized. Generally, the fabricated structures are larger than intended. This effect depends in a complicated way on dose, development time, etch rate, and other fabrication-related factors. The phase imparted by the structures in this work is size-dependent, so one would expect fabrication imperfections to have a notable effect on the polarization ellipses observed on the diffraction orders, relative to design. Here we present additional data chronicling

Optics EXPRESS

Table 1. **Extended polarization state data for tetrahedron grating, as presented in Fig. 2(b). The azimuth (θ) and ellipticty (ϵ) angles for each diffraction order (target, FDTD, and measured) are given in radians. Note that the azimuth of the target polarization state for the $m = +2$ order is not defined since this state was designed to be circular.**

Tetrahedron Grating			
$m = -2$ order			
Quantity	Target	FDTD	Measured
Azimuth angle θ	0	-0.0092	-0.0995
Ellipticity angle ϵ	0.1699	0.2049	0.3066
$m = -1$ order			
Quantity	Target	FDTD	Measured
Azimuth angle θ	1.0472	1.0399	0.8789
Ellipticity angle ϵ	0.1699	0.2168	0.3191
$m = +1$ order			
Quantity	Target	FDTD	Measured
Azimuth angle θ	-1.0472	-1.2464	-1.3687
Ellipticity angle ϵ	0.1699	0.1089	0.2165
$m = +2$ order			
Quantity	Target	FDTD	Measured
Azimuth angle θ	undefined	0.3589	-0.0218
Ellipticity angle ϵ	-0.7854	-0.7568	-0.7244

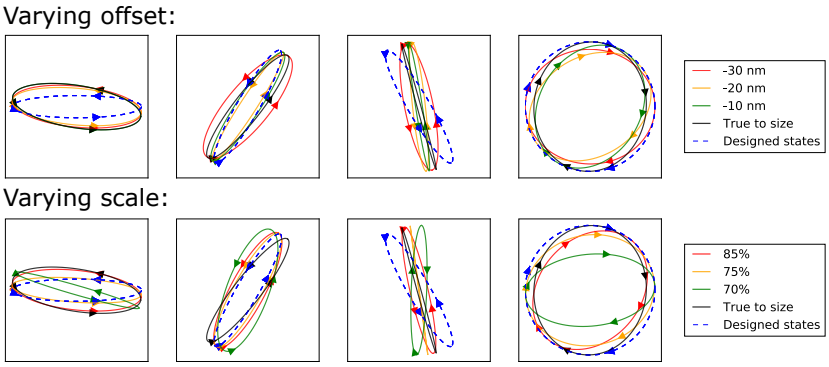

Fig. 5. Effect of changing nominal fabrication CAD given to e-beam system on polarization ellipses produced on the $m = -2, -1, +1$, and $+2$ on the *tetrahedron* grating.

this effect.

For each grating design, several samples were fabricated with either fixed size offsets in the CAD (10, 20, or 30 nm smaller than desired) or fixed size scaling factors (all dimensions scaled by 85, 75, or 70%). The polarization states on the diffraction orders from all such gratings were recorded.

We illustrate this by depicting the polarization ellipses recorded from the *tetrahedron* grating with different size offsets and scalings in Fig. 5. It can be seen that varying the nominal size of the fabricated structures has a significant effect on the observed polarization ellipses, which

Optics EXPRESS

Table 2. **Extended polarization state data for the four-state grating, as presented in Fig. 2(b). The azimuth (θ) and ellipticty (ϵ) angles for each diffraction order (target, FDTD, and measured) are given in radians. Note that the azimuth of the target polarization state for the $m = -1$ and $m = +1$ orders are not defined since these states were designed to be circular.**

Four Polarization Grating			
$m = -2$ order			
Quantity	Designed	FDTD	Measured
Azimuth angle θ	-0.7854	-0.7867	-0.8840
Ellipticity angle ϵ	0	-0.0026	-0.0299
$m = -1$ order			
Quantity	Designed	FDTD	Measured
Azimuth angle θ	undefined	-0.2638	1.4019
Ellipticity angle ϵ	0.7854	0.7212	0.7462
$m = +1$ order			
Quantity	Designed	FDTD	Measured
Azimuth angle θ	undefined	1.4905	-0.0428
Ellipticity angle ϵ	-0.7854	-0.7432	-0.7249
$m = +2$ order			
Quantity	Designed	FDTD	Measured
Azimuth angle θ	0.7854	0.7912	0.7282
Ellipticity angle ϵ	0	-0.0297	-0.0274

is to be expected. The data presented in the text came from samples with -20 nm offset for the four-polarization grating and -30 nm size offset for the tetrahedron grating; these samples produced ellipses closest to the target polarizations.

C. Additional detail on polarimeter comparison

What do the histograms presented in Fig. 4 mean? In each histogram, we examine a statistical distribution of the difference between the set of measured values and (what we take to be) the true values, those reported by the commercial RWP. Each plots the distribution of some practical quantity derived from the Stokes vector. Depending on the polarization states of the test points selected, these distributions could be artificially broadened or narrowed. For example, if all the test polarization states are located near the poles of the Poincaré sphere, the azimuth histogram will be broader; if the test states are all located on the equator, the distribution will narrow. The deviation in the polarimetric parameters measured by both polarimeters will vary in a vectorial way as a function of the Stokes vector, as dictated by the error in the instrument matrix (which is a matrix quantity; see Appendix D).

In order to be unbiased, the measurement test points should be uniformly distributed in the entire range of the given parameter, so that all of the best cases and the worst cases receive equal representation. If this is done, the standard deviation of the distribution of differences between measurement and a reference can be indicative of the accuracy of the polarimeter with regards to that particular quantity; the mean is indicative of some systematic error that causes the polarimeter to be off by a constant amount relative to a reference.

In this work, we have endeavored to explore (somewhat uniformly) all possible values of DOP, azimuth, and ellipticity relative to what we treat as an absolute polarization reference, that being the RWP. To a good approximation, then, we can treat the σ of our histograms to be a measure of

Optics EXPRESS

Table 3. **Details of the design of the two gratings presented in this work. For each of the two gratings, the $\tilde{x}$ and $\tilde{y}$ phase profiles are provided (in radians). Corresponding to each pair $\{\phi_x, \phi_y\}$ are the lateral dimensions $\{w_x, w_y\}$ of a rectangular pillar of a-TiO_2, 600 nm in height best implementing this pair of phases (in nanometers).**

Grating Design Parameters								
	Tetrahedron Grating				Four State Grating			
Element #	ϕ_x	ϕ_y	w_x	w_y	ϕ_x	ϕ_y	w_x	w_y
1	5.85	0	197	218	1.40	5.22	101	252
2	5.55	2.25	252	113	1.07	5.28	10	252
3	0.62	5.33	252	181	1.39	2.30	113	147
4	2.97	0.30	252	59	0.91	3.80	92	20
5	2.70	5.72	118	252	1.11	3.40	10	185
6	2.83	5.59	122	252	3.91	3.92	155	155
7	0.99	5.62	252	193	4.94	4.41	181	155
8	5.81	1.69	252	109	4.33	5.06	155	189
9	5.25	4.52	189	160	4.86	5.28	168	189
10	3.54	6.24	134	252	4.74	5.31	164	193
11	4.88	1.55	231	105	4.78	5.16	164	189
12	6.14	2.59	252	123	5.91	4.48	239	147
13	4.99	2.69	218	122	6.22	2.03	46	239
14	4.49	2.76	189	130	5.63	2.18	252	113
15	2.31	2.84	134	147	5.01	2.00	227	113
16	2.09	2.97	126	151	4.03	2.14	172	126
17	1.94	3.30	122	160	4.67	2.42	206	122
18	0	5.39	239	164	4.13	2.52	172	130
19	2.74	5.89	122	252	5.20	0.77	248	92
20	0	0	42	42	1.12	0.17	193	42

Table 4. **Efficiency data for the tetrahedron grating.**

Tetrahedron grating efficiencies		
Order	Power as fraction of incident power (%)	Power as fraction of all orders (%)
$m = -2$	5.71	9.0
$m = -1$	8.5	13.4
$m = +1$	4.5	7.0
$m = +2$	4.9	7.7
All orders	63.4	-

the accuracy for azimuth, ellipticity, and DOP.

The results of this are listed in Table 5, with values for the RWP obtained from its datasheet (as of this writing listed on ThorLabs' webpage at this link). We do not know how the specified accuracies of the RWP are obtained, so whether they are directly comparable is unknown. Additionally, we treat the RWP as an absolute polarization reference. Any degree to which this is not the case will increase the perceived error of the metasurface grating polarimeter.

The overall point we wish to make here is that the accuracies for the metasurface grating polarimeter closely approach those of the RWP, despite the former being a monolithically integrated device with no moving parts or bulk polarization optics.

Optics EXPRESS

Table 5. **Comparison of the two polarimeters.**

Quantity	Metagrating Polarimeter	ThorLabs Spec Sheet (RWP)
Degree of Polarization (DOP)	1.6%	0.5%
Azimuth	1.32°	0.2°
Ellipticity	0.43°	0.2°

D. Dependence of polarimetric accuracy on angle-of-incidence

A polarimeter is calibrated with a beam impinging at one angle of incidence; if it is then used at a different angle of incidence, the determined Stokes vector will consequently contain error. This is an effect relevant to all polarimeters, including the rotating waveplate polarimeter.

We conducted a small study on the metasurface grating polarimeter to determine its susceptibility to angle dependent effects, an important question in assessing its technological relevance. If the polarimeter is calibrated for a 0° angle-of-incidence, how much could an end user accidentally tilt the device and still expect to obtain reasonably accurate results? The study presented here is by no means exhaustive.

D.0.1. Description of error analysis scheme

We imagine a scenario in which the polarimeter is used assuming a "perceived" instrument matrix A_p which the user erroneously applies believing that it is correct and an "actual" instrument matrix A_a that reflects the true behavior of the polarimeter. If the user makes an observation in the form of an intensity vector $\vec{I}_{\text{meas}}$, they will report a measured Stokes vector $\vec{S}_p = A_p^{-1}\vec{I}_{\text{meas}}$. The Stokes vector in actuality, however, is $\vec{S}_a = A_a^{-1}\vec{I}_{\text{meas}}$, meaning that there is measurement error which we can express in vector form as

$$\vec{\Delta}(\vec{S}_a) = (A_p^{-1} - A_a^{-1})\vec{I}_{\text{meas}} = (A_p^{-1} - A_a^{-1})A_a\vec{S}_a = (A_p^{-1}A_a - \mathbb{I})\vec{S}_a. \tag{11}$$

The error accrued from use of the incorrect instrument matrix (because of e.g., an angular tilt of the polarimeter) has a polarization dependence that is fully governed by the matrix $(A_p^{-1}A_a - \mathbb{I})$ ($\mathbb{I}$ is the 4×4 identity matrix). The eigenvectors of the matrix $A_p^{-1}A_a$ will merely be stretched or compressed along the same direction, and will suffer no distortion of azimuth, ellipticity, or DOP.

The above discussion suggests a Monte-Carlo-like error analysis scheme, depicted in Fig. 6. Beginning with a sampled set of actual Stokes vectors, $\{\vec{S}_a\}$, we compute a set of measured intensity vectors that would actually be observed by the user, $\{\vec{I}_{\text{meas}}\} = A_a\{\vec{S}_a\}$, corresponding to each of the actual Stokes vectors. Making use of the perceived (incorrect) instrument matrix A_p, the user will compute a set of perceived Stokes vectors $\{\vec{S}_p\} = A_p^{-1}\{\vec{I}_{\text{meas}}\}$. An error analysis can be carried out between $\{\vec{S}_a\}$ and $\{\vec{S}_p\}$ (Fig. 6), with respect to any number of possible quantities derived from the Stokes vector.

This error analysis scheme reveals how a given Stokes vector will be measured by a polarimeter that is out of its calibration condition. In general, the whole Stokes vector will be deformed, so a user measuring a given beam will not only observe a different polarization ellipse, but may also report a different beam power or a beam that appears artificially polarized or depolarized.

D.0.2. Incident angle error analysis of meta-grating polarimeter

The discrepancy between A_a and A_p could stem from any error source, though here we wish to examine the effect of angle of incidence. To this end, we begin by calibrating the polarimeter

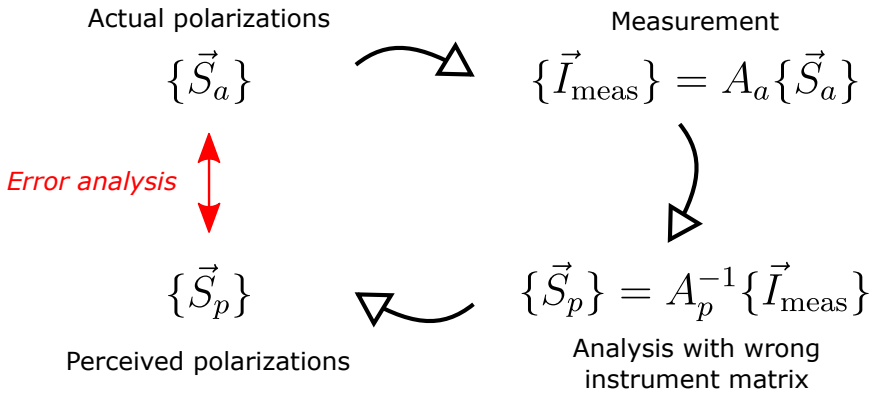

Fig. 6. A schematic of the procedure used to analyze the effect of errors in the angle of incidence, or more generally of any effect that contributes to error in the instrument matrix, on reported Stokes vectors from the polarimeter.

at normal incidence. Then, with the meta-grating placed on a rotation mount, the calibration is repeated at incident angles of 5°, 10°, 15°, and 20°.

In a realistic situation, a user will believe that they are using the instrument matrix from normally-incident calibration, that is, $A_p = A_{0^\circ}$. If, however, the device is tilted at angle θ, $A_a = A_\theta$. We perform the analysis detailed above for each incident angle. We take $\{\vec{S}_a\}$ to be a uniform sampling of points on the surface of the Poincaré sphere. (In a more general analysis, the entire volume of the sphere would be included too to account for partially polarized inputs).

The results of this analysis are depicted in Fig. 7. For each Poincaré sphere in Fig. 7, the dots represent the set of test polarizations $\{\vec{S}_a\}$. For each angle, the deviation in azimuth, ellipticity, and DOP is computed between all of the members of $\{\vec{S}_p\}$ and $\{\vec{S}_a\}$. These errors are shown as the color of the dot on the sphere, with red corresponding to higher error. It can be seen that for different incident angles and different quantities of interest, different regions of polarization state-space experience higher error. The maximum and minimum errors for each quantity/angle, as well as the standard deviation, are also given. We stress again that the positions of the dots in Fig. 7 represent the *actual* Stokes vectors, not the measured ones; one could track the way in which the Poincaré sphere distorts under the influence of the matrix $(A_p^{-1}A_a - \mathbb{I})$ as well.

The Stokes vectors constituting the rows of the instrument matrix are sometimes referred to as *analyzer vectors* because any incident Stokes vector is projected on these to produce the measured intensities $\vec{I}$. Also shown inscribed in the spheres of Fig. 7 (in pink) are the analyzer Stokes vectors at angle θ (the rows of the instrument matrix A_θ) alongside the ideal tetrahedron (gray line) for each case.

D.0.3. Discussion/conclusion

From the previous study whose results are detailed in Table 5, the uncertainty in the DOP, azimuth, and ellipticity of measured polarization ellipses are known for normal-incidence polarimetry.

In Fig. 7 the average and variance (μ and σ) of the errors in these same quantities for each angle of incidence are given. In order to evaluate the effect of off-normal incidence on polarimetric performance, $\mu + \sigma$ (or $\mu - \sigma$, whichever is larger in absolute value) for each quantity should be compared to the precisions in Table 5. If these are of comparable magnitude, it can be said that

Optics EXPRESS

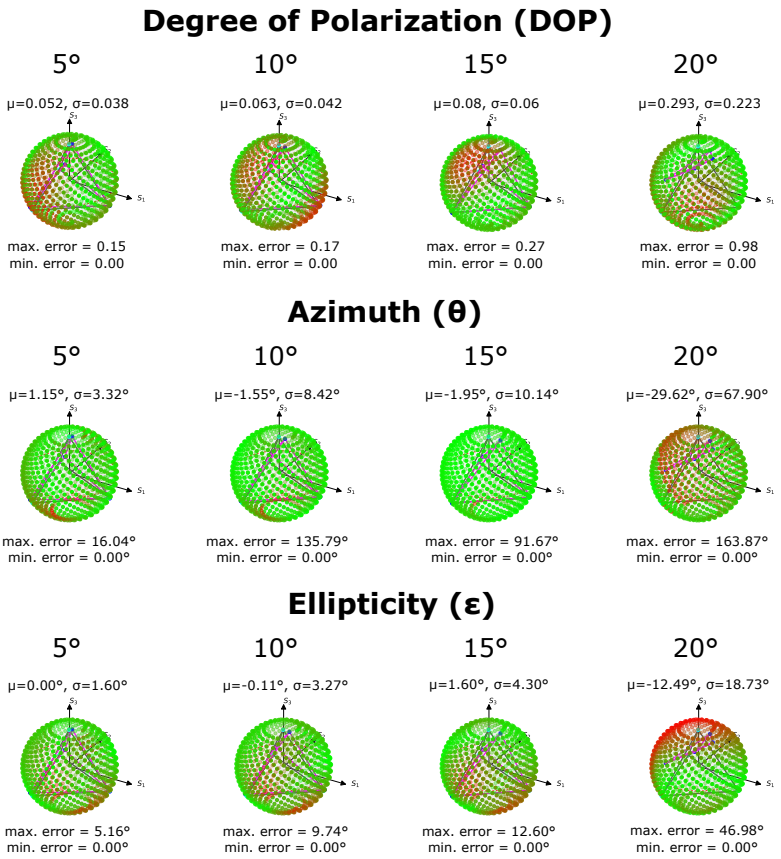

Fig. 7. Results of angle-dependent polarimetry study. Note that DOP errors are expressed in absolute terms (i.e., not in %). For each quantity of interest (DOP, azimuth, and ellipticity) and each incident angle (5°, 10°, 15°, 20°), a Poincaré sphere populated with dots representing a sample set of Stokes vectors is shown. The color of each dot represents the error in that quantity a user would report at that accidental misalignment, with red representing higher error. Also given are the maximum, minimum, mean, and variance of the error over the sample set for each quantity and angle.

Optics EXPRESS

the expected error from an accidental tilt is inside the measurement uncertainty of the polarimeter at normal incidence anyway, and its effect is minimal. Even at a 5° misalignment, the errors ($\mu \pm \sigma$) exceed the uncertainties measured at normal incidence, but not exceedingly so (9% vs. 1.6% for DOP, 4.42° vs. 1.32° for azimuth, and 1.60° vs. 0.43° for ellipticity). Qualitatively, then, the polarimeter could suffer an accidental misalignment of 5° or less and still offer reasonable accuracy, with some polarization states that would yield particularly high error (clustered around the red regions in Fig. 7). Even if the misalignment exceeds this, the grating can still be used for polarimetry assuming a new calibration is carried out. For this reason the grating can still be used in a polarization imaging application where a wide angular bandwidth is required, so long as the angular variations are characterized.

E. Comment on reciprocity, symmetry, and correspondence between polarization analyzers and generators

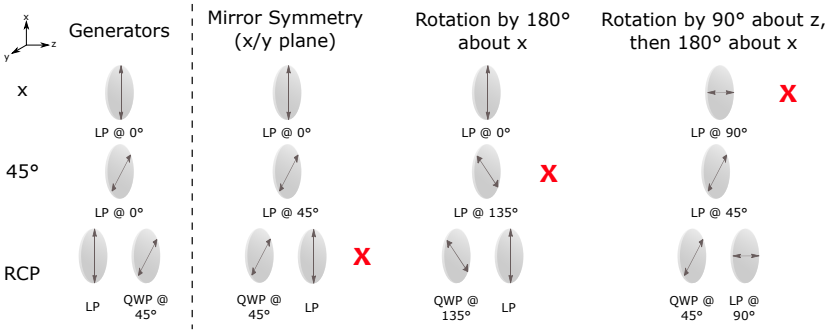

Fig. 8. On the left, generators (combinations of linear polarizers (LP) and quarter-wave plates (QWP) that generate x, 45°, and RCP (the cardinal directions on the Poincaré sphere) are shown. On the right, analyzers constructed from these generators by three different linear transformations are shown. In each case, one of the three analyzers (marked by a red 'x') shown passes the *orthogonal* polarization rather than the one produced by the generator. Intuitively, this demonstrates that the analyzer's Stokes vector differs from the generator's Stokes vector in a way that depends on the symmetry of the transformation between the two.

A configuration of polarization optics implementing a singular Jones matrix (meaning it contains a polarizer-like element) is known as a polarization state generator. No matter the state of incident light illuminating the generator, the polarization state—that is, the Stokes vector—of light exiting the generator will always be the same, though its intensity will vary. We denote the characteristic polarization state produced by a polarization state analyzer as $\vec{S}_c$.

A polarization state analyzer is a configuration of polarization optics that provides an intensity modulation depending on the incident polarization. In particular, the analyzer has its own characteristic polarization $\vec{S}_c'$, and the intensity detected at the exit of the analyzer follows the trend $I \propto \vec{S}_{\text{inc}} \cdot \vec{S}_c'$. If $\vec{S}_c'$ corresponds to a fully polarized Stokes vector with $p = 1$, then the modulation of intensity with incident polarization state will have perfect contrast (that is, there is an $\vec{S}_{\text{inc}}$ for which $I = 0$). If not, there is no incident polarization which can completely extinguish the output intensity.

Polarization optics is reciprocal, and a configuration of polarization optics working as a generator can also be used as an analyzer. What is the relation, then, between $\vec{S}_c$ and $\vec{S}_c'$? This depends on the symmetry by which the generator is converted to an analyzer to face the beam.

Optics EXPRESS

This is considered in Fig. 8. On the left side, polarization generators for three cardinal polarization directions on the Poincaré sphere are shown (x, 45°, and RCP). On the right, analyzers constructed from these generators are depicted, having been created from three different transformations of the generator. In viewing Fig. 8, it may be of help to imagine light propagating from left to right through each of the generators and passing through the analyzers in each of the three columns on the right.

It can be seen that for each transformation, one analyzer will, instead of passing the characteristic polarization produced by its generator, pass the orthogonal polarization. For example, in the first column in the right section of Fig. 8, the analyzers produced will pass x and 45° linear polarizations, but the circular analyzer produced will pass LCP instead of RCP. In order to pass RCP and extinguish LCP, the QWP fast axis would have need to rotate 90°. This discrepancy is a consequence of the change in propagation direction.

If instead the generator is rotated 180° around the x-axis, the generator for 45° polarized light converts into an analyzer for 135° polarized light, while the generators for x and RCP become analyzers for those same polarizations.

Finally, a transformation in which the polarizer is first rotated about z by 90° and then 180° about x converts the x polarization generator into a y polarization analyzer, while the generators for 45° and RCP become analyzers for those same polarizations.

In each of these example transformations, $\vec{S}_c{}'$ is the same as $\vec{S}_c$ except for the exchange in the sign of one Stokes component (S_3 in the first case, S_2 in the second, and S_1 in the third). For a more general transformation, the analyzer vector $\vec{S}_c'$ is related to the generator's characteristic polarization $\vec{S}_c$ by a linear transformation in which vectors in some plane of the Poincaré sphere are left unchanged but the Stokes vector perpendicular to this plane is mirrored about it.

In this work, each order of the diffraction grating is taken to be a polarization state generator when combined with an initial polarizer oriented at 45°. When transitioning from polarization generation to analysis, we move the polarizer oriented at 45° from the incident side of the grating to the output side while changing nothing about the grating's orientation. The diattenuator and the retarder commute, so they can be thought of as a single optical element. The effect of moving the polarizer is the same as a reflection, the leftmost column of the right panel of Fig. 8. In the case of this work, then, $\vec{S}_c'$ *is the same as* $\vec{S}_c$ *save for a reversal of* S_3*, the chiral Stokes component*. This fact is not used explicitly in the work (since the analyzer vectors are absorbed into the polarimeter calibration process), but aids in the intuitive understanding of the grating.

This assumes that the polarizer looks the same to light passing through normally (in the polarization generation scenario) and to light passing through at a diffraction angle (in the polarimetry case) since only a single polarizer is used for all orders in this work (Fig. 3(c)); any discrepancy from this is absorbed into the polarimeter calibration.

We note that this coordinate transformation between generators and analyzers is well-known and more generally understood in polarization optics [69], as well as in quantum mechanics and linear systems theory. We provide this explanation here to aid in the intuitive understanding of this work.

F. Packaged prototype

The simplicity of the polarimeter (as is evident from Fig. 3(b)) admits easy packaging into a prototype laboratory-grade polarimeter.

The grating can be rigidly mounted in front of four simple silicon photodiodes at the correct angular positions. After amplification, a microcontroller transmits this data serially to a computer where the computation of the polarization state by Eq. (1) takes place.

Such a prototype is depicted in Fig. 9.

Optics EXPRESS

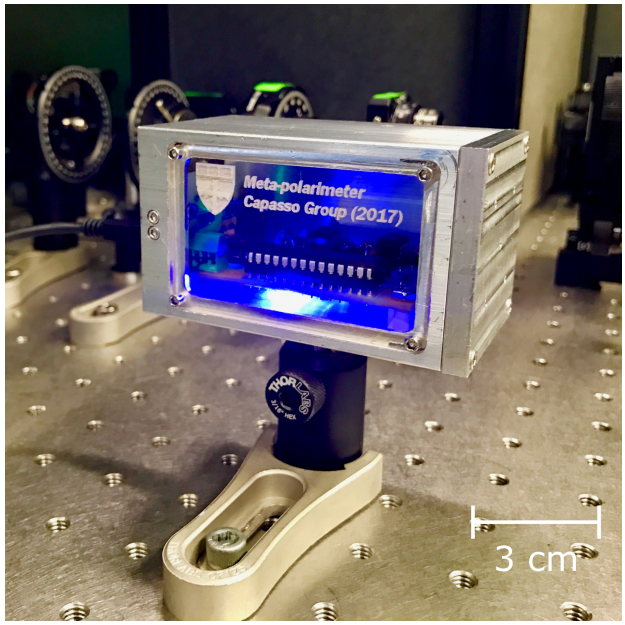

Fig. 9. Schematic of a prototype laboratory-grade polarimeter utilizing the tetrahedron grating presented in this work, which is mounted in the faceplate at the right of the enclosure.

Funding

National Science Foundation (DGE1144152, 1541959); United States Air Force Office of Scientific Research (FA9550-14-1-0389, FA9550-16-1-0156).

Acknowledgments

The authors thank M. Piccardo, A. Ambrosio, and M. Tamagnone for helpful comments on the manuscript. NAR acknowledges support from the National Science Foundation Graduate Research Fellowship Program (GRFP) under grant no. DGE1144152. Additionally, we acknowledge support from the US Air Force Office of Scientific Research (MURI, grants no. FA9550-14-1-0389 and No. FA9550-16-1-0156). This work was performed in part at the Center for Nanoscale Systems (CNS), a member of the National Nanotechnology Coordinated Infrastructure (NNCI), which is supported by the National Science Foundation under NSF award no. 1541959. CNS is part of Harvard University.

Paper IV

Metasurface Polarimeter on Optical Fiber Facet by Nano-Transfer to UV-Curable Hybrid Polymer

Michael Juhl, J. P. Balthasar Mueller, and Kristjan Leosson

Submitted for publication

Metasurface Polarimeter on Optical Fiber Facet by Nano-Transfer to UV-Curable Hybrid Polymer

Michael Juhl, Jan Philipp Balthasar Mueller and Kristjan Leosson

Michael Juhl is with Innovation Center Iceland and University of Iceland, Reykjavík, Iceland.
J. P. Balthasar Mueller is with Harvard School of Engineering and Applied Sciences, Cambridge, MA02138, USA.
Kristjan Leosson is with Innovation Center Iceland and University of Iceland, Reykjavík, Iceland (e-mail: kristjan.leosson@nmi.is).

Index Terms: Nanostructured fibers, Polarimetry, Optical metasurfaces, Transfer nanolithography.

Abstract

A simple, cost-effective, and high-throughput method of patterning an optical fiber facet using template stripping to transfer a gold pattern to a UV-curable hybrid polymer is presented. The template stripping transfer method is demonstrated with two different approaches: A fiber exposure approach where the position of the transferred nanostructure relative to the fiber can be aligned by optical curing of polymer through the fiber, and a flood exposure approach that allows the transfer of a larger area of nanostructure. An in-line metasurface polarimeter patterned on a 1550 nm single-mode fiber facet using this technique is reported, demonstrating the capacity of the miniaturization of the metasurface polarimeter. The demonstrated fiber-based metasurface polarimeters are ultra-compact, cost-effective, robust, simple, and deliver high-performance polarization measurements. They are fully viable alternatives to existing solutions with applications mainly in polarization state generation and fiber optics communication.

Introduction

Metasurfaces are quasi-two-dimensional optical nanostructures that enable spatially dependent tailoring of the amplitude, phase or polarization of light. There has been a growing interest in this new class of optically engineered nanostructures over the past few years as a result of reports of unconventional light-matter interaction and the promise of miniaturization of optical components [1]–[3]. Integration of nanostructures onto optical fiber facets has the potential of opening new applications for highly miniaturized optical devices, such as surface-enhanced Raman scattering sensors, surface-plasmon-resonance sensors, beam steering structures, fiber optical tweezers,

polarization state generators, and devices for polarization monitoring in telecommunications networks [4]–[6].

Fabricating nanoscale structures on a fiber tip is a challenging task. The large aspect ratio and microscopic cross-section of the fiber are not compatible with conventional wafer-based processing platforms, originating from the semiconductor industry. Instead, many different approaches have been demonstrated, employing technologies such as focused ion beam milling, nanoimprinting, two-photon polymerization, and transfer lithography [7]–[9].

Transfer lithography techniques offer convenient methods of high-resolution optical fiber tip patterning suitable for parallel processing. Many of the reported methods, however, require complicated processing like mold preparation, manual transfer by mechanical contact, or multiple film delamination [10]–[12]. In this work we demonstrate a simple nano-transfer technique that we use to define patterns of metallic nanoantennas on fiber facets. The method involves only a few simple processing steps, easy alignment and potential for low-cost production.

Metasurfaces enable the fabrication of planar optical components, thereby in many cases reducing the cost, size, and complexity of existing devices. A few examples are flat lenses [13]–[15], spectrometers [16], and polarimeters [17]–[19]. A particular instance of devices for polarization measurement is the in-line polarimeter, which performs non-terminating polarization measurements of optical signals. Whereas current in-line polarimeters are constructed with multiple optical components in series [20], a metasurface polarimeter requires only one ultrathin surface of nanoantennas [17], while matching state-of-the-art fiber-based in-line polarimeters in terms of speed and precision. In-line polarimeters play a critical role in monitoring and controlling the polarization in optical communication networks. Integrating the metasurface polarimeter on an optical fiber would therefore not only represent an important step towards the ultimate miniaturization of the polarimeter but also be very useful in applications like optical networks.

Fabrication

The principle of the template stripping transfer processes is illustrated in Fig. 1. The metasurface pattern was initially written into a layer of polymethyl methacrylate (PMMA) on a silicon wafer using electron beam lithography. Gold was subsequently deposited on the resist and patterned in a lift-off process. A 1550-nm single-mode fiber was mechanically cleaved, dipped in a UV-

curable organic/inorganic hybrid polymer (OrmoComp®, micro resist technology GmbH), leaving a droplet of polymer on the fiber tip, and brought into near proximity to the patterned silicon wafer (Fig. 1a). The polymer was then cured with 365-nm ultraviolet light using one of two approaches. With the fiber exposure approach the UV-light was transmitted through the fiber itself, thus forming a cylindrical polymer rod between the fiber and the wafer as a result of confinement within the fiber and a self-guiding phenomenon within the optically-cured polymer. After UV exposure, the fiber was retracted, delaminating the gold from the wafer and transferring it to the surface of the cured polymer rod, as a result of low adhesion between gold and silicon. This simple delamination process is known as template stripping [21], [22]. Template stripping uses the fact that some metals, gold included, have low adhesion when deposited directly on silicon. The adhesion is high enough that structures do not delaminate during the liftoff process, but low enough that stripping from the wafer is straightforward. UV-curing through the fiber ensures that the nanostructure is automatically transferred only to the area corresponding to the fiber-core (Fig. 1b). Uncured polymer was removed with a developer (OrmoDev®, micro resist technology GmbH). Fig. 1c illustrates an alternative flood-exposure approach where the polymer was cured from outside the fiber, thus curing the entire droplet of polymer on the fiber tip. The metasurfaces transferred to the polymer rod can subsequently be fully embedded in polymer by repeating the process using a clean silicon wafer without nanoantennas. This is illustrated in Fig. 1d with the fiber exposure approach.

Electron micrograph images of the patterned fibers are shown in Fig. 2. The diameter of the polymer rod in Fig. 2a is 10 – 10.5 μm corresponding well to the core size of an SMF-28 optical fiber. Fig. 3 shows a micrograph of the silicon wafer after transfer lithography with the fiber exposure approach. It is observed that all antennas in a circular area, corresponding to the mode size of an SMF-28 optical fiber, are successfully detached from the sample.

Polarimeter on a Fiber Facet

We have previously presented a new in-line, polarization preserving polarimeter design [17] based on an optical metasurface formed by arrays of nanoantennas [23]. Identical gold nanorods (250 nm x 50 nm x 20 nm) are arranged with subwavelength-spacing in parallel arrays (see Figs. 2 and 3). The metasurface consists of two antenna arrays with columns of antennas, individually oriented ±45° with respect to the orientation of the columns of each array. The distance between

the two columns of perpendicularly oriented antennas is $\lambda(1+1/4)$ and the column-pairs are spaced 2λ, where λ is the design wavelength in the polymer material, corresponding also roughly to the resonance wavelength of the individual antennas. When near-infrared light (C-band wavelengths) is normally incident on the metasurface, a fraction of the intensity is scattered in polarization-dependent in-plane and out-of-plane meta-grating orders; each order serving as a polarization analyzer [24]. The in-plane grating orders stay in the plane of the metasurface, whereas light in the out-of-plane orders is scattered at an angle close to 45° from the metasurface plane after refraction at the polymer/air interface. Only out-of-plane orders are used for intensity measurements, since in-plane orders suffer from lensing and scattering from imperfections at the edge of the structure. The rescattering of the in-plane orders at the fiber-cladding/air interface is observed in images in Fig. 4 using an infrared camera and a reflective microscope objective from Ealing. Aside from mapping the fiber facet to the image plane, the reflective objective serves to block most of the light from the fiber to avoid overexposing the image. The images of the rescattering demonstrate the polarization-dependent light scattered by the metasurface.

The transfer lithography processes allows for two different polarimeter designs, a fiber exposure design that is self-aligned to the fiber core and a flood exposure design, as illustrated in Figs. 1b and 1c. Obviously, the fiber exposure design is the most compact solution and transfers a far smaller area of the patterned gold than the flood exposure design. However, the signal intensity of the self-aligned polarimeter is much smaller than the intensity from the flood exposure polarimeter due to increased scattering from the polymer cylinder itself and the smaller overall number of antennas. This results in larger error on the measured Stokes vector.

The patterned optical fiber was connected to a fiber laser at a wavelength of 1550 nm, followed by a deterministic polarization controller (DPC). The intensity of four out-of-plane orders was measured to obtain information about the polarization of the incoming light. The full information about the polarization is contained in the 4-element Stokes vector [25]. Output intensity is related to the polarization by a 4-by-4 analyzer matrix, which is found by calibration to known polarizations [26]. With at least four intensity measurements the Stokes vector of the incoming light can therefore be reconstructed using a linear transformation. Four InGaAs photodiodes were fitted in a 3D-printed holder and aligned to the scattered light from the grating orders with the help of an xyz stage. The out-of-plane grating orders can be observed in Fig. 5. The images were recorded by placing the structured fiber directly in front of the infrared camera. The signal from

the diodes was amplified and sampled using a microcontroller [24]. The transmitted light was coupled back into a second fiber, which was attached to another xyz stage and positioned approximately 100 µm from the metasurface, obtaining a coupling efficiency of about 50 % (-3 dB) where about 3 % can be related to reflection losses. The unstructured fiber was connected to a commercial in-line polarimeter (IPL). Since transmission through the optical fibers affects the polarization of the light, the polarization at the metasurface polarimeter and the in-line polarimeter were calibrated to the polarization set by the DPC using a commercial free-space polarimeter (POL) and two manual polarization controllers (MPC), which were placed on the fibers before and after the metasurface polarimeter. First the MPC on the metasurface fiber was employed to calibrate the polarization at the position of the metasurface to the DPC by removing the fiber attached to the IPL and measuring the output polarization with the POL. Then the unstructured fiber was aligned to the metasurface fiber and the polarization of the IPL was calibrated to the DPC using the MPC on the unstructured fiber. Schematics of the measurement setup are shown in Fig. 6 together with measurements from the metasurface polarimeter with the fiber exposure design. The results in Fig. 6c consist of polarization states measured by the metasurface fiber polarimeter, reference polarizations measured by the deterministic polarization controller, and polarization measurements using the in-line polarimeter; all represented on the same Poincaré sphere, viewed from opposing angles. The discrepancy between the DPC and the IPL polarization measurements is caused by inaccuracy in correction of polarization changes in the fiber (a 3-dimensional rotation on the Poincaré sphere) and polarization-dependent losses between the DPC and the IPL that causes a slight asymmetry of the polarization measurements on the Poincaré sphere (they are stretched towards the polarization state with the highest transmission). The root-mean-square error (RMSE) between measured and reference polarizations on all state-of-polarization parameters was around 0.006. Conversely, the RMSE for the device made using the flood exposure method was around 0.004. The lower error with the flood exposure approach is expected, due to an increased signal to the detectors. The improvement in error is, however, to a certain degree compensated by an improved polarization sensitivity of the polarization analyzers belonging to the device using the fiber exposure method. The RMSE obtained with the fiber-based metasurface polarimeters corresponds to the same level of precision that we earlier obtained with 4-output metasurface polarimeters on fused silica wafers (see appendix), implying that transferring the metasurface to the tip of a fiber does not

deteriorate the performance of the polarimeter. Furthermore, the presented accuracy is obtained with a power at each photodetector of less than 1 % of the input signal. These results show that the template stripping transfer lithography method is an effective method for fabricating high quality optical componts and they suggest that a fiber-based metasurface in-line polarimeter is a viable alternative to in-line polarimeters based on, e.g., pairs of tilted fiber Bragg gratings separated by birefringent fiber sections. Due to the inherent wavelength sensitivity of the metasurface design, we have shown that the metasurface polarimeter furthermore has a potential to extend its functionality to act as a wavemeter [27].

Conclusion

We have presented a new transfer-lithography process based on template stripping for nanostructuring of optical fiber facets. The applicability of this novel approach has been demonstrated by transferring a 4-output metasurface polarimeter to the facet of a 1550 nm single-mode fiber. The results show that the performance of the metasurface polarimeter is not negatively affected by the transfer from a wafer to an optical fiber.

The metasurface polarimeter-on-a-fiber is an excellent candidate for telecommunication applications with exceptional stability and compactness and no subsequent pigtailing requirements. The presented transfer technique may also be useful for sensor applications, such as fiber-based surface-enhanced Raman scattering probes and surface-plasmon-resonance sensors. By including active alignment of the silicon wafer base, the future prospect of the technique also includes integration of wavefront shaping elements like flat lenses and q-plates (spin-to-orbital angular momentum converters) directly onto the fiber facet. Furthermore, the demonstration of multiple-layer hybrid polymer structures opens for fiber-based devices with several consecutive layers of metasurfaces.

Appendix

We compare the performance of the fiber-based metasurface polarimeters with the performance of a fiber-coupled wafer-based metasurface polarimeter. The antenna arrays of the wafer-based metasurface polarimeter are embedded in layers of benzocyclobutene (BCB) polymer on top of a fused silica wafer. More fabrication details can be found in [24]. Polarization measurements (red circles) of a wafer-based polarimeter are shown in Fig. A1 together with reference polarization

(blue dots). The polarimeter is measured in an out-of-plane configuration. Measurements using the two different fiber-based metasurface polarimeter designs are shown in Figs. A2-A3 for comparison. The uncertainty on the polarization measurements (red error bars) is calculated from uncertainty in the intensity measurements and from error propagation through the calibration process using the general error propagation formula [28]. The uncertainty of the degree of polarization (DOP) is calculated from the uncertainty of the Stokes parameters [29].
The root-mean-square error (RMSE) between polarization states measured by the wafer-based metasurface polarimeter and reference polarization states for the wafer-based polarimeter is 0.005. We can therefore conclude that we have obtained the same level of precision with the fiber-based polarimeter as with the wafer-based polarimeter. It should be noted, however, that the variation in the polarization response between the polarization analyzers of the three devices affects the error and causes an uncertainty in the RMSE. Also the variance of the measured intensities, caused by electronic noise, is higher for the wafer-based metasurface polarimeter.

Acknowledgment
The authors acknowledge the fruitful collaboration with Prof. Federico Capasso of Harvard SEAS. The results in this article is based on his pioneering work on metasurfaces. The authors thank Carlos Mendoza (Innovation Center Iceland) for help with the characterization setup and Kesara M. Jónsson (University of Iceland) for help with SEM imaging. M. Juhl thanks Noah Rubin (Harvard SEAS) and Rou Ping Li (University of Waterloo) for helpful discussions about polarimetry.

References

[1] N. Yu and F. Capasso, “Flat optics with designer metasurfaces,” *Nat. Mat*, vol. 13, 2014.

[2] H.-H. Hsiao, C. H. Chu, and D. P. Tsai, “Fundamentals and applications of metasurfaces,” Small Methods, vol. 1, no. 4, p. 1600064, 2017.

[3] L. Zhang, S. Mei, K. Huang, and C.-W. Qiu, “Advances in full control of electromagnetic waves with metasurfaces,” *Adv. Opt. Mat.*, vol. 4, no. 6, 818–833, 2016.

[4] G. Kostovski, P. R. Stoddart, and A. Mitchell, “The optical fiber tip: An inherently light-coupled microscopic platform for micro- and nanotechnologies,” *Adv. Mat.* vol. 26, no. 23, pp. 3798–3820, 2014.

[5] N. Yu and F. Capasso, “Optical metasurfaces and prospect of their applications including fiber optics,” *J. Lightwave Technol.*, vol. 33, no. 12, 2015.

[6] J. P. B. Mueller, “Polarization in nanophotonics,” Ph.D. dissertation, Harvard Univ., Cambridge, MA, 2016.

[7] M. Principe, M. Consales, A. Micco, A. Crescitelli, G. Castaldi, E. Esposito, V. L. Ferrara, A. Cutolo, V. Galdi, and A. Cusano, “Optical fiber meta-tips,” *Light Sci. Appl.*, vol. 6, no. 3, 2017.

[8] G. Calafiore, A. Koshelev, F. I. Allen, S. Dhuey, S. Sassolini, E. Wong, P. Lum, K. Munechika, and S. Cabrini, “Nanoimprint of a 3D structure on an optical fiber for light wavefront manipulation,” *Nanotechnology*, vol. 27, no. 37, p. 375301, 2016.

[9] H. E. Williams, D. J. Freppon, S. M. Kuebler, R. C. Rumpf, and M. A. Melino, “Fabrication of three-dimensional micro-photonic structures on the tip of optical fibers using SU-8,” *Opt. Express*, vol. 19, no. 23, pp. 22910–22922, 2011.

[10] S. Scheerlinck, P. Dubruel, P. Bienstman, E. Schacht, D. V. Thourhout, and R. Baets, “Metal grating patterning on fiber facets by UV-based nano imprint and transfer lithography using optical alignment,” *J. Lightwave Technol.*, vol. 27, no. 10, pp. 1415–1420, 2009.

[11] B. Wang, T. Siahaan, M. A. Dündar, R. Nötzel, M. J. van der Hoek, S. He, and R. W. van der Heijden, “Photonic crystal cavity on optical fiber facet for refractive index sensing,” *Opt. Lett*., vol. 37, no. 5, pp. 833–835, 2012.

[12] E. J. Smythe, M. D. Dickey, G. M. Whitesides, and F. Capasso, “A technique to transfer metallic nanoscale patterns to small and non-planar surfaces,” *ACS nano*, vol. 3, no. 1, pp. 59–65, 2008.

[13] M. Khorasaninejad and F. Capasso, “Metalenses: Versatile multifunctional photonic components,” *Science*, vol. 358, 2017.

[14] W. T. Chen, A. Y. Zhu, V. Sanjeev, M. Khorasaninejad, Z. Shi, E. Lee, and F. Capasso, “A broadband achromatic metalens for focusing and imaging in the visible,” *Nat. Nanotech.*, vol. 13, pp. 220–226, 2018.

[15] A. Arbabi, E. Arbabi, S. M. Kamali, Y. Horie, S. Han, and A. Faraon, “Miniature optical planar camera based on a wide-angle metasurface doublet corrected for monochromatic aberrations,” *Nat Commun*., vol. 7, p. 13682, 2016.

[16] A. Y. Zhu, W.-T. Chen, M. Khorasaninejad, J. Oh, A. Zaidi, I. Mishra, R. C. Devlin, and F. Capasso, “Ultra-compact visible chiral spectrometer with metalenses,” *APL Photonics*, vol. 2, no. 3, p. 036103, 2017.

[17] J. P. B. Mueller, K. Leosson, and F. Capasso, "Ultracompact metasurface in-line polarimeter," *Optica*, vol. 3, no. 1, pp. 42–47, 2016.

[18] N. Rubin, A. Zaidi, M. Juhl, R. Li, J. P. B. Mueller, R. Devlin, K. Leosson, and F. Capasso, "Polarization state generation and measurement with a single metasurface," *Opt. Express*, vol. 26, pp. 21455-21478, 2018.

[19] A. Pors and S. I. Bozhevolnyi, "Waveguide metacouplers for in-plane polarimetry," *Phys. Rev. Applied*, vol. 5, no. 6, p. 064015, 2016.

[20] P. S. Westbrook, T. A. Strasser, and T. Erdogan, "In-line polarimeter using blazed fiber gratings," *IEEE Photonics Technol. Lett*., vol. 12, no. 10, pp. 1352–1354, 2000.

[21] P. Nagpal, N. C. Lindquist, S.-H. Oh, and D. J. Norris, "Ultrasmooth patterned metals for plasmonics and metamaterials," *Science*, vol. 325, no. 5940, pp. 594–597, 2009.

[22] N. Vogel, J. Zieleniecki, and I. Köper, "As flat as it gets: Ultrasmooth surfaces from template-stripping procedures," *Nanoscale*, vol. 4, no. 13, pp. 3820–3832, 2012.

[23] J. Lin, J. P. B. Mueller, Q. Wang, G. Yuan, N. Antoniou, X.-C. Yuan, and F. Capasso, "Polarization-Controlled Tunable Directional Coupling of Surface Plasmon Polaritons," *Science*, vol. 340, pp. 331–334, 2013.

[24] M. Juhl, C. Mendoza, J. P. B. Mueller, F. Capasso, K. Leosson, "Performance characteristics of 4-port in-plane and out-of-plane in-line metasurface polarimeters," *Opt. Express*, vol. 25, pp. 8697–8709, 2017.

[25] R. M. A. Azzam, "Stokes-vector and Mueller-matrix polarimetry," *J. Opt. Soc. Am. A*, vol. 33, pp. 1396–1408, 2016.

[26] B. Boulbry, J. C. Ramella-Roman, and T. A. Germer, "Improved method for calibrating a Stokes polarimeter," *Appl. Opt.*, vol. 46, pp. 8533–8541, 2007.

[27] E. B. Magnusson, J. P. B. Mueller, M. Juhl, C. Mendoza, and K. Leosson, "Neural polarimeter and wavemeter," *ACS Photonics*, vol. 5, no. 7, pp. 2682–2687, 2018.

[28] A. A. Ramos and M. Collados, "Error propagation in polarimetric demodulation," Applied Optics, vol. 47, no. 14, pp. 2541–2549, 2008.

[29] J. Taylor, *An introduction to error analysis, the study of uncertainties in physical measurements.* University Science Books, 1997, pp. 209-212.

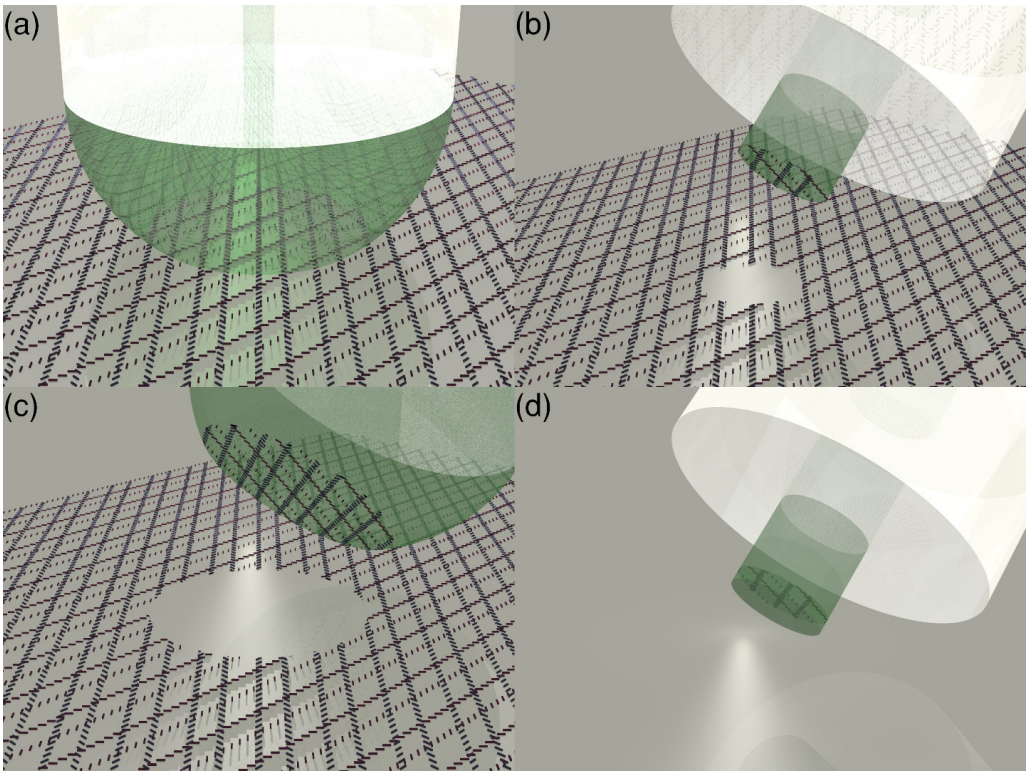

Fig. 1. (a) An optical fiber (white cylinder) with a drop of polymer (green hemisphere) on the tip in proximity to a metasurface consisting of arrays of gold nanoantennas. The metasurface is made of two superimposed gratings of antenna columns arranged in a pattern where the antennas in each column are rotated 90° relative to antennas in the neighboring column. (b) The polymer is UV-cured through the fiber core resulting in only the antennas under the center of the fiber being released from the wafer. (c) The polymer is UV-cured using flood exposure resulting in a larger metasurface area being released from the surface. (d) A second layer of polymer is cured on top of the existing polymer. The polymer is cured on an unstructured surface to ensure a flat end face.

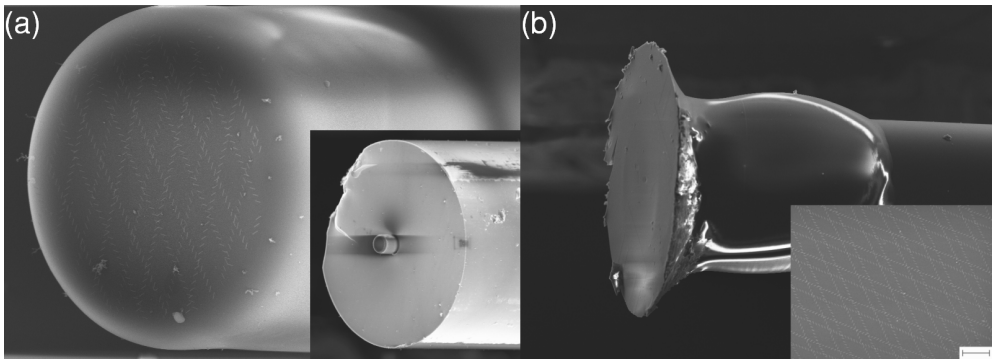

Fig. 2. Micrograph images of patterned fibers. (a) Image of a polarimeter fabricated with the fiber exposure approach, showing the 10 µm-diameter polymer rod with gold nanoantennas on the top. The inset shows a zoom-out of the entire fiber tip that has diameter of 125 µm. (b) Image of a patterned fiber facet using the flood exposure approach, where a much larger area of nanoantennas arrays is transferred. The inset shows a zoom-in of the transferred nanoantenna arrays (the scale bar represents a length of 2 µm).

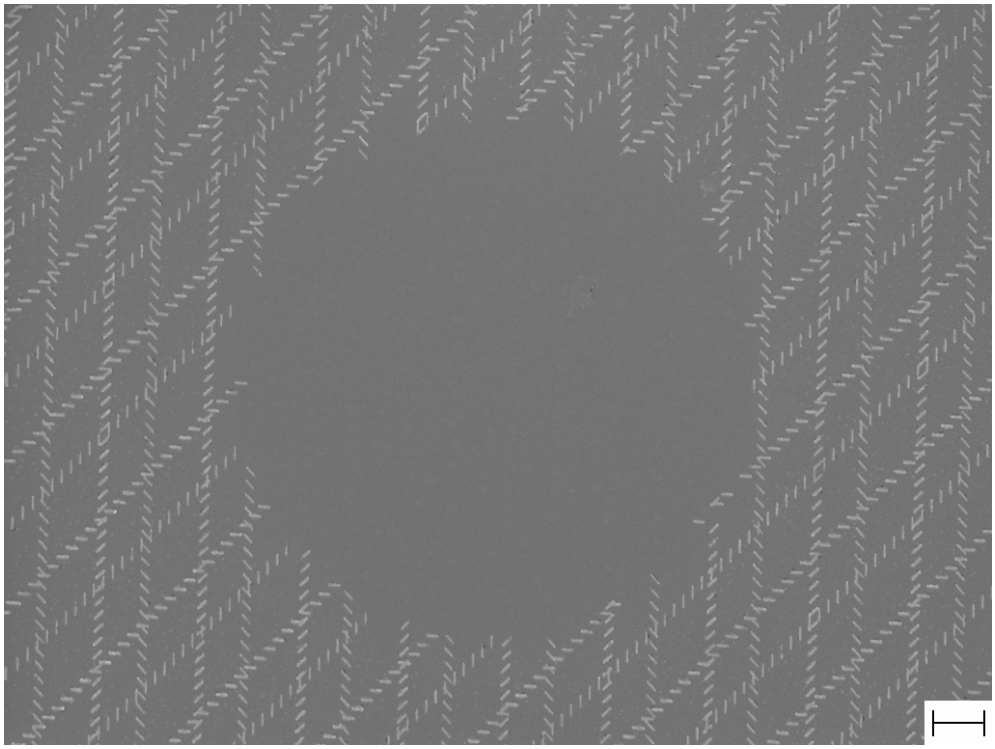

Fig. 3. Electron micrograph of metasurface on a silicon wafer after stripping. In the middle of the image is a circle with a diameter of about 10 µm, where the gold nanoantennas have been transferred to the fiber tip. The scale bar represents a length of 1 µm.

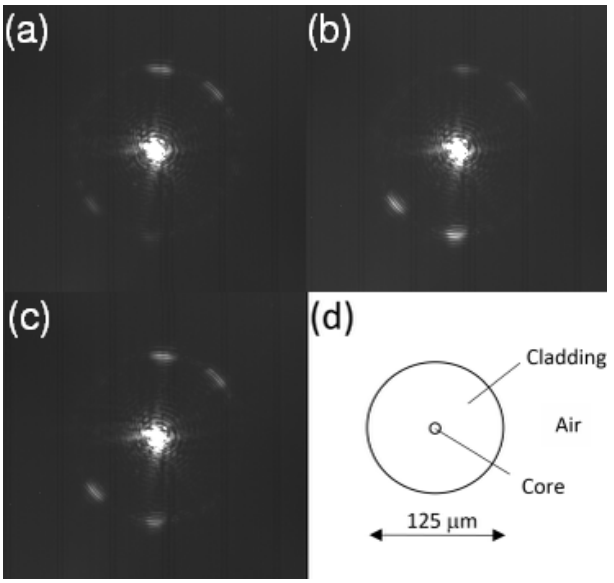

Fig. 4. Fiber-cladding images of an optical fiber facet patterned with a flood exposure metasurface polarimeter design. In-plane orders are seen rescattered out of plane at the fiber-cladding/air interface. The bright spot in the middle is the light emitted from the fiber that escapes being blocked by the reflective objective. The relative intensity of scattered orders varies with the polarization of the incoming light. (a) Right-hand circular polarization. (b) Left-hand circular polarization. (c) Horizontal linear polarization. (d) Schematic of fiber facet showing the dimensions of the cladding.

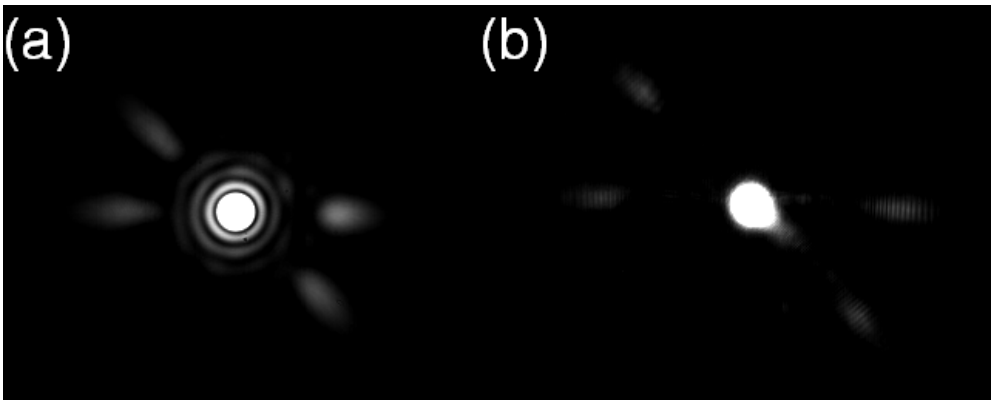

Fig. 5. Images of the out-of-plane orders for (a) fiber exposure design and (b) flood exposure design.

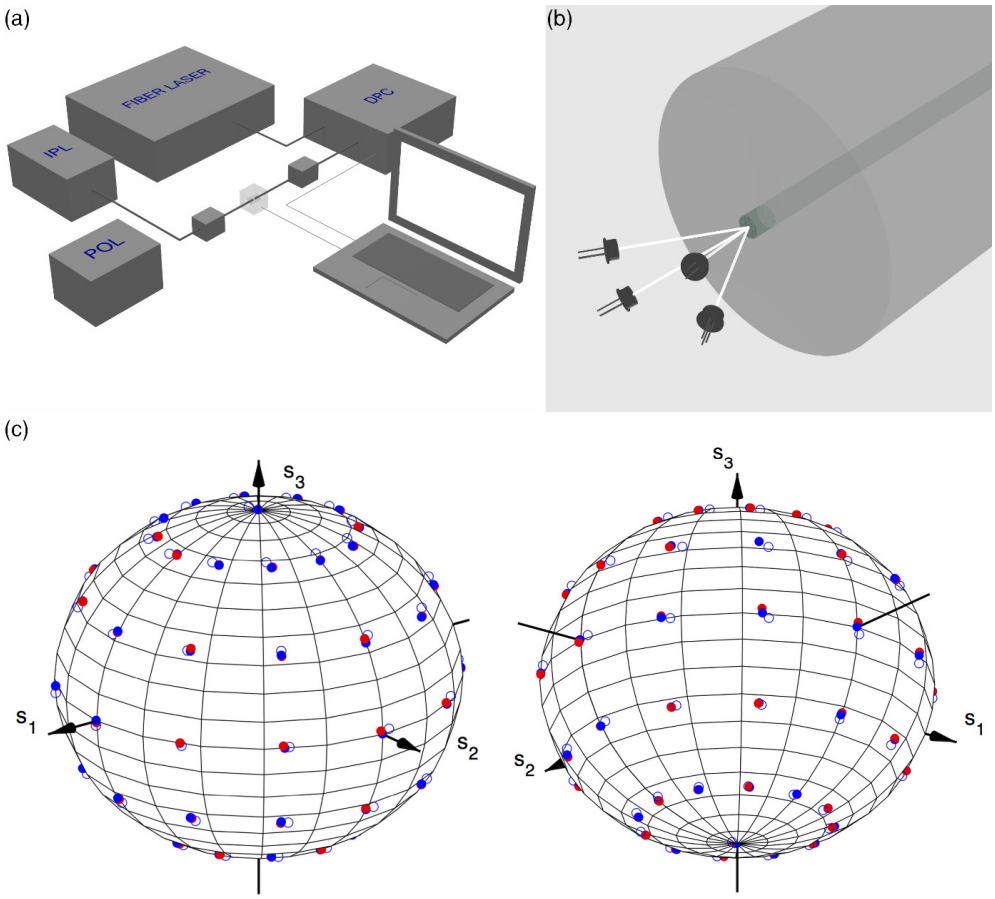

Fig. 6. (a) A schematic of the measurement setup showing a fiber laser connected to a deterministic polarization controller (DPC) with a 1550 nm single-mode fiber. The nanostructured fiber is connected to the output of the DPC and aligned to four photodiodes using a 3D-printed holder (the semitransparent box). An optical fiber with an unstructured tip is aligned to the nanostructured fiber to couple the signal into a commercial in-line polarimeter (IPL). The commercial free-space polarimeter (POL) and the manual polarization controllers (the two small boxes on the fibers) are used to calibrate the polarization. (b) The configuration of the photodetectors is illustrated. The diodes are scaled down in size relative to the fiber. (c) Measurements of the polarization state depicted on a Poincaré sphere, viewed from two opposite angles. Red dots are measurements using the metasurface polarimeter with the fiber exposure design, blue dots are reference polarization states measured by the DPC. The open blue circles are polarization states measured by the IPL.

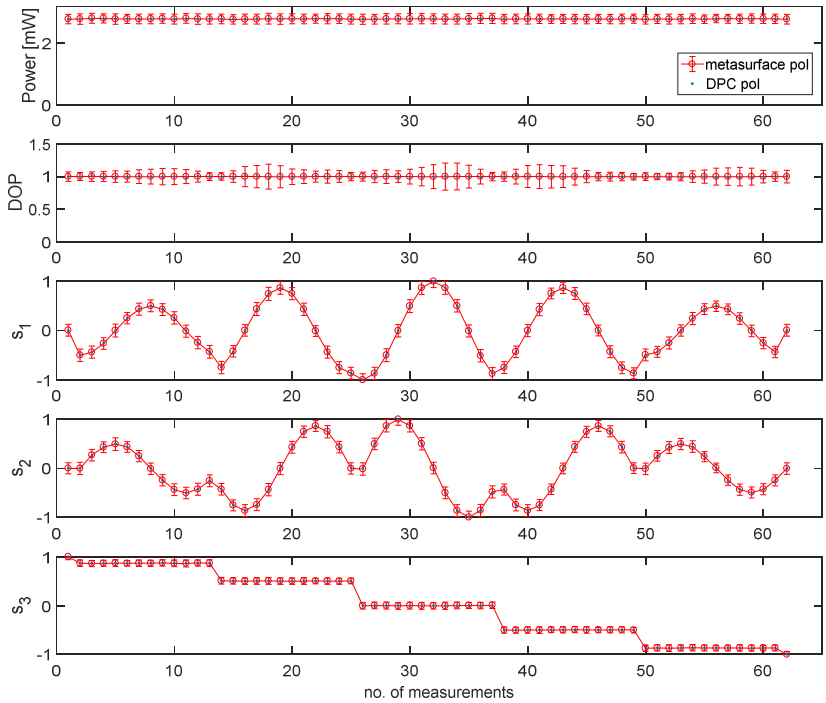

Fig. A1. Polarization measurements at a wavelength of 1550 nm using a wafer-based metasurface polarimeter. The first subplot is the power of the incident light, which is proportional to the first element of the Stokes vector, S_0. The next subplot is the degree of polarization (DOP) and the three last subplots are the parameters characterizing the state of polarization (SOP), $s_1 - s_3$. The red circles are the polarization measurements of the metasurface polarimeter, the blue dots are the reference polarizations set by the deterministic polarization controller (DPC). Standard deviation on the reference polarization measurements is not depicted on the plot, since the size of the error bars would be smaller than the size of the marker.

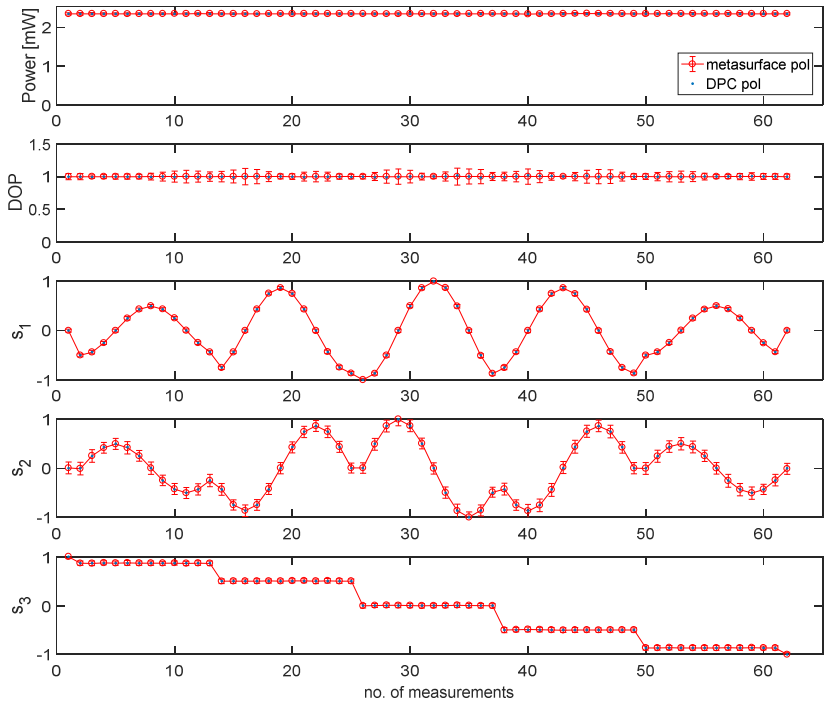

Fig. A2. Polarization measurements at 1550 nm using the fiber-based flood exposure metasurface polarimeter.

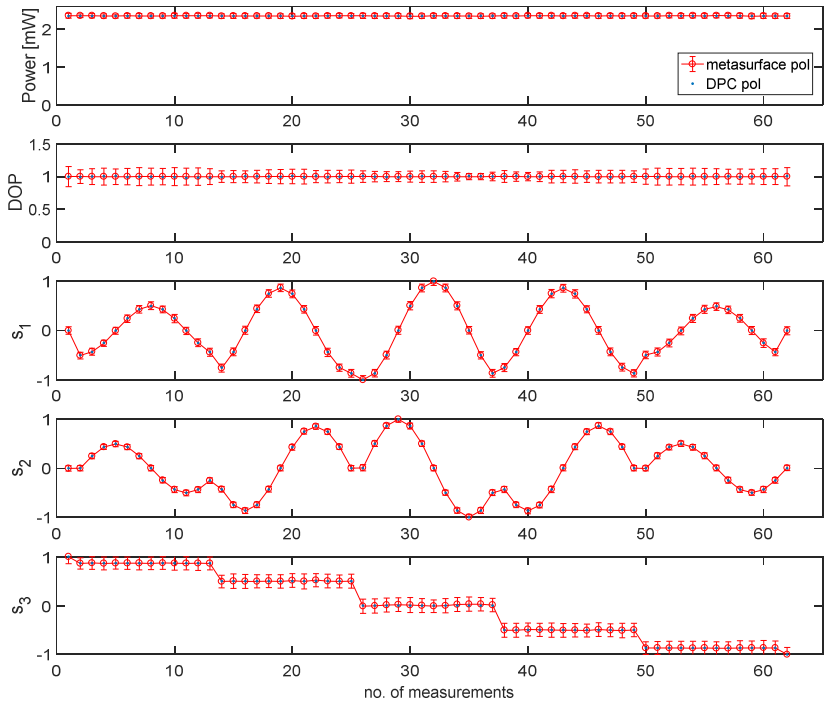

Fig. A3. Polarization measurements at 1550 nm using the fiber-based fiber exposure metasurface polarimeter.